Search for New Physics with a Single Top Quark Signature in the Boosted All Hadronic Final State

by

Kevin Nash

A dissertation submitted to The Johns Hopkins University in conformity with the requirements for the degree of Doctor of Philosophy.

Baltimore, Maryland

February, 2015

Abstract

We present two searches for massive resonances decaying with a single top-quark signature. First, we present a search for the W' boson decaying to a top and bottom quark, then a search for the singly produced b* quark decaying to a top quark and W boson. The data analysed for these searches corresponds to an integrated luminosity of 19.7 fb^{-1} collected by the CMS detector in proton-proton collisions at $\sqrt{s} = 8$ TeV. The use of cutting edge jet substructure algorithms allows the top quark jet to be distinguished from standard model hadronic jet backgrounds and is the central feature of these analyses.

We set 95% C.L. limits on the production cross section of a right-handed W' boson, together with constraints on the left and right-handed couplings of the W' boson to quarks. The production of a right-handed W' boson with a mass below 2.02 TeV decaying to an all-hadronic final state is excluded. This mass limit increases to 2.15 TeV when both all-hadronic and semileptonic decays are considered.

Additionally, limits on the production cross section of the right-handed, left-handed, and vectorlike b* quark boson are obtained. The masses of the left-handed,

ABSTRACT

right-handed and vectorlike b*-quark states are excluded in the range of 880-1390 GeV, 820-1430 GeV, and 800-1530 GeV respectively when considering the all-hadronic channel only. The masses of the left-handed, right-handed and vectorlike b*-quark states are excluded below 1390, 1420 and 1520 GeV when considering the combined all-hadronic, semileptonic, and dileptonic channels.

Primary Reader: Petar Maksimovic

Secondary Reader:

Acknowledgments

I would first like to thank my parents for their constant encouragement and love. Thanks to my Mom for getting me interested in physics by discussing the mysteries of the universe, and to my Dad who taught me to like math at a young age. When something went wrong they were always there to put it in perspective, and when something went well they were always there to congratulate me.

I would like to thank my advisor, Petar Maksimovic, for his guidance and optimism. He taught me both how to perform a physics analysis, and (possibly more important) how to deal with people in such a large collaboration. I thank him for teaching me that the better is the enemy of the good, for telling me to calm down when things look bleak, and for taking analysis ending problems and turning them into 30 minute cross-checks.

There are many to thank for my education in the technical details of experimental high energy physics analyses, but probably none more than Salvatore Rappoccio. Sal was there from my first attempts at getting things to work and had the patience to answer all of my basic questions. Many thanks to Guofan Hu, Gavril Giurgiu, Justin

Pilot, and James Dolen for helping me with specific analysis questions.

I would like to thank my friends and colleagues in the physics department. Thanks to Marc Osherson for putting up with me in the same office for four years. Thanks for discussing silly physics ideas with me, and reminding me to not take everything so seriously. Thanks to Dave Fehling, Ian Anderson, Chris Martin, Yongjie Xin, Matt Morris, Keith Redwine, Justin Bankert, Kevin Grizzard, and everyone else in the department for the lunches, parties, happy hours, and just being there to talk to.

I would like to thank the JHU physics staff for making sure my exams were scheduled on time and my forms were in order. Thanks for making sure I did not encounter any problems during my time here.

Without the hard work of everyone contributing to the construction and maintenance of the LHC and the CMS detector none of this would be possible. Also, thanks to everyone at Fermilab for making sure the LPC Cluster was working when approval was looming over my head.

Last but not least I would like to thank Grace for preserving my happiness regardless of what challenge I was facing. Thank you for putting up with the QFT all-nighters, the late night Higgs discovery announcement, the early morning meetings, and all of my stress and worry.

Contents

List of Tables

List of Figures

Chapter 1

Introduction

Modern particle physics is described by a theory called the standard model (SM). The SM describes a universe in which visible matter consists of particles of half-integer spin[1] called fermions. These fermions interact with each other through force mediating integer spin particles called bosons. This section provides a basic outline of this theory, and motivates a need for a more basic theory that underlies the SM.

1.1 Fundamental Particles

The known SM matter in the universe is around 98% Hydrogen and Helium with the final 2% being heavier elements. To a very good approximation, the known matter in the universe consists of protons, neutrons, and electrons. Electrons are categorized in the standard model as leptons and are fundamental. Protons and

[1] Intrinsic angular momentum

neutrons are composites of three quarks. The up quark (u) has $+2/3e^2$ charge, and the down quark (d) has -1/3e charge, so the proton is an up-up-down combination and the neutron is down-down-up. These quark compounds are called hadrons and are categorized into two families: baryons (three quarks), and mesons (two quarks).

Although this is a good approximation of the known universe, we know that there are more exotic phenomena that can be described by extending the quarks and leptons to three generations. The three lepton generations are defined by the electron, muon, tau and their corresponding neutrinos. The +2/3e charge quarks are the up, charm, and top; whereas the -1/3e charge quarks are the down, strange, and bottom. These quarks and leptons are summarized in Table 1.1 along with their charge and mass.

Quarks and leptons define all known fermionic matter, with gauge boson particles being responsible for particle interactions. The final particle, the Higgs boson, is responsible for the mechanism by which particles acquire mass.

1.2 Fundamental Interactions

Interactions in the SM can be described by the four fundamental forces: electromagnetic, weak nuclear, strong nuclear, and gravity. These forces manifest in the exchange of a corresponding elementary boson. The intrinsic properties of these force carrying particles are responsible for the range and relative strength of the interaction.

The electromagnetic force is responsible for well-known phenomena such as molec-

[2] e is the magnitude of the charge of the electron

particle	charge (e)	mass (MeV)
e	-1	0.5110
μ	-1	105.7
τ	-1	1777
ν_e, ν_μ, ν_τ	0	$< 2 \times 10^{-6}$
u	+2/3	2.3
d	-1/3	4.8
s	-1/3	95
c	+2/3	1.275×10^3
b	-1/3	4.18×10^3
t	+2/3	173.2×10^3

Table 1.1: List of SM fermions with their charge and mass. These particles all have spin 1/2 [1].

ular bonds. This force is mediated be the photon, a massless, chargeless, spin 1 particle, which photon interacts with charged particles only. The fact that the photon is massless leads to the infinite range of the electromagnetic force.

The weak nuclear force is the mechanism behind nuclear decay, and is described by three force carrying bosons; the W^+,W^-, and Z. These bosons are massive, which leads to the apparent short range nature of the weak force. The $W^\pm$ bosons have a charge of $\pm$1e whereas the Z boson is neutral, and all three have a spin equal to 1. The weak force is responsible for transitions between different types of quarks (see Table 1.1, and Section 1.6). Quarks and leptons both interact by the weak force.

The strong nuclear force is responsible for binding quarks together to form hadrons. The strong force describes the interactions of particles that carry color. Color is an intrinsic property of fundamental particles; and has three varieties; commonly labeled as red, green and blue. This force is mediated by gluons, which are massless and in-

particle	charge (e)	spin	mass (GeV)
γ	0	1	0
$W^{\pm}$	± 1	1	80.4
Z	0	1	91.2
gl	0	1	0
gr	0	2	$< 6 \times 10^{-38}$

Table 1.2: List of SM force carrying bosons with their charge, mass and spin. The graviton has not yet been observed [1].

teract with quarks. The theory behind the strong force is described in more detail in Section 1.4

The fourth known force, gravity, is both the most recognizable and least understood of the forces. All attempts at including gravity into the SM have failed, but hypothetically gravity should be mediated by the spin 2 graviton, which interacts with massive particles.. Gravity is by far the weakest of the fundamental forces.

The force carrying bosons and their properties are listed in table 1.2

1.3 Feynman Diagrams

Calculations in theoretical particle physics are facilitated by the use of Feynman diagrams. Feynman diagrams are pictorial representations of terms in the quantum mechanical scattering or decay amplitudes, and as such, aid in the calculation of physical observables like rates of particle interactions and decays. An example Feynman diagram is shown in Figure 1.1. In this diagram, an electron and a positron[3] interact

[3]Shown as an electron with an inverted line direction

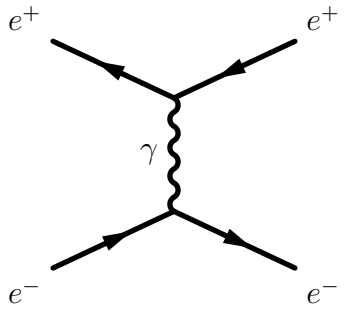

Figure 1.1: Feynman diagram depicting electron-positron scattering via the electromagnetic interaction.

with a "virtual" photon (γ); this diagram represents Bhabha scattering, responsible for electromagnetic attraction.

The rules governing the calculation of physical observables from these diagrams are defined by the theory of Quantum Electrodynamics (QED). Using these diagrams, the rules of QED let us calculate the matrix element ($\mathcal{M}$).

$\mathcal{M}$ can by related to physical quantities through the square modulus ($|\mathcal{M}|^2$), which is the probability density for a process to occur. From this, relevant quantities such as the cross section (see Section 2.1) of the process can be calculated.

Additionally, in the case that a particle decays we can evaluate the decay width (Γ). When a particle of mass $\mathrm{M_O}$ decays, the observed values of the invariant mass of the decay products ($\mathrm{M_i}$) follows a Breit-Wigner distribution centered at $\mathrm{M_O}$ [3].

$$\mathrm{P_{BW}}(\mathrm{M_i};\Gamma,\mathrm{M_O}) \;=\; \frac{1}{\pi}\frac{\Gamma/2}{(\mathrm{M_i}-\mathrm{M_O})^2+\Gamma^2/4} \tag{1.1}$$

The decay width represents the width of this distribution at half the maximum.

The average lifetime of the particle is $1/\Gamma$.

For a given process there can be multiple contributing diagrams, for instance for a calculation involving the Coulomb attraction shown in Figure 1.1, one must also consider the diagram shown in Figure 1.3, which has the same incoming and outgoing particles. Diagrams such as this interfere with each other constructively or destructively in the calculation of the matrix element, which can increase or decrease the cross section of the full process.

Each of the vertices in a Feynman diagram contributes a factor of the coupling constant α to the matrix element computation. In the calculation of the full matrix element for the electron positron scattering shown in Figures 1.1 and 1.3, we must consider diagrams with higher vertex multiplicity such as those seen in Figure 1.4. To approximate $\mathcal{M}$ in QED, we can perform an expansion in the vertex multiplicity n, summing over matrix elements within the same order i ($\mathcal{M}_{\mathrm{i}}^{\mathrm{n}}$). .

$$\mathcal{M} = \sum_{\mathrm{n}=1}^{\infty} \sum_{\mathrm{i}} \mathcal{M}_{\mathrm{i}}^{\mathrm{n}} \tag{1.2}$$

Due to the fact that the coupling constant α in QED is $1/137$, this expansion terminates quickly because high n diagrams contribute much less to $\mathcal{M}$. A calculation involving all diagrams with the least number of vertices is called leading order. Calculations involving all diagrams with higher order contributions as well are called

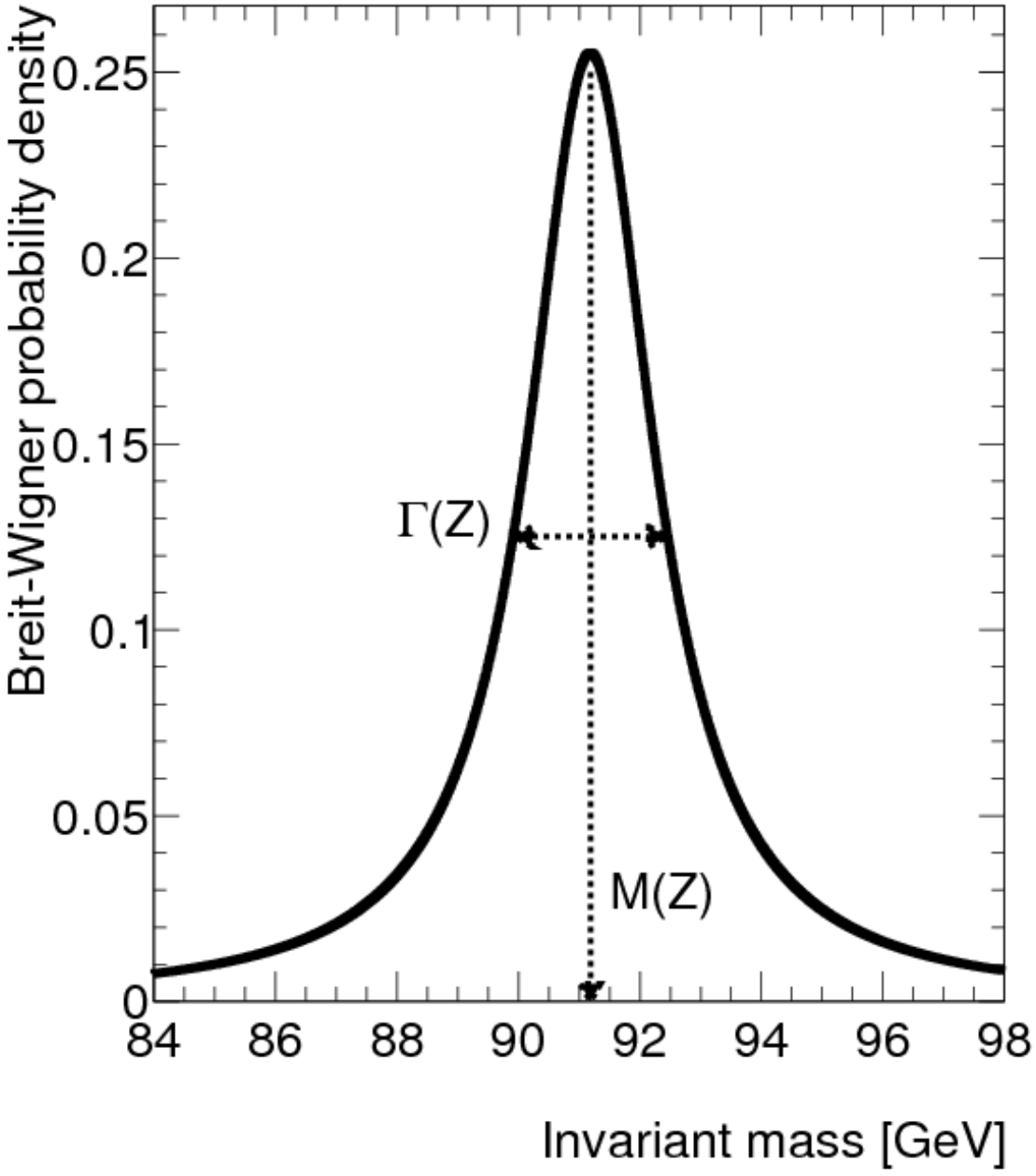

Figure 1.2: Breit-Wigner distribution centered on the Z mass [3].

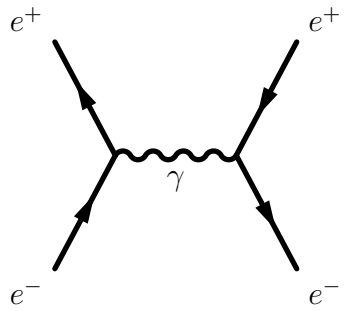

Figure 1.3: Feynman diagram depicting electron-positron scattering via the electromagnetic interaction in the s channel.

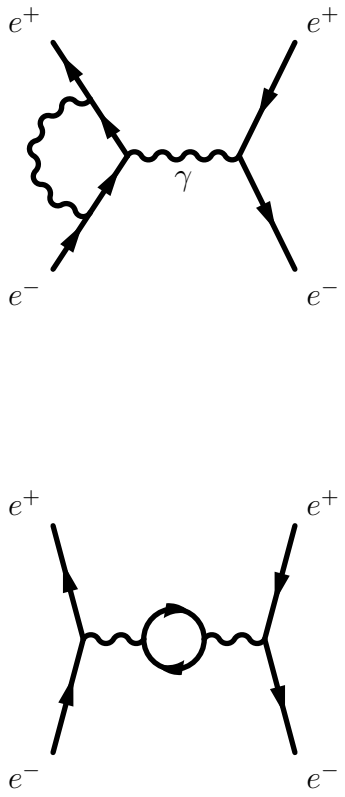

Figure 1.4: Feynman diagrams depicting NLO electron-positron scattering.

next-to leading order (NLO), next-to-next-to leading order (NNLO), etc.

Once the matrix element has been determined to an acceptable accuracy, we can extract the cross section in a straight forward manner. For the example electron-positron scattering process above the differential cross section has the following simplified equation due to the special case of identical mass particles:

$$\left(\frac{\mathrm{d}\sigma}{\mathrm{d}\Omega}\right)_{\mathrm{CM}} = \frac{|\mathcal{M}|^2}{64\pi^2 \mathrm{E}_{\mathrm{cm}}^2} \tag{1.3}$$

1.4 Quantum Chromodynamics

Quantum chromodynamics (QCD) is the theory describing the strong force, and is of particular importance for this thesis. The strong force is mediated by gluons which interact with particles that carry color. In QED, the photon is not charged, and thus can not interact with itself, however in QCD the gluon carries color and thus can interact with itself. Additionally, while in QED the addition of a vertex greatly reduces the cross section, the strong coupling constant α_s is of order 1, so higher order diagrams can contribute substantially to the measurement. This means that QCD processes are much more difficult to calculate than QED processes.

However, α_s is not constant, and in fact increases as the distance scale of an interaction increases (see Figure 1.5). This property of the the strong interaction is

called asymptotic freedom. For high $|q^2|$, α_s has the following form:

$$\alpha_{\mathrm{s}}(|\mathrm{q}^2|) = \frac{\alpha_{\mathrm{s}}(\mu^2)}{1 + (\alpha_{\mathrm{s}}(\mu^2)/12\pi)(11\mathrm{n} - 2\mathrm{f})\ln(|\mathrm{q}^2|/\mu^2)} \tag{1.4}$$

where n is the number of colors (3), f is the number of flavors (6), and μ^2 is an arbitrary energy scale where $\alpha_{\mathrm{s}}(\mu^2) < 1$. Because $11\mathrm{n} > 2\mathrm{f}$, α_{s} decreases as energy increases.

Therefore as the distance between two quarks increases, so do the forces holding them together. This large force at a characteristic distance ($\sim 10^{-15}$ m) is the reason why it is impossible to observe a free quark (quark confinement). Although quarks can not be observed alone, there are ways of precisely determining the physical properties of free quarks through reconstruction of their decay products.

Consider a quark pair that is produced in a high energy interaction. The quarks will have a high momentum relative to each other, and their separation increases quickly, and, together with it, the energy of the QCD field between them increases as well. Eventually, the energy between the quarks will reach a threshold where quark pair production is energetically favorable. At this threshold, the constituent quarks are then joined by these pair produced quarks. Additional quark pairs can be created many times, and the initial quark is detected as many hadrons that are collimated into a stream of particles called a jet. This process is called hadronization.

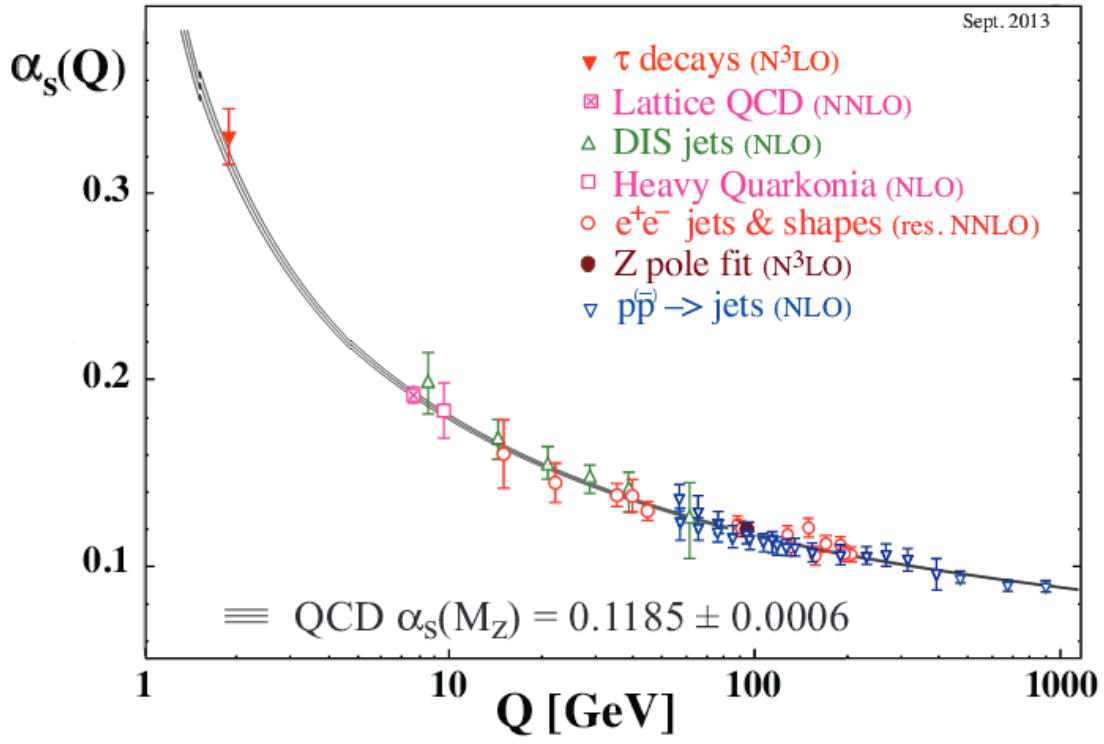

Figure 1.5: The QCD coupling constant α_S as a function of the energy scale Q [1].

The α_s parameter is low at short distances (or equivalently high energy); just like in QED, the impact of higher order diagrams is small. In this regime, QCD calculations using a finite expansion is possible. This allows us to only consider free quarks in calculations involving the scattering of highly energetic particles. The characteristic interaction energy where free quarks can be considered is above the constant Λ, which is in the range of 100 MeV to 500 MeV. This is much lower than energy scales considered in this thesis, so we will only be referring to free quark interactions [4].

1.5 Parton Distribution Functions

Hadrons are composite objects made up of two or three "valence" quarks, but also contain virtual quark-antiquark pairs ("sea quarks") and gluons (see Figure 1.6). These sea quarks and gluons are very important to consider when analyzing hadrons. Take for instance the quark masses listed in Table 1.1. Summing the valence quark mass for a proton, we would obtain a mass of 9.4 MeV, instead of the measured mass of 938.3 MeV. Therefore, the energy of a proton is shared among many partons, and for calculations it is useful to define parton distribution functions (PDFs). PDFs define the probability of a parton to carry a fraction x of the hadron. Figure 1.7 shows parton distribution functions for the proton at two characteristic energy scales.

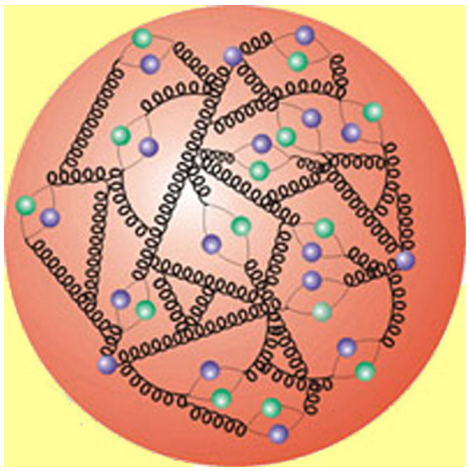

Figure 1.6: An illustration of a proton emphasizing the sea quark contribution [5].

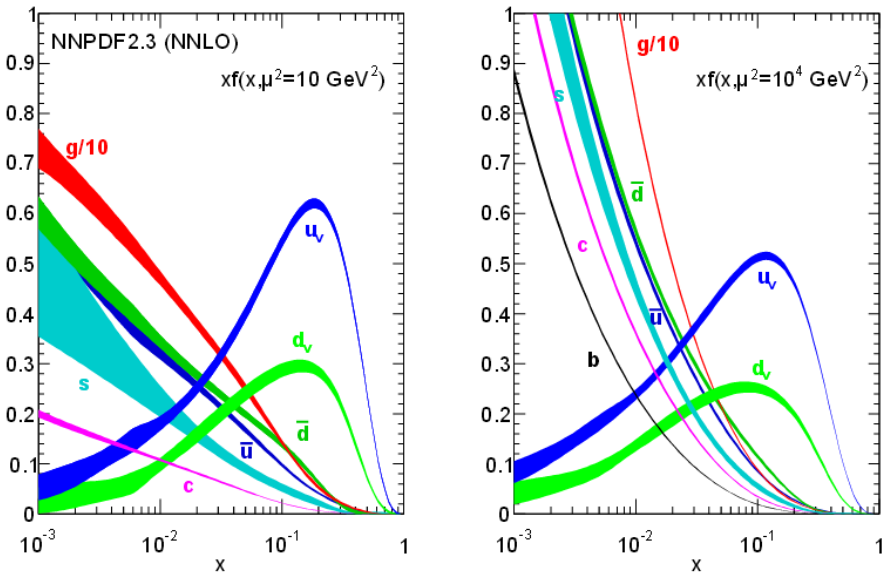

Figure 1.7: Parton distrubution functions for the proton. The left plot is evaluated at an energy scale of $\mu^2 = 10$ GeV^2, and the right plot at $\mu^2 = 10^4$ GeV^2 [1].

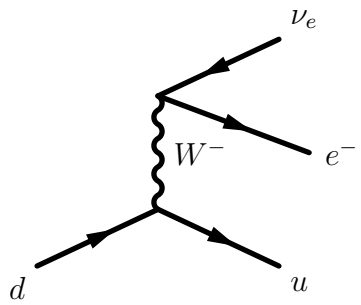

Figure 1.8: Feynman diagram depicting beta decay via the weak interaction.

1.6 The Weak Force

Both quarks and leptons interact via the weak force. As can bee seen in Figure 1.8 (beta decay), this force is carried by massive W and Z bosons. It is weaker than both the electromagnetic and the strong force, which leads to longer decay times for weakly decaying particles. The weak force is responsible for changing of quark flavor in an interaction. In the decay of a light quark, the W lies far away from the real mass, and thus the decay is suppressed. A vertex involving a change is quark flavor contributes a factor of V_{ij} to the matrix element, where V_{ij} is an element of the Cabibbo Kobayashi Maskawa (CKM) matrix (shown in Figure1.9). For example, the calculation of the diagram in Figure 1.8 includes a factor of $V_{ud} = 0.97427$. The CKM matrix is roughly diagonal, which means that a process which changes quark generation is rare.

Weak force interactions are dependent on the chirality of the interacting particle. Chirality for massless particles is dependent on the relative orientation of the momentum and spin axes. Particles with momentum and spin aligned are referred to as right-handed, and particles with the momentum axis opposite to spin are left-

$$V_{\mathrm{CKM}} = \begin{pmatrix} 0.97427 \pm 0.00014 & 0.22536 \pm 0.00061 & 0.00355 \pm 0.00015 \\ 0.22522 \pm 0.00061 & 0.97343 \pm 0.00015 & 0.0414 \pm 0.0012 \\ 0.00886^{+0.00033}_{-0.00032} & 0.0405^{+0.0011}_{-0.0012} & 0.99914 \pm 0.00005 \end{pmatrix}$$

Figure 1.9: The CKM quark mixing matrix [1].

handed[4]. For massive particles the concept of chirality is generalized such that right- and left-handed components of a wavefunction can be extracted by using the right-handed operator $(1+\gamma^5)/2$ and the left-handed operator $(1-\gamma^5)/2$. The W boson only interacts with left-handed chiral fermions whereas the Z boson interacts with right- and left-handed fermions with differing strengths.

1.7 Electroweak Symmetry Breaking

Through the electroweak symmetry breaking mechanism, the mass of the W and Z bosons, and all fermions can be generated in the SM. We consider a scalar potential of the form:

$$\mathrm{V}(\Phi) = \mathrm{m}^2\Phi^\dagger\Phi + \lambda(\Phi^\dagger\Phi)^2 \tag{1.5}$$

$$\Phi = \frac{1}{\sqrt{2}}\begin{pmatrix} \sqrt{2}\phi^+ \\ \phi^0 + \mathrm{i}a^0 \end{pmatrix} \tag{1.6}$$

where Φ is the Higgs field. A plot of this potential can be seen in Figure 1.10. The minimum of the potential is not at V(0), and this point is unstable. The Higgs field

[4]This convention is reversed for anti-particles

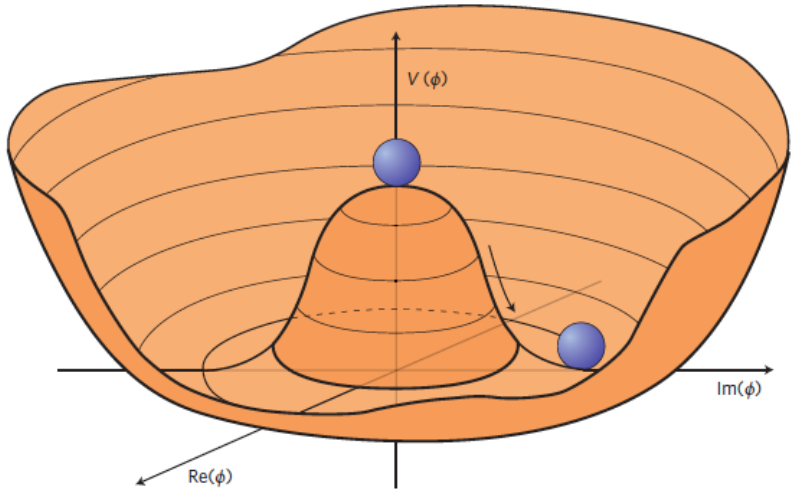

Figure 1.10: A diagram of the the Higgs potential.

has a non-zero vacuum expectation value (VEV).

Using the Higgs Lagrangian

$$\mathcal{L} = (\mathrm{D}_\mu\Phi)^\dagger(\mathrm{D}_\mu\Phi) - \mathrm{V}(\Phi) \tag{1.7}$$

$$(\mathrm{D}_\mu\Phi) = (\partial_\mu + \mathrm{ig}\sigma^\alpha \mathrm{W}_\mu^\alpha/2 + \mathrm{ig}^{'}\mathrm{YB}_\mu/2)\Phi \tag{1.8}$$

we can extract the masses of the W and Z bosons as

$$M_W^2 = \frac{g^2v^2}{4} \tag{1.9}$$

$$M_Z^2 = \frac{(g^{'2} + g^2)v^2}{4} \tag{1.10}$$

One new particle is predicted, a massive, chargeless, spin 0 boson called the Higgs.

A particle consistent with the Higgs boson has been discovered in 2012 at the LHC.

1.8 Beyond the Standard Model

The SM is possibly the most successful theory in physics, but also one that is ultimately incomplete. We know that there are physical phenomena that the SM does not predict. The presence of dark matter and dark energy in the universe [6] is not currently explained by the SM. Dark matter and energy account for approximately 95% of the universe. The SM does not explain the observation of neutrino oscillations [7], which implies that neutrinos have mass. The SM also does not naturally explain the relative values of fundamental constants such as why the weak force is 10^{29} times as strong as gravity. This issue is known as the hierarchy problem, and it is assumed that a complete theory would have a natural explanation for the seemingly random values of these constants.

It is essential for a complete understanding of the universe that we probe beyond the standard model (BSM) theories that provide solutions to these issues. Theories involving compact extra dimensions [8] for example provide a natural explanation to the hierarchy problem. In these theories forces propagate in higher dimensions that are compactified. In this theory, the propagation of SM massive fields in higher dimensions leads to discrete modes, which are detectable as new massive particles. The propagation of the SM W or Z leads to excited modes that are referred to as

the W′ and Z′. A novel way to look for BSM physics then is to attempt the creation and detection of massive states such as these bosons. In this thesis we discuss one such search for a W' boson, which is additionally predicted by many BSM theories such as Little Higgs [9], Composite Higgs models [10], and Noncommuting Extended Technicolor [11].

Chapter 2

Experimental Setup

One way to search for BSM physics is to produce new particles directly. For this, we collide lighter particles at a high energy. The energy released in the collision can manifest in more massive particles[1] via mass-energy equivalence ($E=mc^2$). The collision may create one or more of these new particles, and from it's decay products an experimenter can reconstruct the properties of the new BSM massive state and study the properties (mass, decay width, spin, SM couplings etc.).

For the measurements presented in this thesis, we collide high energy proton beams, which are designed to produce a high collision energy in comparison to fixed-target or electron-positron collisions.

[1] In SUSY there will usually be two

2.1 Luminosity and Cross Section

To understand how many occurrences of any physical process to expect in a set of collisions, we need to define at a minimum the concepts of luminosity, L, and cross section, σ.

The cross section of a process is a measure of the probability that a collision will produce the particles of interest. The phrase cross section refers to the physical cross section of a classical target and is thus measured in units of area. In a high energy collision, the cross section no longer refers to the physical dimensions of the target, and can be calculated directly from Feynman diagrams. The areas associated with these cross sections is very small and is measured in barns (b), which is $10^{-28}m^2$. BSM physics signatures have cross sections that are generally on the order of picobarns (pb) or femptobarns (fb). The process cross section is highly dependent of the energy of the collision and is why it is very important to have large, high energy accelerators for the discovery of new physics. The cross section of some SM processes are shown in Figure 2.1.

Luminosity is a measure of the intensity of the colliding beams and is the number of collisions expected per unit time per unit area. To look for BSM physics, we need to collect an ensemble of useful collisions (events), and thus higher luminosity leads to a larger ensemble, and consequently higher statistical precision of the measurement . Additionally, collecting data over time leads to a larger ensemble, so the time-integrated luminosity is a more useful variable to describe the total amount of

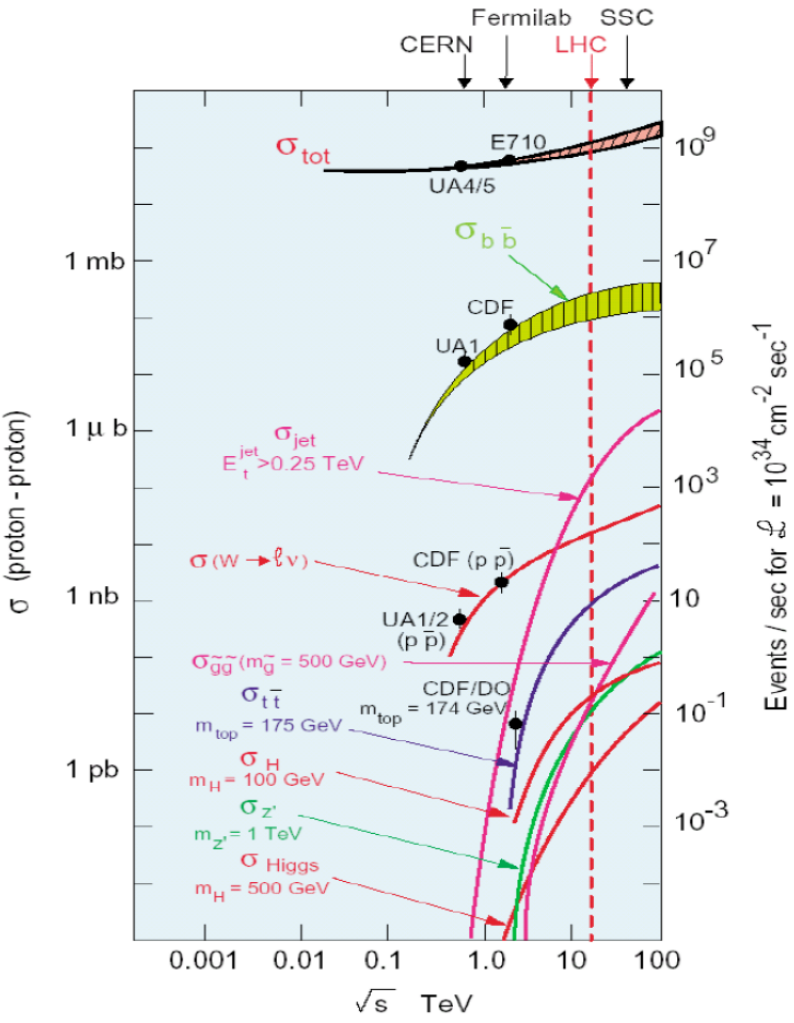

Figure 2.1: Standard model cross sections as a function of collision energy.

data collected, which is reported in fb^{-1}. Given in relevant collider properties, the luminosity can be defined as [12]:

$$\mathrm{L} = \frac{\gamma \mathrm{f} \mathrm{k_B} \mathrm{N_p^2}}{4\pi\epsilon\beta^*}\mathrm{F} \tag{2.1}$$

where γ is the Lorentz factor, f is the frequency of revolution, k_B is the number of bunches in the beam, N_p is the number of protons per bunch, ϵ is the transverse emittance, β^* is the betatron function, and F is a reduction factor based on the crossing angle.

With these two concepts we can extract the predicted number of events, N_i, for a given process i:

$$N_\mathrm{i} = \int L\mathrm{d}t \times \sigma_\mathrm{i} \tag{2.2}$$

2.2 The LHC

The Large Hadron Collider (LHC) is a particle accelerator designed to reach collisions energies far surpassing any previous design. The LHC is a synchrotron that accelerates protons to 99.999997% the speed of light. These protons beams are then collided at a center-of-mass energy ($\sqrt{s}$) of 8 TeV. The accelerator segments and detectors at the LHC are shown in Figure 2.2.

A proton at the LHC starts out as hydrogen gas within the injector of LINAC 2

linear accelerator. The atoms are ionized using an electric field, stripping the electron. The resulting proton is accelerated using an oscillating electric field. The protons are accelerated in a straight line to an energy of 50 MeV, or 31% the speed of light.

At this energy, linear acceleration is not practical, and the protons enter the Proton Synchrotron Booster (PSB). The PSB is composed of four 157 m circumference superimposed synchrotrons that accelerate the protons using electric fields that are synchronized to the revolution frequency of the beams. The protons are kept on the circular accelerator with a magnetic field directed into the plane formed by the accelerator ring, which increases in strength as the protons gain energy. After the acceleration from the booster, the protons are at en energy of 1.4 GeV, or 92% the speed of light.

After the PSB, the protons enter the Proton Synchrotron (PS), a 628 m circumference synchrotron, which accelerates the protons to 25 GeV, or 99.93% the speed of light. After the PS, the protons enter the Super Proton Synchrotron (SPS), a 7 km circumference synchrotron, which accelerates the protons to 450 GeV, or 99.9998% the speed of light.

Finally, the beams enter the LHC. This is the final synchrotron ring, with a circumference of 27 km. After the SPS, the protons are inserted into the LHC in one of two evacuated tunnels depending on which direction around the ring the beam is to travel.

The LHC uses 1232 dipole magnets to keep the protons in the ring as they acceler-

ate. which provide an 8.3 T field over their length. In order to deliver such a field, the magnets use superconducting niobium-titanium cables. These cables are cooled by superfluid helium to -271.3 C in order to achieve this superconductivity. During each revolution the energy of each proton in the LHC ring increases by 5 MeV. After being fully accelerated in the LHC, the protons are at an energy of 4 TeV, or 99.999997 %the speed of light.

The proton beams are then directed together for collisions in four positions around the ring. Each beam in the LHC ring contains 2808 bunches of protons, and each bunch contains 110 billion protons. These bunches need to be collimated in order to maximize collision frequency, which is accomplished by the use of 392 focusing quadrupole magnets. Each of these collision points houses its own detector, ALICE (A Large Ion Collider Experiment), ATLAS (A Toroidal LHC Apparatus), CMS (Compact Muon Solenoid), and LHCb (Large Hadron Collider beauty). The ALICE detector is primarily used for experiments involving heavy ion collisions that expand the current understanding of concepts such as the quark-gluon plasma and quark confinement LHCb is specialized for physics involving b quarks, such as measuring CP violation parameters from b-hadron interactions.

CMS and ATLAS are large general purpose detectors. These detectors are used for many different types of physics searches, and are the two detectors responsible for the Higgs boson discovery. For the purposes of this thesis we will be concentrating on the CMS detector

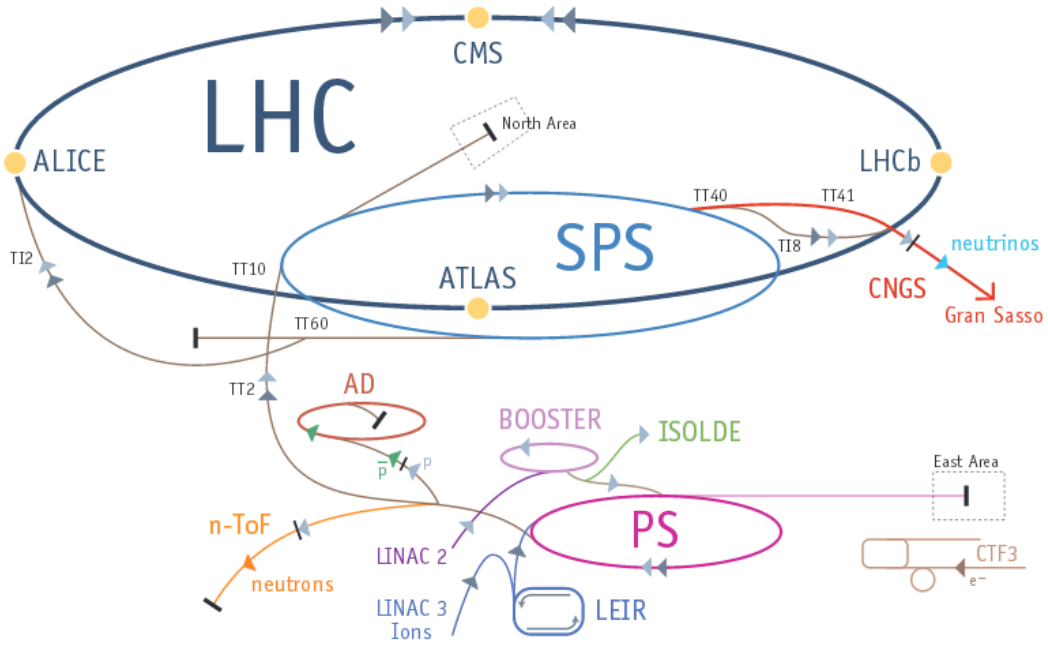

Figure 2.2: A diagram of the LHC [2].

2.3 CMS detector

Here we will detail the basics of the CMS detector subsystems, for a more complete description, see Reference [12]. The purpose of the CMS detector is to measure properties of particles that are created in a collision such as the energy and trajectory. The detector needs to collect enough information so that particles can be reconstructed and classified. Generally, we can reconstruct most physics signatures by analyzing electrons, muons, photon, charged hadrons, and neutral hadrons. The CMS detector has dedicated algorithms and systems that are specifically designed to identify each of these categories. In order to reconstruct these particles, we impose a uniform axial magnetic field throughout the inner detector with the use of a superconducting magnet.

The trajectory of charged particles is important for extracting information such as charge and momentum. The process of reconstructing the trajectory of these particles is called tracking. Near the interaction point tracks are very dense, and tracking becomes very difficult. In this region we use a fine array of silicon pixels that register a charge particles position based on charge deposited in the device. Additional measurements are made by a second series of silicon detectors called the Silicon Strip Tracker. Using a series of these position measurements, we can fit a charged particle track.

Energy can be measured by the use of calorimeter systems. A calorimeter is a detector designed such that a particle will deposit all of its energy within its volume

in the form of photons, which can be detected to extract a measure of the total energy. These systems are subdivided into the Electromagnetic Calorimeter (ECAL) and Hadronic Calorimeter (HCAL). The ECAL uses scintillation crystals to detect particles that interact primarily with the electromagnetic force such as electrons and photons. Hadrons pass through the ECAL with minimal loss and deposit energy in the HCAL, which uses layers of absorber and scintillator to first create a shower of secondary particles, and then measure the total energy of these secondary particles.

The detection of muons requires a specially designed system that lies outside of the ECAL, HCAL, and magnet. Muons pass through the ECAL and HCAL without losing a substantial fraction of their energy. To reconstruct the trajectory of muons, we use several different systems both inside and outside the magnet.

See Figure 2.3 for a diagram of the full detector, and Figure 2.4 for a cross-sectional view of the detector subsystems.

2.3.1 Pixel Tracker

The closest detector system to the interaction point is the silicon pixel tracking system (see Figure 2.5). . This system extends from a radius of 4 cm to 11 cm in the barrel, and is designed to track charged particles in a very dense environment. This is achieved with three arrays of two dimensional silicon pixels placed at a radii of 4.4 cm, 7.3 cm, and 10.2 cm, as well as two endcap disks for a total of 65 million pixels. When a charged particle traverses one of the 100 μm $\times$ 150 μm pixels, it

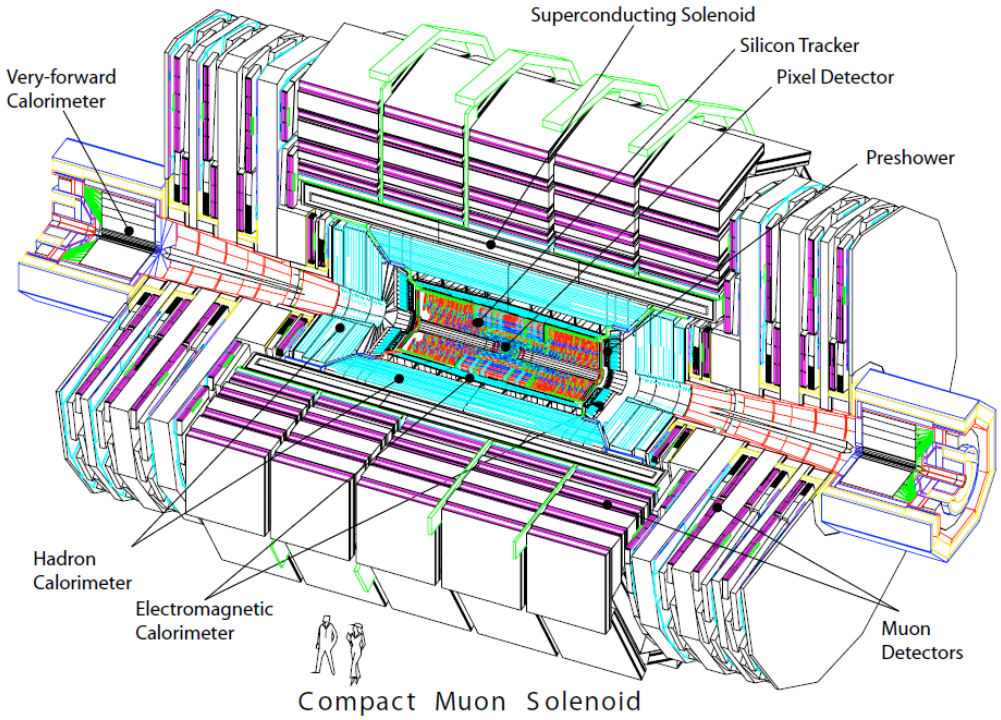

Figure 2.3: A diagram of the full CMS detector.

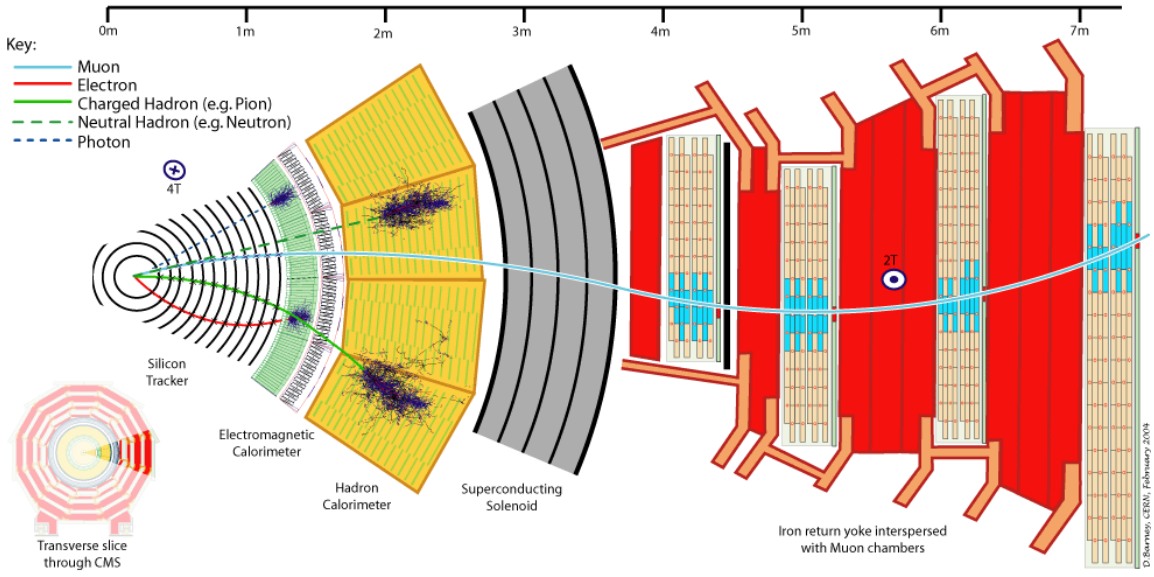

Figure 2.4: A cross-sectional view of the CMS detector.

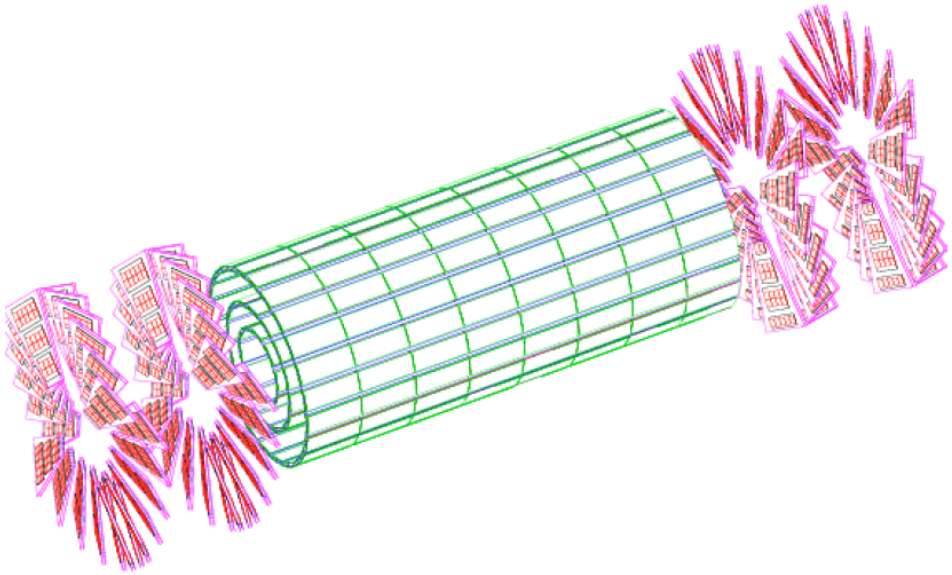

Figure 2.5: A diagram of the pixel detector.

imparts enough energy to the silicon to eject an electron. The electrons and their corresponding hole are detected on the pixel surface as a signal. This signal allows us to extract a position measurement for the charged particle.

The entire system exists in a magnetic field, so the trajectory of the electrons and holes are deflected in the r,ϕ plane before detection. The angle of this Lorentz drift is 23°, which causes the electron-hole pairs to be detected over a wide region covering multiple pixels. This effect improves the spacial resolution to 10 μm in r-ϕ space due to the fact that the charge center can be reconstructed by more measurements, whereas the z resolution is 20 μm due to the fact that there is no magnetic deflection in this direction. The pixel detectors in the endcap disks are angled at 20° in a turbine-like design to take advantage of this effect.

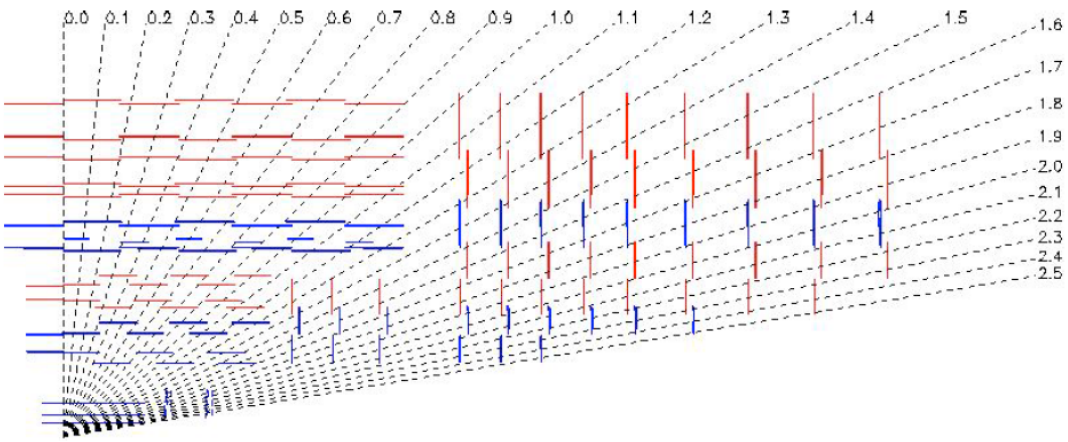

Figure 2.6: A diagram of the silicon tracking system.

2.3.2 Silicon Strip Tracker

Outside of the silicon pixel tracker (see Figure 2.6) out to a radius of 130 cm in the barrel lies the silicon strip tracking system.

The system in segmented into the inner barrel, outer barrel, inner disk, and endcap segments. The inner barrel segment (20 cm $<$ r $<$ 55 cm) uses four arrays of 10 cm $\times$ 80 μm silicon microstrips . The outer barrel (55 cm $<$ r $<$ 130 cm) uses six arrays of large pitch 25 cm $\times$ 180 μm silicon microstrips.

The endcap silicon strip detector consists of nine disks from 120 cm $<$ z $<$ 280 cm. The inner disk segment contains three smaller disks that connect the inner barrel and endcap segments.

2.3.3 Electromagnetic Calorimeter

The ECAL (see Figure 2.7) is designed to provide energy information for electrons and photons. These particles will typically deposit all of their energy within the detector, which is detectable as photons.

To do this, the ECAL uses 61200 lead tungstate ($PbWO_4$) scintillation crystals in the barrel and 7324 in each endcap. Lead tungstate is chosen as a scintillation material because it has a short radiation length (0.89 cm), fast response (25 ns for 80% of light), and can withstand harsh radiation environments (10 Mrad). The light emitted is around 30 photons per MeV for the energy of the particle of interest, which is somewhat low. Therefore, the ECAL uses avalanche photodiodes in the barrel and voltage phototriodes in the endcap segments to amplify the signal upon readout.

The endcap regions of the ECAL include a preshower detector that is used to distinguish high energy photons from decaying pions. A pion decaying to two closely spaced photons can mimic one high energy photon to the 2.2 cm wide ECAL crystals. The preshower is able to distinguish these events with a finer granularity (2 mm) silicon strip detector.

2.3.4 Hadronic Calorimeter

The HCAL (see Figure 2.8) is designed to give the energy of charged and neutral hadrons, which generally lose very little energy in the ECAL. The HCAL is segmented

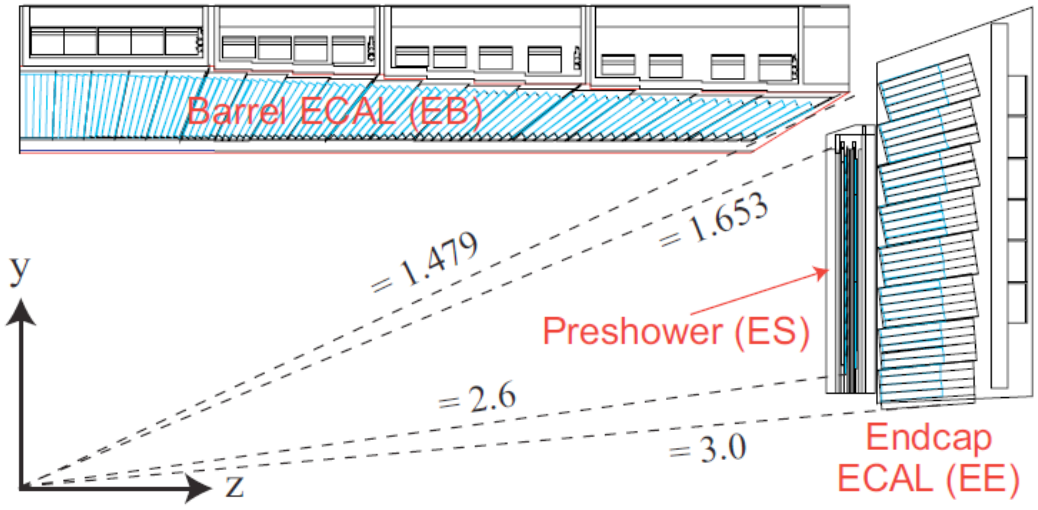

Figure 2.7: A diagram of the ECAL system.

into the inner barrel (inside the magnet), outer barrel (outside the magnet), endcap, and forward (close to the beamline).

The HCAL uses alternating layers of absorber and scintillator to calculate the energy of these hadrons. The absorber creates a cascade of secondary particles that emit photons in the scintillator which can then be detected and summed to reconstruct the energy of the initial hadron. The photons emitted in the scintillator are carried to the photodetectors by optical waveguides. The HCAL uses hybrid photodiodes to detect the scintillation light and provide a signal that can be used to extract the total energy of the hadron.

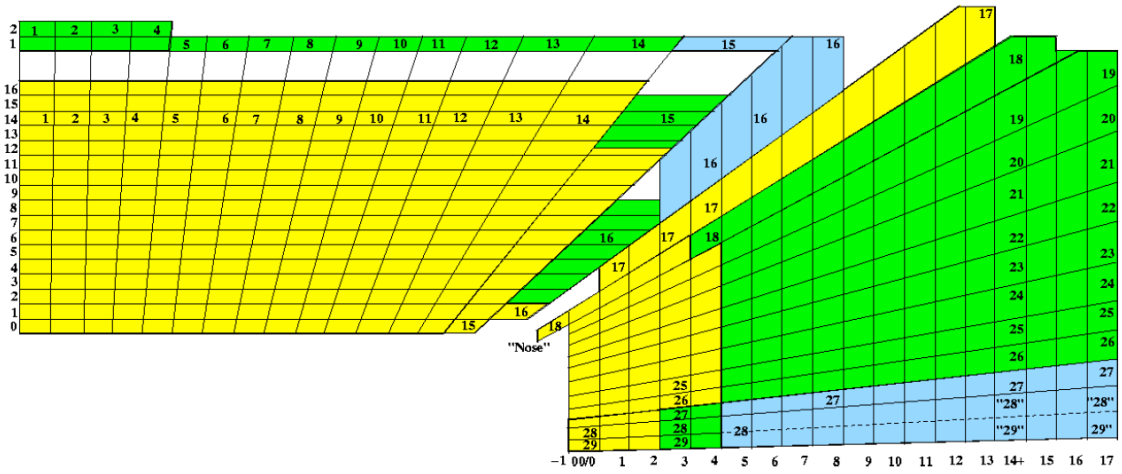

Figure 2.8: A diagram of the HCAL system.

2.3.5 Magnet

A charged particle moving perpendicular to a magnetic field follows a helical trajectory. The curvature of this helix is dependent on the momentum of the particle, and the handedness is dependent on the charge. Therefore, by immersing the tracking volume in an axial magnetic field we can get an accurate measurement of these properties. The stronger the magnetic field, the more precise these measurements can be for a high energy particle due to the more distinct curvature. To produce this field, CMS employs the largest superconducting magnet ever built.

The design goal for the magnet is to be able to reproduce high momentum muons. The benchmark used for this is to have a momentum resolution of $\Delta p/p \leq 10\%$ at a muon momentum of 1 TeV. To achieve this, we employ a solenoid with a length of 12.9 m and bore of 5.9 m. The coils of this solenoid are superconducting niobium-titanium, which produce a uniform 3.8 T magnetic field in the interior. The coils are

wound in four layers, for a total of 2168 turns that carry 19.5 kA of current.

The magnet additionally provides structural support to withstand the weight of the CMS detector as well as the magnetic force exerted from it's own magnetic field.

2.3.6 Muon System

The reconstruction of muons and electrons starts at the inner silicon tracking system. Whereas electrons deposit their energy in the ECAL, a muon will traverse the ECAL and HCAL without significant interaction because a muon is around 200 times as massive. Muons are of interest to the Higgs discovery as well as BSM physics, and an accurate determination of the muon energy is also required for determination of the total event energy and missing energy. Therefore, the CMS detector has a large system purely designed to reconstruct muons, which lies outside all other detector systems at CMS.

The muon system is comprised of a gaseous detectors interleaved with iron. The iron is saturated with the return field of the magnet, which creates a magnetic field at one half of the internal field strength and oriented in the opposite direction. The three layers of this "return yoke" system bends muons to get an accurate measure of the momentum outside of the magnet.

The trajectory of the muons is reconstructed with three types of gaseous detectors. The detectors work on the same basic principle, where an incoming muon ionizes the gas creating an electron-hole pair. The electron is detected by the anode, and the

hole is detected by a cathode. A coincidence of these two measurements gives a measure of the position and time that a muon traversed the detector. With a series of these measurements, a trajectory can be fit, and physical quantities of interest can be reconstructed.

In the barrel region ($|\eta| < 1.2$), drift tubes are used because the neutron flux and magnetic field are low. A drift tube is a detector consisting of a gas filled tube with an anode wire. The ionized electron from the gas volume travels to the anode wire, and a measurement of position is made. The detection of this electron registers the position along the wire (z coordinate). The r-ϕ coordinate within the drift tube cross sectional can be calculated by using the drift time of the ionized electrons to the anode.

In the endcap region, where the magnetic field and neutron flux are high, cathode strip chambers are used. Cathode strip chambers are trapezoidal in shape with six gas gaps for ionization. These gas gaps each have one plane of cathode strips pointing radially outward and one plane of anode wires oriented perpendicular to the cathode.

In both the barrel and endcap regions, resistive plate chambers are used. These detectors are composed of two parallel resistive plates separated by a gas gap. The design goal of the resistive plate chambers is to complement the cathode strip chambers and drift tubes to give two independent measurements of position. Additionally, resistive plate chambers offer very quick and accurate time resolution. This offers a quick approximation of the muon momentum which is useful for the trigger system

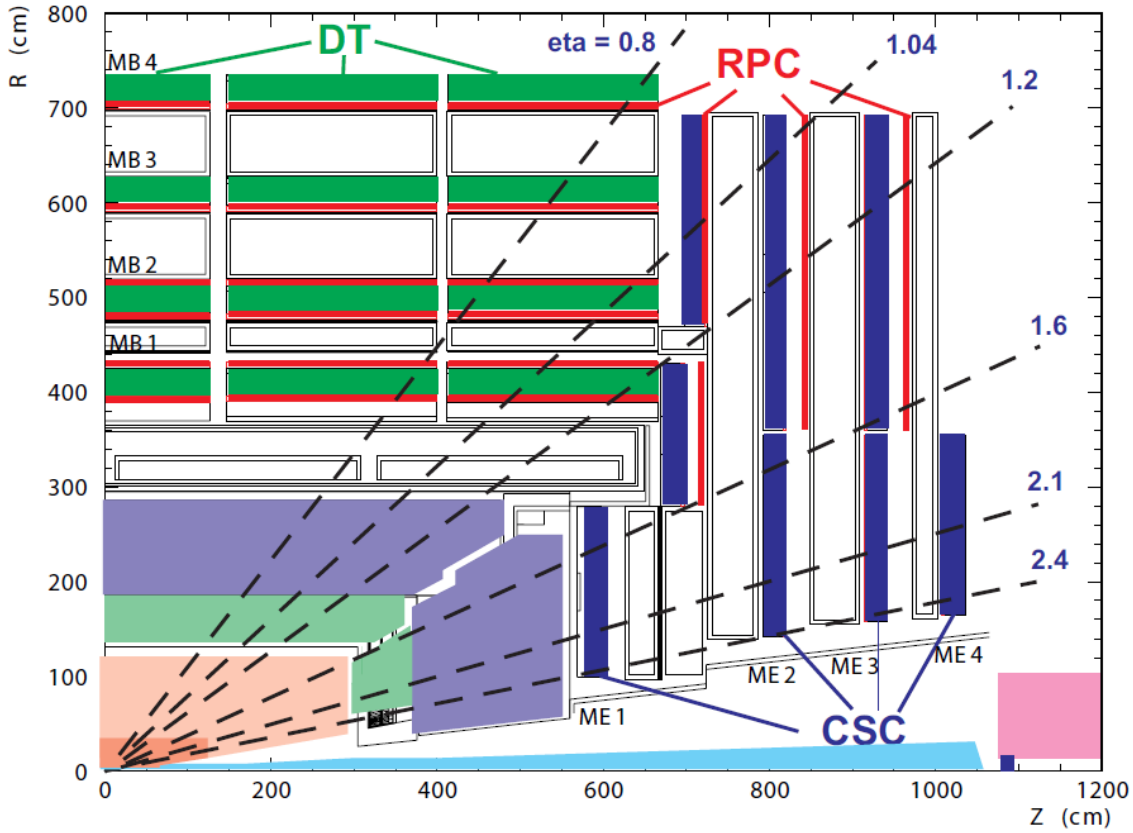

Figure 2.9: A diagram of the muon system.

and matching a muon track to a bunch crossing.

The muon system and inner tracker both contribute to the trajectory measurement of a muon. In terms of momentum resolution, the inner tracker offers much better sensitivity up to around 200 GeV. After 200 GeV, the muon system starts to significantly improve the momentum measurement.

Figure 2.9 shows a diagram of the muon system.

2.3.7 Trigger

The LHC delivers around 1 billion proton-proton collisions per second. However, because of the current computing limitations, the CMS detector system can only write around 100 collisions per second as data. Therefore, a trigger system is developed to distinguish the most potentially interesting physics signatures.

The L1 trigger takes information from the calorimeter and muon systems and their correlations. When one of these detectors produces a signal, the information takes 3.2 μs to reach the L1 processing area and return to the detector. The L1 processing time for the information for a maximum of 1 μs where the decision is made to keep the event to search for potential physics signatures. The L1 has various algorithms designed to keep "trigger primitives", which can be objects such as high p_T muons, electrons, jets or full event information like total energy or E_T^{miss}. The L1 trigger only saves on average of 1 out of every 1000 events.

After the L1 trigger, the trigger primitive events are processed by the high level trigger (HLT). The HLT again saves only 1 out of 1000 of these events. The processing time for the HLT algorithm is longer than the L1 system, and to extract the potentially exciting physics objects the algorithm performs partial event reconstruction. An event that enters the HLT algorithm is first analyzed based on the output of the calorimeters and muon system, then pixel tracking is performed, then finally full tracking. An event that passes the L1 and HLT is then put into storage for analysis.

Chapter 3

The W' Search

3.1 Introduction

Many beyond the BSM theories predict new massive gauge bosons. This note presents a search for a heavy partner of the SM W gauge boson, generally referred to as the W' (see Chapter 1.8). We focus on the $\mathrm{W}' \to \mathrm{t\bar{b}}$ decay mode motivated by the ability to lower QCD multijet background in this channel when compared to light flavor hadronic decay modes.

The primary signal under investigation is a W' particle in which the interaction with quarks is defined by the following Lagrangian,

$$\mathcal{L} = \frac{V_{q_i q_j}}{2\sqrt{2}} g_w \overline{q}_i \gamma_\mu \big(a^R_{q_i q_j}(1+\gamma^5) + a^L_{q_i q_j}(1-\gamma^5)\big) \mathrm{W}' q_j + \mathrm{H.c.}\,, \tag{3.1}$$

This is the most general, lowest-dimensional, model-independent effective Lagrangian for the W′ boson. Here $a^L_{qi,qj}$, $a^R_{qi,qj}$ are the left- and right-handed chiral couplings of W′ to quarks. For a SM-like W′, $a^L_{qi,qj}$=1, $a^R_{qi,qj} = 0$.

Searches for a high mass W′ resonance have been performed at the Tevatron [13,14] and at CMS [15–17] and ATLAS [18] at the LHC. Currently, the most stringent limits on W′ cross-sections exclude a right-handed W′ particle with mass below 2.05 TeV at the 95% C.L. In this analysis we do not consider W′ lighter than $\sim$ 1.3 TeV since there are stringent limits on W′ production at these masses.

We present a search for $W' \to t\bar{b}$ followed by the fully hadronic decay chain $t \to W + b$ followed by $W \to$ hadrons. This differs from [15] since the final state is comprised of only jets. In our kinematic regime of interest ($M_{W'} \gtrsim 1.3$ TeV) the top quark is quite energetic, and due to its Lorentz boost, the angular separation between its immediate decay products will be small. The jets resulting from the hadronization of the b quark and the light quarks from W boson from the top decay usually overlap, resulting in one 'fat' jet. This search uses special techniques to identify the substructure of this top jet, and further selection based on substructure information as well as b-tagging strongly suppresses the QCD background.

The search uses 19.7 fb^{-1} of 8 TeV data collected from the CMS experiment in 2012.

3.1.1 Analysis Strategy

The focus of this analysis are heavy resonances decaying into $t\bar{b}$. Thus the $W' \to t\bar{b}$ decay results in a mostly dijet topology, with the b and top jets being predominantly back-to-back.

After requiring a high transverse momentum, the primary sources of background are QCD multijet and SM $t\bar{t}$ production due to the high abundance of QCD present by requiring a dijet topology and the high $t\bar{t}$ production contribution fraction that remains after top jet discrimination.

Of these two main sources, QCD multijet production is dominant and is estimated by a data driven technique similar to [19]. We invert certain substructure cuts used to identify top jets to define sideband regions; we keep the cut on the mass of the top jet to avoid the kinematic bias in forming the invariant mass distribution of the top-b candidate. One sideband region is used to measure the average b-tagging rate, which is then applied to pre-b-tag data to obtain the QCD estimate. The other sidebands are then used to check the performance of the QCD estimation in data.

The SM $t\bar{t}$ contribution is estimated from Monte Carlo (MC) simulation. We also subtract the pre-tagged $t\bar{t}$ from the pre-tagged data sample when measuring the average b-tagging rate. The measurement of the average b-tagging rate is then independent of $t\bar{t}$, and the $t\bar{t}$ contribution is added at the end as a separate background component. The contribution of the single top production to the background was found to be negligible.

The data and background components are then used as templates by the Bayesian statistical procedure to set the exclusion limits on W′. This procedure uses a binned likelihood to calculate limits for the signal cross-section in the $W' \to t\bar{b}$ branching fraction. We use the limit setting framework "Theta" [20], which calculates exclusion limits using a shape based approach.

3.2 Data Sample

The data sample used for this analysis corresponds to 19.7±0.5 fb^{-1} of integrated luminosity collected in 2012 at $\sqrt{s}$ = 8 TeV. See Table 3.1 for a summary of the datasets used in the analysis. Generation of SM $t\bar{t}$ and single top events is performed by Powheg [21]. The MC simulation samples used for background estimation can be found in table 3.1.

3.2.1 Signal Samples

The Lagrangian presented in equation 3.1 has been implemented in CompHEP [24] and used for event generation. The mass of the top quark was set to 172.5 GeV. Pythia was used for hadronization. The CTEQ6M parton distribution functions were selected and the QCD scale was set to the W′ invariant mass. The width of the W′ resonance and cross-sections were obtained from CompHEP numerical calculations. The generation was performed using the $2 \rightarrow 4$ process W′ → t ; t → Wb ; W → $q_i q_j$, where q_i and q_j represent quarks. W decays including b quarks are not considered due to the negligible branching fraction. The process preserves all spin correlations between production and decay.

The W′ generation can be performed using three different couplings.

- W'_R - The purely right-handed W′ where $a^L_{qi,qj}$=0 , $a^R_{qi,qj}$=1
- W'_L - The purely left-handed W′ where $a^L_{qi,qj}$=1 , $a^R_{qi,qj}$=0

Jet Datasets	
Dataset	**Luminosity** (pb^{-1})
/Jet/Run2012A-22Jan2013-v1/AOD	888
/JetHT/Run2012B-22Jan2013-v1/AOD	4403
/JetHT/Run2012C-22Jan2013-v1/AOD	7052
/JetHT/Run2012D-22Jan2013-v1/AOD	7414
Total Analyzed Luminosity	19757

MC Datasets	
Dataset	**Cross-section(pb)**
TT_Mtt-700to1000_CT10_TuneZ2star_8TeV-powheg-tauola	245.8 **(NNLO)**
TT_Mtt-1000toInf_CT10_TuneZ2star_8TeV-powheg-tauola	245.8 **(NNLO)**
T_t-channel_TuneZ2star_8TeV-powheg-tauola	56.4 **(NNLO)**
Tbar_t-channel_TuneZ2star_8TeV-powheg-tauola	30.7 **(NNLO)**
Tbar_tW-channel-DR_TuneZ2star_8TeV-powheg-tauola	11.1 **(NNLO)**
T_tW-channel-DR_TuneZ2star_8TeV-powheg-tauola	11.1 **(NNLO)**
T_s-channel_TuneZ2star_8TeV-powheg-tauola	3.79 **(NNLO)**
Tbar_s-channel_TuneZ2star_8TeV-powheg-tauola	1.76 **(NNLO)**
QCD_Pt-300to470_TuneZ2star_8TeV_pythia6	1759.6
QCD_Pt-470to600_TuneZ2star_8TeV_pythia6	113.9
QCD_Pt-600to800_TuneZ2star_8TeV_pythia6	27.0
QCD_Pt-800to1000_TuneZ2star_8TeV_pythia6	3.57
QCD_Pt-1000to1400_TuneZ2star_8TeV_pythia6	0.738
QCD_Pt-1400to1800_TuneZ2star_8TeV_pythia6	0.0335

Table 3.1: Primary datasets and MC samples used. Including the corresponding integrated luminosity or cross-section of each dataset [22, 23].

- W'_{LR} - The mixed-coupling W′ where $a^L_{qi,qj}$=1 , $a^R_{qi,qj}$=1

Because of the SM-like couplings of W'_L and W'_{LR}, we must consider the interference between SM single top and signal. The W'_R MC samples were generated without SM single top. The right-handed W′ samples used in this analysis are given in table 3.2. The cross-sections listed here are leading order. The cross-sections used in the main analysis are scaled to next-to leading order with a multiplicative k factor of 1.2 which is extracted from [25]. The left-handed and mixed-coupling W′ samples used in this analysis are given in table 3.3 and 3.4 respectively. In order to have sufficient statistical precision in the signal region, these samples have a loose generator level p_T cut of 200 GeV set on the b jet from the W′ decay. The effect of this pre-selection is investigated in section 3.2.3.

3.2.2 Trigger Selection

Due to our interest in highly boosted jets, our data was taken using the `HLT_HT750` trigger, which requires the event to have H_t of at least 750 GeV. The trigger efficiency is measured in data and MC by investigating the looser `HLT_HT550` trigger. The selection used for this measurement includes a loose kinematic selection. We require two jets with $p_T > 300$ GeV and the cut described in Section 3.2.9. The denominator is defined as passing this selection and the `HLT_HT550` trigger, whereas the numerator is required to pass the selection and both the `HLT_HT550` and `HLT_HT750` trigger. The efficiency is shown in Figure 3.1 and is parameterized as a function of summed

Right-Handed Signal Samples

Dataset	$\Gamma_{W'}$(GeV)	**(LO) Cross-Section (pb)**
SingletopWprimeTToHad_M-1300_right_TuneZ2star_8TeV-comphep	**43.7**	**0.4852**
SingletopWprimeTToHad_M-1500_right_TuneZ2star_8TeV-comphep	**50.0**	**0.2198**
SingletopWprimeTToHad_M-1700_right_TuneZ2star_8TeV-comphep	**57.3**	**0.1038**
SingletopWprimeTToHad_M-1900_right_TuneZ2star_8TeV-comphep	**64.1**	**0.0507**
SingletopWprimeTToHad_M-2100_right_TuneZ2star_8TeV-comphep	**70.9**	**0.0254**
SingletopWprimeTToHad_M-2300_right_TuneZ2star_8TeV-comphep	**77.6**	**0.0131**
SingletopWprimeTToHad_M-2700_right_TuneZ2star_8TeV-comphep	**91.2**	**0.0039**

Table 3.2: Signal samples used in the analysis. Quoted cross-section and $\Gamma_{W'}$ were obtained from the CompHEP generator. A k factor of 1.2 is implemented on the quoted cross-sections.

Left-Handed Signal Samples

Dataset	$\Gamma_{W'}$(GeV)	(LO) Cross-Section (pb)	Selection Efficiency
SingletopWprimeTToHad_M-1300_left_TuneZ2star_8TeV-comphep	43.7	0.4248	0.157
SingletopWprimeTToHad_M-1500_left_TuneZ2star_8TeV-comphep	50.0	0.2622	0.104
SingletopWprimeTToHad_M-1700_left_TuneZ2star_8TeV-comphep	57.3	0.1669	0.0679
SingletopWprimeTToHad_M-1900_left_TuneZ2star_8TeV-comphep	64.1	0.1237	0.0507
SingletopWprimeTToHad_M-2100_left_TuneZ2star_8TeV-comphep	70.9	0.1047	0.0429
SingletopWprimeTToHad_M-2300_left_TuneZ2star_8TeV-comphep	77.6	0.0971	0.0397
SingletopWprimeTToHad_M-2700_left_TuneZ2star_8TeV-comphep	91.2	0.0933	0.0379

Table 3.3: Left-Handed signal samples used in the analysis. Quoted cross-section and $\Gamma_{W'}$ were obtained from the CompHEP generator. A k factor of 1.2 is implemented on the quoted cross-sections. The cross sections listed here take into account the generator level b jet p_T cut, and represent the visible cross section. The efficiency of this cut is provided under the column labeled Selection Efficiency.

Mixed Signal Samples

Dataset	$\Gamma_{W'}$(GeV)	(LO) Cross-Section (pb)	Selection Efficiency
SingletopWprimeTToHad_M-1300_mixed_TuneZ2star_8TeV-comphep	**87.4**	**0.9327**	**0.290**
SingletopWprimeTToHad_M-1500_mixed_TuneZ2star_8TeV-comphep	**101.0**	**0.4743**	**0.172**
SingletopWprimeTToHad_M-1700_mixed_TuneZ2star_8TeV-comphep	**114.6**	**0.2700**	**0.105**
SingletopWprimeTToHad_M-1900_mixed_TuneZ2star_8TeV-comphep	**128.2**	**0.1776**	**0.0711**
SingletopWprimeTToHad_M-2100_mixed_TuneZ2star_8TeV-comphep	**141.7**	**0.1334**	**0.0540**
SingletopWprimeTToHad_M-2300_mixed_TuneZ2star_8TeV-comphep	**155.3**	**0.1128**	**0.0458**
SingletopWprimeTToHad_M-2700_mixed_TuneZ2star_8TeV-comphep	**182.4**	**0.0986**	**0.0400**

Table 3.4: Mixed-Coupling signal samples used in the analysis. Quoted cross-section and $\Gamma_{W'}$ were obtained from the CompHEP generator. A k factor of 1.2 is implemented on the quoted cross-sections. The cross sections listed here take into account the generator level b jet p_T cut, and represent the visible cross section. The efficiency of this cut is provided under the column labeled Selection Efficiency.

leading and sub-leading jet p_T. The extracted trigger efficiency is used to weight the MC samples used in the analysis to account for the loss in efficiency in the turn-on. We do not observe perfect agreement in data and MC, so we use the trigger efficiency derived from data to weight our MC samples.

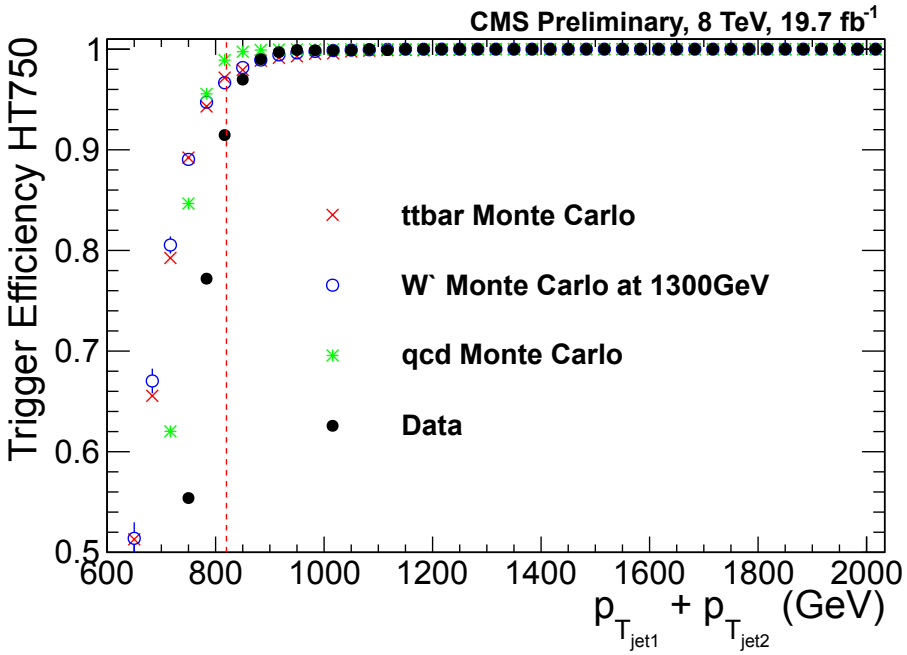

Figure 3.1: Trigger efficiency of HLT_HT750 measured as a function of the summed p_T of the leading and sub-leading jets. The red dashed line indicates the minimum for the analysis, at which point the trigger is nearly fully efficient.

3.2.3 Signal Characteristics

The W′ boson of interest is very massive, and produces highly boosted top quarks. The decay products of these top quarks become more collimated as the boost increases. When the top decays hadronically, we observe one merged jet over the two

distinct jets that would be detected at a lower boost. This jet has a large characteristic radius and a distinct substructure. This high energy jet merging is investigated in Figure 3.2. Here, the 'top candidate' is just the leading jet in the event. It is also required to be hemispherically separated from a MC truth b jet. This jet is generally a merged W boson at low p_T and a merged top at high p_T. The 'W candidate' (used for the bottom plots) is assembled from the pair of generator level non-b quarks that are close to the W mass (within 2.0 GeV). The central feature of this analysis is using this jet merging to discriminate signal from background.

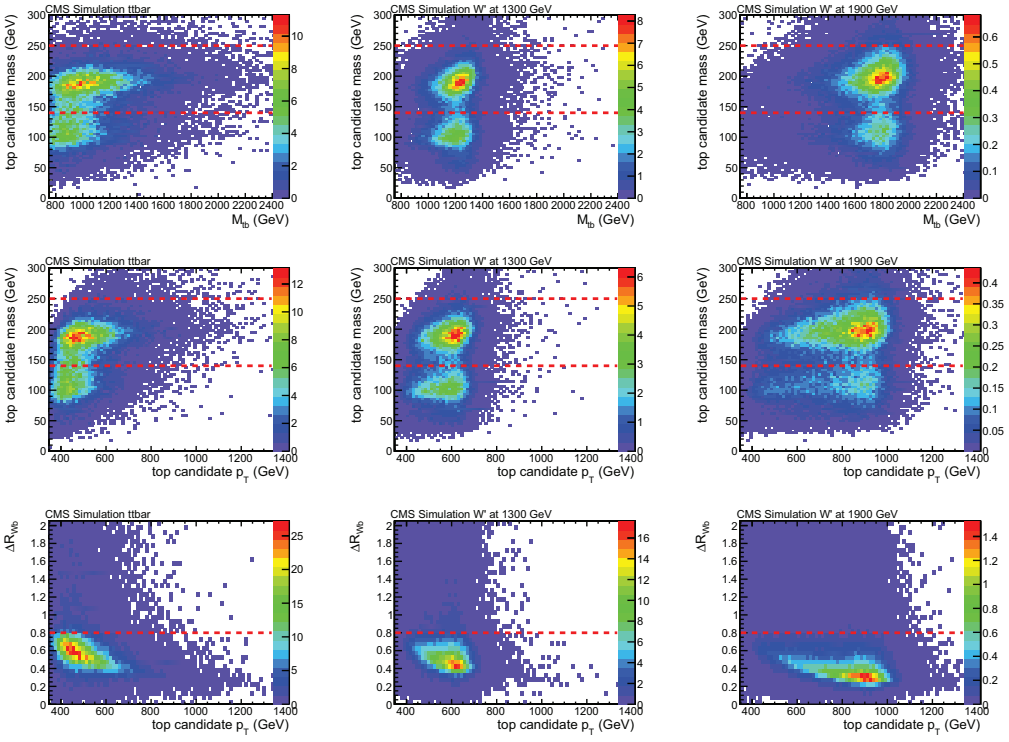

Figure 3.2: Investigation of top merging within MC samples of interest. $t\bar{t}$ (left) W'_R MC at 1300GeV (middle) W'_R MC at 1900GeV (right). The red lines on the top and middle plots indicate the top candidate mass cut in the full selection (see Section 3.2.8). The red line on the bottom plots indicate the characteristic jet radius used to investigate fully merged top jets (see Section 3.2.4).

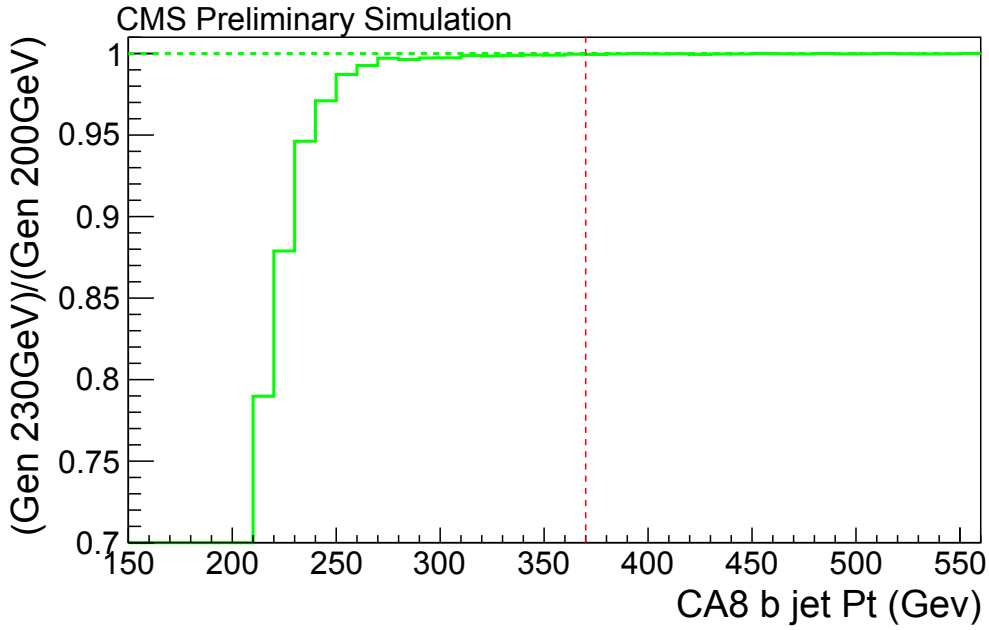

Figure 3.3: Ratio of CA8 p_T using the generation level b pt cut of 230 GeV and 200 GeV. The red line is the analysis level p_T cut of 370 GeV. The sample used for this study is W'_{LR} at 1300 GeV

We place a generator level p_T cut on the b quark from the W′ decay in the left-handed and mixed-coupling W′ samples (see Section 3.2.1). To investigate the effect of this pre-selection, we look at the effect of an even tighter cut. Figure 3.3 shows the ratio of generator level b p_T cuts. The denominator requires a generation level pt cut of 200 GeV and the numerator requires a generation level pt cut of 230 GeV. This ratio is parameterized in the p_T of the CA8 jet that the generation particle is matched to ($\Delta R < 0.5$ is used for matching). The turn on of this tighter cut is well below the analysis level cut of 370 GeV. Thus, the effect of the generation level b p_T cut on selections requiring the analysis level p_T cut is negligible.

3.2.4 Jet Reconstruction

All data are reconstructed using CMSSW 5.3.x, and we use jet energy corrections from `FT_53_V21_AN5` [26]. The Particle Flow reconstruction algorithm is used to reconstruct all data and MC samples used for the analysis. This algorithm uses information from all sub-detectors to categorize particles as muons, electrons, photons as well as charged and neutral hadrons. Charged hadrons identified as pileup are removed from the inputs to the jet clustering algorithms by Charged Hadron Subtraction (CHS). Pileup vertices are identified as vertices that have a lower p_T than the primary vertex. Isolated charged leptons are removed, and neutral pileup components are removed with a residual area-based method. For more detail, see [19]. The PF candidates are then used to create 'Particle Flow jets' as follows. Jet clustering is performed with a sequential recombination algorithm which compiles jets by merging the minimum of $d_{ij} = \min(k_{Ti}^{2m}, k_{Tj}^{2m})\Delta_{ij}/R$ where $\Delta_{ij} = \sqrt{(y_i - y_j)^2 + (\phi_i - \phi_j)^2}$. We use the Cambridge-Aachen (CA) [27,28] algorithm implemented by FastJet 3 [29,30], which assigns a value of $m = 0$, and thus is not weighted by p_T. An R value of 0.8 is used for the analysis. The CA algorithm has been shown to be more efficient than the the k_T and the anti-k_T algorithms for finding hard subjets [31].

We use anti-k_T jet energy corrections for all jets in the analysis. The jet energy corrections derived are adequate for the CA R = 0.8 jet algorithm for the jet momenta considered here as can be seen from 7 TeV studies in simulation comparing AK5 and CA8 jets [19]. We use the 2012 prescription for jet energy corrections [32]. We

apply AK7 Particle Flow with charged hadron subtraction (AK7PFchs) jet energy corrections for all data and MC samples.

3.2.5 Event Pre-selection

The following pre-selection is applied:

- The event must have a good primary vertex as computed by a deterministic annealing filter (DAF) ($|z_{\text{Primary Vertex}}| < 24$ cm, $N_{\text{DOF}} > 6$).
- Two jets with $|y| < 2.4$
- Only two jets with $\text{p}_\text{T} > 150$ GeV
- Leading Jet $\text{p}_\text{T} > 450$ GeV & Sub-leading Jet $\text{p}_\text{T} > 370$ GeV
- Loose Particle Flow jet identification [33] is applied
- Leading and sub-leading jet are separated by $|\Delta y| < 1.6$. This cut is described in Section 3.2.9.
- Beam background events are removed using the following requirements:
  - In events with at least 10 tracks, a minimum of 25% of these tracks must be high purity tracks.

The requirement that there are only two jets with $\text{p}_\text{T} > 150$ GeV is useful for vetoing "three-prong" trijet events, which could impact the kinematics of the top-W

candidate invariant mass distribution and bias the background estimate.

3.2.6 $t\bar{t}$ p_T Re-weighting

In order to correct for known differences in the top p_T spectrum between data and $t\bar{t}$ MC, we re-weight MC using the Generator level p_T of the top and anti-top with the recommended prescription. With p_{T_t} and $p_{T_{\bar{t}}}$ being the generator p_T of the top and anti-top respectively, the scale factor applied to each event in the $t\bar{t}$ MC expectation is:

$$SF = \sqrt{e^{0.156-.00137 p_{T_t}} \times e^{0.156-.00137 p_{T_{\bar{t}}}}} \tag{3.2}$$

Although this procedure was not designed for the kinematic range in our analysis, we prefer to use the prescription as it is more consistent with our measurement of the $t\bar{t}$ normalization (see Section 3.3.5).

3.2.7 Pileup Correction

We re-weight our MC samples to account for differences due to pileup using the recommended procedure. To create a scale factor for number of primary vertices, we use MC truth to extract the number of pileup interactions. Then we compare this to the mean number of interactions per crossing from data. This is extracted using the pileup distribution from the rereco datasets listed in table 3.1. For this

calculation we use the suggested minbias cross-section of 69.4 mb. The scale factor is then the data distribution divided by the distribution in MC and is applied to the signal and $t\bar{t}$ MC samples to improve data to MC agreement. Figure 3.5 shows the distribution of reconstructed primary vertices in Data, $t\bar{t}$, and signal MC before and after the re-weighting has been applied. The pileup correction has very little effect on the eventual M_{tb} full selection, as seen in Figure 3.6, for W'_R signal MC at the 1900 GeV mass point. Similarly, there is little effect $t\bar{t}$ MC as can be seen in Figure 3.7. A study has been conducted to investigate the effect of the suggested systematic uncertainty of 5% on the as can be seen in Section 3.5. Figure 3.4 shows the number of primary vertices in data and signal MC with respect to discrimination variables used to separate signal from background.

3.2.8 Combined CMS Top Tagging Algorithm

The CMS top tagging algorithm takes CA jets with $R = 0.8$ as input. The algorithm first attempts to decompose the CA jet into two primary subjets, and then performs a secondary decomposition to attempt to split the subjets into secondary subjets [34]. In this process, particles with low p_T or a large angular distance from the jet center are omitted. The top tagging algorithm is based on the following cuts

- **Jet Mass** 140 GeV $< m_{jet} <$ 250 GeV - The mass of the CA jet is required to be consistent with the top quark mass.

- **Number of Subjets** $N_{subjets} > 2$ - The number of subjets found by the algorithm must be at least 3.

- **Minimum Pairwise Mass** $m_{min} > 50$ GeV - The three highest p_T subjets are taken pairwise, and each pair's invariant mass is calculated. m_{min} is the mass of the pair with the lowest invariant mass. The minimum pairwise mass must be close to the W mass.

Figure 3.8 shows the comparison of Signal and QCD MC for the above top tagging selection. Here, the N-subjettiness and subjet b-tagging cuts are not applied.

The N-subjettiness algorithm can be used for boosted top jet identification [35]. N-subjettiness defines τ_N variables as follows

$$\tau_N = \frac{1}{d_0} \sum_i p_{T_i} \min\{\Delta R_{1,i}, \Delta R_{2,i}, ..., \Delta R_{N,i}\} \tag{3.3}$$

where $\Delta R_{J,i}$ is between the subjet candidate and a constituent particle. d_0 is a normalization factor

$$d_0 = \sum_i p_{T_i} R_0 \tag{3.4}$$

where R_0 is the characteristic jet radius used by the jet clustering algorithm. For this analysis we use the one pass kt method of subjet axes minimization. τ_N is a measure of how consistent the jet energy is with originating from N subjets. Additional dis-

crimination power when using N-subjettiness variables is achieved by cutting on the ratio of two of these variables. Figure 3.9 shows τ_3/τ_2 comparison using signal and QCD MC samples. We use the standard operating point of $\tau_3/\tau_2 < 0.55$ [34] in the full selection.

The use of b-tagging algorithms on subjets is described in [36]. We apply the Combined Secondary Vertex b-tagging algorithm to all of the subjets found by the CA declustering sequence described above. The optimal discrimination variable when using subjet b-tagging is the maximum discriminant out of the three or four subjets found. Figure 3.10 shows the maximum subjet CSV b discriminant comparison using signal and QCD MC samples. We use the standard CSV working point $SJ_{\mathrm{CSVMAX}} > 0.679$.

Substructure variables in the signal region have known differences in data and MC [34]. We use the top tagging scale factor with the addition of subjet b-tagging and N-subjettiness discrimination that is extracted from efficiency comparisons of data and MC in a highly pure semileptonic $t\bar{t}$ sample. The scale factor for this effect is 1.04 and is applied to the signal MC samples used in the main analysis. There is a 13% uncertainty on this scale factor which is purely statistical, as the study is dominated by statistical uncertainty. The scale factor is obtained from the plots shown in Figure 3.11.

3.2.9 Delta Rapidity Cut

At high $M_{t\bar{b}}$, jets that originate from QCD multijet production are widely separated in rapidity (high Δy). However the jets originating from a high mass $t\bar{b}$ resonance do not exhibit such pronounced separation. The effect is not pronounced over the entire $M_{t\bar{b}}$ spectrum, but for high values of $M_{t\bar{b}}$ the analysis can achieve greater separation of signal and background. We therefore place a cut on $|\Delta y| < 1.6$ for the full selection. The value for this cut was chosen by investigating the Signal/$\sqrt{\text{Background}}$ distribution in events that have $M_{t\bar{b}} > 2000$ GeV. Because it is not as effective over the entire $M_{t\bar{b}}$ range, the value is set slightly off the peak to minimize loss of signal efficiency. Figure 3.12 shows the comparison of $|\Delta y|$ for high $M_{t\bar{b}}$ in signal and QCD MC. Here, the N-subjettiness and subjet b-tagging cuts are not applied.

3.2.10 b-jet Identification

To enhance the sensitivity of the analysis, the Combined Secondary Vertex (CSV) b-tagging algorithm is applied to the subleading jet. We use the standard operating point CSVM (CSV > 0.679). Due to the fact that our signal content contains only $t\bar{b}$ and the only MC used in background estimation is $t\bar{t}$, the MC to data scale factor used in the analysis for b-tagging is the b-tagging Scale Factor for b quarks (SF_b). We use the suggested scale factor parameterized in p_T with the following functional

form for b candidate jet $p_T < 800$ GeV

$$SF_b = 0.938887 + 0.00017124 \times p_T - 2.76366 \times 10^{-07} \times {p_T}^2 \quad (3.5)$$

Any b candidate jet with $p_T > 800$ GeV is weighted with SF_b evaluated at 800 GeV. The parameterized SF_b is the suggested EPS13 prescription [36] from the b-tagging POG generated from measurements in both muon-jet and ttbar data representing 20 fb^{-1} of integrated luminosity. The uncertainty associated with this scale factor parameterization is described in Section 3.5. b-tagging operating points and scale factors have been validated for use with anti-kt jets with a R value of 0.5 (AK5 jets). In our kinematic regime it is assumed that the change in cone size will have a small effect. We apply an additional 2% systematic uncertainty to the signal MC samples used in the analysis. This is a conservative estimate of the uncertainty, validated by the following study:

For the 2700 GeV signal sample, we included both AK5 and CA8 jets in the event selection. All jets considered were required to be in our pt range ($p_T > 350$ GeV). We attempt to match a CA8 jet to the corresponding AK5 jet using a constraint on η and ϕ ($\Delta R < 0.3$). The results were 579041 CA8 jets pass pt cut, of these, 567155 pass the η , ϕ matching to AK5 jets. Of the matched jets, 96.9% record the same value for the CSVM cut (pass or fail). In addition, the ratio of b-tagging efficiencies

for both AK5 and CA8 were found to be within a 2% deviation (see Figure 3.13). To rule out a bias based on the known differences in pt for CA8 and AK5 jets, the efficiencies and uncertainties were extracted from plots using only the pt of the CA8 jet. The fit on the b-tagging efficiency ratio for CA8 and AK5 jets can be interpreted as an upper bound on the uncertainty due to this effect. We also checked this process for 1300 GeV and 1900 GeV signal samples and found results consistent with this 2% error. We have verified this systematic uncertainty with the BTV group, and it is approved for use in our analysis.

After the full top tagging selection is complete, there is a substantial fraction of $t\bar{t}$ in the full selection. Additionally, there is a large uncertainty in the $t\bar{t}$ MC contribution, so discriminating signal from $t\bar{t}$ becomes important. In W′ signal MC, the sub-leading b candidate jet is usually a true b jet, but in $t\bar{t}$ this jet is commonly a merged W or top jet. To this effect, the b candidate jet is required to have a mass $M_b < 70$ GeV in the full selection. The value for this cut is set near the peak of the Signal/$\sqrt{\text{Background}}$ distribution (see Figure 3.14).

3.2.11 Reconstruction of W' Invariant Mass

The full selection for the reconstruction of the W′ invariant mass then includes the following offline cuts.

- One jet with $p_T > 450$ GeV identified with the CMS top tagging algorithm as well as subjet b-tagging and N-subjettiness discrimination.

- One jet with $p_T > 370$ GeV with a CSVM b tag and mass$<$ 70 GeV
- $|\Delta\phi| > \pi/2$ between the two jets
- $|\Delta y|$ between the two jets < 1.6

The cutflow for this selection in data, $t\bar{t}$ MC, and right-handed W′ signal MC can be found in Table 3.5. Figure 3.15 shows this full selection in signal MC for various W′ masses.

Number of Selected Events

Sample	$2jets$	p_T	$\|\Delta y\|$	M_{top}	$Nsubjets$	$Minmass$	SJ_{CSVMAX}	τ_3/τ_2	M_b	CSV
Data	13854873±3722	4305244±2075	3376771±1838	992949±996	557489±747	318520±564	50642±225	7200±85	4463±67	277±17
QCD	—	—	—	—	—	—	—	—	—	248±4
ttbar	12185±27.3	4718±17.9	4220±16.9	3217±14.4	2742±13.3	2508±12.6	1689±10.0	1024±7.8	178±3.6	37±1.4
$M(W'_R) = 1900$	806±1.4	739±1.3	553±1.2	429±1.0	340±0.9	304±0.9	170±0.6	88±0.4	68±0.4	16±0.2
$M(W'_R) = 2100$	401±0.7	372±0.7	268±0.6	209±0.5	163±0.4	143±0.4	76±0.3	38±0.2	29±0.2	6±0.1
$M(W'_L) = 1900$	796±2.4	703±2.3	531±2.0	414±1.8	312±1.6	274±1.5	138±1.0	58±0.6	44±0.6	10±0.3
$M(W'_L) = 2100$	430±1.6	364±1.5	268±1.3	205±1.1	152±1.0	130±0.9	63±0.6	27±0.4	20±0.3	4±0.2

Table 3.5: The number of selected events after successive selections as scaled to an integrated luminosity of 19.7 fb^{-1}. Table reads left to right where the current column implies the previous selection. The quoted uncertainty is statistical only. QCD background expectation is only recorded for the full selection, as the average b-tagging rate takes into account the QCD background b fraction increase from b-tagging and subjet b-tagging. The first column additionally represents the hemispherical $\delta\phi$ selection between the leading jets. The column labeled p_T represents the p_T selection placed on both leading jets. The signal events are normalized to theory cross-section.

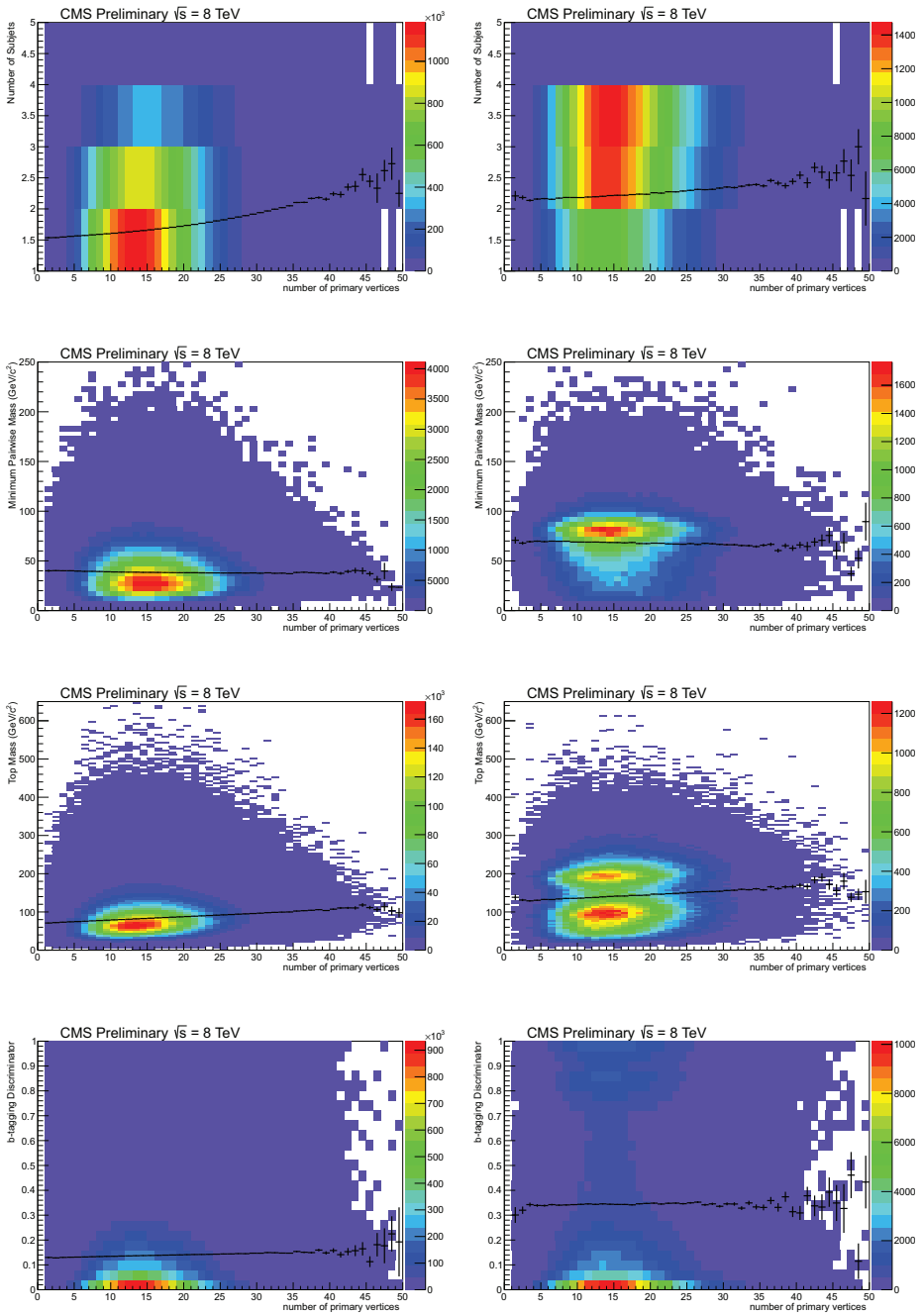

Figure 3.4: Number of primary vertices in data and signal MC vs (a) Number of Subjets (b) Minimum Pairwise Mass (c) Top Mass (c) CSV b discriminant

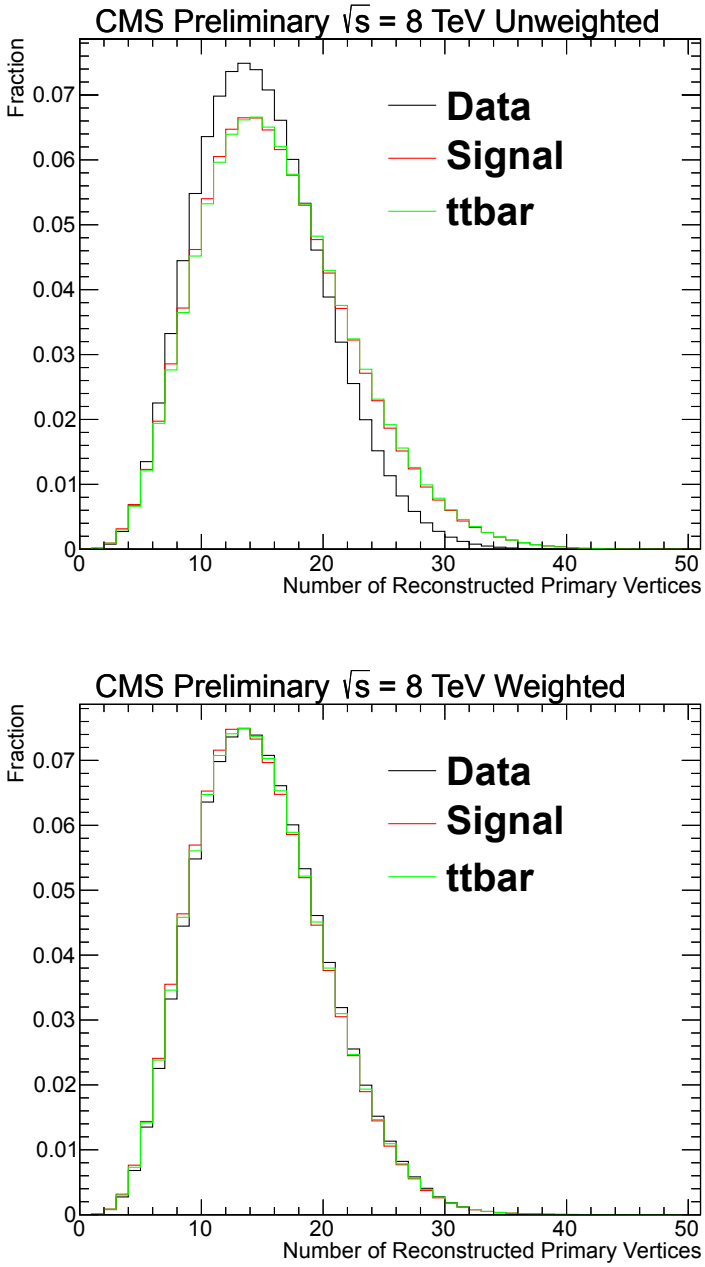

Figure 3.5: Number of reconstructed primary vertices before pileup re-weighting (top) and after pileup re-weighting (bottom). Here, no analysis cuts have been applied and the signal mass point is 1900 GeV

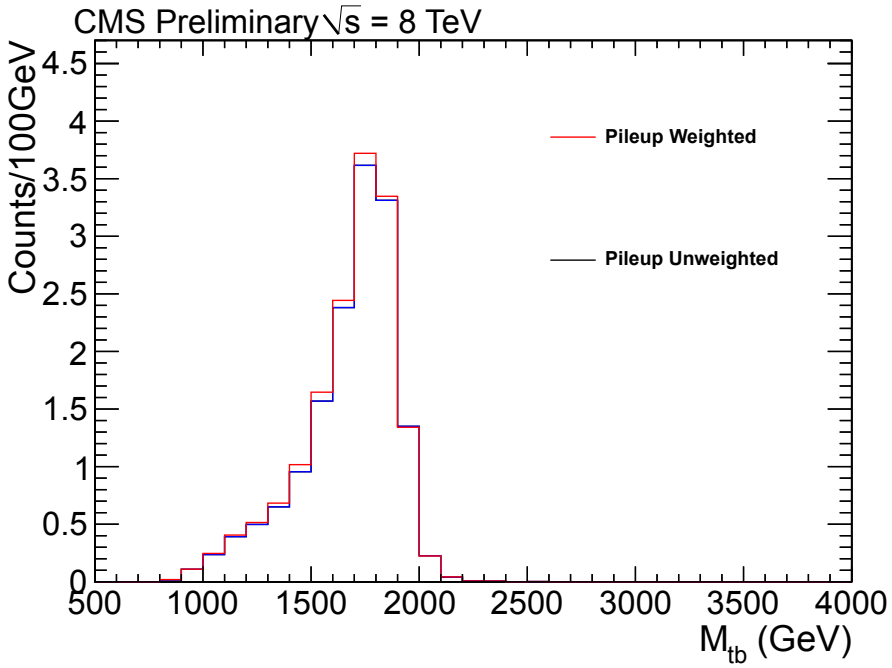

Figure 3.6: Effect of pileup-re-weighting on the Signal MC.

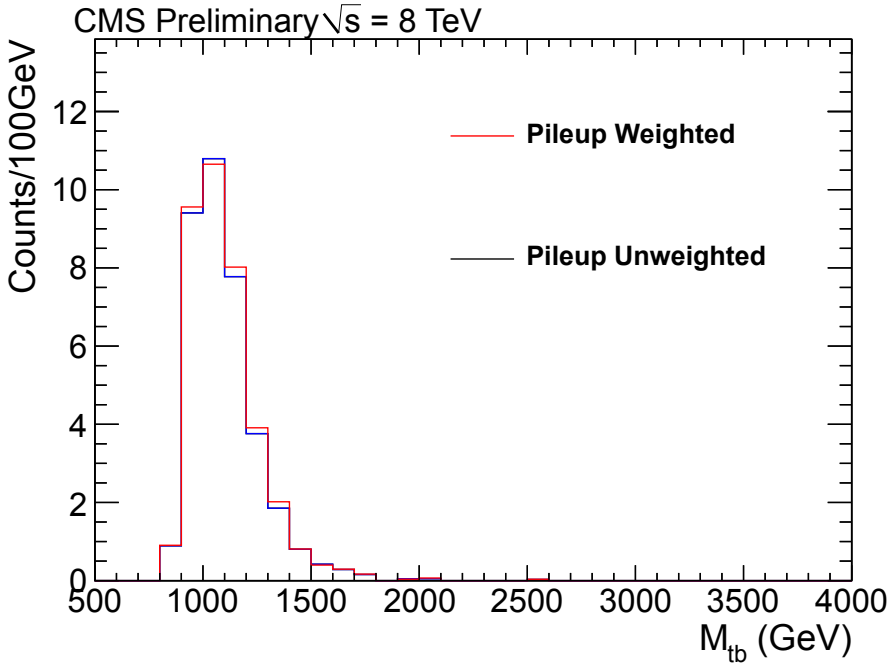

Figure 3.7: Effect of pileup-re-weighting on the $t\bar{t}$ MC.

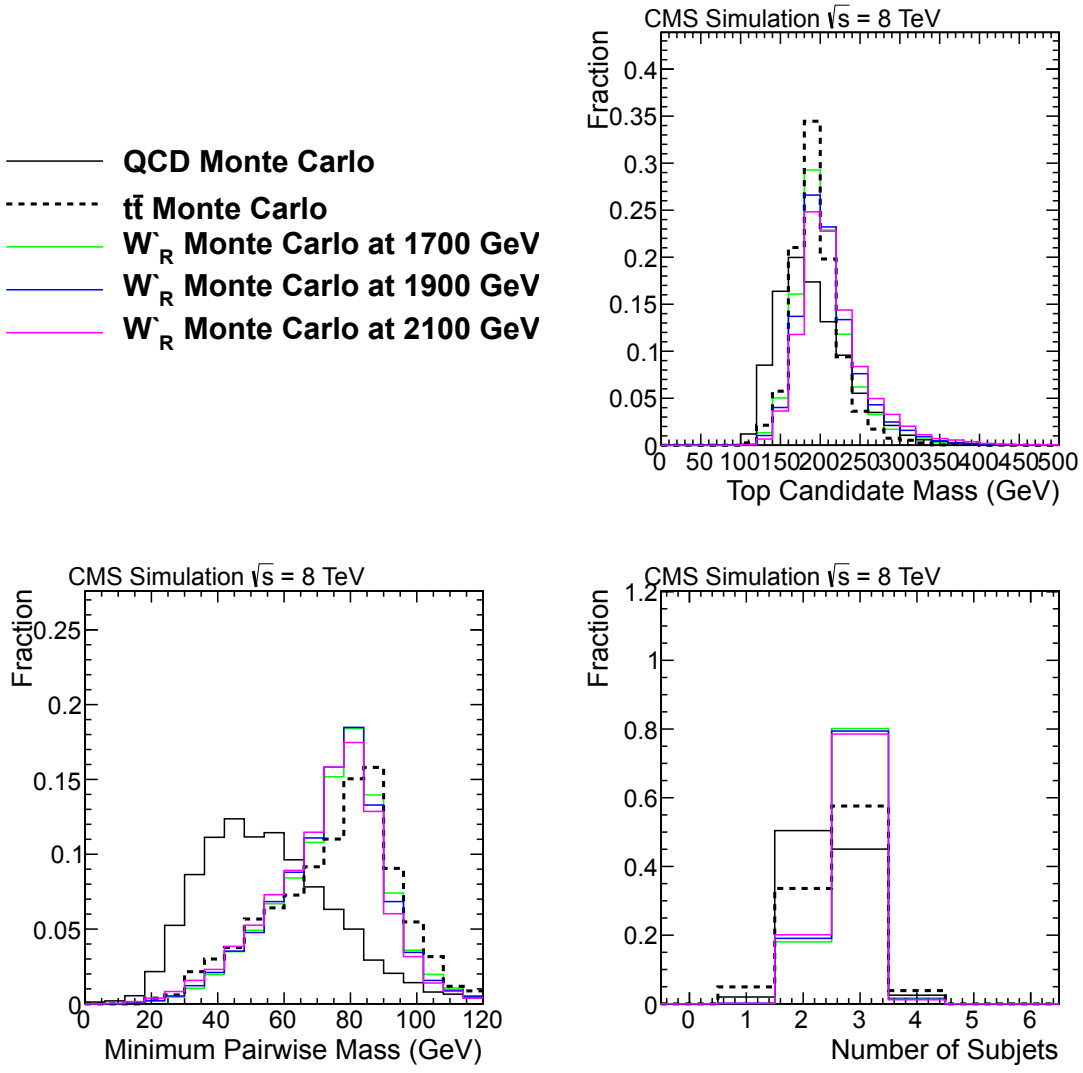

Figure 3.8: Comparison of the top Jet Mass, Number of Subjets, and Minimum Pairwise Mass in Signal and QCD MC. The cms top tagging selection is applied with the exception of the variable being plotted.

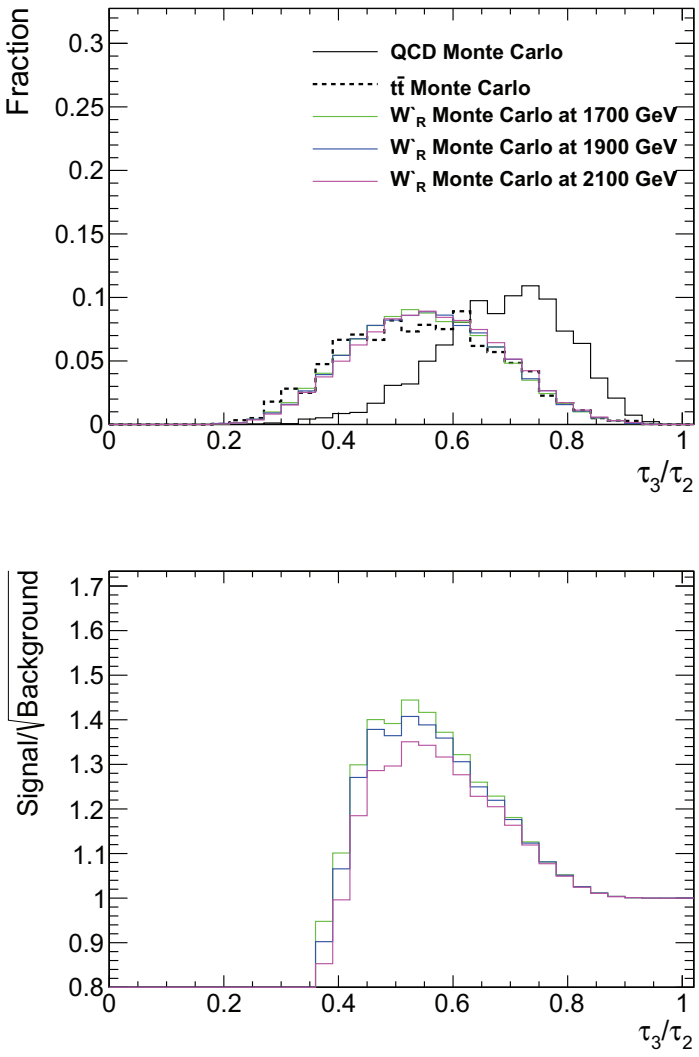

Figure 3.9: τ_3/τ_2 distributions in Signal and QCD MC samples (top). Plot of Signal/$\sqrt{\text{Background}}$ (bottom), derived from the top plot.

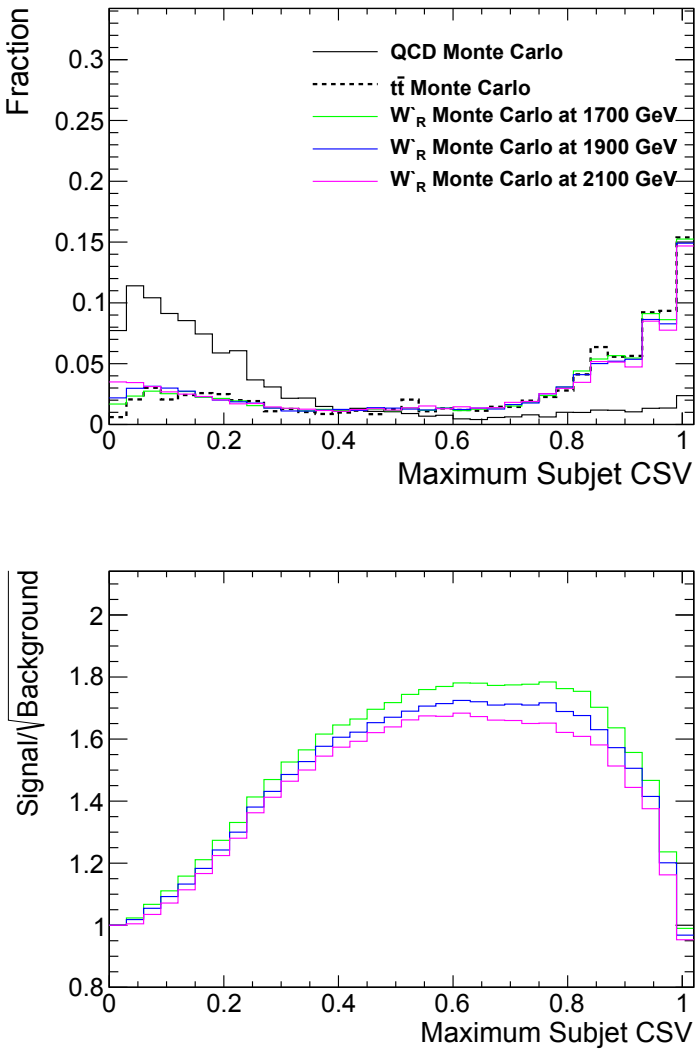

Figure 3.10: Maximum subjet CSV distributions in Signal and QCD MC samples (top). Plot of Signal/$\sqrt{\text{Background}}$ (bottom), derived from the top plot.

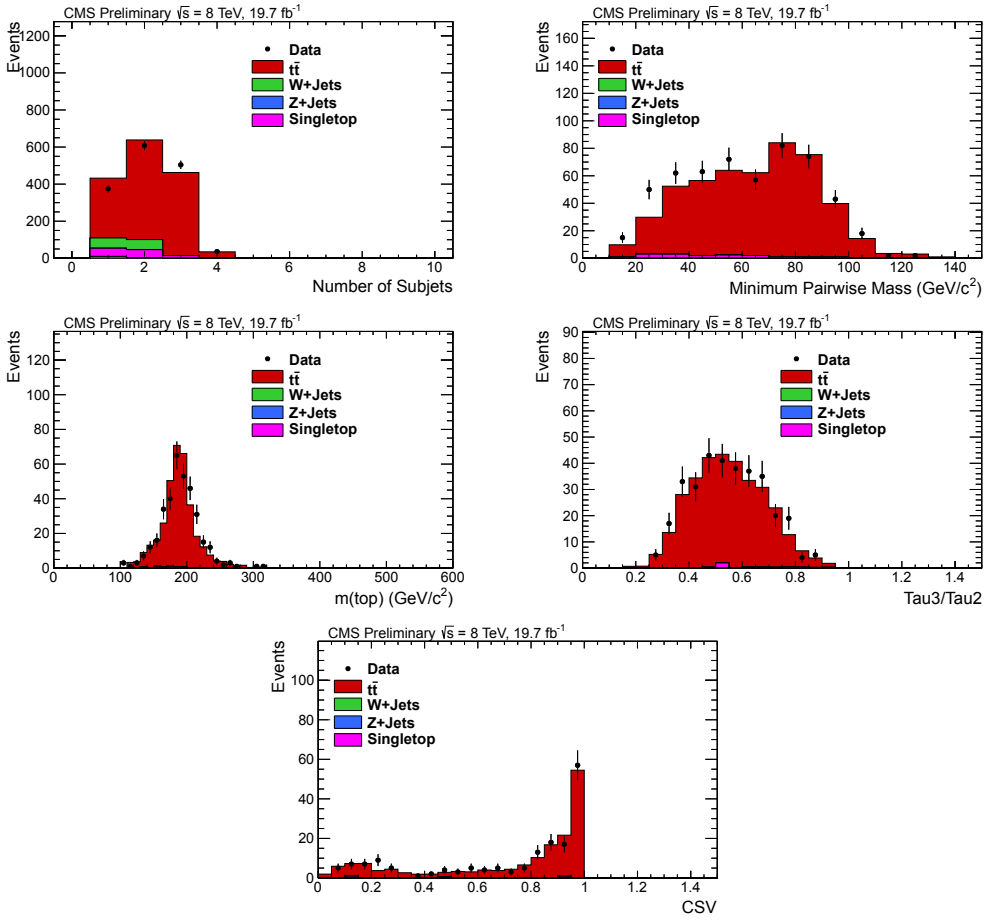

Figure 3.11: a.)Number of subjets, b.)minimum pairwise subjet mass, c.)jet mass, d.)τ_3/τ_2, and e.)maximum subjet CSV for fully-merged top candidates found in the semileptonic $t\bar{t}$ sample, used to evaluate the top-tagging efficiency SF. These Figures are extracted using the Powheg $t\bar{t}$ MC Sample.

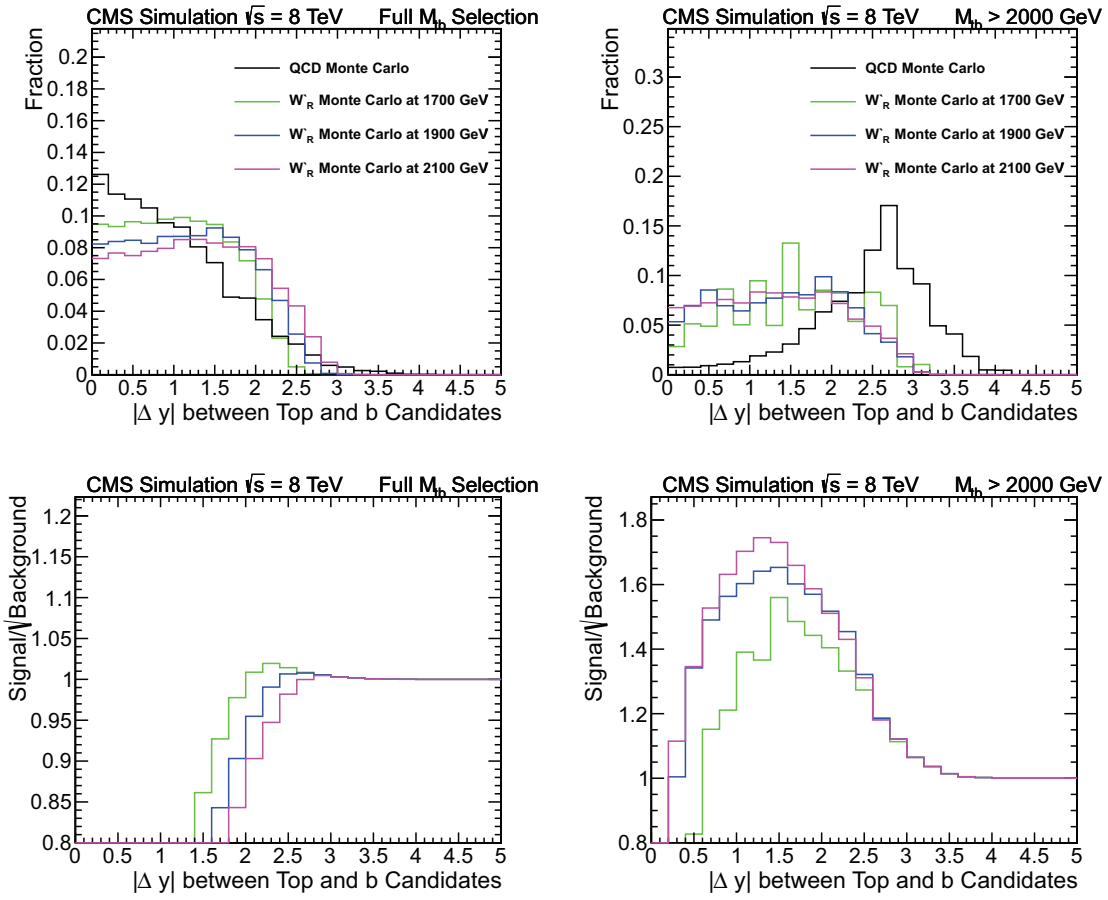

Figure 3.12: Comparison of $|\Delta y|$ in signal and QCD MC for the full selection and only events with $M_{t\bar{b}} > 2000$ GeV

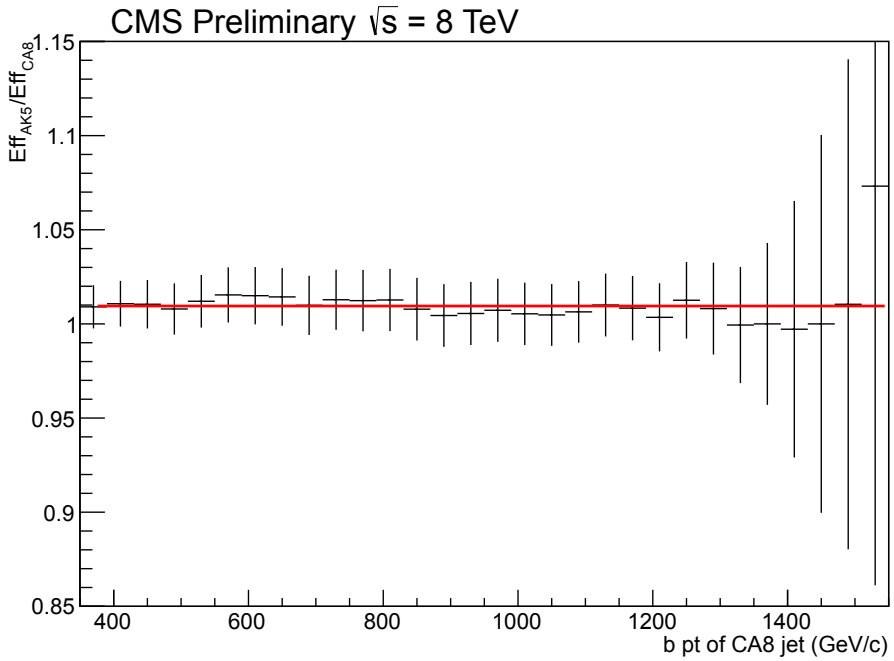

Figure 3.13: Ratio of the AK5 b-tagging rate to the CA8 b-tagging rate. Fitting this to a constant gives us a value of 1.0098 ± 0.0031. This can be considered an upper limit on the uncertainty for the change in SF_b for CA8 jets

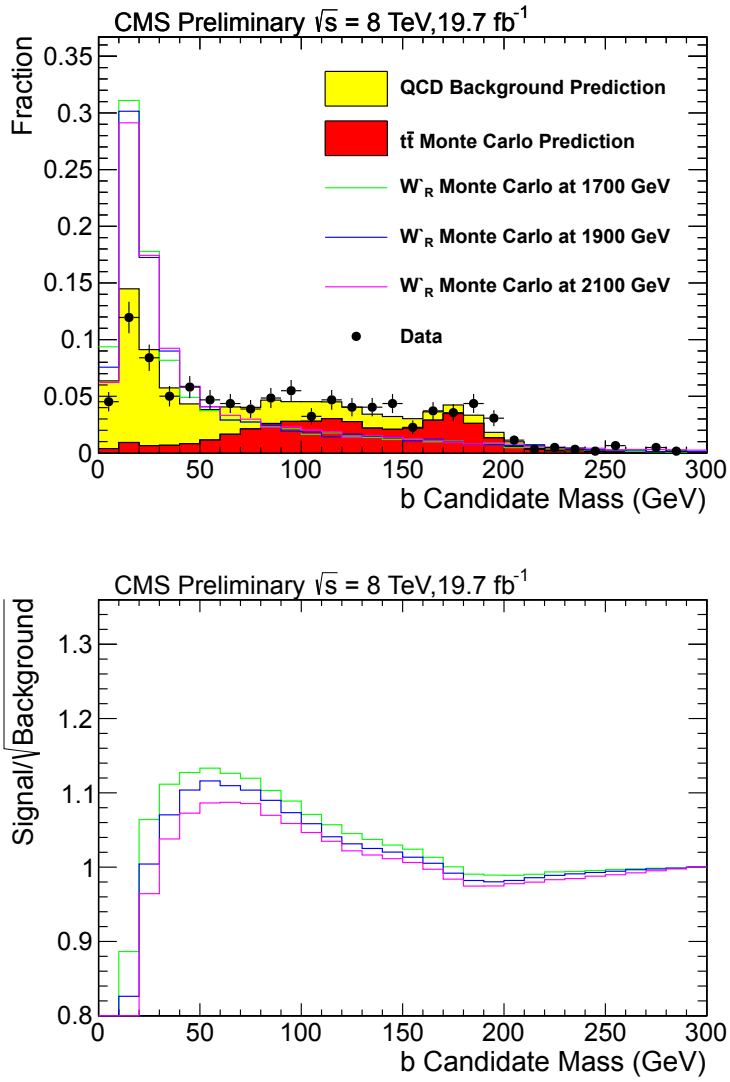

Figure 3.14: b candidate mass distributions in data, background, and signal. Plot of Signal/$\sqrt{\text{Background}}$ (bottom), derived from the top plot. This plot includes the full top tagging selection using the background estimation procedure outlined in Section 3.3.

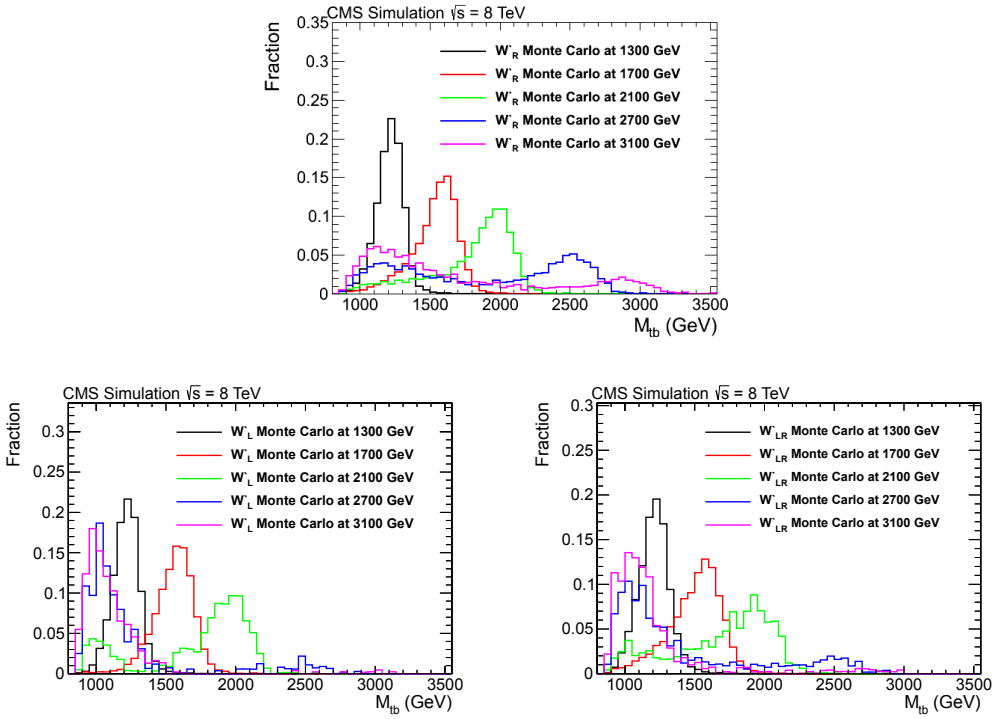

Figure 3.15: Full selection applied to W'_R (top) W'_L (bottom-left) and W'_{LR} (bottom-right). The bimodal structure seen in the M_{tb} spectrum for high W′ mass is a feature common to high-mass large-width resonances and represents the superposition of a W′ resonance and a rapidly falling parton distribution function.

3.3 Background Estimation

An essential part of the analysis is the data driven estimation of the QCD background. The background estimate relies on extracting the average b-tagging rate of a QCD jet in our signal region. We extract this rate by making use of the following sideband.

3.3.1 Substructure Sideband

We define the substructure sideband as events passing all signal region cuts but explicitly failing the top jet substructure cut on the number of subjets. Additionally, to ensure similar parton flavor distributions in the signal region and sideband (Figure 3.16), we also include subjet CSV discrimination. The top jet sideband is defined as:

$$140 < \mathrm{m_{jet}} < 250\mathrm{GeV} \tag{3.6}$$

$$\mathrm{N_{subjets}} \leq 2 \tag{3.7}$$

$$\mathrm{SJ_{CSVMAX}} \geq 0.679 \tag{3.8}$$

The Minimum Pairwise Mass variable described in Section 3.2.8 is not defined in this choice of sideband.

3.3.2 QCD Background Estimation

The estimation of QCD background is performed by extracting the probability to tag a b jet in the sideband. The primary assumption used in background estimation is that the average b-tagging probability for QCD multijets in the signal region is nearly identical to the sideband. Figure 3.16 shows the parton flavor distribution for signal region and sideband in QCD MC, the nearly identical composition can be considered motivation for the previous assumption.

To extract a QCD background estimate, we weight the events that pass the full selection in the signal region before the b-tagging requirement is applied by the average b-tagging probability (measured in the top jet sideband). This gives us an accurate expectation of the QCD background in the signal region. The b-tagging rate is defined as the inverse ratio of the number of b candidate jets, defined as $p_T > 370$ GeV jets in the hemisphere opposite the top jet to the number of b candidate jets that are b-tagged.

The parameterization of the average b-tagging rate is two dimensional and considers both the $|\eta|$ and p_T of the b candidate jets. We break down data into three distinct regions in $|\eta|$.

- Low $(0.0 < |\eta| \leq 0.5)$
- Transition $(0.5 < |\eta| \leq 1.15)$
- High $(1.15 < |\eta| \leq 2.4)$

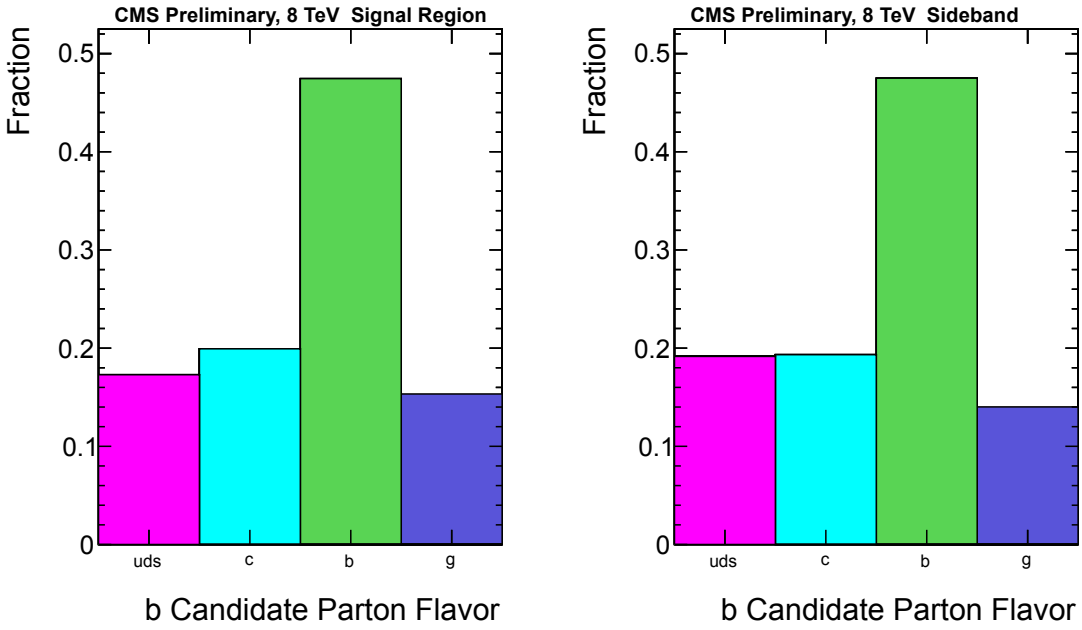

Figure 3.16: Comparison of jet parton flavor composition from the signal region and sideband.

The regions in $|\eta|$ are then individually parameterized in $\mathrm{p_T}$ to produce the average b-tagging rate. We perform this parameterization of the b-tagging rate in an attempt to constrain the kinematic correlations inherent in b-tagging.

To smooth out the binning of the average b-tagging rate, a study of functional fits was conducted for the average b-tagging rate (see Figure 3.39). We chose the bifurcated polynomial fit based on observed representation of the data. The fitting function is as follows

$$f(x) = \begin{cases} p_0 + p_1 x + p_2(x - \mathrm{a})^2, & \text{if x} < \text{a} \\ p_0 + p_1 x + p_3(x - \mathrm{a})^2, & \text{if x} \geq \text{a} \end{cases} \tag{3.9}$$

Here, the parameters p_0 through p_3 are inputs to the fitting algorithm, and x is the $\mathrm{p_T}$ of the b candidate jet. The parameter a is the bifurcation point, and is chosen manually for each region in η. It is chosen to be 500 GeV, 500 GeV, and 550 GeV for the low, transition, and high η regions respectively. This piecewise function allows for two characteristic ranges to fit a polynomial, which makes a good fit for the different functional forms of the average b-tagging rate regions that we use.

The errors on the average b-tagging rate are then extracted using the full covariance matrix as obtained from output of the fitting algorithm. Additionally, we assign a systematic uncertainty to cover the choice of the fit function (see Section 3.5) based on several alternative functional forms. Figure 3.17 shows the tags (numerator) and

probes (denominator) of the tagging rate. Figure 3.18 shows the three fitted average b-tagging rates parameterized in p_T.

3.3.3 $t\bar{t}$ Subtraction

The $t\bar{t}$ contribution to background is computed from MC that passes the full selection. To avoid double-counting, we must remove $t\bar{t}$ from our QCD estimate. In creating the b-tagging rate, the $t\bar{t}$ contribution to the numerator and denominator is subtracted away using $t\bar{t}$ MC. Additionally, we account for the $t\bar{t}$ contamination of the QCD background estimate by applying the average b-tagging rate to $t\bar{t}$ MC in the same way as data. This is a measure of $t\bar{t}$ that is expected to fall through the QCD background estimate and is subtracted away.

3.3.4 Sideband Closure

In order to investigate the applicability and versatility of the QCD background estimation in data, we apply the average b-tagging rate to sideband regions of our top tagging selection. First, we define the following sideband:

- **Jet Mass** 140 GeV $< m_{jet} <$ 250 GeV
- **Number of Subjets** $N_{subjets} > 2$
- **Minimum Pairwise Mass** $m_{min} \leq 50$ GeV

	η_1	η_2	η_3
pretag QCD	15922 (99.77%)	14396 (99.79%)	5494 (99.81%)
tagged QCD	924 (99.17%)	847 (99.16%)	285 (99.54%)
pretag $t\bar{t}$	37 (0.23%)	31 (0.21%)	11 (0.19%)
tagged $t\bar{t}$	8 (0.83%)	7 (0.84%)	1 (0.46%)
pretag signal at 1300GeV	108 (0.67%)	77 (0.53%)	17 (0.30%)
tagged signal at 1300GeV	37 (3.94%)	24 (2.87%)	4 (1.44%)
pretag signal at 1500GeV	62 (0.39%)	39 (0.27%)	8 (0.14%)
tagged signal at 1500GeV	17 (1.86%)	11 (1.28%)	2 (0.67%)
pretag signal at 1700GeV	31 (0.19%)	19 (0.13%)	3 (0.06%)
tagged signal at 1700GeV	8 (0.82%)	4 (0.53%)	1 (0.25%)
pretag signal at 1900GeV	15 (0.09%)	9 (0.06%)	1 (0.02%)
tagged signal at 1900GeV	3 (0.31%)	2 (0.20%)	0 (0.07%)
pretag signal at 2100GeV	7 (0.04%)	4 (0.03%)	0 (0.01%)
tagged signal at 2100GeV	1 (0.13%)	1 (0.09%)	0 (0.03%)

Table 3.6: Number of tagged and pretagged events for each background sample and percent contribution to overall average b-tagging rates. Additionally, signal samples are investigated. The percents indicated are out of the total QCD + $t\bar{t}$ expectation and the signal samples are scaled to theory cross-section.

- **N-subjettiness** $\tau_3/\tau_2 \geq 0.55$

- **Subjet b-Tagging** $\mathrm{SJ_{CSVMAX}} \geq 0.679$

This region lies outside of the signal region and sideband used for average b-tagging rate determination. The selection also has a very low yield of $t\bar{t}$, making it ideal for investigating the QCD background contribution. The average b-tagging rate used for this closure test is extracted from the same sideband as the signal region, and applied to pre-b-tagged events. The closure test can be seen in Figure 3.19.

Additionally, we can define the following sideband

- **Jet Mass** 140 GeV $< \mathrm{m_{jet}} <$ 250 GeV

- **Number of Subjets** $N_{subjets} > 2$
- **Minimum Pairwise Mass** $m_{min} > 50$ GeV
- **N-subjettiness** $\tau_3/\tau_2 < 0.55$
- **Subjet b-Tagging** $SJ_{CSVMAX} \leq 0.679$

The closure test can be seen in Figure 3.20.

3.3.5 Deriving the normalization of the SM $t\bar{t}$ production

In order to study the contribution from $t\bar{t}$ to tbe full background estimate, we turn to a sideband defined by inverting the b candidate mass requirement in the signal region. This selection has an amplified $t\bar{t}$ fraction and is statistically independent from all other sidebands in the analysis. This makes the selection ideal for extracting the $t\bar{t}$ fraction in data. In order to extract this fraction, we compare the data-driven QCD background and $t\bar{t}$ MC expectation to the selection in data.

We perform a template fit to the invariant mass of the b candidate, using scaled $t\bar{t}$ MC as one template, and the QCD background prediction as the other. The fit allows the QCD background template to move only within its errors, whereas the normalization on $t\bar{t}$ is unconstrained. The optimal parameterization for this fit is in a variable that has distinctly different shapes in $t\bar{t}$ and QCD. We therefore use the b

candidate mass, which minimizes the correlation between the QCD and $t\bar{t}$ templates within the fit. The fit can be seen in Figure 3.21. For this maximum likelihood fit we use the Theta package.

Additionally, the fit implements the $t\bar{t}$ subtraction in the QCD estimate by fitting un-subtracted QCD to the $t\bar{t}$ full selection. The output of the fitter is then corrected by (1+S/F), where S/F is the ratio of the number of events in $t\bar{t}$ subtracted selection to the $t\bar{t}$ full selection.

This study suggests after all scale factors applied in the analysis, the $t\bar{t}$ contribution needs to be amplified by 1.23 ± 0.24. This normalization is used for all $t\bar{t}$ distributions in the analysis, and the uncertainty is then the full normalization uncertainty for $t\bar{t}$.

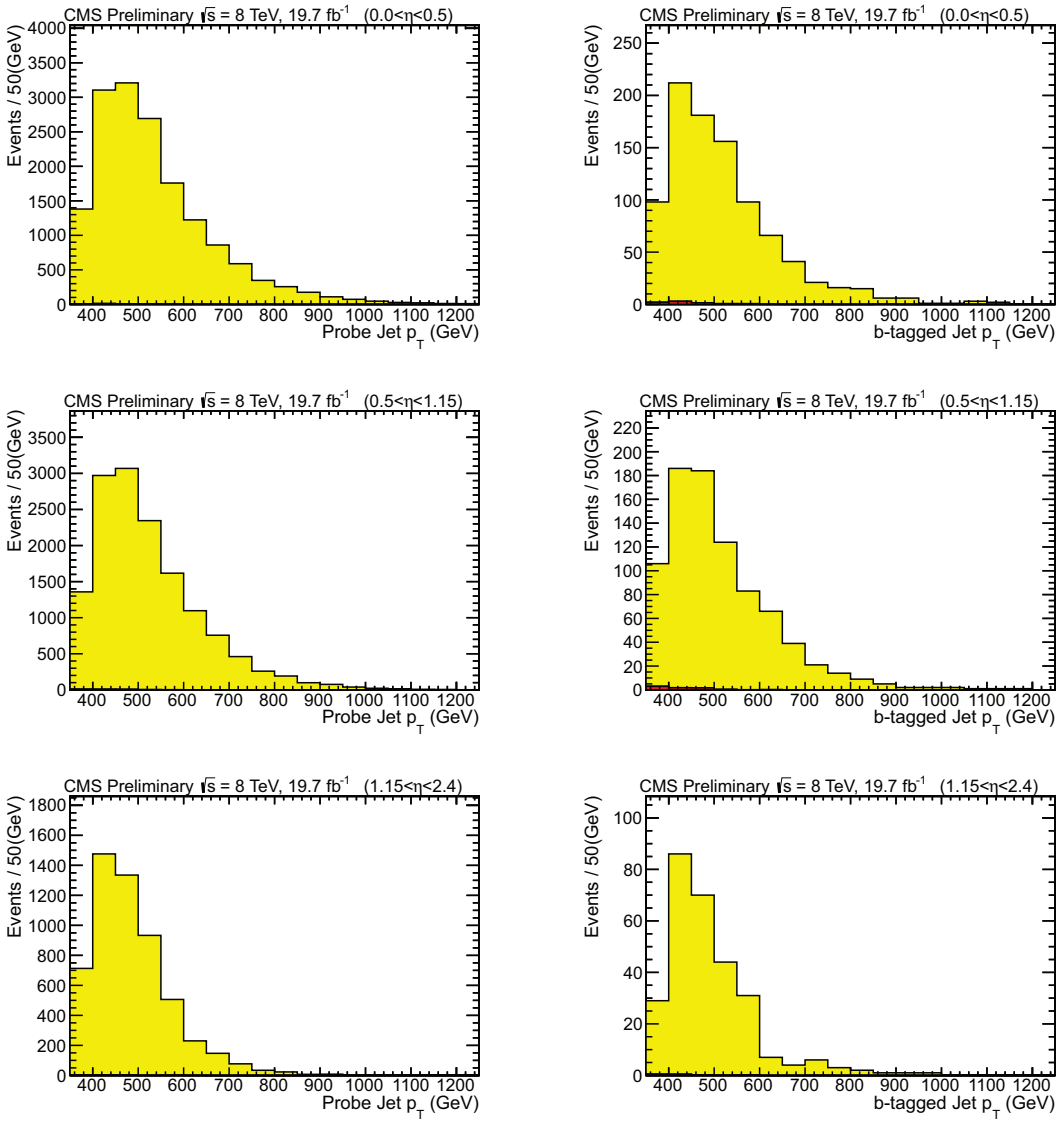

Figure 3.17: The tags and probes used for the average b-tagging rate in each of the three regions in $|\eta|$. Here, tags are the numerator and probes are the denominator of the average b-tagging rate

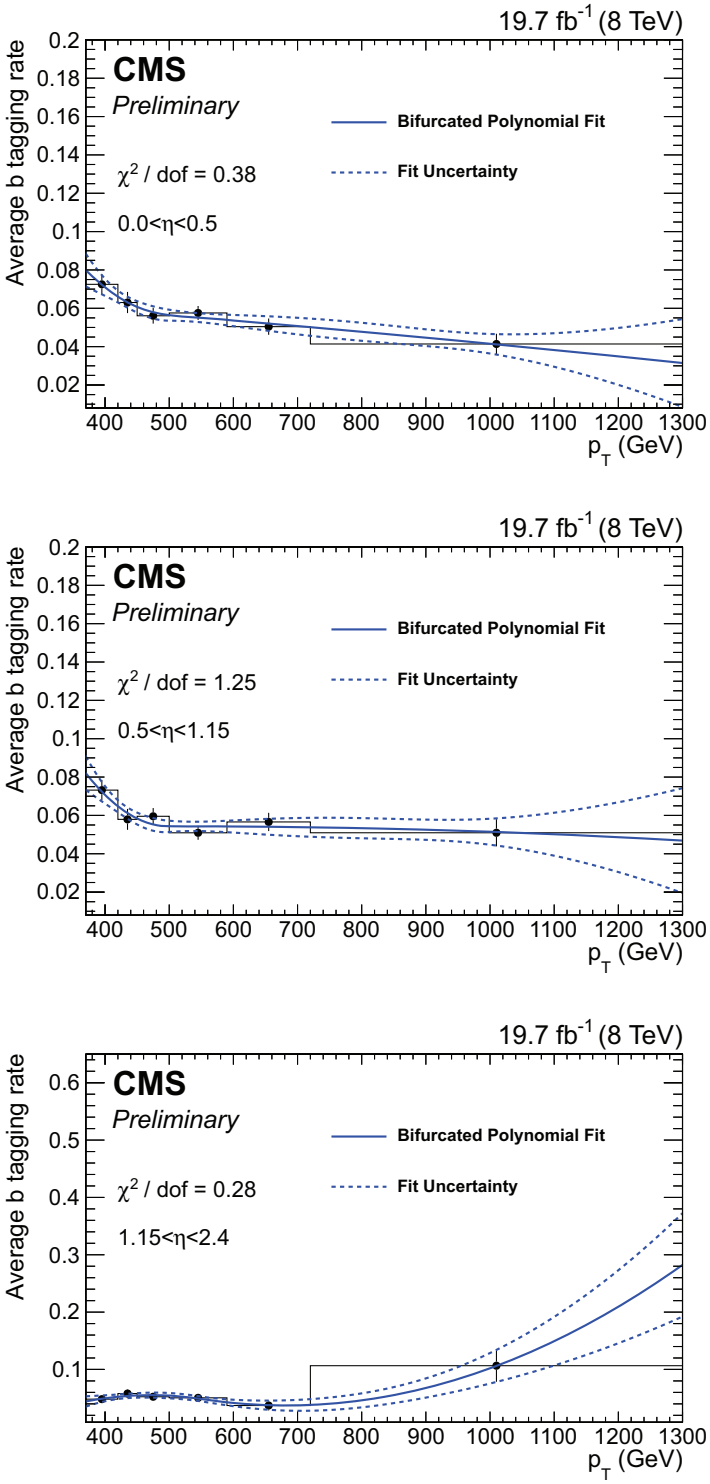

Figure 3.18: p_T parameterized average b-tagging rate from (a) Low η region (b) Transition η region (c) High η region. The average b-tagging rate is shown in black, the polynomial fit is shown in blue, and the propagated errors from the fit are shown as a blue dashed line.

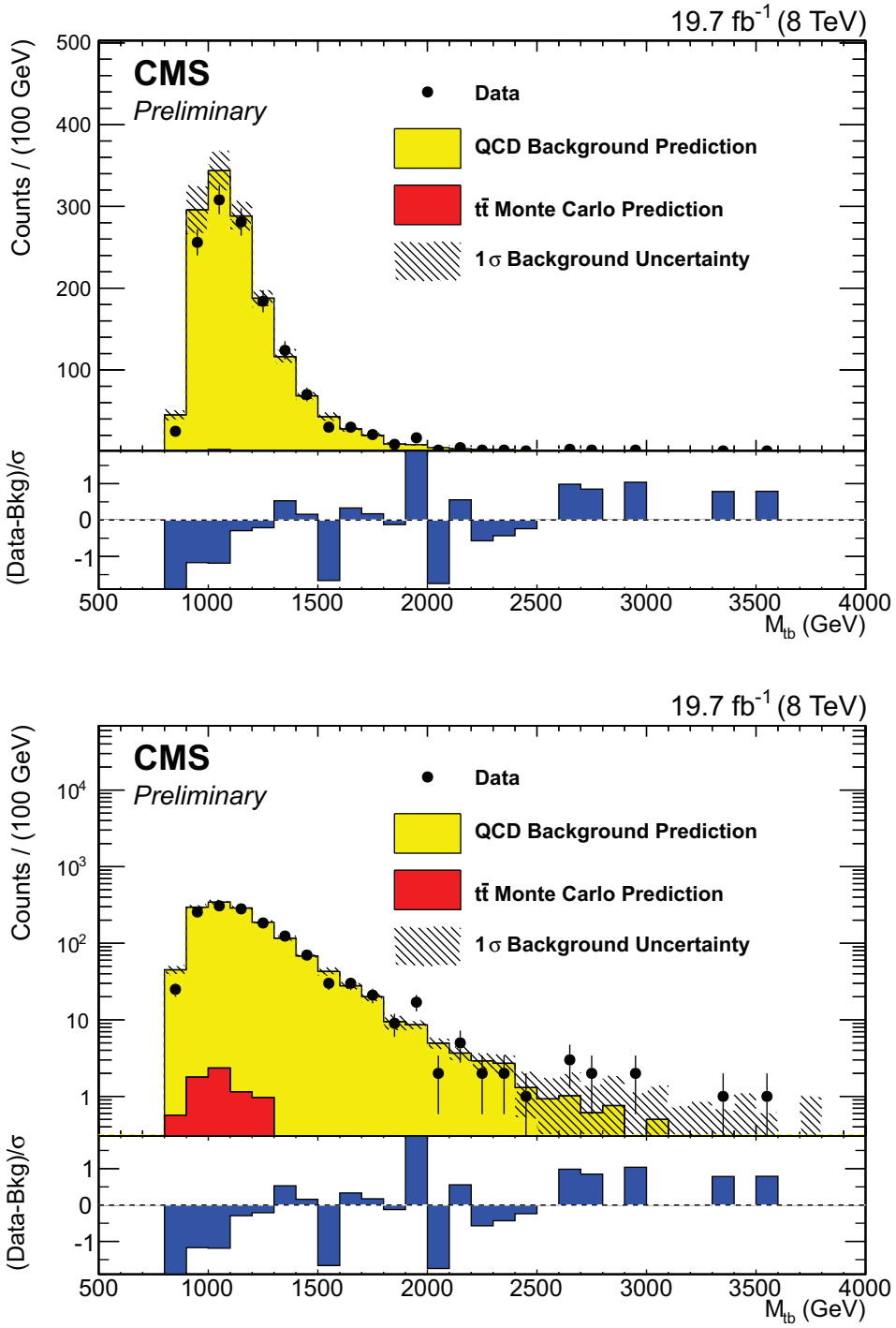

Figure 3.19: A plot of M_{tb} in the control region defined by inverting the minimum pairwise mass and N-subjettiness cuts used in the full selection. The top and bottom plots are the same but with linear and log y-axis scale.

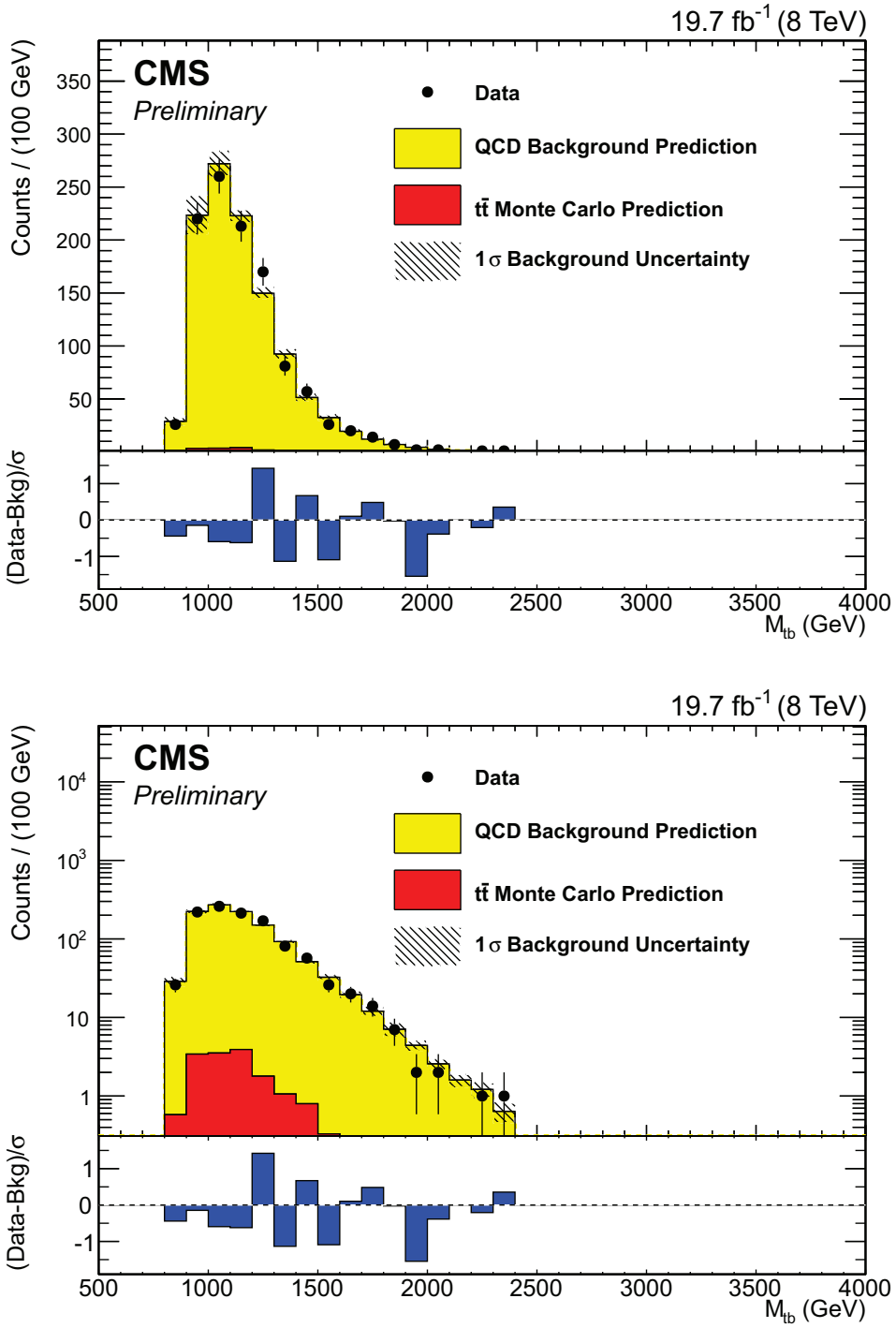

Figure 3.20: A plot of M_{tb} in the control region defined by inverting the subjet b tagging cut used in the full selection. The top and bottom plots are the same but with linear and log y-axis scale.

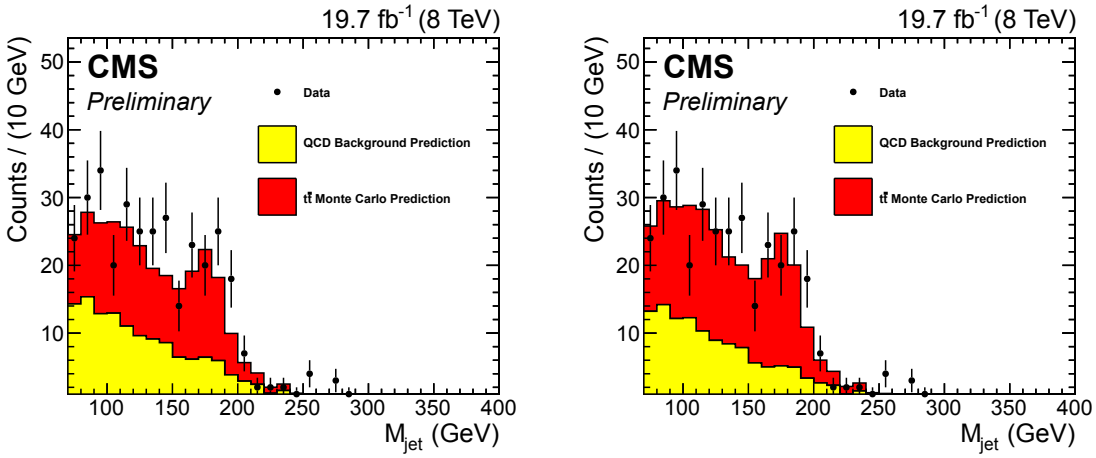

Figure 3.21: b candidate mass as extracted from the b candidate mass inverted sideband. Pre fraction fit (left) and post fraction fit (right).

3.4 Data Results

After closure of the background estimation procedure within control regions, we first apply the background estimate to a loose selection that contains all of the full selection cuts with the exception of subjet b-tagging and N-subjettiness. The agreement using this selection can be seen in figure 3.22.

After observing agreement is the loose selection, we investigate the full selection. The final results are shown in Figure 3.23. We proceed to compute limits on the W′ cross-section. Background estimation of selected relevant variables can be seen in Figures 3.24 and 3.25.

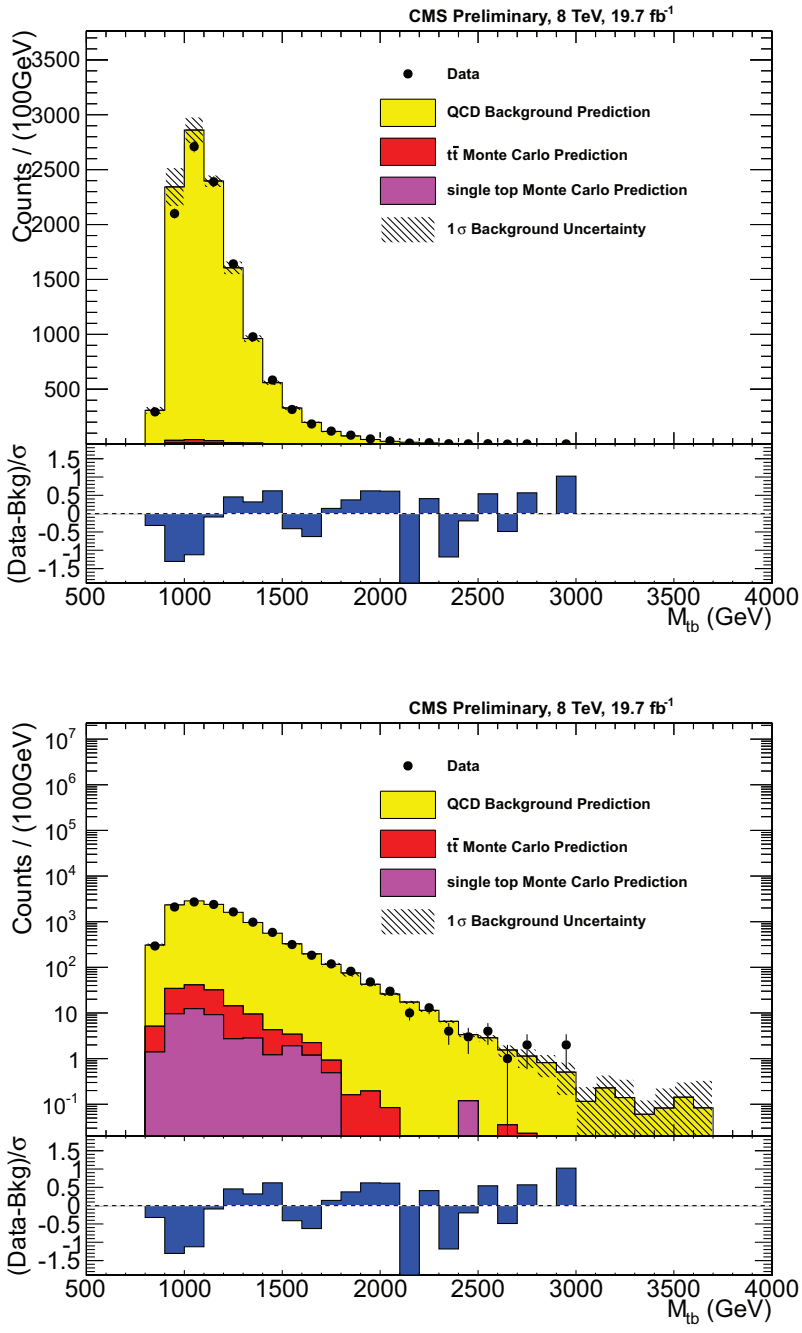

Figure 3.22: A plot of the full selection before N-subjettiness and subjet b-tagging discrimination. Here we investigate the data-background agreement in a loose selection before looking at the full top tagging selection. Top and bottom plots are the same but with linear and log y-axis scale.

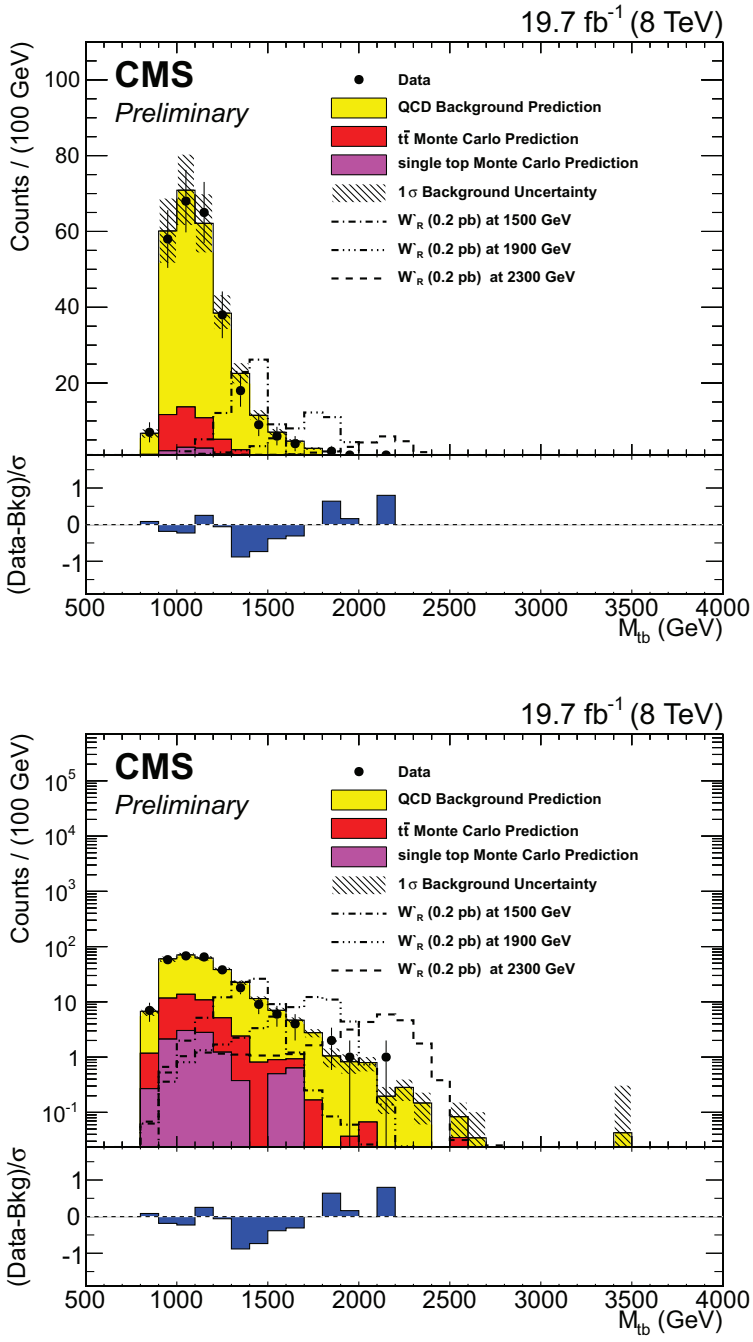

Figure 3.23: A plot of the full selection comparing data, signal and background. The single top contribution is not considered when setting limits. The normalization for the signal samples is set to a cross-section of 0.2 pb. Top and bottom plots are the same but on linear and log y-axis scale.

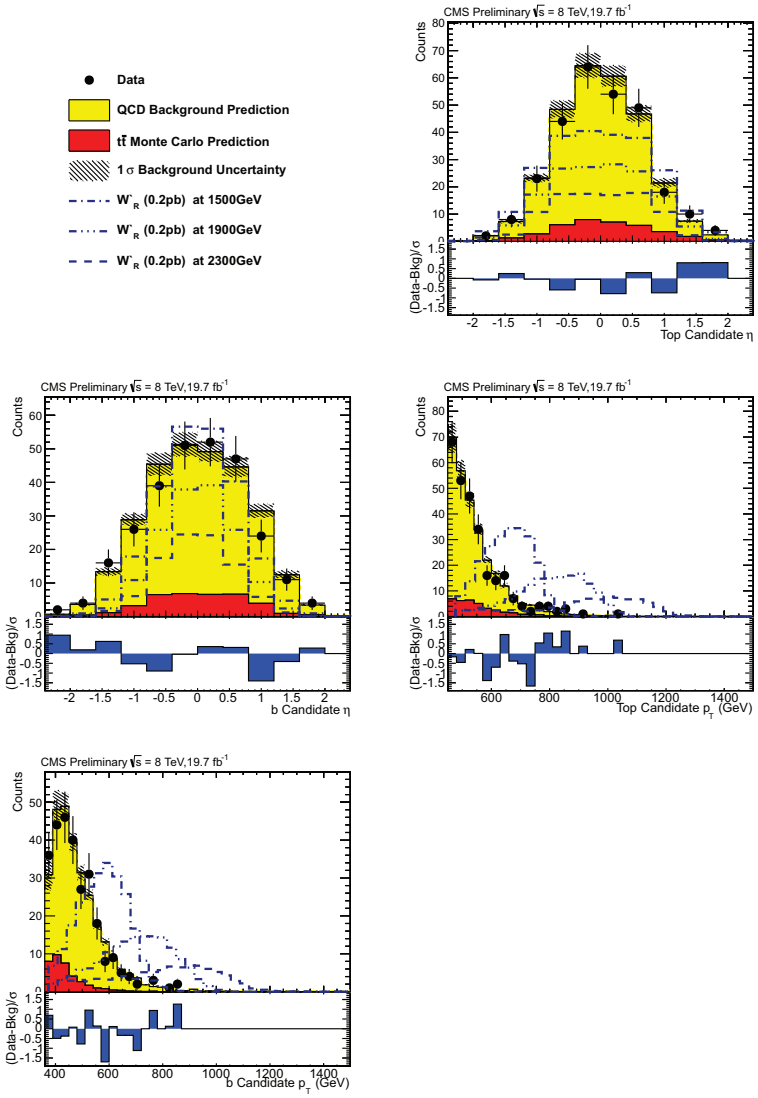

Figure 3.24: Background estimation of kinematic variables. The error bars shown are from the three primary sources; uncertainty on the fit, choice of fit, $t\bar{t}$ normalization, and $t\bar{t}$ Q^2 uncertainty

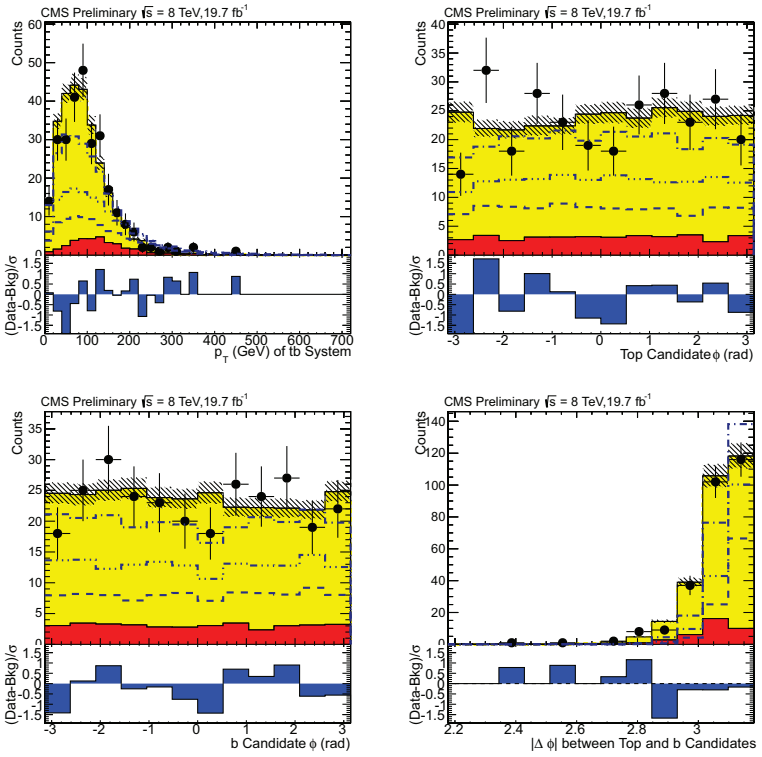

Figure 3.25: Background estimation of kinematic variables. The error bars shown are from the three primary sources; uncertainty on the fit, choice of fit, $t\bar{t}$ normalization, and $t\bar{t}$ Q^2 uncertainty

3.5 Systematic Uncertainties

Various systematics are taken into account, both on our expected signal and background estimate. Some systematic uncertainties will affect only the normalization of certain event rates, and are reported as overall normalization uncertainties. Other systematics affect the shapes of the reconstructed signal or backgrounds, as well as their normalization. The Systematic uncertainties that are used in the analysis are summarized in table 3.10.

3.5.1 Jet Energy Scale

We evaluate the effect of uncertainty on the jet energy scale on samples derived from MC simulation. To do so, we vary the jet four-momentum up and down by the jet energy scale uncertainty, which we take to be 3%. We include p_T and η dependent corrections to the jet energies, as well as uncertainties from the difference in measured and simulated W masses [37].

Varying the jet momentum can cause a jet to fall below or rise above the p_T cut in the analysis, thus shifting the invariant mass spectrum of the signal and reconstructed $t\bar{t}$ samples. Figure 3.29 shows the systematic shapes from the jet energy scale on the $t\bar{t}$ distribution. Jet Energy scale variation on signal MC is shown in Figure 3.28 for 1300 GeV, 1900 GeV, and 2300 GeV mass points.

3.5.2 Trigger

We include an uncertainty based on the measured trigger efficiency for all MC Samples. The trigger efficiency is discussed in Section 3.2.2. To obtain shape systematics from this effect, we vary the trigger by half the trigger *in*efficiency. The effects of this on the $t\bar{t}$ distribution is shown in Figure 3.31. Trigger weighting on signal MC is shown in Figure 3.30 for 1300 GeV, 1900 GeV, and 2300 GeV mass points. The uncertainty is low in the mass range of interest for limit setting.

3.5.3 Jet Energy Resolution

We apply a systematic due to the known differences in jet energy resolution in data and simulation. We use η dependent smearing (see [37]) as recommended by the JER group. We apply this systematic uncertainty to the $t\bar{t}$ distribution (as seen in Figure 3.33). Jet Energy Resolution variation on signal MC is shown in Figure 3.32 for 1300 GeV, 1900 GeV, and 2300 GeV mass points.

3.5.4 Jet Angular Resolution

A smearing of 10% is assumed on η and ϕ and shape uncertainties are generated by considering smearing 10% lower and higher. We apply this systematic uncertainty to the $t\bar{t}$ distribution (as seen in Figure 3.35). Jet Angular Resolution variation on signal MC is shown in Figure 3.34 for 1300 GeV, 1900 GeV, and 2300 GeV mass

points. The effect is very small and thus not considered in setting limits.

3.5.5 PDF Uncertainty

The uncertainty in the parton distribution function used for MC sample generation is investigated. We take the average of the $\pm 1\sigma$ eigenvalue variation of the pdf master equations [38] for the NNPDF, MSTW2008nnlo, and CT10 pdf sets to weight the signal and $t\bar{t}$ MC samples and investigate the impact on the full selection. The PDF set that provides the maximum uncertainty is then used for the $\pm 1\sigma$ PDF uncertainty. For $t\bar{t}$ and signal this set is NNPDF. PDF variation on signal MC is shown in Figure 3.36 for 1300 GeV, 1900 GeV, and 2300 GeV mass points. PDF variation on $t\bar{t}$ MC is shown in Figure 3.37. The effect is very small and thus not considered in setting limits.

3.5.6 Pileup

A study of pileup uncertainty is conducted by varying the minimum bias cross-section by 5% as a measure of systematic uncertainty. The results can be seen in figure 3.38. The effect is very small and thus not considered in setting limits.

p_T **range**	**Absolute Error on** SF_b
320 GeV $< p_T <$ 400 GeV	0.0313175
400 GeV $< p_T <$ 500 GeV	0.0415417
500 GeV $< p_T <$ 600 GeV	0.0740446
600 GeV $< p_T <$ 800 GeV	0.0596716

Table 3.7: Absolute Error applied to the b-tagging Scale Factor

3.5.7 b-Tagging Scale Factor Uncertainty

The uncertainty in the b-tagging scale factor described in Section 3.2.10 is applied based on the b candidate pt. The binning and associated errors listed below are the suggested EPS13 prescription generated from measurements in both muon-jet and ttbar data representing 20 fb^{-1} of integrated luminosity. The absolute uncertainty on SF_b for a b candidate jet within the listed p_T range is applied as shown in table 3.7 for $p_T < 800$ GeV. B candidate jets with $p_T > 800$ GeV are assigned an uncertainty equal to twice the listed value for 600 GeV $< p_T <$ 800 GeV

3.5.8 Q^2 Scale Uncertainty

We use additional $t\bar{t}$ samples generated with twice and half the nominal Q^2 scale used in the $t\bar{t}$ samples listed in table 3.1. These samples vary the renormalization and factorization scales to account for missing higher order corrections in our simulation. Figure 3.26 shows the shape based uncertainty due to this effect.

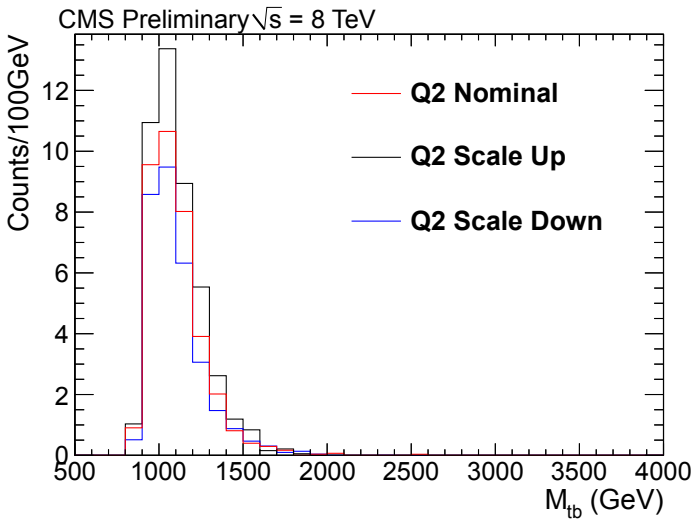

Figure 3.26: Q^2 systematic variation for $t\bar{t}$ MC

3.5.9 $t\bar{t}$ p_T Re-weighting

The uncertainty related to the p_T re-weighting scheme presented in Section 3.2.6 is taken as the difference between the weighted and unweighted $t\bar{t}$ spectrum. This uncertainty can be seen in figure 3.27. This is the dominant uncertainty for $t\bar{t}$.

3.5.10 Normalization Uncertainties

As mentioned in Section 3.3.5, the uncertainty due to the overall normalization scale factor used for $t\bar{t}$ is extracted from data and is 19%.

We must apply a 13% uncertainty on the top tagging scale factor described in Section 3.2.8 to signal MC events due to uncertainty in the difference in subjet efficiency from data to MC.

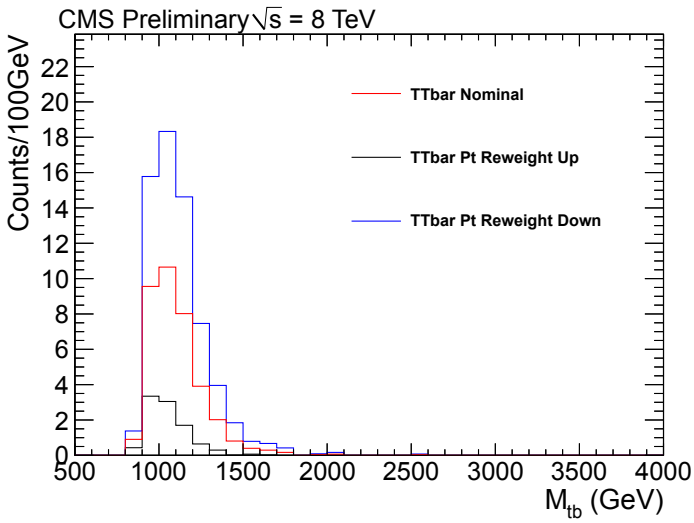

Figure 3.27: p_T re-weighting systematic variation for $t\bar{t}$ MC

As mentioned in Section 3.2.10, we add a 2% uncertainty to the signal estimates from the AK5 vs. CA8 scale factor on b-tagging efficiency.

We also include a 2.6% uncertainty in the luminosity for the signal MC [39].

3.5.11 Uncertainties related to the QCD Background Estimate

We use the result of the fit to the average b-tagging rate (see Section 3.3) to weight pre b-tagged events in order to create the QCD background estimate. Uncertainties in the fitting algorithm and statistical uncertainties in the sideband are taken into account (see figure 3.18). Statistical uncertainties in the pre b tagged signal region are also taken into account.

3.5.11.1 Choice of the functional form for the average b-tagging rate

The functional form used is a bifurcated polynomial. However there is a systematic uncertainty associated with this choice. The uncertainties due to this effect are taken into account by studying alternative functional forms seen in figure 3.39. The background estimation from these alternative fits are seen in figure 3.40. The uncertainty due to the choice of fit is taken as the Mean Squared Error of these alternative backgrounds bin by bin and can be seen in figure 3.41.

3.5.11.2 Two-dimensional vs. three-dimensional parameterization of the average b-tagging rate

Additionally, we place an uncertainty on the inability of the background estimate to capture all kinematic correlations through the parameterization of the average b-tagging rate in p_T and η. This uncertainty is calculated by investigating a parameterization in p_T η and M_{tb}. We define P_i as the average b-tagging rate described in Section 3.3 in one η bin and P_{ij} as the average b-tagging rate if parameterized with M_{tb} as well. P_{ij} can be seen in figure 3.42. Each bin in P_i can be thought of as a column average over all M_{tb} bins per p_T bin. If P_{ij} a function of M_{tb} (index j) is not constant, then averaging over P_{ij} over j while projecting onto M_{tb} axis to obtain the QCD background estimate can result in a bias. For more in-depth discussion on this effect, please see Section 6.1.3.

We assess the approximate size of the uncertainty due to our choice of parameterization by explicitly comparing the three-dimensional and two-dimensional background estimates in the sideband. Using these two parameterizations, the uncertainty in the M_{tb} distribution due to parameterization is approximately $\sum_{j=0}^{n} m_{ij}(P_{ij}-P_i)$ where m_{ij} refers to the number of pretag events for a bin in p_T and M_{tb}. Fig. 3.43 shows the uncertainty due to this effect. These uncertainties are taken in quadrature to produce an overall uncertainty in the data derived background estimate that is applied in a shape based manner in the limit-setting macro.

Rate Effects of Systematic Uncertainties

Sample	CA btag SF	QCD total	b-tagging	JES	Lumi	p_T Reweight	JER	Q^2	Subjet SF	Trigger	$t\bar{t}$ Norm
qcd	—	+9.05,-8.94	—	—	—	—	—	—	—	—	—
ttbar	—	—	+4.49,-4.49	-0.42,+0.49	+16.49,-15.27	—	+21.77,-14.96	-74.04,+77.89	—	+0.30,-0.30	+19.00,-15.97
1300	+2.00,-1.96	—	+6.08,-6.08	-0.27,+0.29	+2.06,-3.85	+2.60,-2.53	—	—	+12.50,-11.11	+0.06,-0.06	—
1500	+2.00,-1.96	—	+6.48,-6.48	-0.03,+0.17	-0.29,-0.19	+2.60,-2.53	—	—	+12.50,-11.11	+0.02,-0.02	—
1700	+2.00,-1.96	—	+6.94,-6.94	-0.02,+0.12	-1.27,+1.17	+2.60,-2.53	—	—	+12.50,-11.11	+0.01,-0.01	—
1900	+2.00,-1.96	—	+8.12,-8.12	-0.08,+0.02	-1.76,+1.78	+2.60,-2.53	—	—	+12.50,-11.11	+0.01,-0.01	—
2100	+2.00,-1.96	—	+9.39,-9.39	+0.06,-0.05	-1.81,+1.61	+2.60,-2.53	—	—	+12.50,-11.11	+0.01,-0.01	—
2300	+2.00,-1.96	—	+10.01,-10.01	+0.02,+0.09	-1.76,+1.24	+2.60,-2.53	—	—	+12.50,-11.11	+0.02,-0.02	—
2700	+2.00,-1.96	—	+9.49,-9.49	-0.25,+0.08	-0.33,+0.47	+2.60,-2.53	—	—	+12.50,-11.11	+0.04,-0.04	—

Table 3.8: Rate effects of the systematic uncertainties as extracted from Theta. The numbers listed under sample specify W'_R signal MC mass.

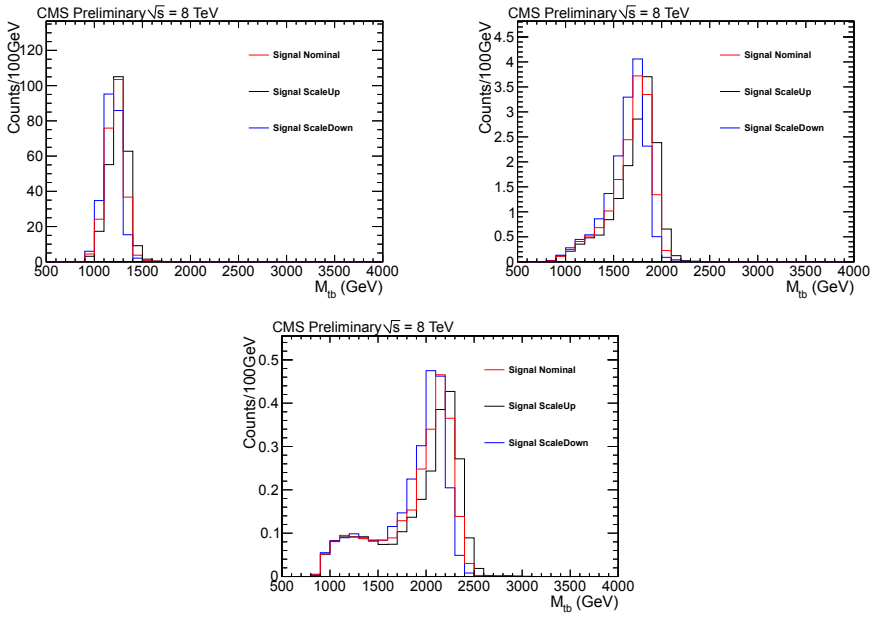

Figure 3.28: Jet Energy Scale systematic variation for Right-handed W′ MC at the following mass points (a) $M_{W'} = 1300$ GeV (b) $M_{W'} = 1900$ GeV (c) $M_{W'} = 2300$ GeV

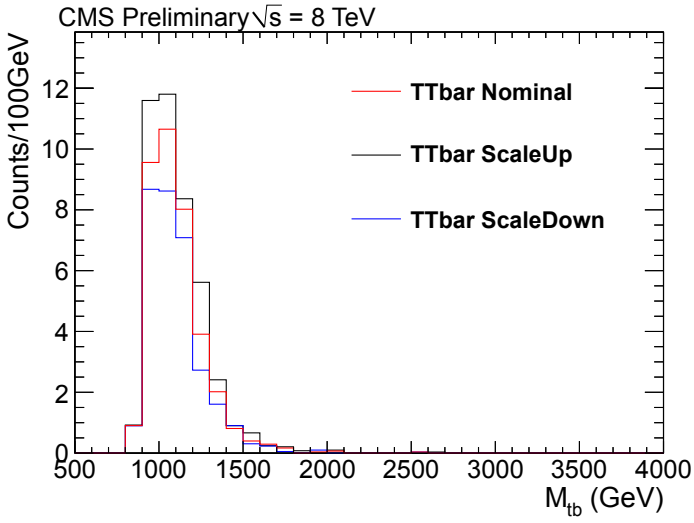

Figure 3.29: Jet Energy Scale systematic variation for $t\bar{t}$ MC

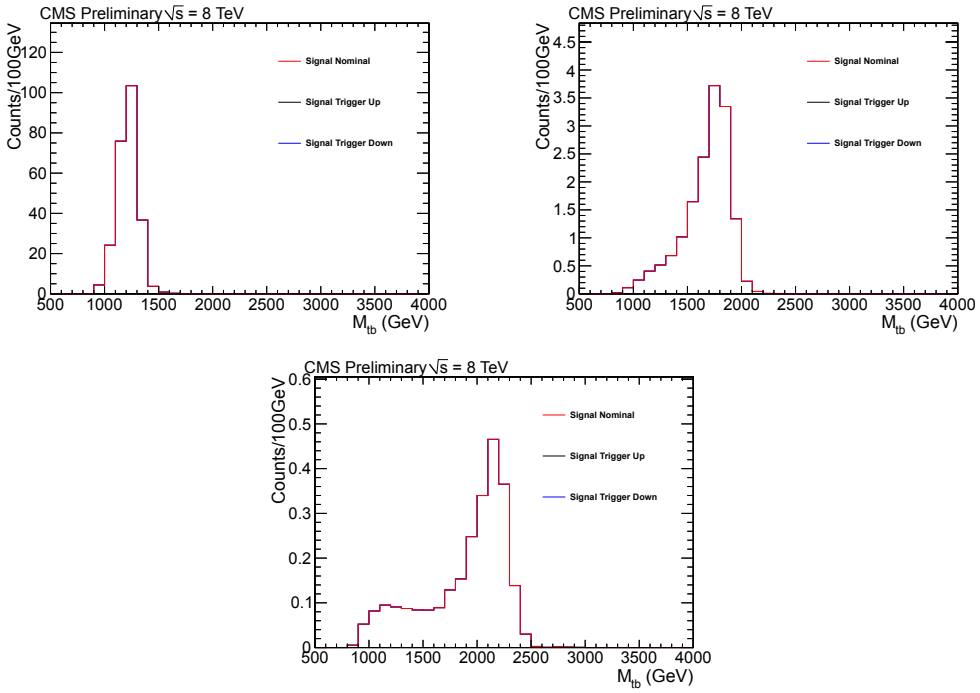

Figure 3.30: Trigger Weighting systematic variation for Right-handed W′ MC at the following mass points (a) $M'_{\mathrm{W}} = 1300$ GeV (b) $M'_{\mathrm{W}} = 1900$ GeV (c) $M'_{\mathrm{W}} = 2300$ GeV

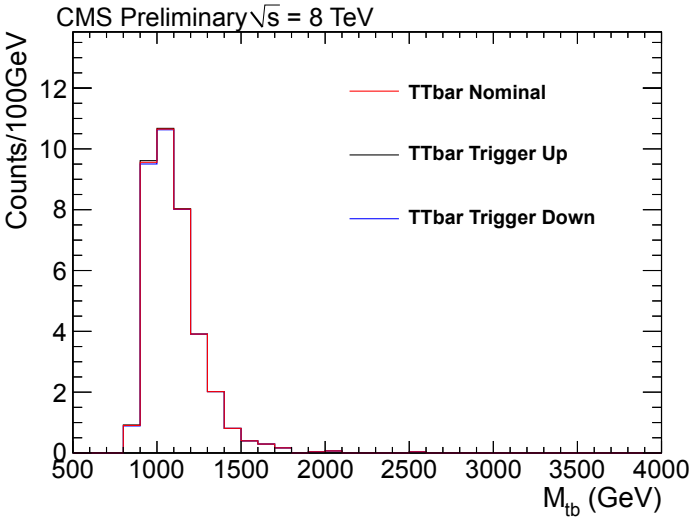

Figure 3.31: Trigger Weighting systematic variation for $\mathrm{t\bar{t}}$ MC

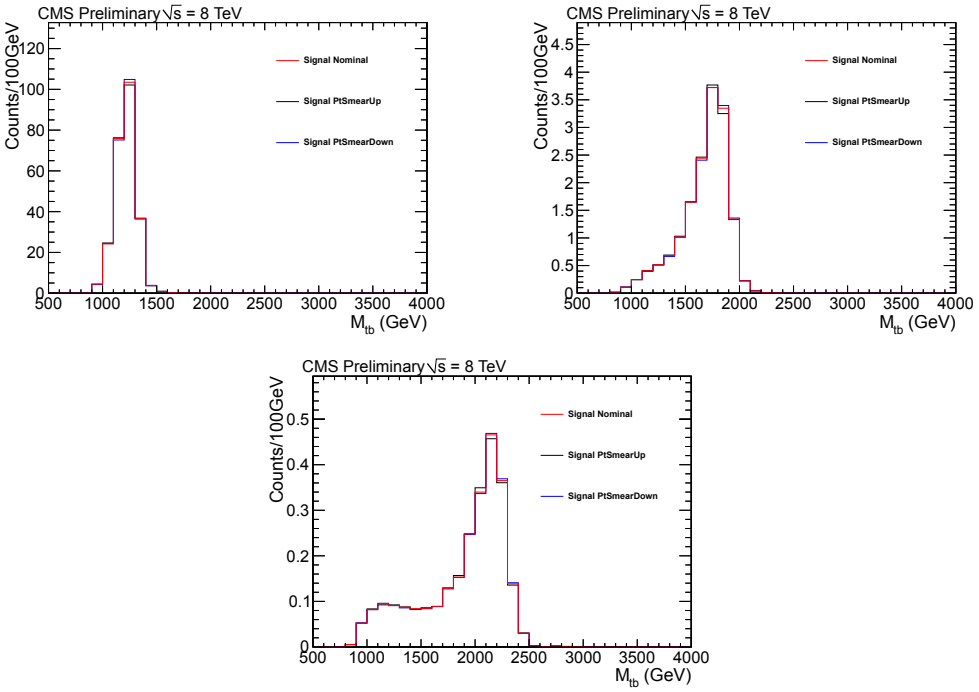

Figure 3.32: Jet Energy Resolution systematic variation for Right-handed W′ MC at the following mass points (a) $M_{W'} = 1300$ GeV (b) $M_{W'} = 1900$ GeV (c) $M_{W'} = 2300$ GeV

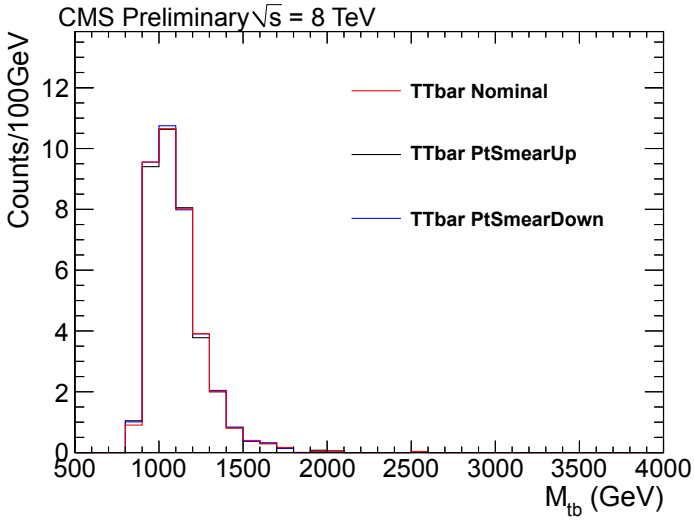

Figure 3.33: Jet Energy Resolution systematic variation for $t\bar{t}$ MC

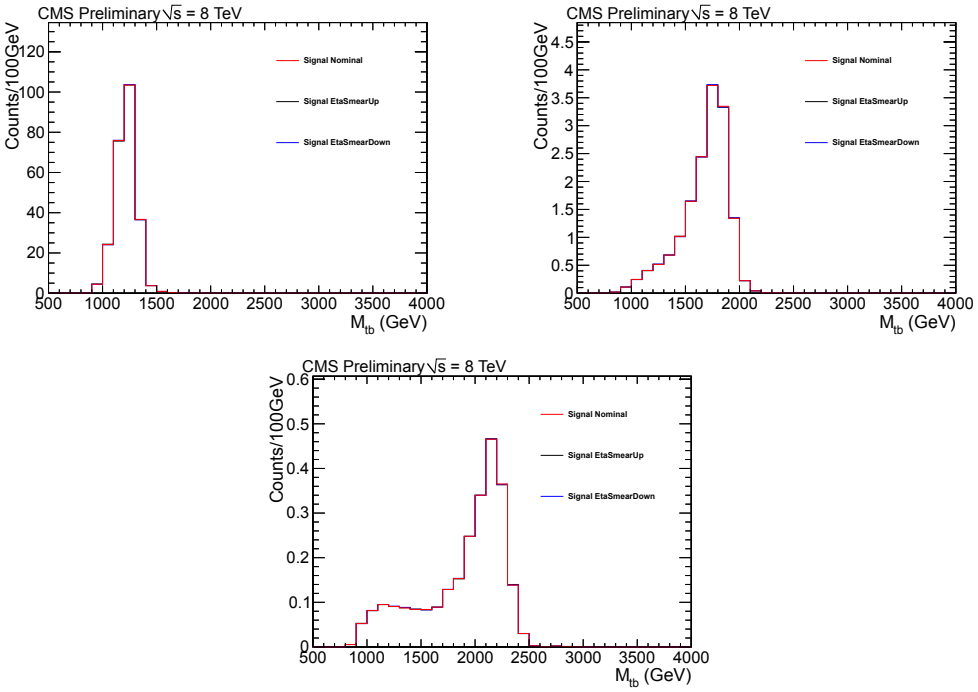

Figure 3.34: Jet Angular Resolution systematic variation for Right-handed W′ MC at the following mass points (a) $M'_{\mathrm{W}} = 1300$ GeV (b) $M'_{\mathrm{W}} = 1900$ GeV (c) $M'_{\mathrm{W}} = 2300$ GeV

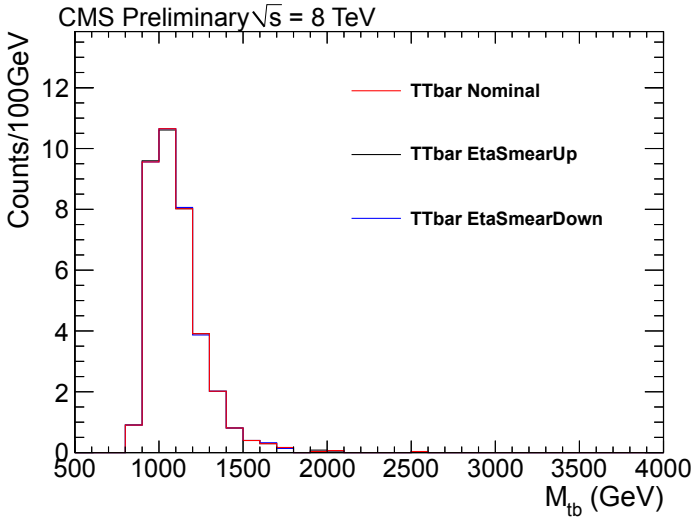

Figure 3.35: Jet Angular Resolution systematic variation for $\mathrm{t\bar{t}}$ MC

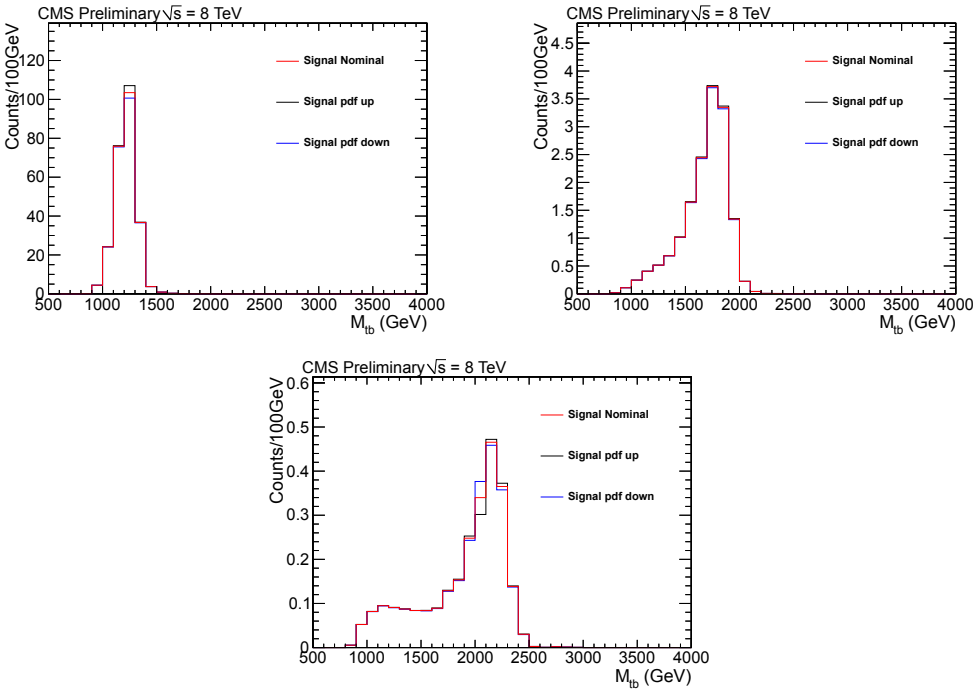

Figure 3.36: PDF systematic variation for Right-handed W′ MC at the following mass points (a) $M'_{\mathrm{W}} = 1300$ GeV (b) $M'_{\mathrm{W}} = 1900$ GeV (c) $M'_{\mathrm{W}} = 2300$ GeV

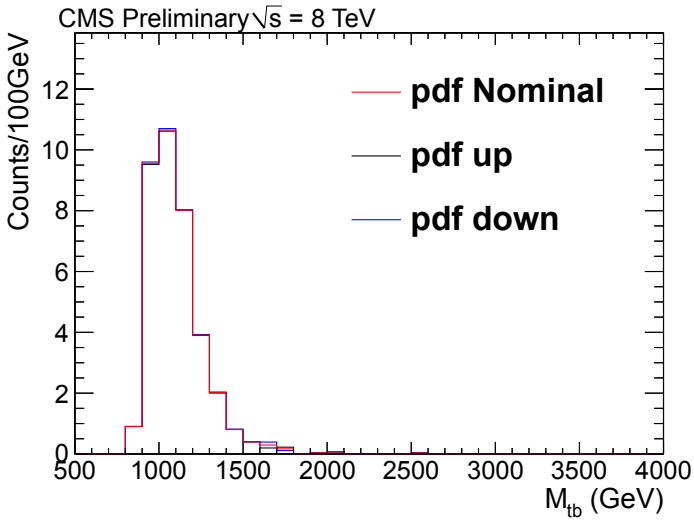

Figure 3.37: PDF systematic variation for $\mathrm{t\bar{t}}$ MC

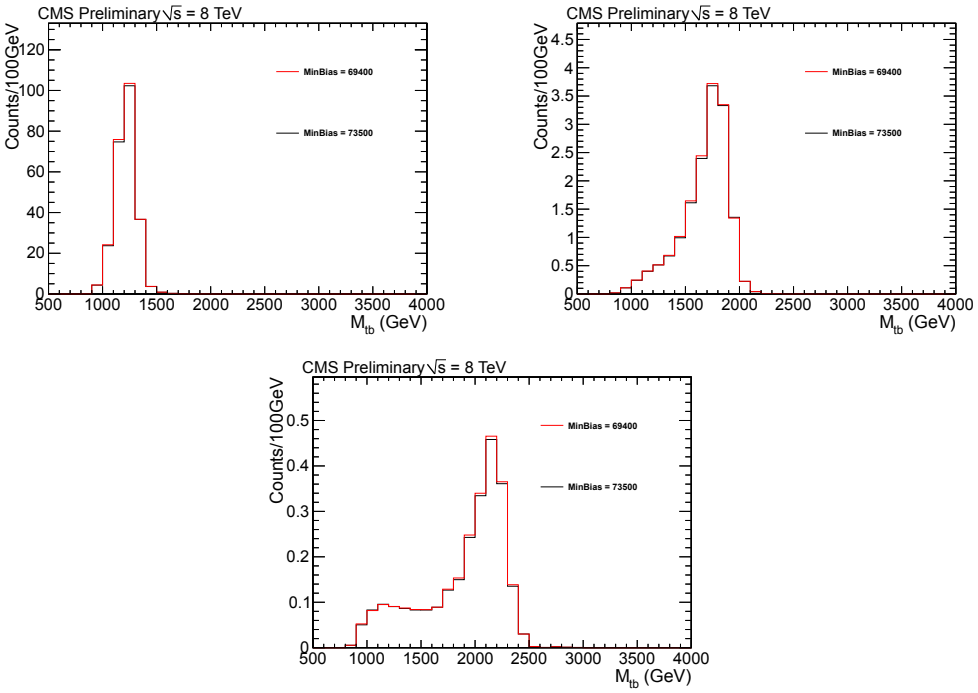

Figure 3.38: Pileup systematic variation for Right-handed W′ MC at the following mass points (a) $M_{\mathrm{W}'} = 1300$ GeV (b) $M_{\mathrm{W}'} = 1900$ GeV (c) $M_{\mathrm{W}'} = 2300$ GeV

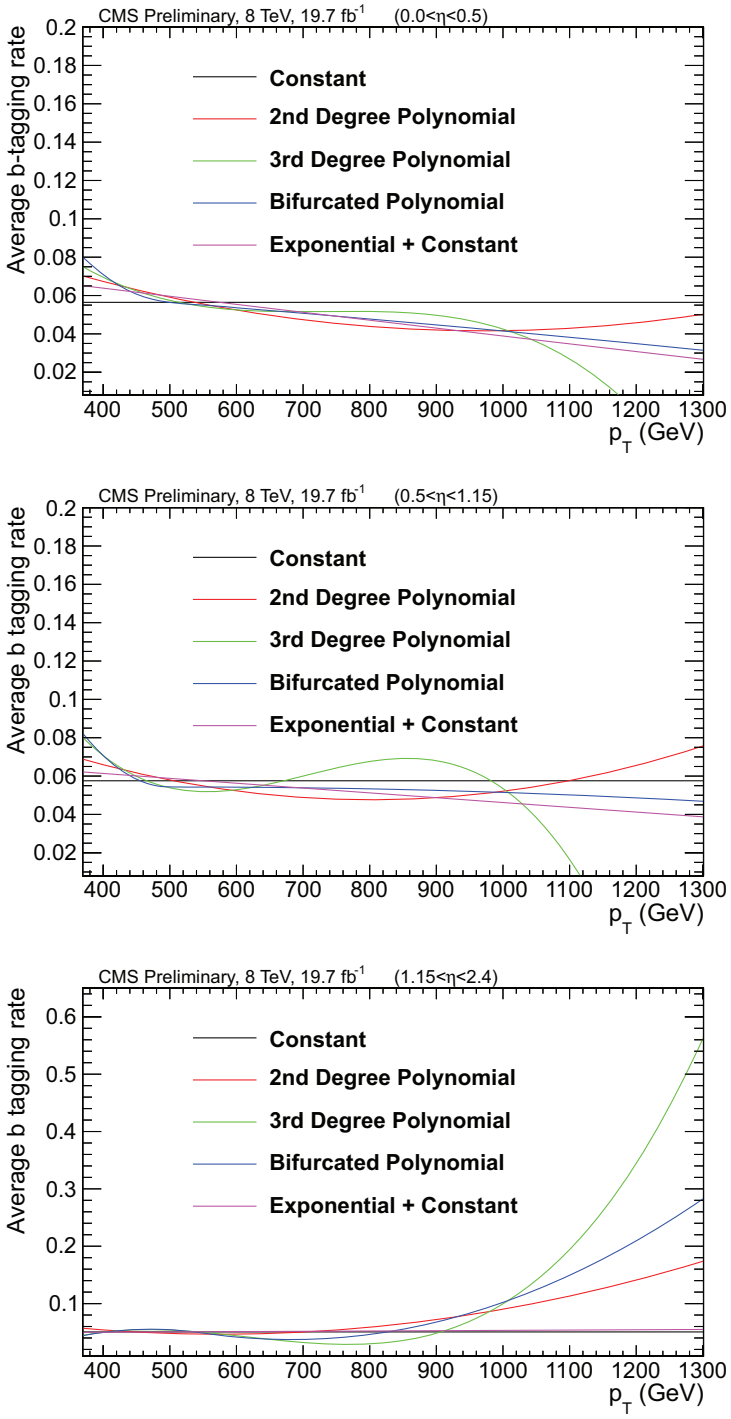

Figure 3.39: Alternative fit functions for the average b-tagging rate in η regions (a) Low (b) Transition (c) High

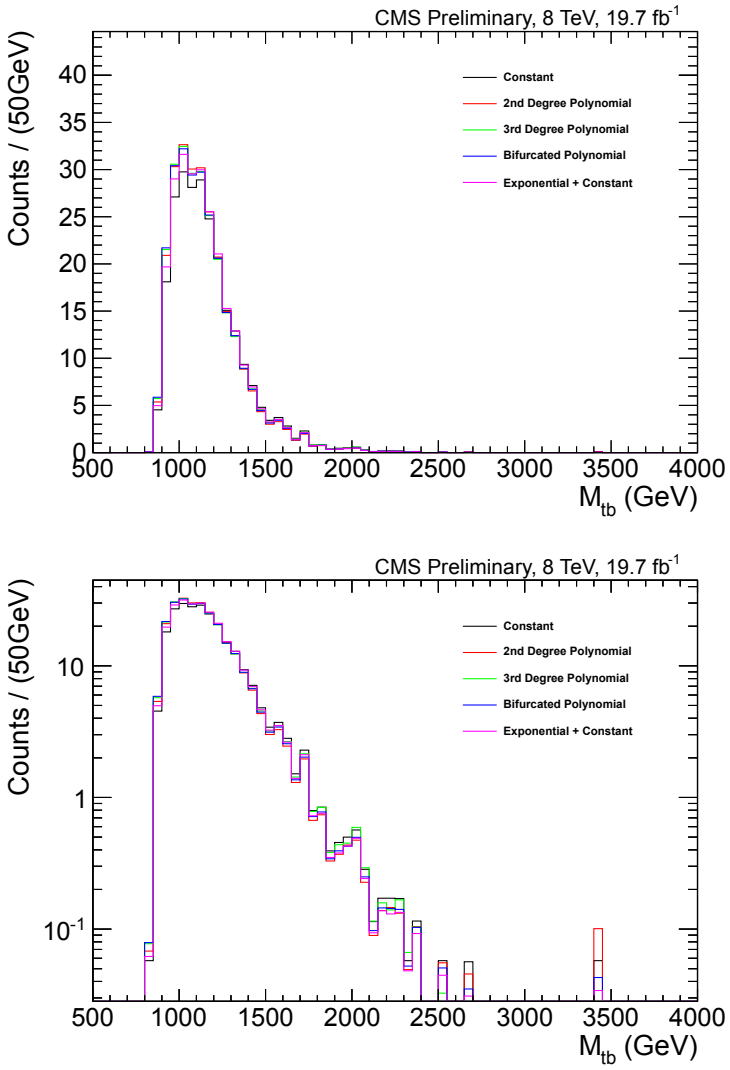

Figure 3.40: QCD background estimation from alternative fit functions seen in 3.39. Top and bottom plots are the same but on linear and log y-axis scale.

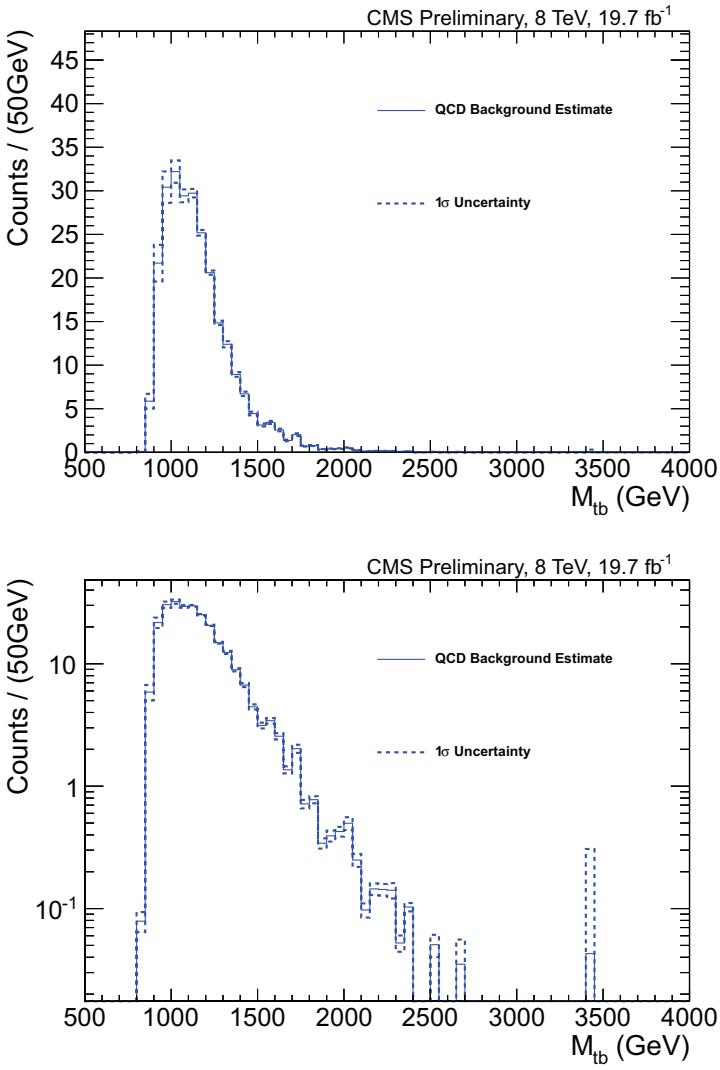

Figure 3.41: Uncertainty on the choice of fit as extracted from the alternative background estimations seen in 3.40. Top and bottom plots are the same but on linear and log y-axis scale.

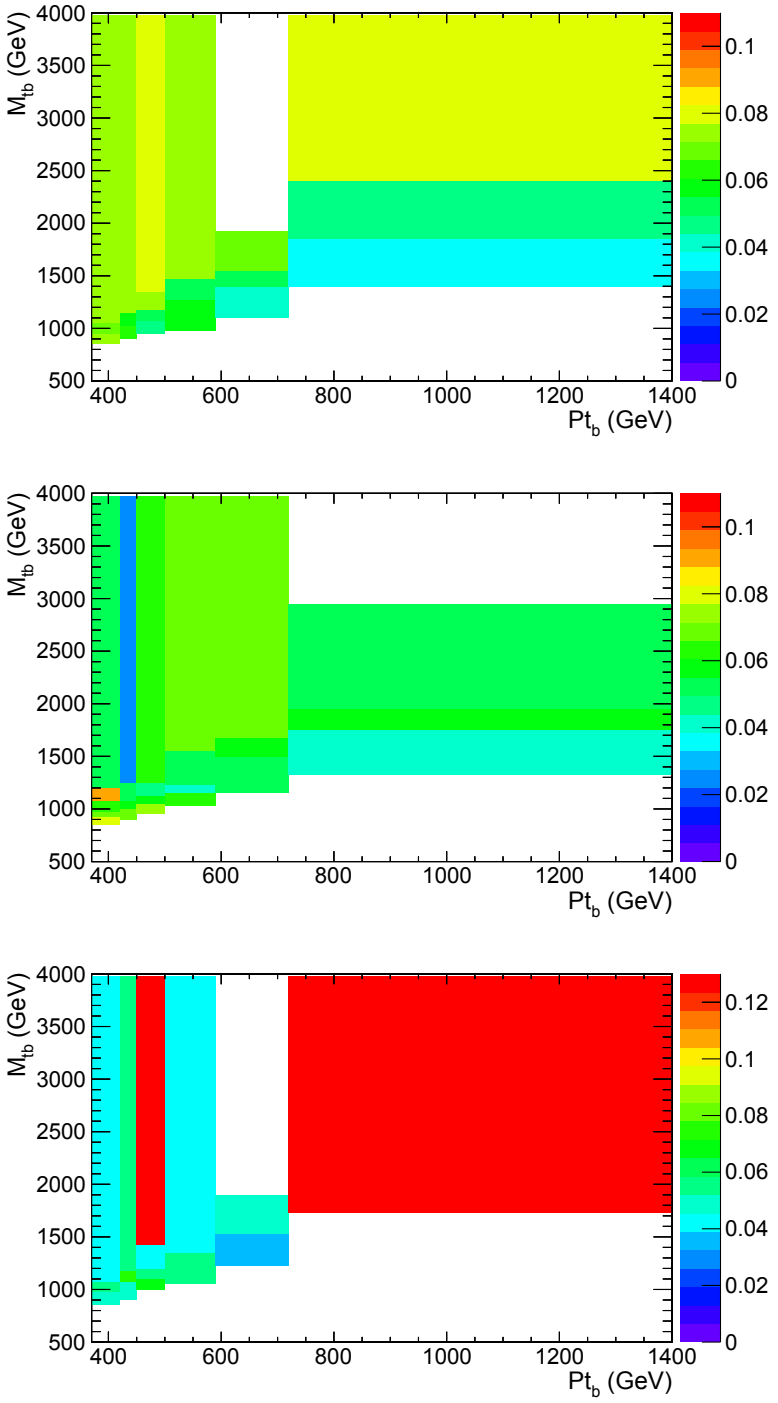

Figure 3.42: Two dimensional parameterization of average b-tagging rate in p_{T_b} and M_{tb}. The x axis binning is identical to the binning in Section 3.3. The y-axis is binned adaptively to approximate equivalent statistics over each y-axis bin per x axis bin. (a) Low η Region (b) Transition η Region (c) High η Region

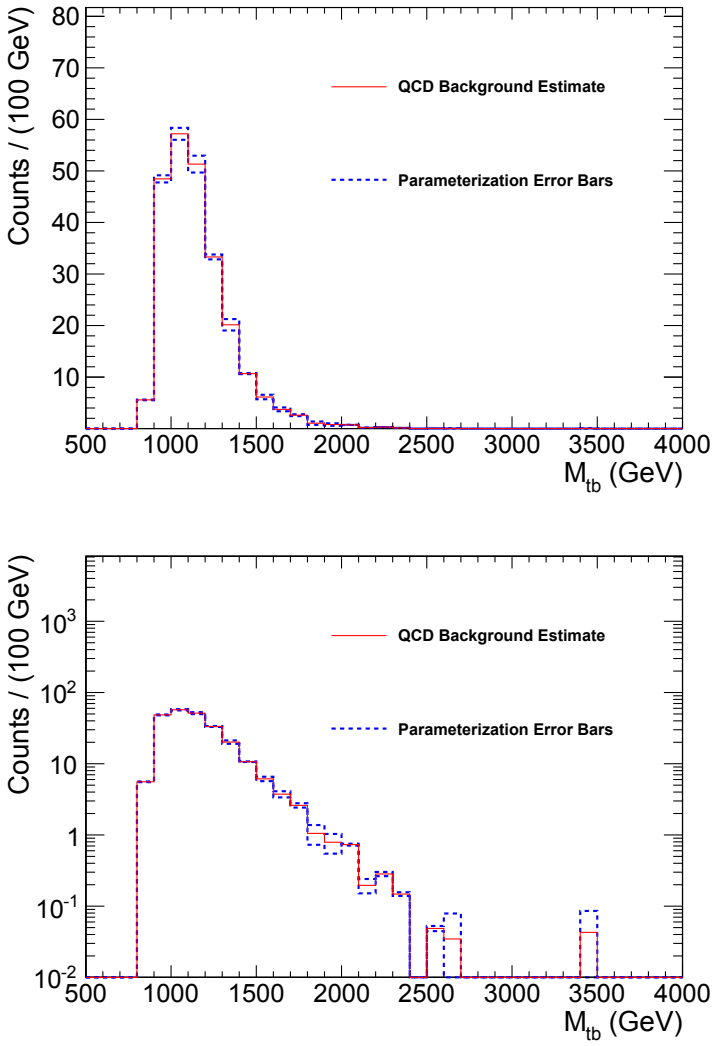

Figure 3.43: Uncertainty on the parameterization choice. Top and bottom plots are the same but on linear and log y-axis scale.

3.6 Results

3.6.1 Limits

We set limits on the production cross-section of the W'_R boson. We compare the number of observed events to the number of events expected given the new physics model. We use the following formula:

$$N_{\text{expected}} = \sigma_{W'_R} \times B_{W'_R \to tb; W \to hadrons} \times \varepsilon \times L \tag{3.10}$$

where $\sigma_{W'_R}$ is the W'_R cross-section, $B_{W'_R \to t\bar{b}; W \to hadrons}$ is the branching ratio $W'_R \to t\bar{b}$ with the W decay constrained to the hadronic branching fraction, ε is the signal efficiency corrected by data-driven scale factors and L is the integrated luminosity of our dataset.

We perform a shape analysis using the M_{tb} distribution. We use a binned likelihood fit to compare the distribution from the W′ boson signal hypothesis with the Standard Model distribution produced by our background estimation procedure.

To set shape based limits, the Theta package [20] is used. We use a Bayesian method to extract 95% CL upper limits on the production of a right-handed W′ particle.

A Poisson model is used in each bin of our analysis. For each bin, the mean of

the Poisson distribution is:

$$\mu_i = \sum_k \beta_k \times T_{k,i} \tag{3.11}$$

here, k includes the signal and background models, and T represents the fraction of events expected for each process k in bin i.

The likelihood function is then:

$$L(\beta_k) = \prod_i^{N_{bins}} \frac{\mu_i \times e^{-\mu_i}}{N_i^{data}!} \tag{3.12}$$

Where μ_i is the mean of the Poisson distribution in bin i, given in terms of T, the number of events expected from the process k.

The Theta package performs pseudoexperiments to calculate 68% and 95% upper bounds on the limit bands. The pseudoexperiments take into account systematic effects as nuisance parameters. These nuisance parameters are varied within their uncertainties and the posterior is refitted for each pseudoexperiment.

The uncertainty in the jet energy scale, Q^2 scale, $\mathrm{p_T}$ re-weighting, trigger, SF_b, QCD background uncertainties, and jet energy resolution are taken as shape based uncertainties, and the other sources of uncertainty are taken as overall normalizations.

The limits from Theta are shown in Figure 3.44.

Cross-Section Upper Limits

$M_{t\bar{b}}$	**observed**	**expected**	**expected 1σ**	**expected 2σ**
1300	**0.146**	**0.117**	**0.080,0.166**	**0.057,0.229**
1500	**0.059**	**0.078**	**0.056,0.112**	**0.040,0.163**
1700	**0.050**	**0.066**	**0.047,0.097**	**0.034,0.130**
1900	**0.055**	**0.062**	**0.043,0.091**	**0.032,0.126**
2100	**0.064**	**0.064**	**0.046,0.093**	**0.036,0.140**
2300	**0.073**	**0.069**	**0.052,0.098**	**0.042,0.147**
2700	**0.093**	**0.106**	**0.082,0.146**	**0.071,0.211**

Table 3.9: W'_R cross-section upper limits for given $M_{t\bar{b}}$ values. Cross-section is in units of pb.

3.6.2 Generalized Coupling Limits

To set limits on generic couplings, we use the procedure outlined in [15]. The full selection for the left-handed and mixed-coupling samples (described in section 3.2) can be seen in Figure 3.15. For limit setting, we weight our templates (single top, W'_R, W'_L, W'_{LR}) using the following cross-sections respectively:

$$\begin{aligned}
\sigma_{SM} &= \sigma_{\text{singletop}} \qquad (3.13)\\
\sigma_R &= \left(\left(a^L_{ud}a^L_{tb}\right)^2 + \left(a^R_{ud}a^R_{tb}\right)^2 - \frac{1}{2}\left(\left(a^L_{ud}a^R_{tb}\right)^2 + \left(a^R_{ud}a^L_{tb}\right)^2\right) - a^L_{ud}a^L_{tb}\right)\sigma_{W'_R}\\
\sigma_L &= \left(a^L_{ud}a^L_{tb} - \frac{1}{2}\left(\left(a^L_{ud}a^R_{tb}\right)^2 + \left(a^R_{ud}a^L_{tb}\right)^2\right)\right)\sigma_{W'_L}\\
\sigma_{LR} &= \frac{1}{2}\left(\left(a^L_{ud}a^R_{tb}\right)^2 + \left(a^R_{ud}a^L_{tb}\right)^2\right)\sigma_{W'_{LR}}
\end{aligned}$$

Where $\sigma_{W'_{ij}}$ refers to the cross-section for right, left or mixed-coupling samples and $\sigma_{singletop}$ is the standard model s-channel single top cross-section. We assume

Nuisance Parameters

Sample	JER	JES	QCD total	b-tagging	Q^2	Trigger	CA btag SF	p_T Re-weight	Lumi	$t\bar{t}$ Norm	Subjet SF
wp1300	0.031 ± 1.186	-0.722 ± 0.855	-0.486 ± 0.657	-0.030 ± 1.014	-0.278 ± 1.337	0.002 ± 1.000	0.000 ± 1.006	0.183 ± 0.649	0.000 ± 1.000	0.105 ± 1.007	0.000 ± 1.001
wp1500	0.067 ± 1.111	-0.905 ± 0.370	-0.483 ± 0.532	0.197 ± 0.884	0.420 ± 0.840	0.006 ± 1.969	0.119 ± 1.683	-0.133 ± 0.481	0.155 ± 1.428	0.116 ± 0.901	-0.116 ± 0.934
wp1700	0.094 ± 1.168	-0.727 ± 0.556	-0.381 ± 0.523	0.058 ± 0.950	0.482 ± 1.097	0.070 ± 1.045	0.013 ± 1.700	-0.051 ± 0.520	0.017 ± 1.462	0.173 ± 0.911	0.093 ± 0.971
wp1900	0.137 ± 1.795	-0.501 ± 0.302	-0.340 ± 0.540	-0.013 ± 1.039	0.128 ± 0.285	-0.004 ± 1.999	0.020 ± 1.981	-0.043 ± 0.473	0.026 ± 1.968	0.109 ± 0.895	0.118 ± 1.136
wp2100	0.086 ± 1.333	-0.617 ± 0.745	-0.468 ± 0.524	-0.011 ± 0.999	0.511 ± 0.947	0.000 ± 1.997	-0.002 ± 1.981	0.030 ± 0.514	-0.003 ± 1.967	0.125 ± 0.905	-0.013 ± 1.129
wp2300	0.074 ± 1.079	-0.685 ± 0.780	-0.500 ± 0.714	-0.016 ± 1.015	0.477 ± 0.714	0.000 ± 1.002	0.000 ± 1.980	-0.001 ± 0.561	0.000 ± 1.964	0.131 ± 0.939	0.000 ± 1.090
wp2700	0.259 ± 1.349	-0.643 ± 1.077	-0.396 ± 0.550	-0.054 ± 1.144	0.316 ± 0.824	-0.004 ± 1.997	0.000 ± 1.994	-0.029 ± 0.476	0.000 ± 1.991	0.103 ± 0.894	0.001 ± 1.793

Table 3.10: Nuisance parameters after the fit. This the nominal value found for the nuisance parameter after the fit in units of input sigma.The numbers listed under sample specify W'_R signal MC mass.

$a_{ud} = a_{tb}$. The templates are then summed and limits can be set using the resultant yield as the signal process for the given values of a^L and a^R. Because the left-handed and mixed-coupling samples cannot be separated from SM single top, we set limits on the couplings a^L and a^R. The Theta package is used for this computation and limits are calculated using combinations of the couplings from 0 to 1 in increments of 0.1. Using these limits, we find where $M_{\mathrm{W}'}$ cross-section limits align with theory prediction and plot these values in the a^L and a^R plane. These points are where we can exclude the a^L and a^R coupling combinations for the standard model plus W′ hypothesis at the given W′ mass. The results are shown in Figure 3.45. For this procedure, no systematic uncertainty is considered for the single top contribution due to the fact that statistical uncertainty dominates in these templates (see Figure 3.46).

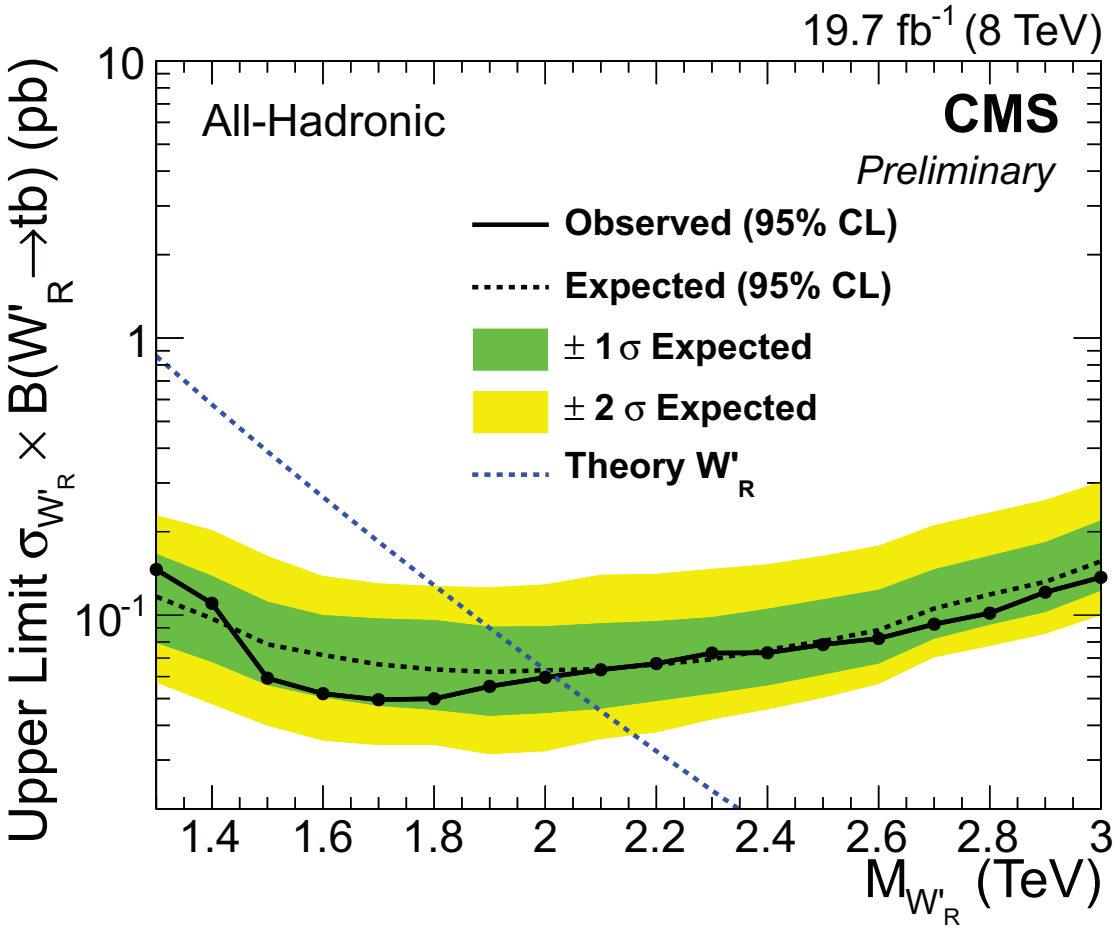

Figure 3.44: The W'_R boson 95% C.L. production cross-section limits. The expected (black) and observed (red) limits as well as W'_R boson theoretical cross-section (blue) are plotted for comparison. The uncertainty in the expected limit band is shown in light ($\pm 1\sigma$) and dark grey ($\pm 2\sigma$). These limits were extracted using the Theta limit setting framework.

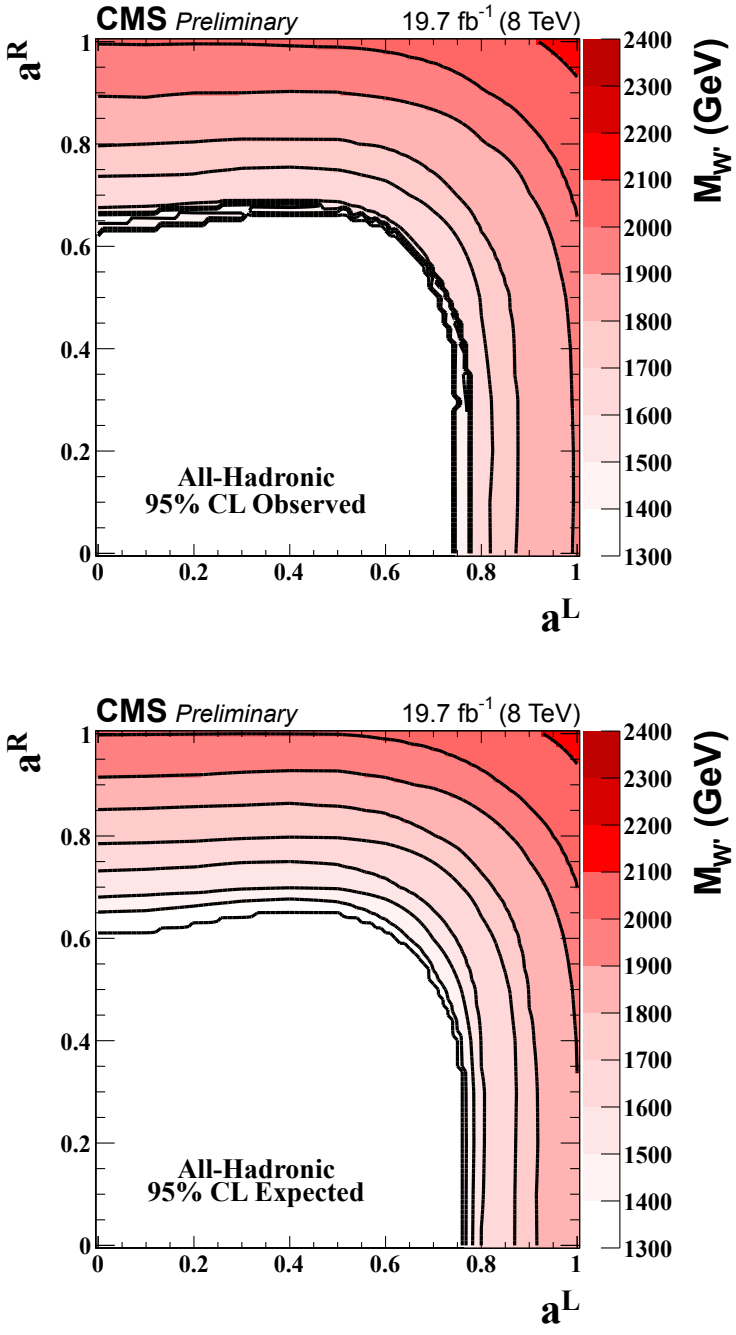

Figure 3.45: Plots of $M_{\mathrm{W}'}$ as a function of a^L and a^R. The z axis colors indicate $M_{\mathrm{W}'}$ where the theoretical cross section intersects the observed or expected limit band. The top (bottom) plot shows observed (expected) limits.

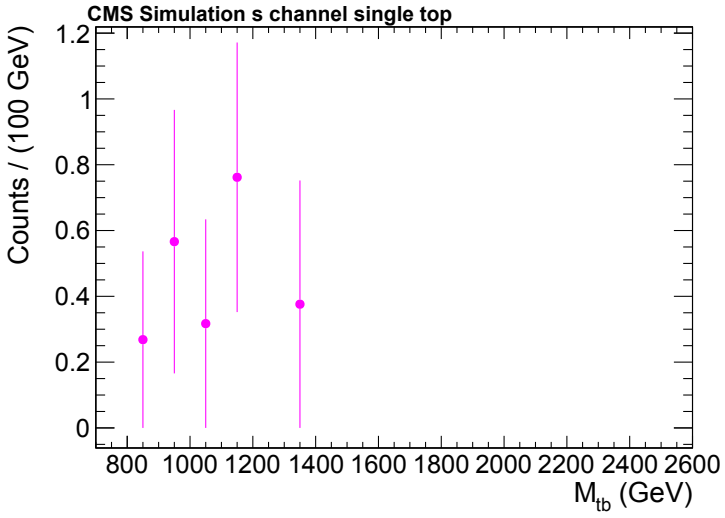

Figure 3.46: Standard model s-channel single top production used for the generalized coupling analysis.

3.7 Combination

To enhance the sensitivity of the measurement of the W′ cross-section upper limit as well as the limit set on coupling strengths, the fully-hadronic and semileptonic ($W' \to tb \to \ell\nu bb$) W′ decay channels have been combined. The analysis of the semileptonic channel is documented in [40]. The fully-hadronic channel includes W′ signal generated from a mass of 1300 GeV to 3100 GeV, whereas the semileptonic channel has mass points generated from 800 GeV to 3000 GeV. Therefore, the region of combined sensitivity ranges from W′ mass of 1300 GeV to 3000 GeV. Below this region, the semileptonic channel limits are quoted.

There are points within the region of combined sensitivity where the signal sample exists for the semileptonic channel but not for the all-hadronic channel. These intermediate mass points are reproduced using RooFit template morphing to interpolate the shape of the M_{tb} spectrum. The generation level b p_T selection placed on the left-handed and mixed coupling W′ samples is taken into account by interpolating the selection efficiency for the interpolated mass points.

In combining the analysis sensitivity, the uncertainty sources Jet Energy Scale, Jet Energy Resolution, b-tagging scale factor, and luminosity 3.5 are correlated, and the remaining are left uncorrelated. Different generators are used for the $t\bar{t}$ production MC simulation, so the Q^2 scale and p_T re-weighting uncertainties are not correlated.

The W'_R combined cross-section upper limits are shown in figure 3.47. Here, a W'_R boson with mass less than 2.15 TeV is excluded at the 95% C.L. Combined limits on

the W′ coupling strengths is shown in figure 3.48.

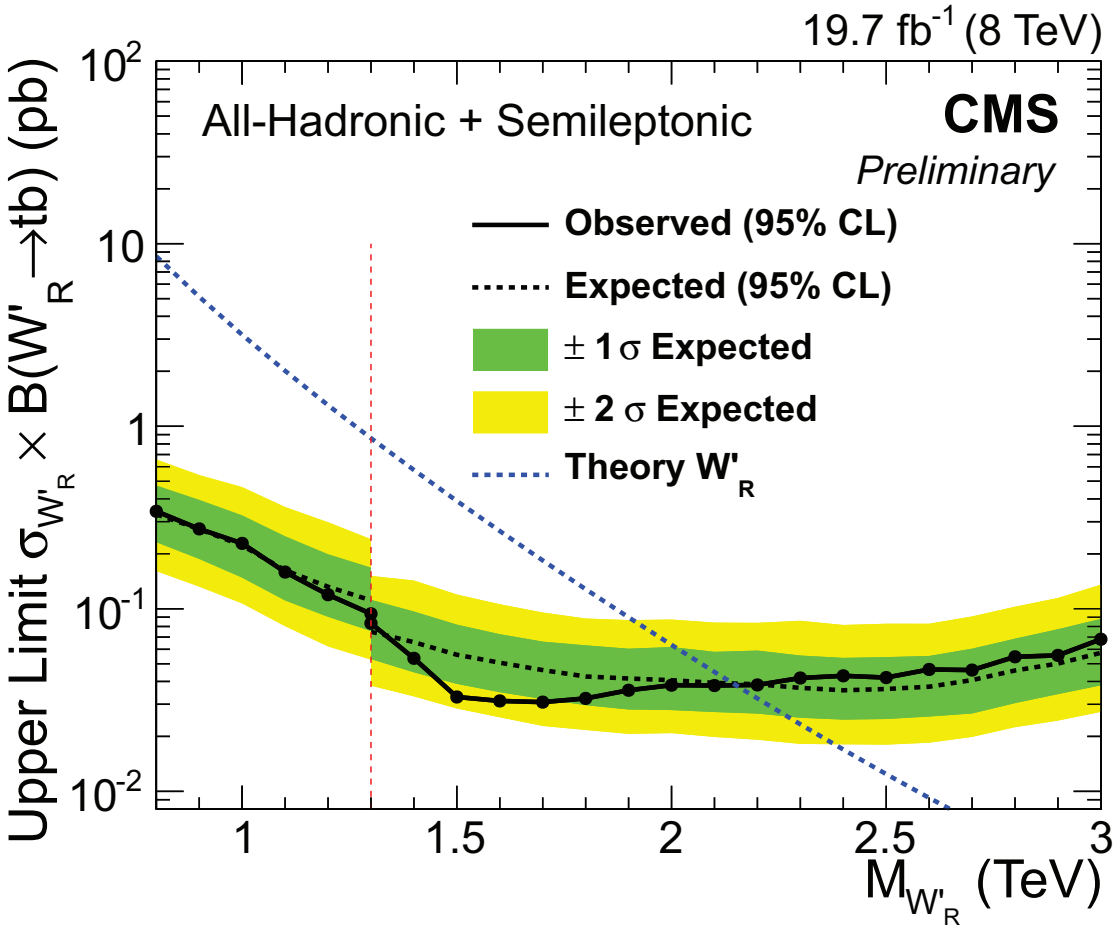

Figure 3.47: The W'_R boson 95% C.L. production cross-section limits for the combined semileptonic and all-hadronic channels. The expected (solid-black) and observed (dashed-black) limits as well as W'_R boson theoretical cross-section (dashed-blue) are plotted for comparison. The uncertainty in the expected limit band is shown in green ($\pm 1\sigma$) and yellow ($\pm 2\sigma$). The left of the red dashed line shows limits purely from the semileptonic channel. The right of the red dashed line shows limits using combined sensitivity from the semileptonic and all-hadronic channels. These limits were extracted using the Theta limit setting framework.

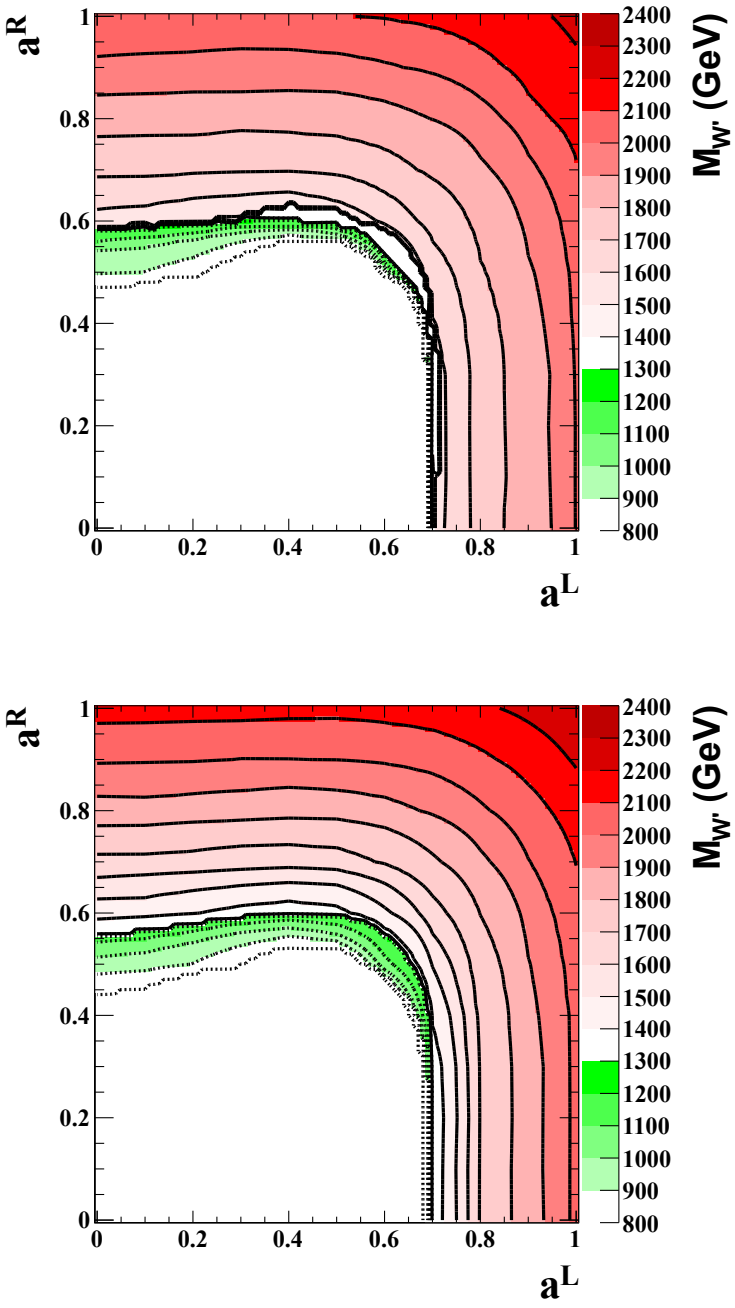

Figure 3.48: Plots of $M_{\mathrm{W}'}$ as a function of a^L and a^R. The z axis colors indicate $M_{\mathrm{W}'}$ where the theoretical cross section intersects the observed or expected limit band. The red coloration indicates combined sensitivity, green indicates that the limits are purely from the semileptonic channel. The top (bottom) plot shows observed (expected) limits.

Chapter 4

The b^* Search

4.1 Introduction

The focus of this analysis is a BSM predicted [41] excited b quark referred to as b^*. The decay mode considered in this analysis is $b^* \rightarrow tW$, as it is dominant in the b^* mass region of interest.

b^* production at the LHC takes place through the strong interaction. The Lagrangian describing this interaction is as follows:

$$\mathcal{L}_{production} = \frac{g_s}{2\Lambda} G_{\mu\nu} \bar{b} \sigma^{\mu\nu} (\kappa_L^b P_L + \kappa_R^b P_R) b^* + H.c. \tag{4.1}$$

$b^* \rightarrow tW$ decay takes place through the weak interaction and is described through

the following Lagrangian.

$$\mathcal{L}_{decay} = \frac{g_2}{\sqrt{2}} W_\mu^+ \bar{t}\gamma^\mu (g_L P_L + g_R P_R) \mathrm{b}^* + H.c. \tag{4.2}$$

We consider three hypotheses for the right- and left-handed couplings.

$$\text{left-handed: } \kappa_L^b = g_L = 1 \text{ and } \kappa_R^b = g_R = 0 \tag{4.3}$$

$$\text{right-handed: } \kappa_L^b = g_L = 0 \text{ and } \kappa_R^b = g_R = 1 \tag{4.4}$$

$$\text{vectorlike : } \kappa_L^b = g_L = 1 \text{ and } \kappa_R^b = g_R = 1 \tag{4.5}$$

Searches for the b* quark in the tW decay mode have been performed at the ATLAS detector at the LHC [42]. Using 19.7fb^{-1} of integrated luminosity at 8TeV, we exclude a left-handed b* quark couplings between 0.99TeV and 1.40TeV

Similar to the W′ search described in the previous chapter, the b* quark region of interest is high mass. Therefore, similar boosted techniques are used to identify the top quark decay products and reduce the QCD background. Additionally, similar methods are used to estimate the background due to the success of these methods in the W′ search.

4.1.1 Analysis Strategy

Similar to the W′ search, the primary sources of background are QCD multijet and SM $t\bar{t}$ production.

The QCD background component is estimated by a tagging rate based data driven technique similar to the W′ search (see Section 3.3.2). We invert the W candidate mass requirement in order to define a control region with negligible signal contribution. This region is used to investigate the mistagging rate for the top tagging algorithm used in the analysis. This top-mistagging rate is then used to weight events in lieu of a top-tag in our full selection. This allows for an estimation of the QCD background component with a low signal pollution component. This procedure is first applied to a control region in order to investigate any potential bias, and is then applied to the signal region selection (see Section 4.3.1).

The shape of the SM $t\bar{t}$ production contribution is estimated from MC simulation. The normalization of this contribution is measured in a third control region that is enriched in $t\bar{t}$ production (see Section 4.3.4).

The data and background components are then used as templates by the Bayesian statistical procedure identical to the W′ search

4.2 Data Sample and Event Selection

The data sample used for this analysis corresponds to 19.7±0.5 fb^{-1} of integrated luminosity collected in 2012 at $\sqrt{s}$ = 8 TeV. See Table 3.1 for a summary of the datasets used in the analysis.

4.2.1 Signal Samples

The b* generation is performed using two different coupling hypotheses.

- b^*_R - The purely right-handed b* where $\kappa^b_L = g_L = 0$, $\kappa^b_R = g_R = 1$
- b^*_L - The purely left-handed b* where $\kappa^b_L = g_L = 1$, $\kappa^b_R = g_R = 0$

The right- and left-handed b* samples used in this analysis are given in table 4.1 and 4.2 respectively. The vectorlike b^*_{LR} signal template is created by summing the right- and left-handed templates after normalization to theory cross-section.

4.2.2 Trigger Selection

Similar to the W′ search, we use the `HLT_HT750` trigger. The trigger efficiency is measured in data and MC by investigating the looser `HLT_HT550` trigger. The selection used for this measurement includes a loose kinematic selection in which we require two jets with $p_T > 300$ GeV. The denominator is defined as passing this selection and the `HLT_HT550` trigger, whereas the numerator is required to pass the selection

Right-Handed Signal Samples

Dataset	Cross-Section (pb)
Bstar_fullHad_right_M-800_TuneZ2star_8TeV-madgraph	**1.36**
Bstar_fullHad_right_M-900_TuneZ2star_8TeV-madgraph	**0.662**
Bstar_fullHad_right_M-1000_TuneZ2star_8TeV-madgraph	**0.336**
Bstar_fullHad_right_M-1100_TuneZ2star_8TeV-madgraph	**0.178**
Bstar_fullHad_right_M-1200_TuneZ2star_8TeV-madgraph	**0.0966**
Bstar_fullHad_right_M-1300_TuneZ2star_8TeV-madgraph	**0.0540**
Bstar_fullHad_right_M-1400_TuneZ2star_8TeV-madgraph	**0.0310**
Bstar_fullHad_right_M-1500_TuneZ2star_8TeV-madgraph	**0.0181**
Bstar_fullHad_right_M-1600_TuneZ2star_8TeV-madgraph	**0.0108**
Bstar_fullHad_right_M-1700_TuneZ2star_8TeV-madgraph	**0.00652**
Bstar_fullHad_right_M-1800_TuneZ2star_8TeV-madgraph	**0.00399**
Bstar_fullHad_right_M-1900_TuneZ2star_8TeV-madgraph	**0.00249**
Bstar_fullHad_right_M-2000_TuneZ2star_8TeV-madgraph	**0.00156**

Table 4.1: Right-handed signal samples along with the cross sections used in the analysis.

Left-Handed Signal Samples

Dataset	Cross-Section (pb)
Bstar_fullHad_left_M-800_TuneZ2star_8TeV-madgraph	**1.36**
Bstar_fullHad_left_M-900_TuneZ2star_8TeV-madgraph	**0.662**
Bstar_fullHad_left_M-1000_TuneZ2star_8TeV-madgraph	**0.336**
Bstar_fullHad_left_M-1100_TuneZ2star_8TeV-madgraph	**0.178**
Bstar_fullHad_left_M-1200_TuneZ2star_8TeV-madgraph	**0.0966**
Bstar_fullHad_left_M-1300_TuneZ2star_8TeV-madgraph	**0.0540**
Bstar_fullHad_left_M-1400_TuneZ2star_8TeV-madgraph	**0.0310**
Bstar_fullHad_left_M-1500_TuneZ2star_8TeV-madgraph	**0.0181**
Bstar_fullHad_left_M-1600_TuneZ2star_8TeV-madgraph	**0.0108**
Bstar_fullHad_left_M-1700_TuneZ2star_8TeV-madgraph	**0.00652**
Bstar_fullHad_left_M-1800_TuneZ2star_8TeV-madgraph	**0.00399**
Bstar_fullHad_left_M-1900_TuneZ2star_8TeV-madgraph	**0.00249**
Bstar_fullHad_left_M-2000_TuneZ2star_8TeV-madgraph	**0.00156**

Table 4.2: Left-handed signal samples along with the cross sections used in the analysis.

and both the HLT_HT550 and HLT_HT750 trigger. The efficiency is shown in Figure 4.1 and is parameterized as a function of summed leading and sub-leading jet p_T. The extracted trigger efficiency is used to weight the MC samples used in the analysis to account for the loss in efficiency in the turn-on. We do not observe perfect agreement in data and MC, so we use the trigger efficiency derived from data to weight our MC samples, and therefore use a conservative uncertainty on the efficiency measurement (see section 4.5). The red dashed line in figure 4.1 indicates the minimum for the analysis, at which point the trigger is nearly fully efficient.

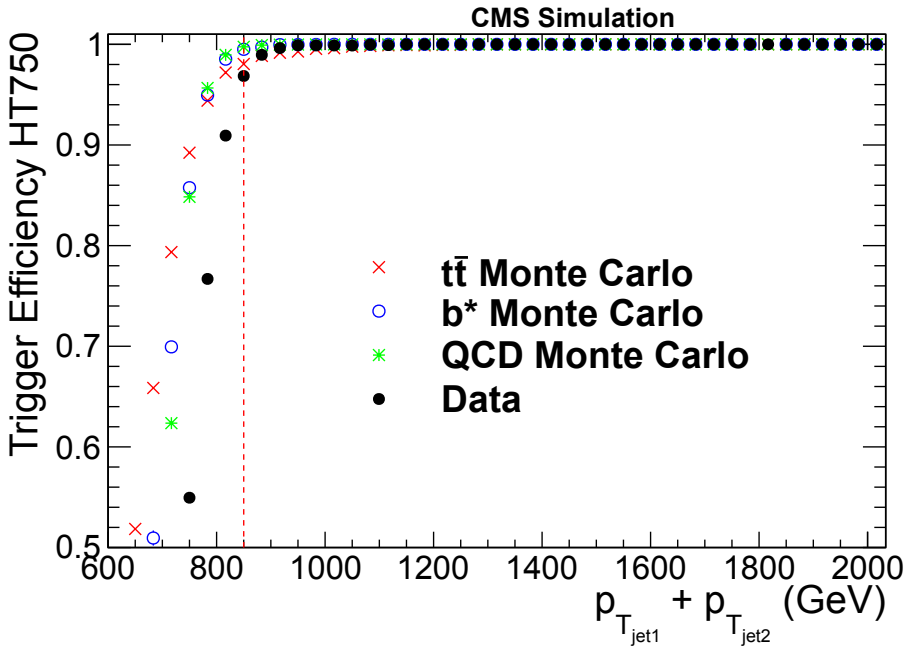

Figure 4.1: Trigger efficiency of HLT_HT750 measured as a function of the summed p_T of the leading and sub-leading jets.

4.2.3 Event Pre-selection

The following pre-selection is applied:

- The event must have a good primary vertex as computed by a deterministic annealing filter (DAF) ($|z_{\text{Primary Vertex}}| < 24$ cm, $N_{\text{DOF}} > 6$).
- Two jets with $|y| < 2.4$
- Exactly two jets with $p_T > 150$ GeV
- Leading Jet & Sub-leading Jet $p_T > 425$ GeV
- Loose Particle Flow jet identification [33] is applied
- Beam background events are removed using the following requirements:
  - In events with at least 10 tracks, a minimum of 25% of these tracks must be high purity tracks.

Here we do not include the $|\Delta y|$ discrimination used in the W′ search due to the fact that the expected b* mass exclusion point is lower, and this cut is highly energy dependent.

4.2.4 Pileup Correction

We re-weight our MC samples to account for differences due to pileup using the recommended procedure (see Section 3.2.7). Figure 4.2 shows the distribution of

reconstructed primary vertices in data, $t\bar{t}$, and signal MC before and after the re-weighting has been applied. The pileup correction has very little effect on the eventual M_{tW} full selection, as seen in Figure 4.3, for b^*_R signal MC at the 1300 GeV mass point. Similarly, there is little effect $t\bar{t}$ MC as can be seen in Figure 4.4. A study has been conducted to investigate the effect of the suggested systematic uncertainty of 5% on the minbias cross-section as can be seen in Section 4.5.

4.2.5 Combined CMS Top Tagging Algorithm

The CMS top tagging algorithm is described in detail in Section 3.2.8. Figure 4.5 shows τ_3/τ_2 comparison using signal and QCD MC samples. We use the standard operating point of $\tau_3/\tau_2 < 0.55$ in the full selection. Figure 4.6 shows the maximum subjet CSV b discriminant comparison using signal and QCD MC samples. We use the standard CSV working point $SJ_{CSVMAX} > 0.679$.

4.2.6 W Jet Identification

The W boson daughter if the b* quark will also be boosted. Just as the CMS top tagging algorithm discriminates signal from background using the merged top jet, the boosted W boson tagging discriminates signal from background by using a merged W jet. For this we constrain the jet mass to the W boson range, and use the N-subjettiness algorithm. To identify the two subjets of the W boson, the N-subjettiness

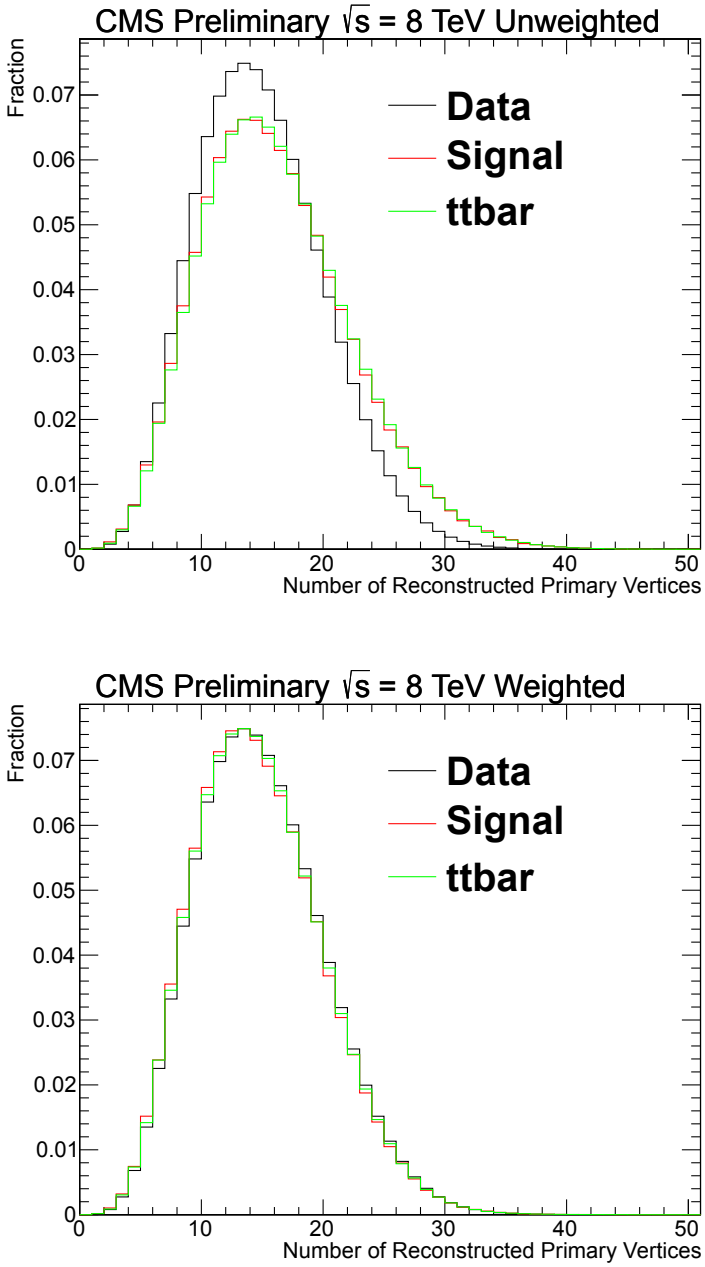

Figure 4.2: Number of reconstructed primary vertices before pileup re-weighting (top) and after pileup re-weighting (bottom). Here, no analysis cuts have been applied and the signal is b^*_R 1000 GeV

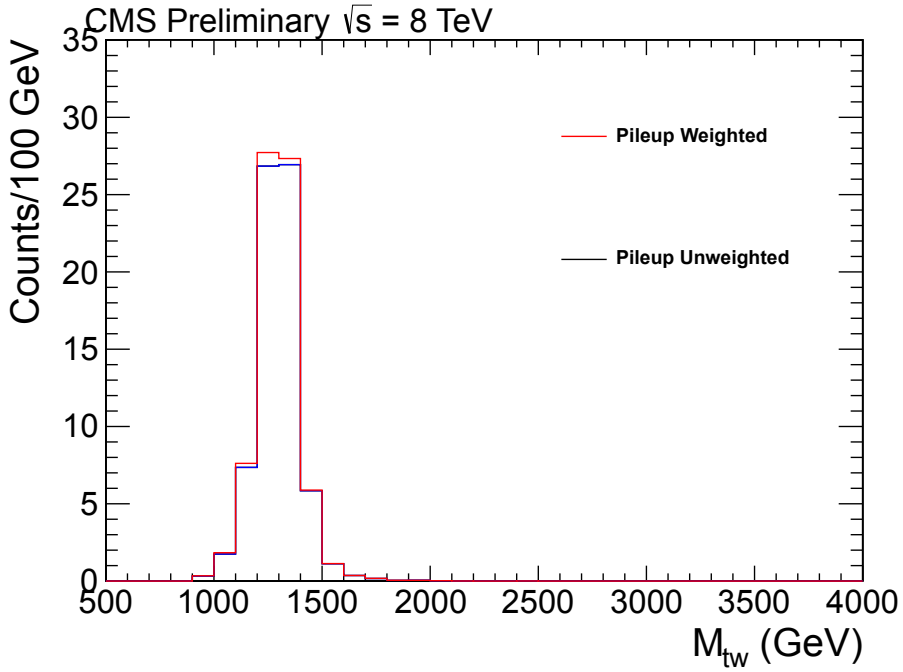

Figure 4.3: Effect of pileup re-weighting on the right-handed b* Signal MC.

variable used is τ_2/τ_1 due to the fact that the jet energy is more consistent with two subjets than one.

- **Jet Mass** 70 GeV $< m_{jet} <$ 100 GeV - The mass of the CA jet is required to be consistent with the W boson mass.

- **N-subjettiness** $\tau_2/\tau_1 < 0.5$ - The ratio of the N-subjettiness variables τ_2 and τ_1 should be low, as the W jet is more consistent with two subjets than one.

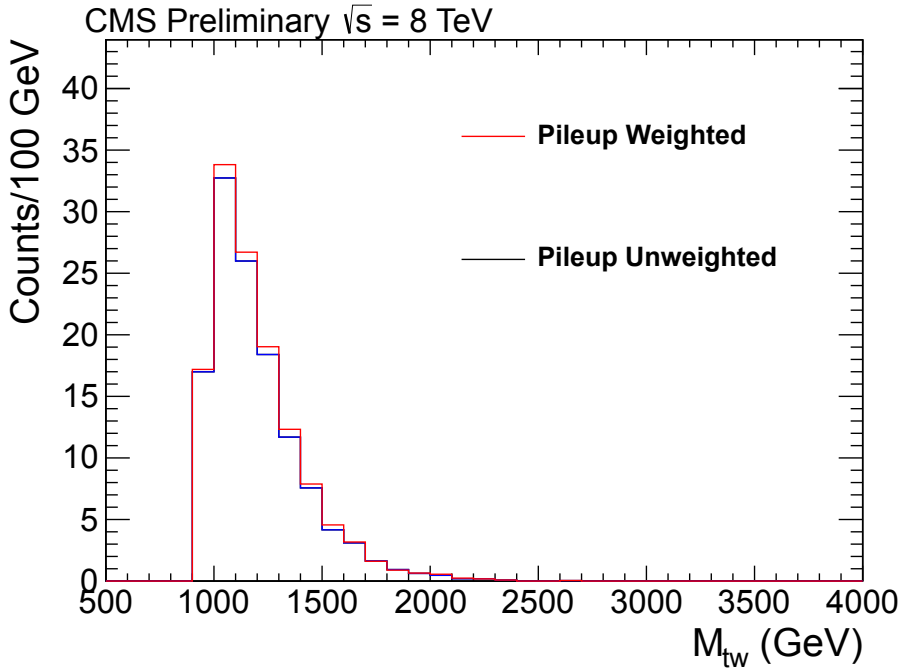

Figure 4.4: Effect of pileup re-weighting on the $t\bar{t}$ MC.

4.2.7 Reconstruction of b* invariant mass

The full selection for the reconstruction of the b* invariant mass then includes the following offline cuts.

- One jet with $p_T > 425$ GeV with the CMS top tagging algorithm as well as subjet b-tagging and N-subjettiness discrimination.
- One jet with $p_T > 425$ GeV with a boosted W tag
- $|\Delta\phi| > \pi/2$ between the two jets

After this selection, the b* invariant mass is reconstructed using the top-W candidate mass (M_{tW}). The cutflow for this selection in data, $t\bar{t}$ MC, and b* signal MC can be

found in Table 4.3. Figure 4.7 shows this full selection in signal MC for various b* masses.

Cutflow										
Sample	$\geq 2jets$	$exactly2jets$	p_T	M_{top}	$Nsubjets$	$Minmass$	τ_3/τ_2	SJ_{CSVMAX}	M_W	τ_2/τ_1
Data	18868018	13854873	3545312	1047669	593104	337754	39409	7334	800	318
QCD	—	—	—	—	—	—	—	—	—	211
ttbar	13214	10453	3533	2683	2338	2146	1295	934	174	129
$M(b*_R) = 800$	3930	3334	388	233	196	175	99	67	40	33
$M(b*_R) = 900$	4300	3782	854	445	385	345	212	149	106	91
$M(b*_R) = 1000$	3136	2769	1407	789	681	614	381	276	217	183
$M(b*_R) = 1100$	1976	1730	1191	732	631	572	350	251	192	161
$M(b*_R) = 1200$	1183	1031	808	538	460	421	254	180	137	114
$M(b*_R) = 1300$	705	607	507	357	304	280	166	116	88	73
$M(b*_R) = 1400$	429	365	318	232	196	181	105	72	55	45
$M(b*_R) = 1500$	255	216	193	145	121	112	64	43	33	27
$M(b*_R) = 1600$	155	131	118	91	76	70	39	26	19	16
$M(b*_R) = 1700$	97	80	74	57	47	43	24	16	12	9
$M(b*_R) = 1800$	59	49	45	35	29	27	15	9	7	5
$M(b*_R) = 1900$	37	30	28	22	18	17	9	6	4	3
$M(b*_R) = 2000$	23	19	18	14	12	10	5	3	2	2
$M(b*_L) = 800$	3855	3259	374	227	179	159	84	55	31	26
$M(b*_L) = 900$	4223	3712	838	472	376	330	186	129	88	75
$M(b*_L) = 1000$	3103	2744	1356	810	637	555	309	221	173	147
$M(b*_L) = 1100$	1959	1722	1172	757	601	532	292	204	157	131
$M(b*_L) = 1200$	1180	1028	797	548	436	389	210	144	109	91
$M(b*_L) = 1300$	703	606	503	365	290	262	138	93	70	58
$M(b*_L) = 1400$	423	361	313	235	187	170	87	58	44	36
$M(b*_L) = 1500$	254	215	191	146	116	105	53	34	25	21
$M(b*_L) = 1600$	155	130	117	92	73	66	33	20	15	12
$M(b*_L) = 1700$	95	79	73	58	45	41	20	12	9	7
$M(b*_L) = 1800$	59	49	45	36	28	25	12	7	5	4
$M(b*_L) = 1900$	37	30	28	23	18	16	8	4	3	2
$M(b*_L) = 2000$	23	19	18	14	11	10	5	3	2	< 1

Table 4.3: Cutflow Table. Table reads left to right where the current column implies the previous cuts. QCD expectation is only recorded for the full selection, due to the fact that the background estimate is only valid after top tagging. The first column implies the $p_T > 150$ GeV preselection for any jet. The second column additionally represents the delta phi selection between the leading jets. The column labeled p_T represents the p_T cut placed on both leading jets.

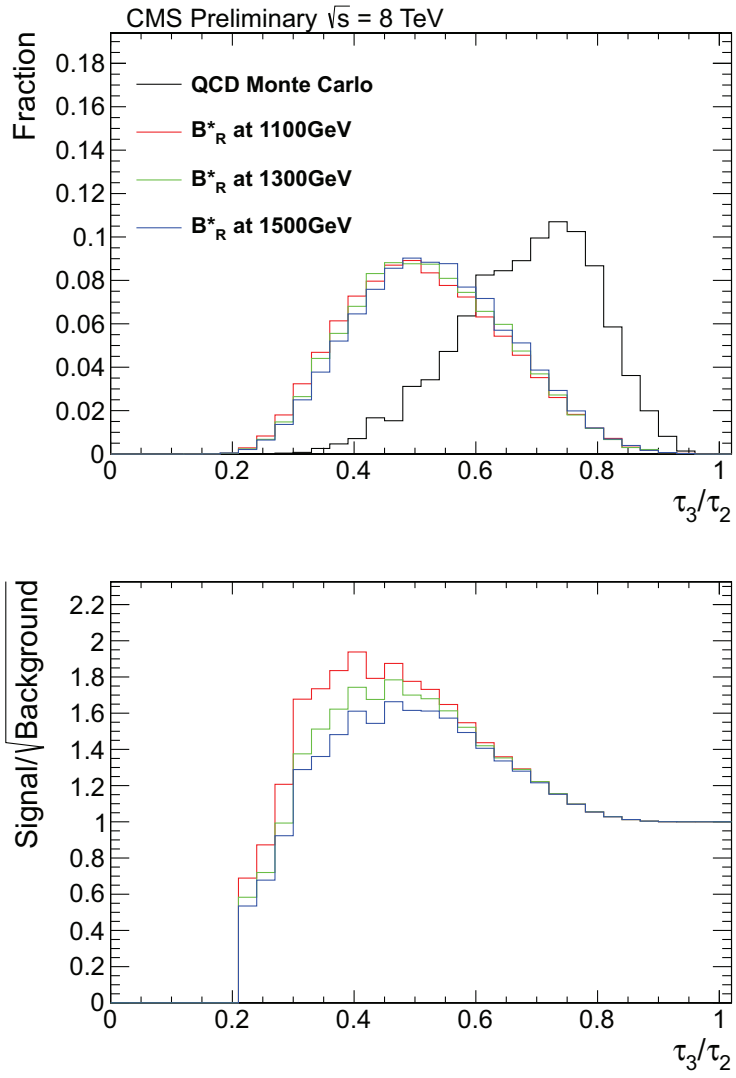

Figure 4.5: τ_3/τ_2 distributions in Signal and QCD MC samples (top). The selection here includes the full signal region with the exception of subjet b-tagging in order to preserve QCD MC statistics. Plot of Signal/$\sqrt{\text{Background}}$ (bottom), derived from the top plot.

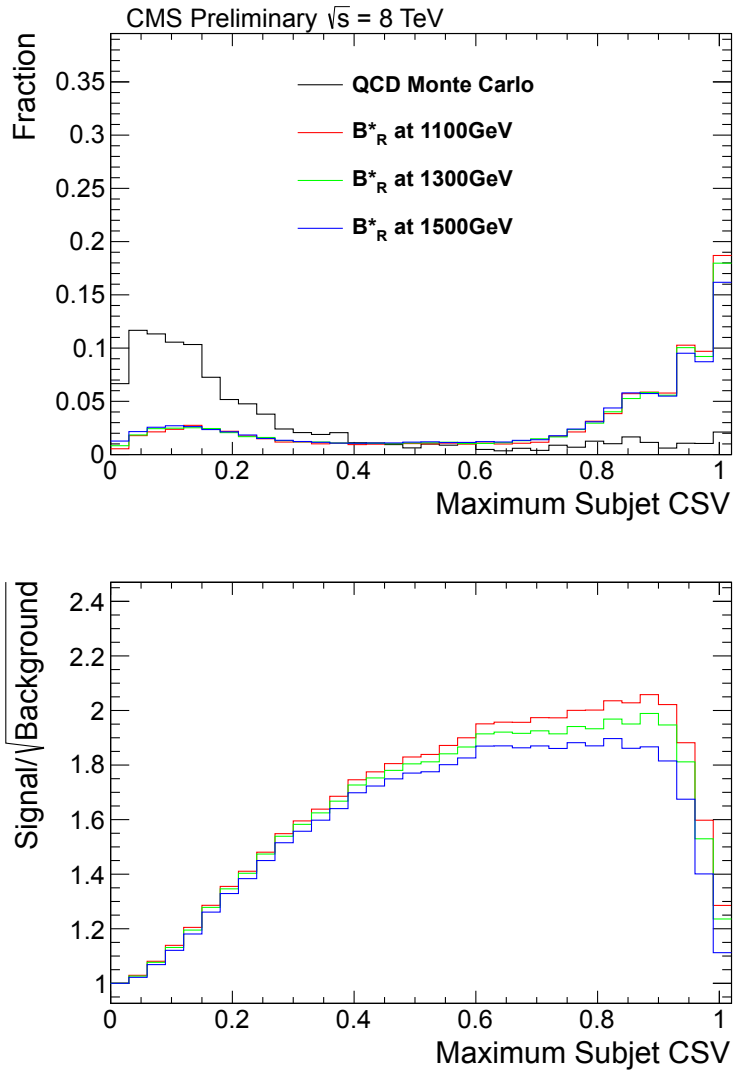

Figure 4.6: Maximum subjet CSV distributions in Signal and QCD MC samples (top). Plot of Signal/$\sqrt{\text{Background}}$ (bottom), derived from the top plot.

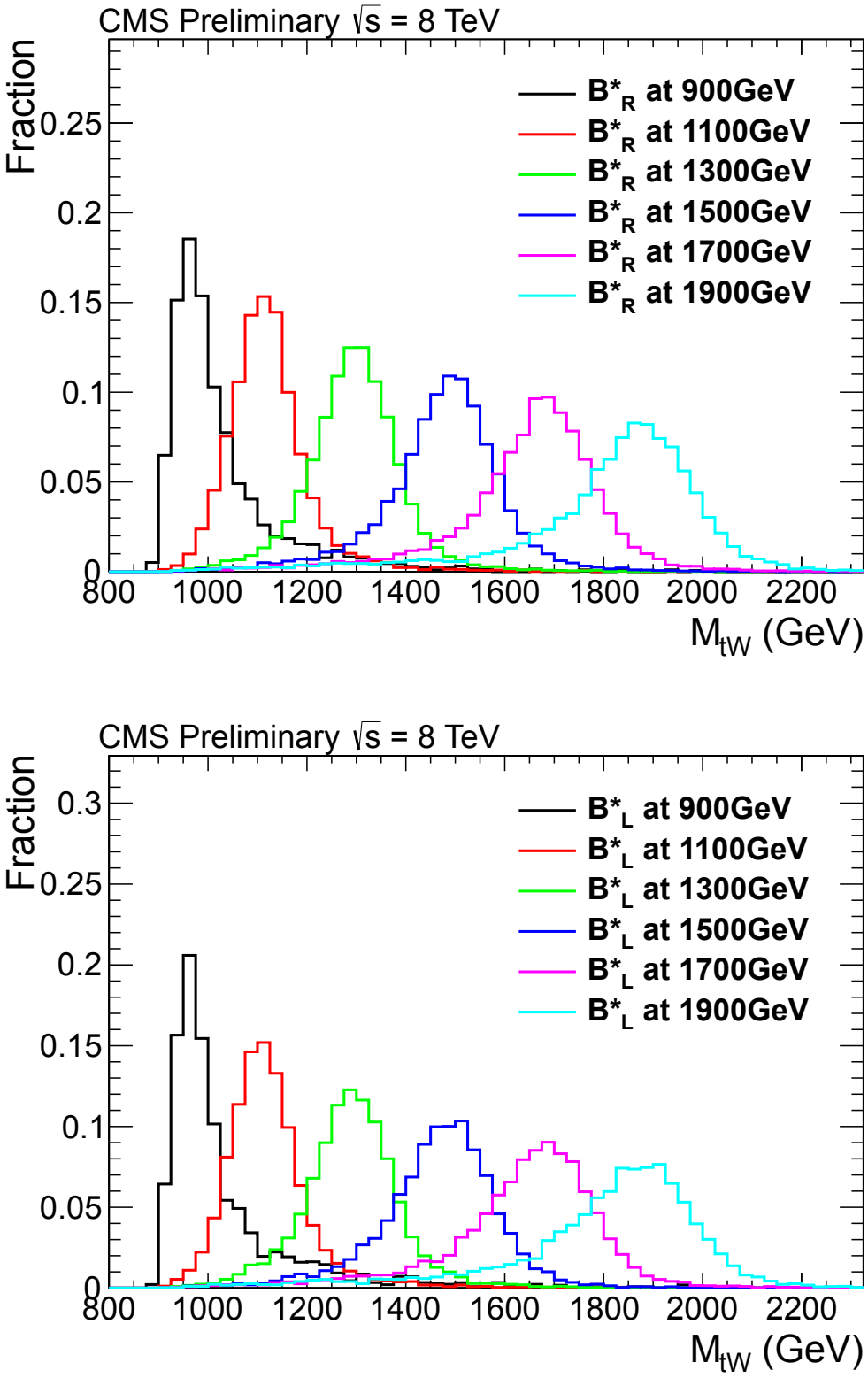

Figure 4.7: Full selection applied to b^*_R (top) and b^*_L (bottom-left).

4.3 Background Estimation

The primary sources of SM background for this analysis are QCD multijet and $t\bar{t}$ production. The shape of the $t\bar{t}$ contribution to the background is taken from MC, and the normalization is derived from data by using a $t\bar{t}$ rich control region. The QCD multijet background contribution is derived from data by inverting the W candidate mass requirement for W-tagging.

4.3.1 QCD Background Estimation

In order to extract the QCD multijet background contribution, we determine the mistagging rate for the CMS top tagging algorithm (see Section 3.2.8). To measure this top mis-tagging rate, we turn to a control region based on inverting the W-tagging mass requirement. We look in a W candidate mass window around of the signal region requirement (30 GeV $< M_{jet} <$ 70 GeV or 100 GeV $< M_{jet}$).

After applying this selection, we take the inverse ratio of top candidate jets to top candidate jets that are top-tagged to define the top-mistagging rate. To keep the kinematics similar in the sideband and similar region when reconstructing M_{tW}, the top candidate mass requirement is kept on the jets in both regions. To extract a QCD background estimate, we weight the events that pass the W-tagging requirements in the full selection by the top-mistagging rate.

The parameterization of the top-mistagging rate is two dimensional and considers

both the $|\eta|$ and p_T of the top candidate jets. We break down data into two distinct regions in $|\eta|$.

- Low ($0.0 < |\eta| \leq 1.0$)
- High ($1.0 < |\eta| \leq 2.4$)

The regions in $|\eta|$ are then individually parameterized in p_T to produce the average top-mistagging rate. We perform this parameterization of the top-mistagging rate in an attempt to constrain the kinematic correlations inherent in top-tagging.

To smooth out the binning of the average top-mistagging rate, a study of functional fits was conducted for the top-mistagging rate (see Figure 4.34). We use the same functional form for the top-mistagging rate fit as the average b-tagging rate in the W′ search (see Section 3.3.2) with the bifurcation points set to be 640 GeV and 590 GeV for the low and high η regions respectively.

The errors on the top-mistagging rate are then extracted using the full covariance matrix as obtained from output of the fitting algorithm. Additionally, we assign a systematic uncertainty to cover the choice of the fit function (see Section 4.5) based on several alternative functional forms. Figure 4.8 shows the tags (numerator) and probes (denominator) of the top-mistagging rate. Figure 4.9 shows the two fitted top-mistagging rates parameterized in p_T.

In the creation of the top-mistagging rate, $t\bar{t}$ is subtracted using the prescription outlined in Section 3.3.3

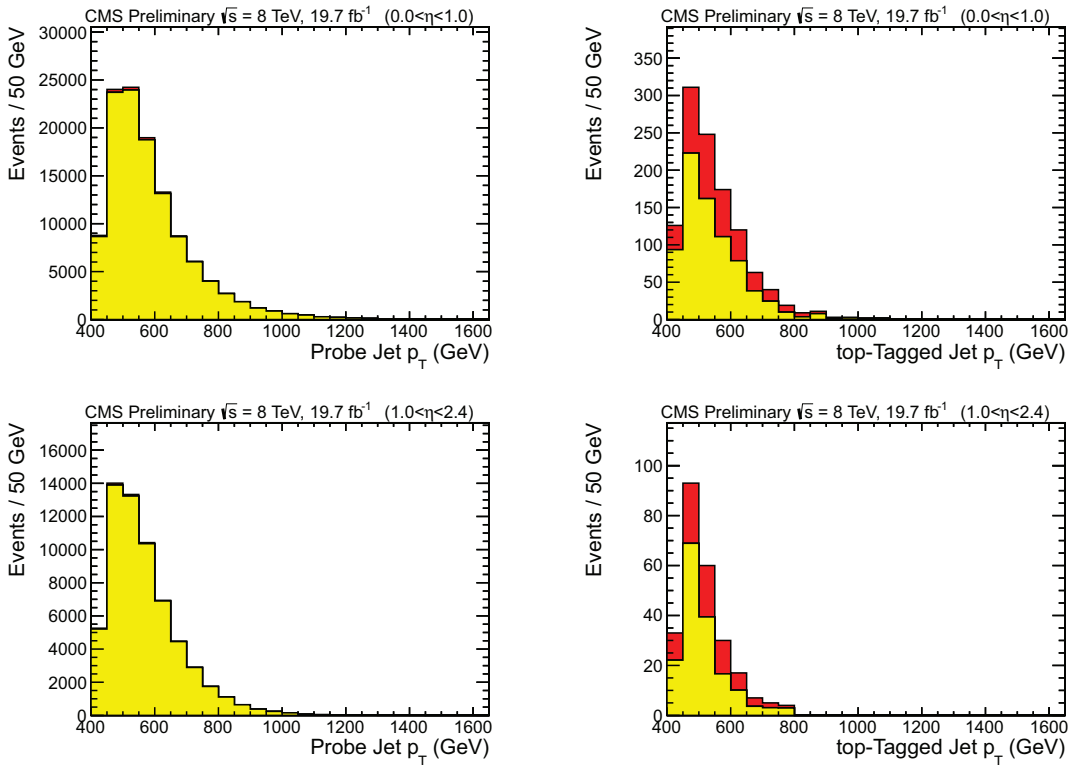

Figure 4.8: The tags and probes used for the average top-mistagging rate for the two regions in $|\eta|$. Here, tags are the numerator and probes are the denominator of the average top-mistagging rate

4.3.2 Top Candidate Mass Correction

The application of the top-mistagging rate on the pre top-tagged sample provides a close approximation of the shape and normalization of the signal region. However, there is a known shape based discrepancy in the modeling of the top-candidate jet mass (see [19]). Before the number of subjets and minimum pairwise mass requirements, the QCD top candidate mass spectrum is a rapidly falling function, whereas after this selection the QCD top candidate mass spectrum is nearly flat. To investigate this discrepancy, we take the top candidate mass spectrum from QCD MC

Background Composition		
region	**pre top-tag**	**post top-tag**
signal region QCD	**37801**	**211**
signal region $t\bar{t}$	**457**	**129**
sideband region QCD	**176741**	**926**
sideband region $t\bar{t}$	**1758**	**456**

Table 4.4: expected QCD and $t\bar{t}$ yields in the signal region and sideband used for extracting the top-mistagging rate. The QCD expected events are measured after $t\bar{t}$ subtraction.

before and after the number of subjets, minimum pairwise mass, and N-subjettiness requirements. The ratio of these normalized templates gives an approximate correction for this effect (see Figure 4.10). The uncertainty for this procedure is taken as half the correction. The correction and uncertainty are both interpolated to roughly correct for binning. This correction can be seen for data in Figure 4.11

The effect of this correction on the M_{tW} and top candidate p_T templates can be seen in figure 4.12.

4.3.3 Sideband Closure

In order to investigate the applicability and versatility of the QCD background estimation in data, we apply the top-mistagging rate to a control region of our W-tagging selection. We define the following W-tagging sideband:

- **Jet Mass** 30 GeV $< m_{jet} <$ 70 GeV or 100 GeV $< m_{jet} <$ 130 GeV
- **N-subjettiness** $\tau_2/\tau_1 \geq 0.5$

This sideband does not overlap with the control region used to extract the top-mistagging rate due to the inverted N-subjettiness window. The selection has a lower yield of $t\bar{t}$ than the full selection, making it ideal for investigating the QCD background contribution. The closure test can be seen in Figure 4.13. The termination of the W candidate mass requirement at 130 GeV is due to the fact that above this region there is an increased yield of fully merged tops that pass the W-tagging sideband selection, which makes this region important for pinning down the $t\bar{t}$ normalization.

4.3.4 Deriving the Normalization of the SM $t\bar{t}$ Production

In order to study the contribution from $t\bar{t}$ to the full background estimate, we investigate the following control region:

- **Jet Mass** $m_{jet} > 130$ GeV
- **N-subjettiness** $\tau_2/\tau_1 \geq 0.5$

This selection has an amplified $t\bar{t}$ fraction and is statistically independent from all other sidebands in the analysis. We extract the $t\bar{t}$ normalization by comparing the QCD background (extracted using the same top-mistagging rate as the signal region) and $t\bar{t}$ MC to the selection in data. The fit allows the QCD background template to move only within its errors, whereas the normalization on $t\bar{t}$ is unconstrained. We use the top candidate mass spectrum for fitting, which minimizes the correlation between

the QCD and $t\bar{t}$ templates within the fit due to the top mass peak. This fit can be seen in Figure 4.14. For this maximum likelihood fit we use the Theta package.

$t\bar{t}$ is subtracted from the numerator and denominator of the top-mistagging rate when extracting the QCD background estimate in the signal region. Additionally, $t\bar{t}$ contamination (se section 3.3.3) is subtracted from the QCD background estimate after the application of the top-mistagging rate. This $t\bar{t}$ contamination is estimated by weighting the pre top-tagged $t\bar{t}$ selection by the top-mistagging rate. The fitting procedure needs to implement both of these subtractions in order to isolate the $t\bar{t}$ normalization constant, because through these mechanisms the QCD shape is dependent on the $t\bar{t}$ normalization.

The fit implements the $t\bar{t}$ subtraction in the QCD estimate by fitting un-subtracted QCD to the $t\bar{t}$ full selection. The output of the fitter is then corrected by (1+S/F), where S/F is the ratio of the number of events in $t\bar{t}$ subtraction to the $t\bar{t}$ full selection.

The fit additionally implements $t\bar{t}$ subtraction in creation of the top-mistagging rate by creating two QCD components. One component is anticorrelated with the $t\bar{t}$ normalization factor, and the other is independent of this normalization factor. The anticorrelated QCD component fraction of the QCD estimate is taken as the difference of the QCD estimate with and without $t\bar{t}$ subtraction. The independent QCD component fraction of the QCD estimate is taken as the difference of the QCD estimate and the anticorrelated component.

This study suggests after all scale factors applied in the analysis, the $t\bar{t}$ contribution needs to be scaled by 0.79±0.17. This normalization is used for all $t\bar{t}$ distributions in the analysis, and the uncertainty is then the full normalization uncertainty for $t\bar{t}$.

4.3.5 Control Region Scale Factors

The W-tagging control regions mentioned in sections 4.3.4 and 4.3.1 are used for measurements that impact the background estimate in the signal region. These inverted selections do not have known scale factors, so we derive them using the semileptonic sample mentioned in section 4.2.5. The scale factor for the control region mentioned in section 4.3.1 is determined to be 0.97 ± 0.06, and the scale factor for the control region mentioned in section 4.3.4 is 1.12 ± 0.09.

The scale factors are a product of the W candidate mass window scale factor and the τ_2/τ_1 window scale factor. The W candidate mass used for this measurement can be seen in figure 4.15. Given the mass window, we then investigate τ_2/τ_1 for the jet. This can be seen in figure 4.16 for the scale factor of the control region mentioned in section 4.3.1 and figure 4.16 for the scale factor of the control region mentioned in section 4.3.4.

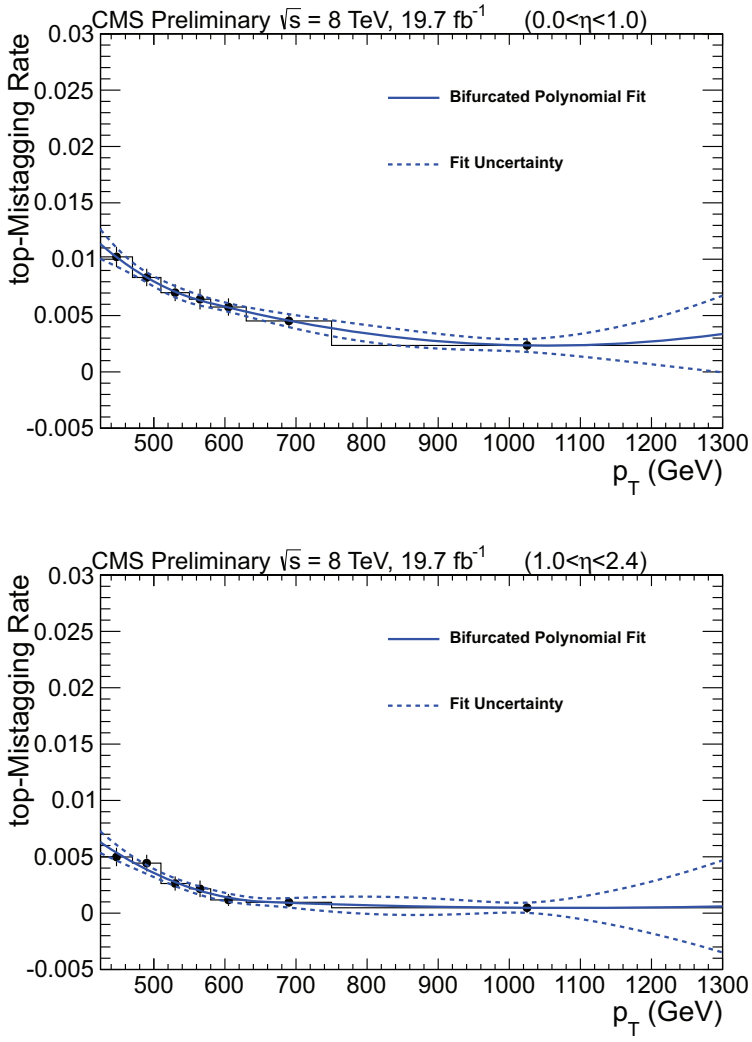

Figure 4.9: p_T parameterized average top-mistagging rate from the low (top) and high (bottom) η regions. the top-mistagging rate is shown in black, the polynomial fit is shown in blue, and the propagated errors from the fit are shown as a blue dashed line.

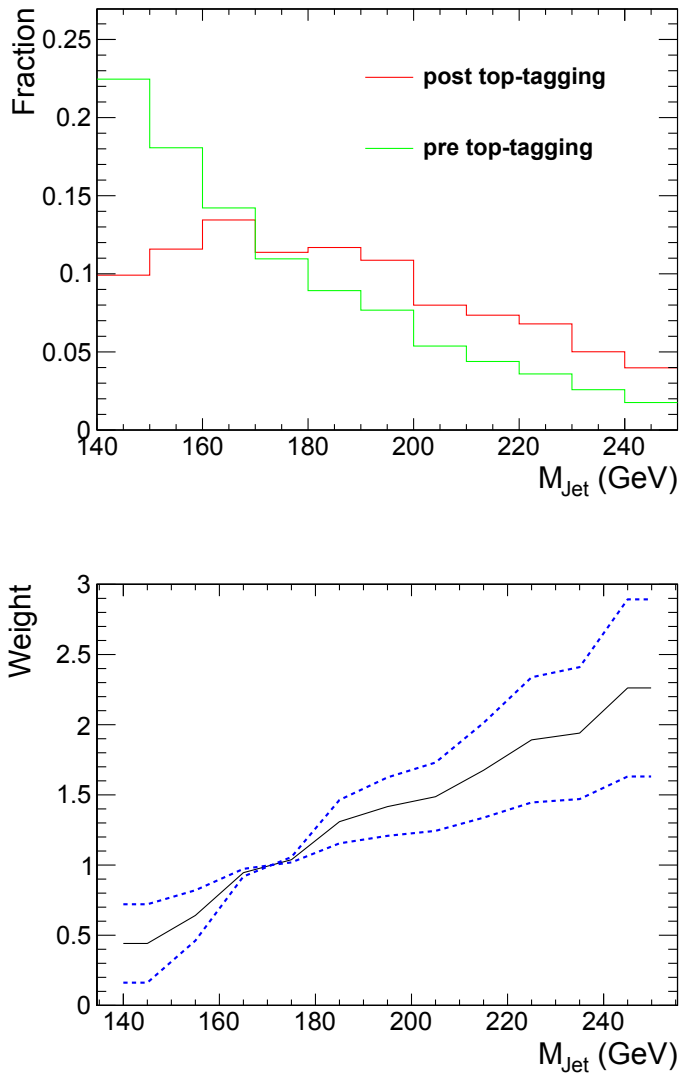

Figure 4.10: A plot of the top candidate mass spectrum in QCD MC before and after top-tagging (top). The correction used for this discrepancy (bottom) created by dividing the templates in the top plot. The uncertainty used for this correction is shown as the blue dashed line.

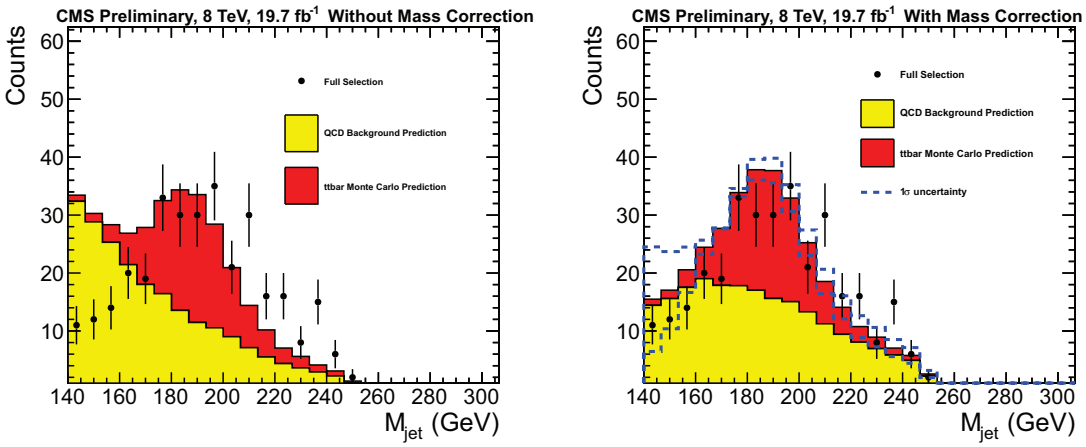

Figure 4.11: Top candidate mass before (left) and after (right) the top candidate mass correction. The selection for this plot is the full selection in the signal region.

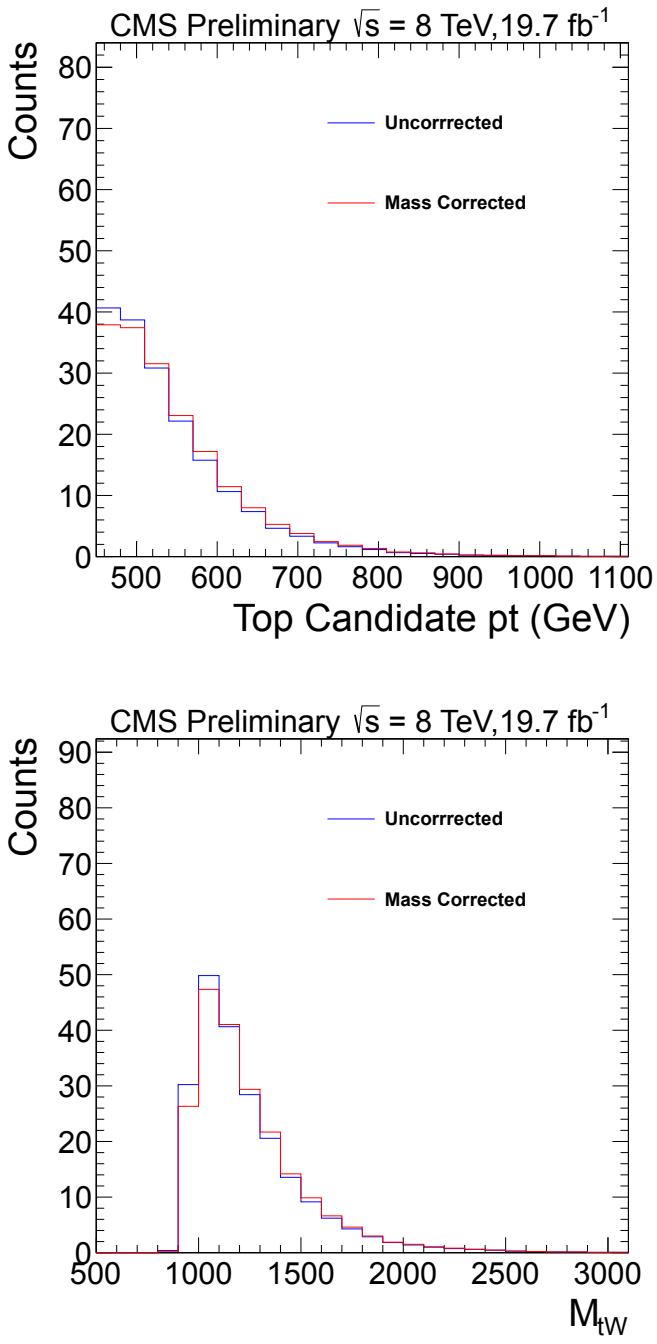

Figure 4.12: A plot of the QCD background estimate before and after the top mass correction. the top plots show the effect on top p_T, and the bottom plot shows the effect on M_{tW}.

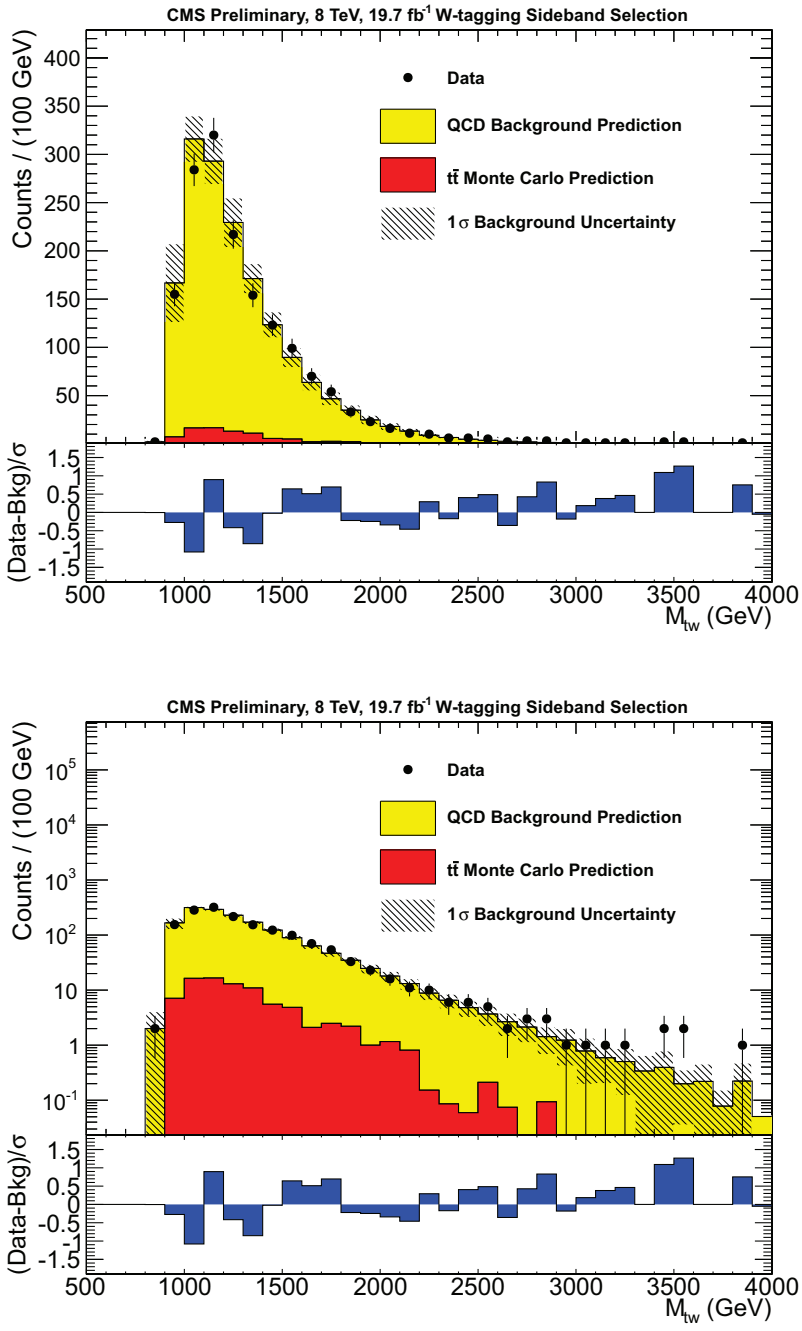

Figure 4.13: A plot of M_{tW} in the W-tagging sideband selection. The top and bottom plots are the same but with linear and log y-axis scale.

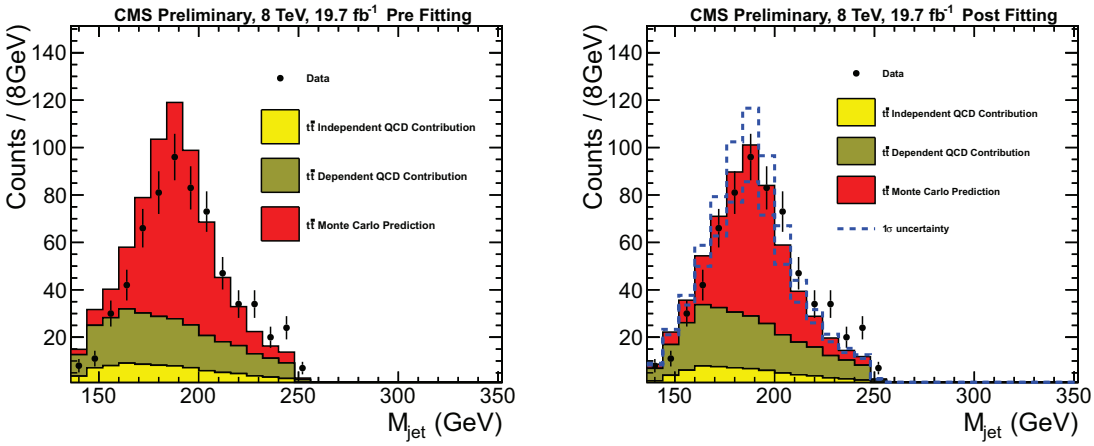

Figure 4.14: top candidate jet mass as extracted from the high mass W-tagging sideband. Pre fraction fit (left) and post fraction fit (right). The two QCD components use identical template shapes, but the normalization is such that one component can be considered independent from $t\bar{t}$, and the other will be anticorrelated $t\bar{t}$ normalization constant.

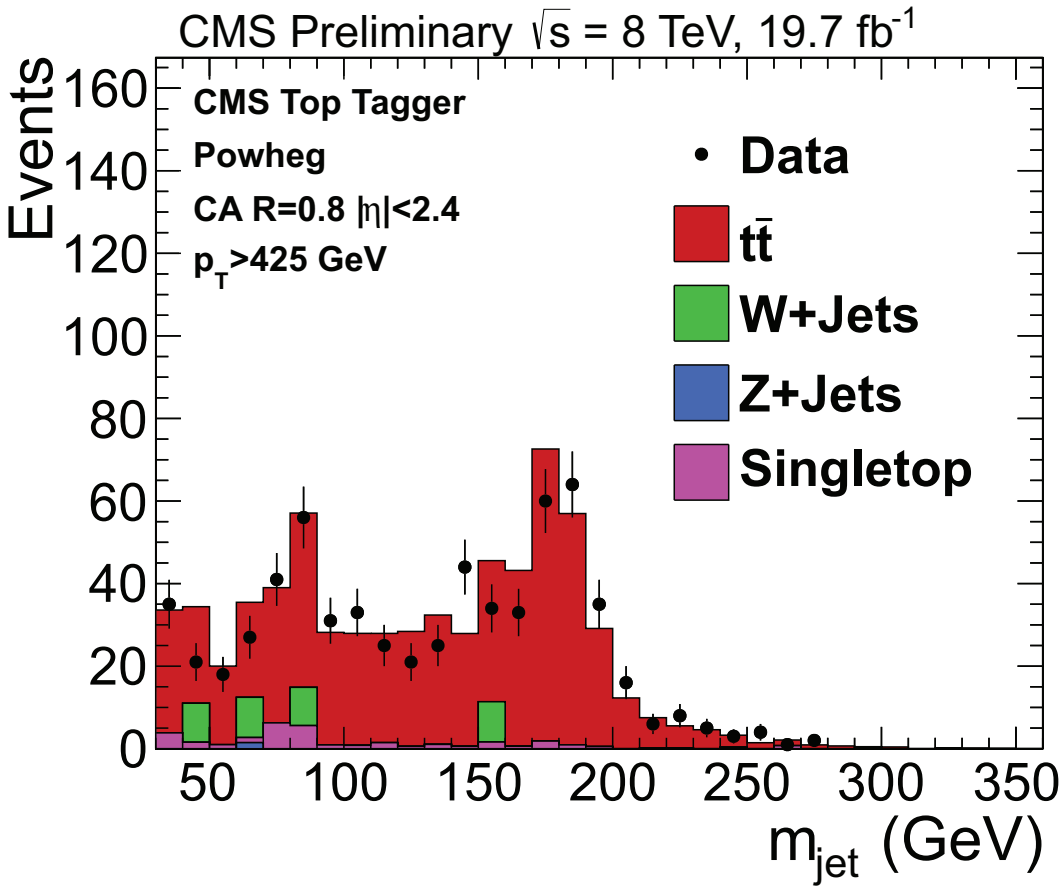

Figure 4.15: A plot of W candidate jet mass used for determination of the control region scale factors.

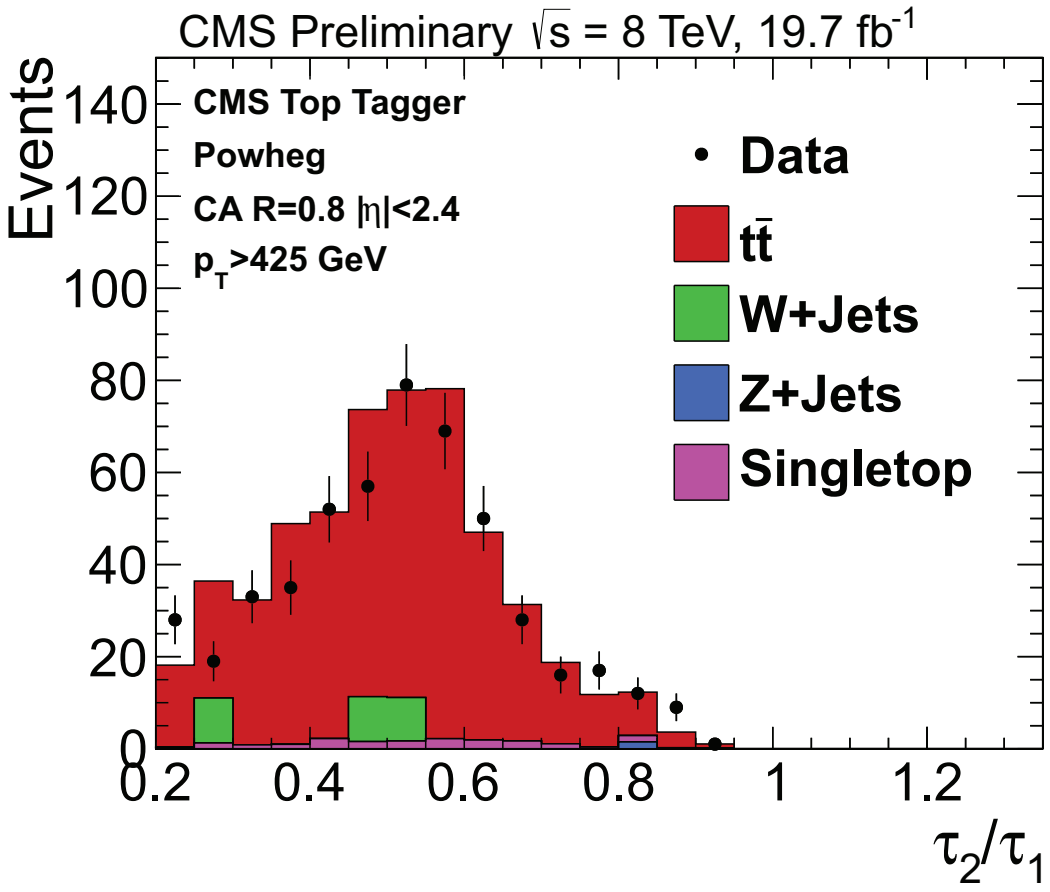

Figure 4.16: A plot of τ_2/τ_1 used for determination of the scale factor for the control region used for extracting the top-mistagging rate.

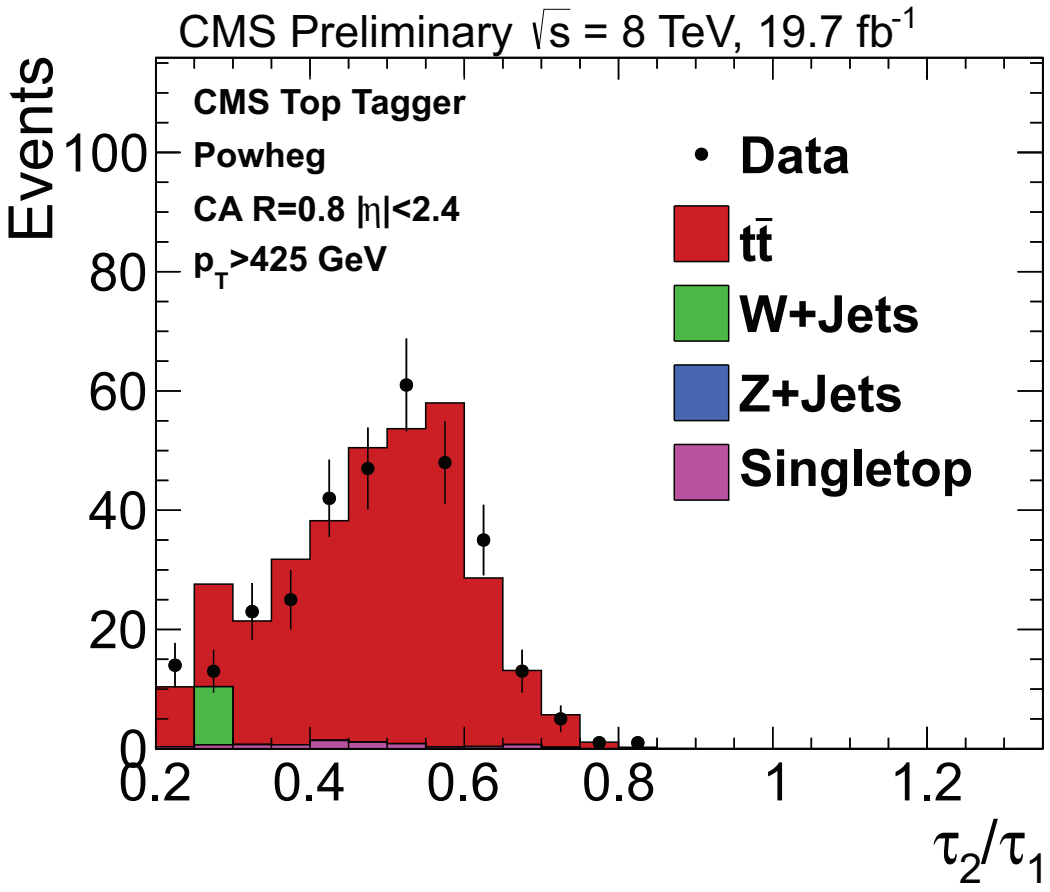

Figure 4.17: A plot of τ_2/τ_1 used for determination of the scale factor for the control region used for extracting the $t\bar{t}$ normalization.

b* signal region efficiency			
M_{b^*}	ϵ_R	ϵ_L	ϵ_{LR}
800	**0.0014**	**0.0010**	**0.0012**
900	**0.0076**	**0.0063**	**0.0070**
1000	**0.0301**	**0.0243**	**0.0272**
1100	**0.0502**	**0.0411**	**0.0456**
1200	**0.0653**	**0.0522**	**0.0588**
1300	**0.0746**	**0.0590**	**0.0668**
1400	**0.0788**	**0.0636**	**0.0712**
1500	**0.0809**	**0.0629**	**0.0719**
1600	**0.0795**	**0.0616**	**0.0706**
1700	**0.0760**	**0.0596**	**0.0678**
1800	**0.0749**	**0.0569**	**0.0659**
1900	**0.0707**	**0.0536**	**0.0622**
2000	**0.0660**	**0.0499**	**0.0583**

Table 4.5: b* signal efficiency for left-handed, right-handed and vectorlike b* samples

4.4 Data Results

After closure of the background estimation procedure within the control region 4.3.3, we investigate signal region. The results in the signal region are shown in Figure 4.18. We proceed to compute limits on the b* cross-section. Background estimation of selected relevant variables can be seen in Figures 4.19 and 4.20.

The expected number of events in the signal region is 359 $\pm$ 58, the observed number of events is 318. Table 4.5 gives the signal efficiency in the signal region for the three signal coupling hypotheses.

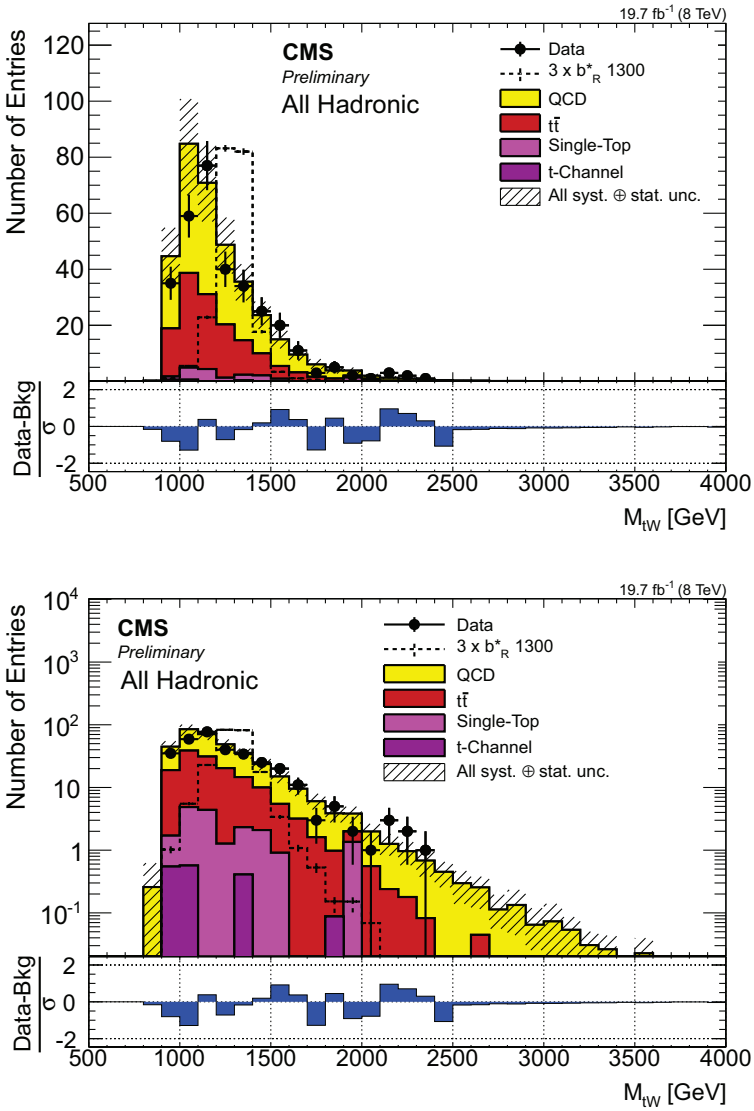

Figure 4.18: A plot of the full selection comparing data, signal and background. Top and bottom plots are the same but on linear and log y-axis scale.

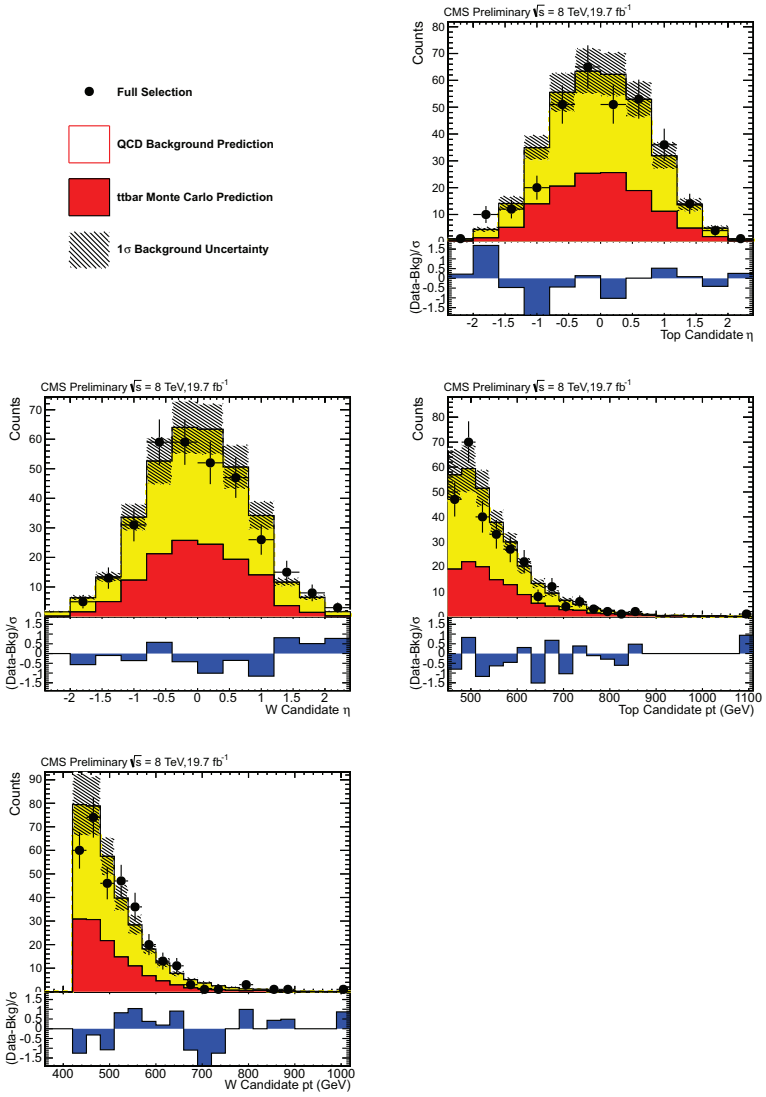

Figure 4.19: Background estimation of kinematic variables. The error bars shown are from the three primary sources; uncertainty on the fit, choice of fit, top mass modification, $t\bar{t}$ normalization, and $t\bar{t}$ Q^2 uncertainty

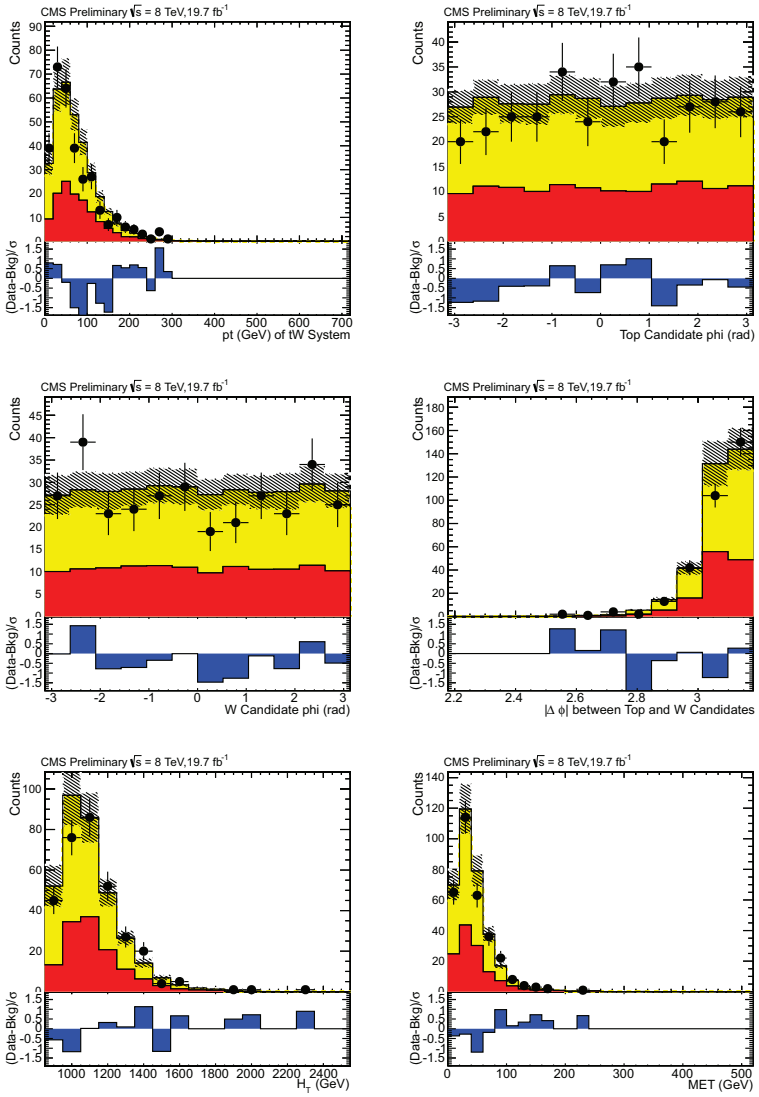

Figure 4.20: Background estimation of kinematic variables. The error bars shown are from the three primary sources; uncertainty on the fit, choice of fit, top mass modification, $t\bar{t}$ normalization, and $t\bar{t}$ Q^2 uncertainty

4.5 Systematic Uncertainties

Various systematics are taken into account, both on our expected signal and background estimate. Some systematic uncertainties will affect only the normalization of certain event rates, and are reported as overall normalization uncertainties. Other systematics affect the shapes of the reconstructed signal or backgrounds, as well as their normalization.

The uncertainty sources of jet energy scale, trigger, jet energy resolution, jet angular resolution, parton distribution functions, pileup, and Q^2 scale are considered and we use the prescriptions outlined in Section 3.5. Figure 4.24 shows the systematic shapes from the jet energy scale on the $t\bar{t}$ distribution. Jet energy scale variation on signal MC is shown in Figure 4.23 for 1200 GeV, 1300 GeV, and 1400 GeV mass points. The effects of this on the $t\bar{t}$ distribution due to the trigger systematic variation is shown in Figure 4.26. The trigger weighting systematic uncertainty on signal MC is shown in Figure 4.25 for 1200 GeV, 1300 GeV, and 1400 GeV mass points. The uncertainty is low in the mass range of interest for limit setting. The jet energy resolution variation in $t\bar{t}$ MC can be seen in Figure 4.28. Jet energy resolution variation on signal MC is shown in Figure 4.27 for 1200 GeV, 1300 GeV, and 1400 GeV mass points. The jet angular resolution variation in $t\bar{t}$ MC can be seen in Figure 4.30 . Jet angular resolution variation on signal MC is shown in Figure 4.29 for 1200 GeV, 1300 GeV, and 1400 GeV mass points. The effect is very small and thus not considered in setting limits. PDF variation on signal MC is shown in Figure

4.31 for 1200 GeV, 1300 GeV, and 1400 GeV mass points. PDF variation on $t\bar{t}$ MC is shown in Figure 4.32. The effect is very small and thus not considered in setting limits. The pileup reweighting uncertainty variation for signal can be seen in figure 4.33. The effect is very small and thus not considered in setting limits. The Q^2 scale uncertainty can be seen in Figure 4.22.

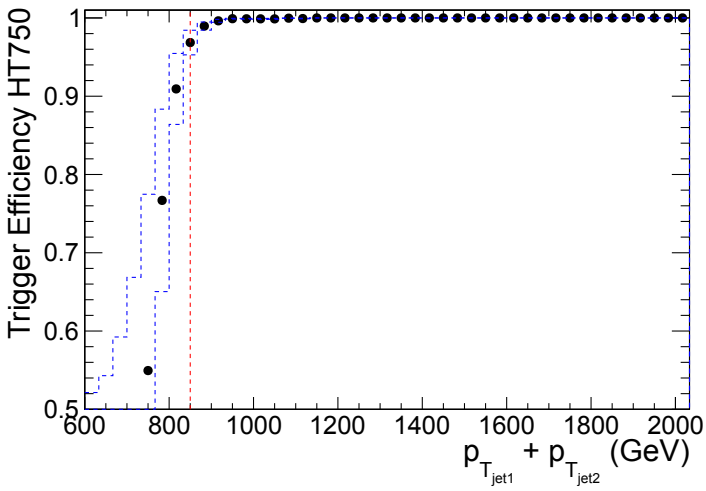

Figure 4.21: Trigger efficiency systematic variation.

4.5.1 Normalization Uncertainties

As mentioned in Section 4.3.4, the uncertainty on the overall normalization scale factor used for $t\bar{t}$ is extracted from data and is 22%.

We must apply a 13% uncertainty on the top tagging scale factor described in Section 3.2.8 to signal MC events due to uncertainty in the difference in subjet efficiency from data to MC.

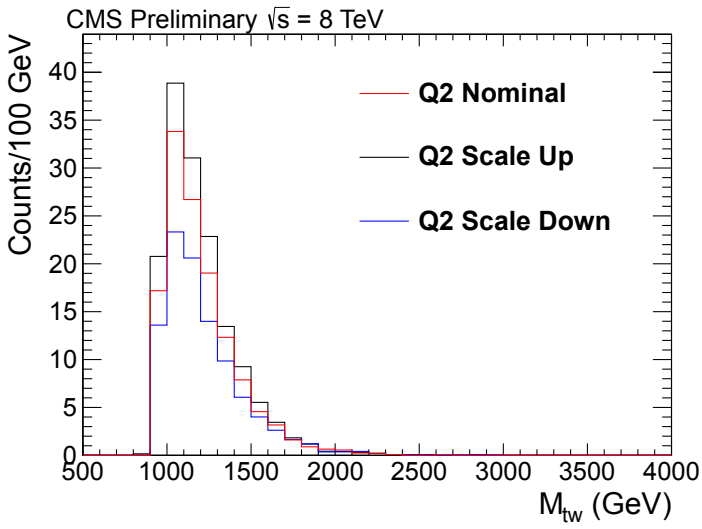

Figure 4.22: Q^2 systematic variation for $t\bar{t}$ MC

The cross-section uncertainty of 20%,15%,30% applies single-top quark background tW,t,and s channels respectively are applied.

We also include a 2.6% uncertainty in the luminosity for the signal MC [39].

4.5.2 Uncertainties Related to the QCD Background Estimate

We use the result of the fit to the top-mistagging rate (see Section 4.3) to weight pre top-tagged events in order to create the QCD background estimate. Uncertainties in the fitting algorithm and statistical uncertainties in the sideband are taken into account (see figure 4.9). Statistical uncertainties in the pre b tagged signal region are also taken into account.

4.5.2.1 Choice of the Functional Form for the Average Top-Mistagging Rate

The functional form used is a bifurcated polynomial. However there is a systematic uncertainty associated with this choice. The uncertainties due to this effect are taken into account by studying alternative functional forms seen in figure 4.34. The background estimation from these alternative fits are seen in figure 4.35. The uncertainty due to the choice of fit is taken as the Mean Squared Error of these alternative backgrounds bin by bin and can be seen in figure 4.36.

4.5.2.2 Top Candidate Mass Correction

The correction of the top candidate mass is detailed in section 4.3.2. The uncertainty on this procedure is taken as one half of the correction and is shown in Figures

4.10 and 4.11.

4.5.2.3 Two-Dimensional vs. Three-Dimensional Parameterization of the Average Top-Mistagging Rate

Additionally, we place an uncertainty on the inability of the background estimate to capture all kinematic correlations through the parameterization of the top-mistagging rate in p_T and η. This uncertainty is calculated by investigating a parameterization in p_T η and M_{tW}. We define P_i as the top-mistagging rate described in Section 4.3 in one η bin and P_{ij} as the top-mistagging rate if parameterized with M_{tW} as well. P_{ij} can be seen in figure 4.37. Each bin in P_i can be thought of as a column average over all M_{tW} bins per p_T bin. If P_{ij} a function of M_{tW} (index j) is not constant, then averaging over P_{ij} over j while projecting onto M_{tW} axis to obtain the QCD background estimate can result in a bias.

We assess the approximate size of the uncertainty due to our choice of parameterization by explicitly comparing the three-dimensional and two-dimensional background estimates in the sideband. Using these two parameterizations, the uncertainty in the M_{tW} distribution due to parameterization is approximately $\sum_{j=0}^{n} m_{ij}(P_{ij} - P_i)$ where m_{ij} refers to the number of pretag events for a bin in p_T and M_{tW}. Fig. 4.38 shows the uncertainty due to this effect. The addition of a dimension to the top-mistagging rate parameterization leads to lower statistical power. The additional uncertainty from including M_{tW} in the top-mistagging rate parameterization is taken into account by

an additional uncertainty on the QCD shape. For this, we use the $\pm 1\sigma$ deviations from the 3d parameterized top-mistagging rate to extract the M_{tW} shape instead of the nominal value. Additionally, the uncertainty due to the 2d parameterization is subtracted from this shape in quadrature due to the fact that this is already included as an uncertainty. The uncertainty due to this can be seen in figure 4.39.

These uncertainties are taken in quadrature to produce an overall uncertainty in the data derived background estimate that is applied in a shape based manner in the limit-setting macro.

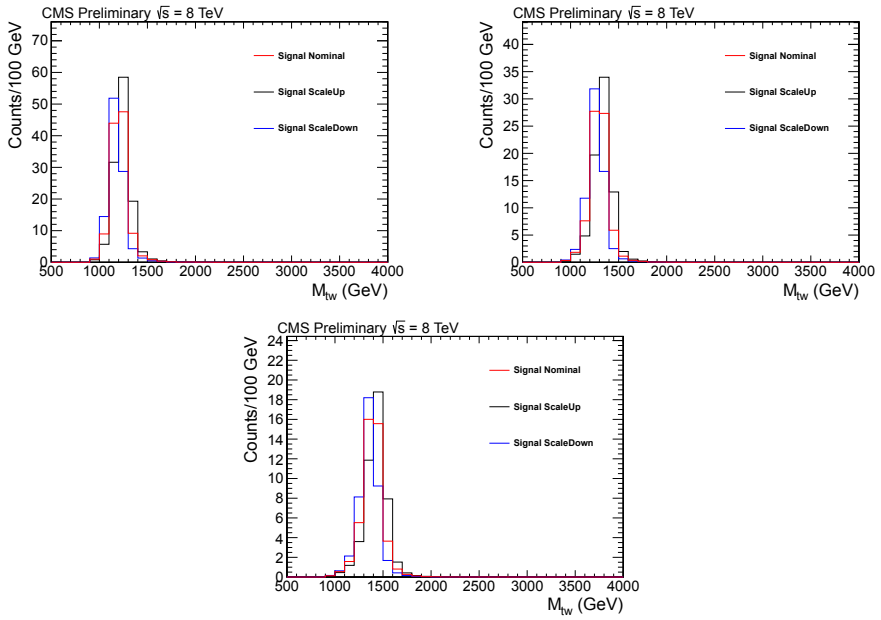

Figure 4.23: Jet Energy Scale systematic variation for right-handed b* MC at the following mass points (a) $M_{b^*} = 1200$ GeV (b) $M_{b^*} = 1300$ GeV (c) $M_{b^*} = 1400$ GeV

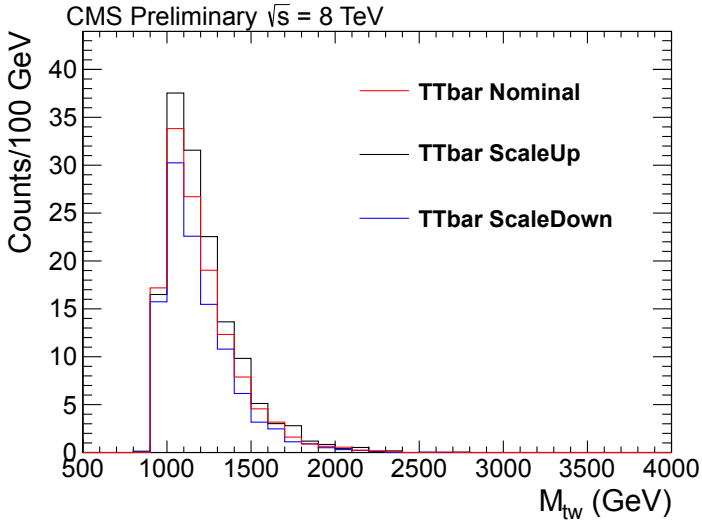

Figure 4.24: Jet Energy Scale systematic variation for $t\bar{t}$ MC

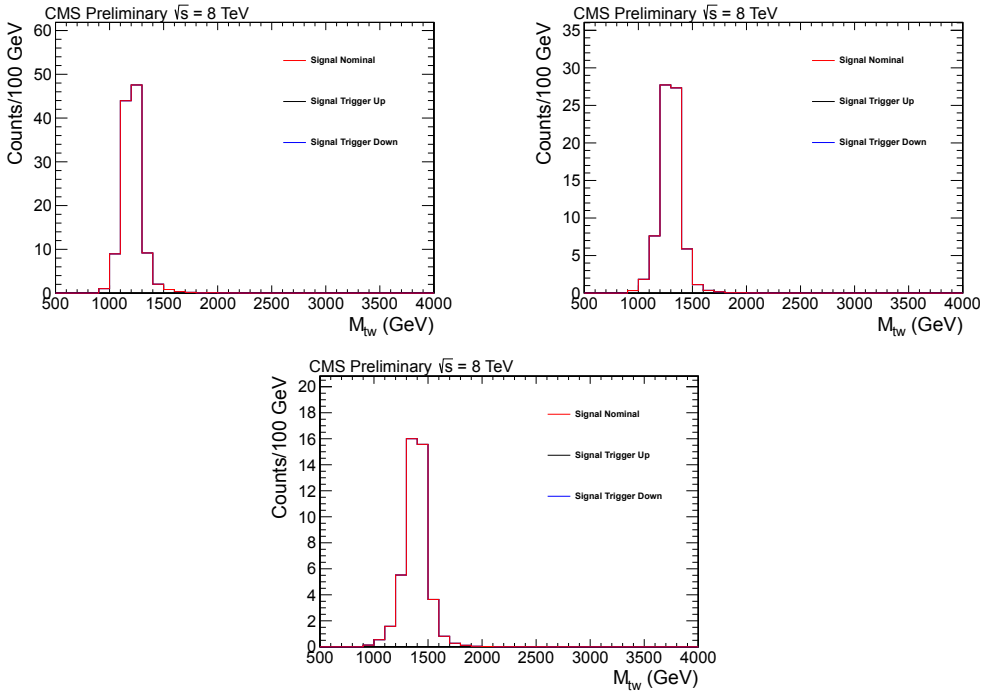

Figure 4.25: Trigger Weighting systematic variation for right-handed b* MC at the following mass points (a) $M_{b^*} = 1200$ GeV (b) $M_{b^*} = 1300$ GeV (c) $M_{b^*} = 1400$ GeV

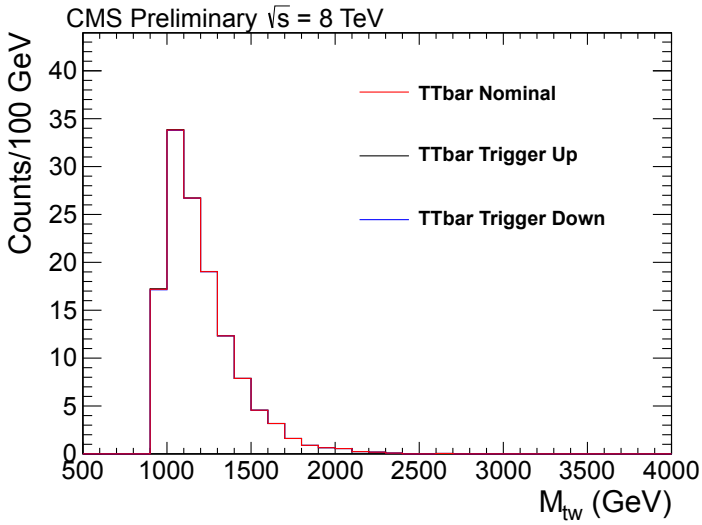

Figure 4.26: Trigger Weighting systematic variation for $t\bar{t}$ MC

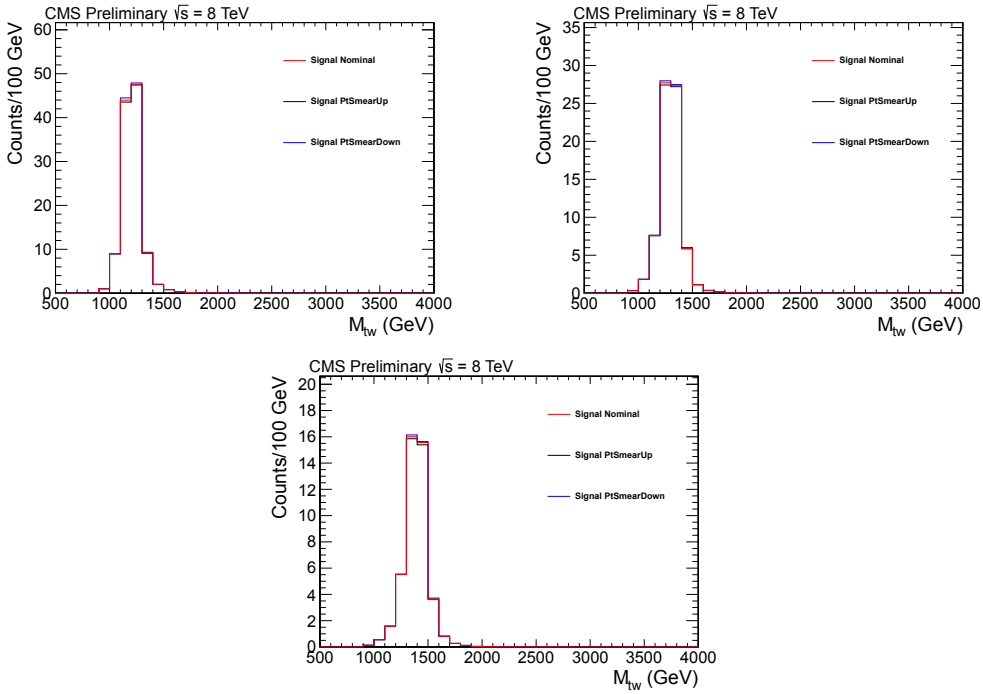

Figure 4.27: Jet Energy Resolution systematic variation for right-handed b* MC at the following mass points (a) M_{b^*} = 1200 GeV (b) M_{b^*} = 1300 GeV (c) M_{b^*} = 1400 GeV

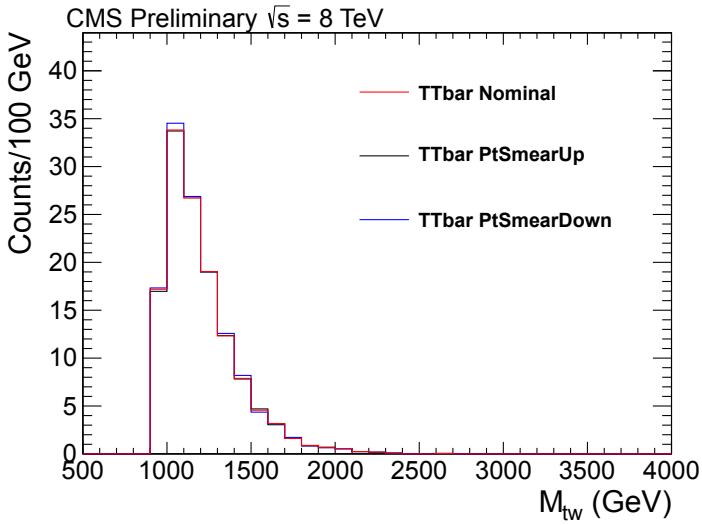

Figure 4.28: Jet Energy Resolution systematic variation for $t\bar{t}$ MC

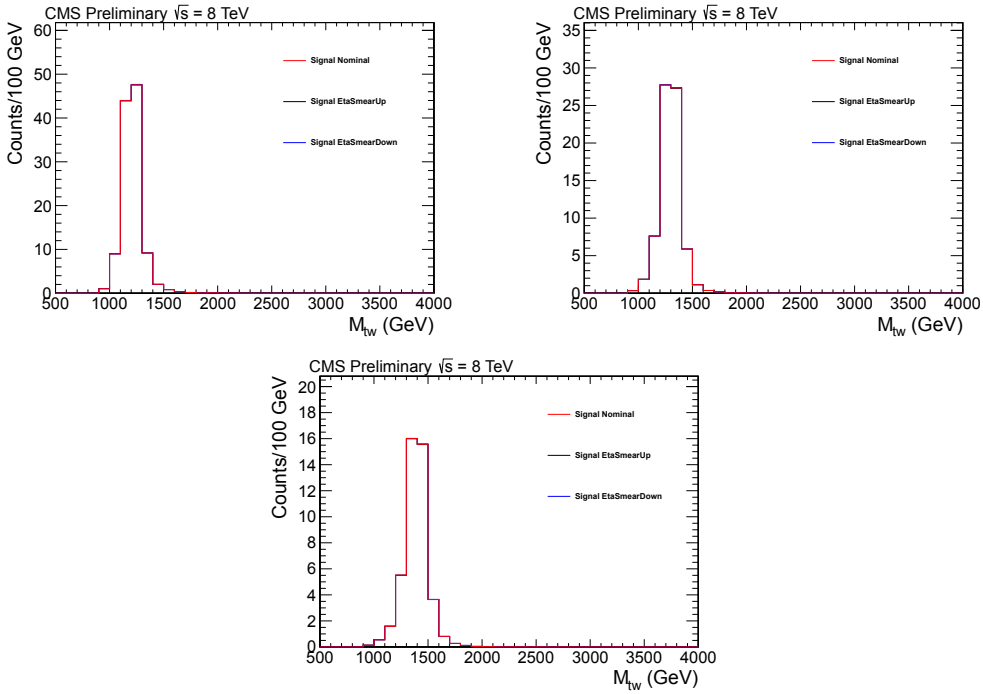

Figure 4.29: Jet Angular Resolution systematic variation for right-handed b* MC at the following mass points (a) M_{b^*} = 1200 GeV (b) M_{b^*} = 1300 GeV (c) M_{b^*} = 1400 GeV

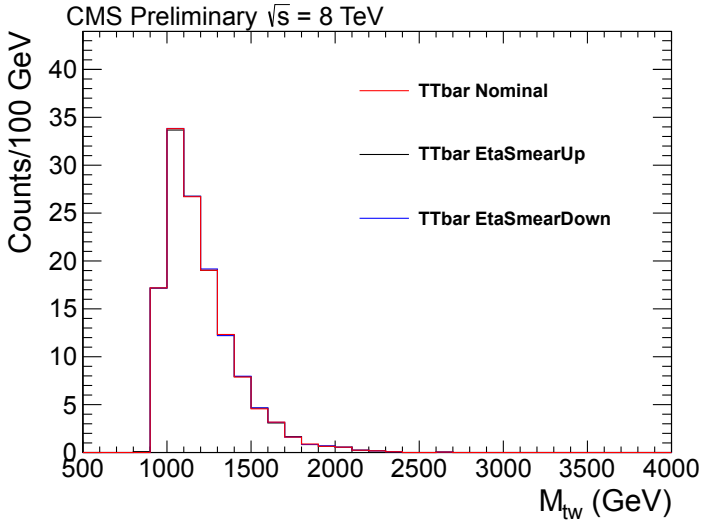

Figure 4.30: Jet Angular Resolution systematic variation for $t\bar{t}$ MC

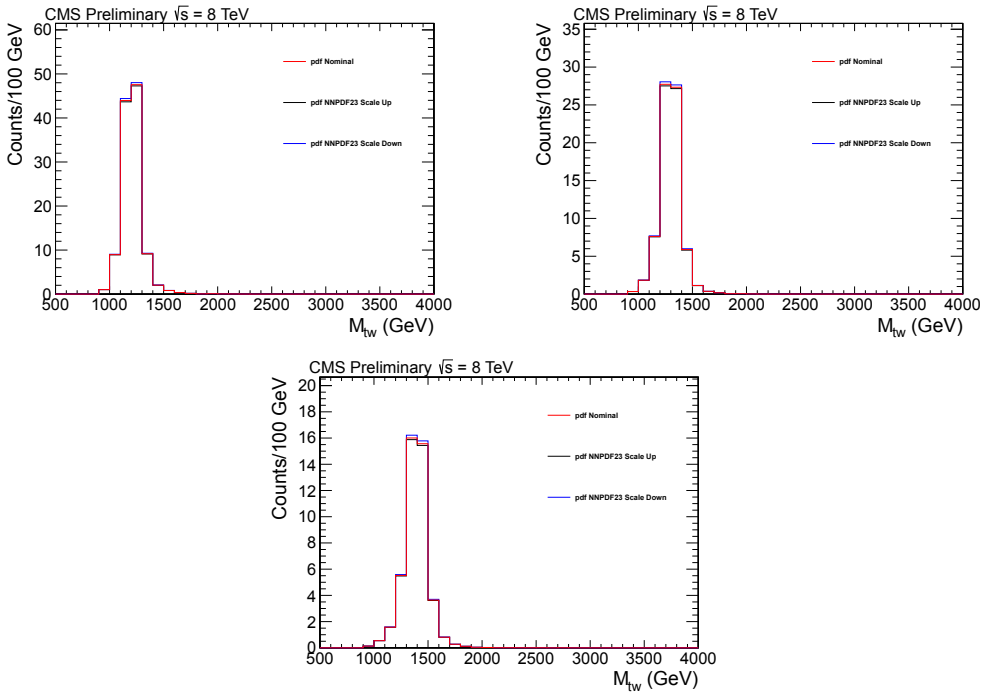

Figure 4.31: PDF systematic variation for right-handed b* MC at the following mass points (a) M_{b^*} = 1200 GeV (b) M_{b^*} = 1300 GeV (c) M_{b^*} = 1400 GeV

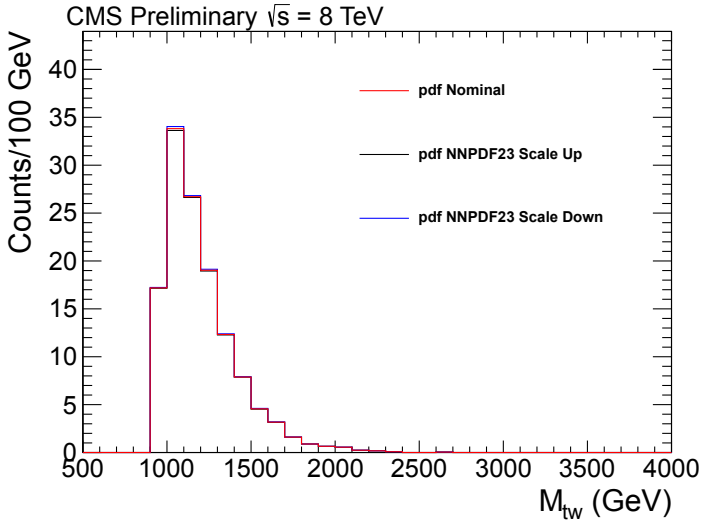

Figure 4.32: PDF systematic variation for $t\bar{t}$ MC

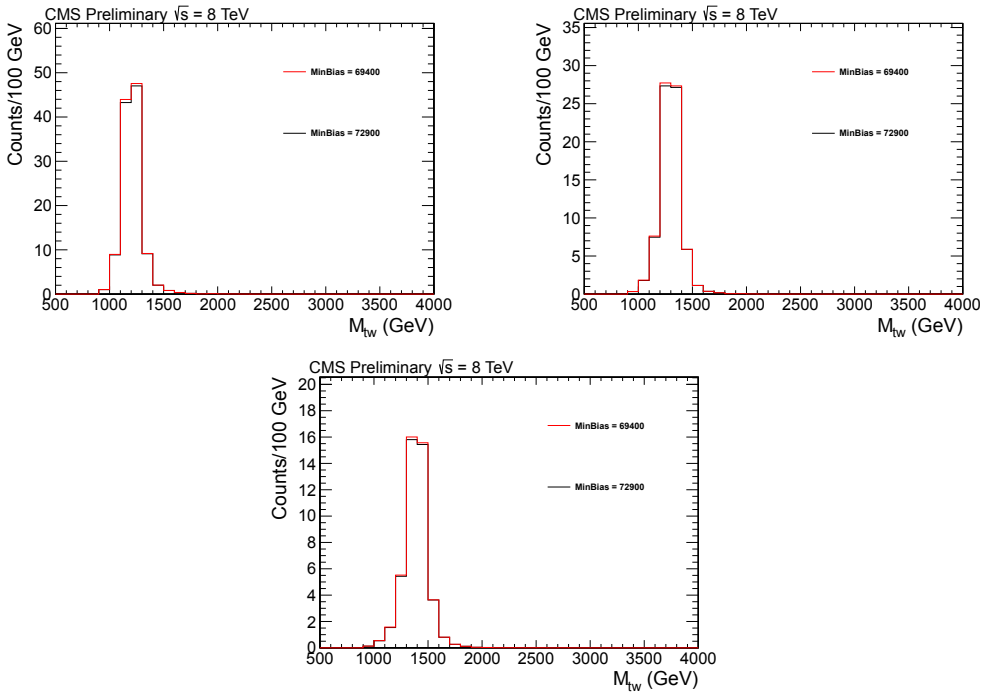

Figure 4.33: Pileup systematic variation for right-handed b* MC at the following mass points (a) M_{b^*} = 1200 GeV (b) M_{b^*} = 1300 GeV (c) M_{b^*} = 1400 GeV

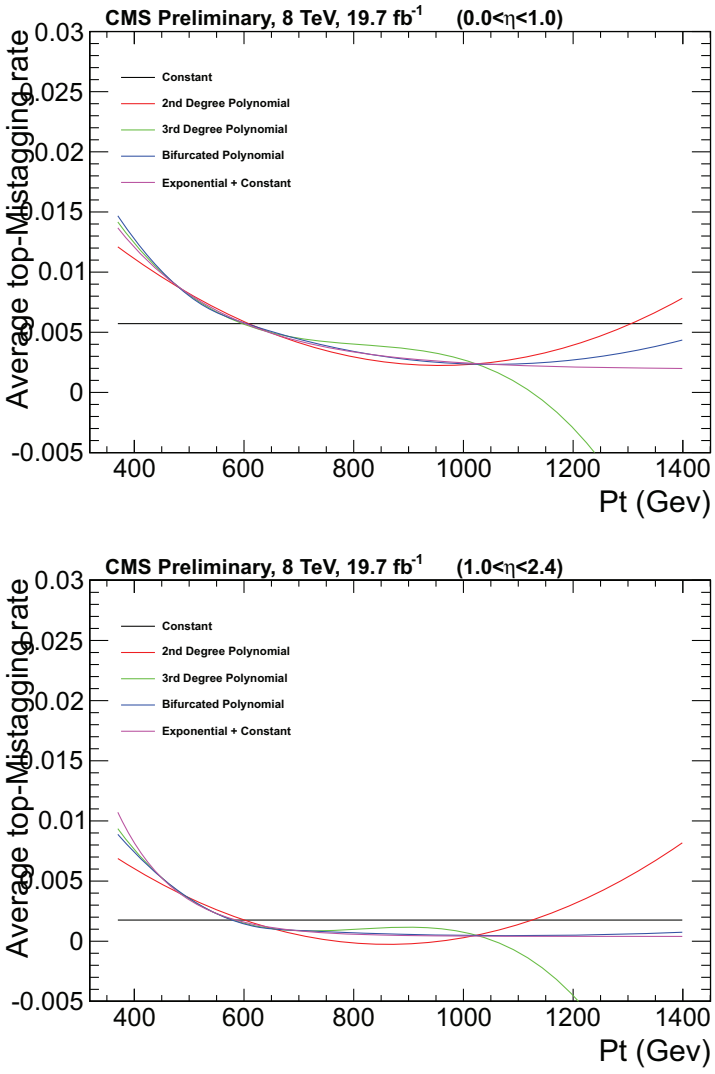

Figure 4.34: Alternative fit functions for the top-mistagging rate in η regions (a) Low (b) High

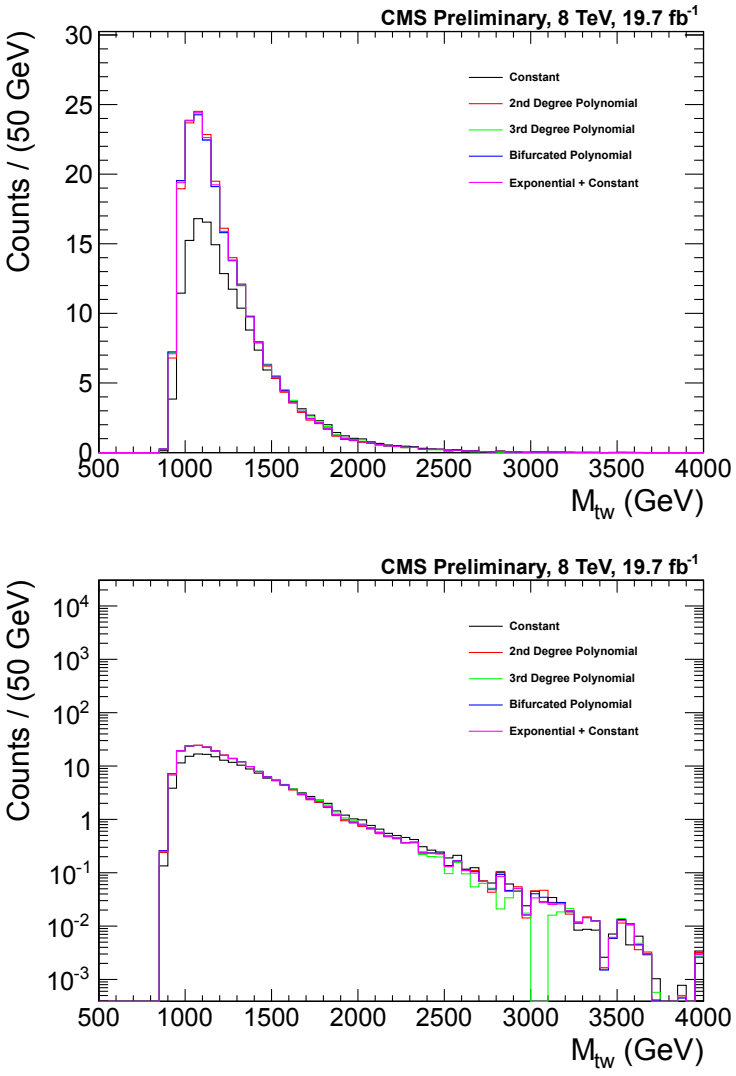

Figure 4.35: QCD background estimation from alternative fit functions seen in 4.34. Top and bottom plots are the same but on linear and log y-axis scale.

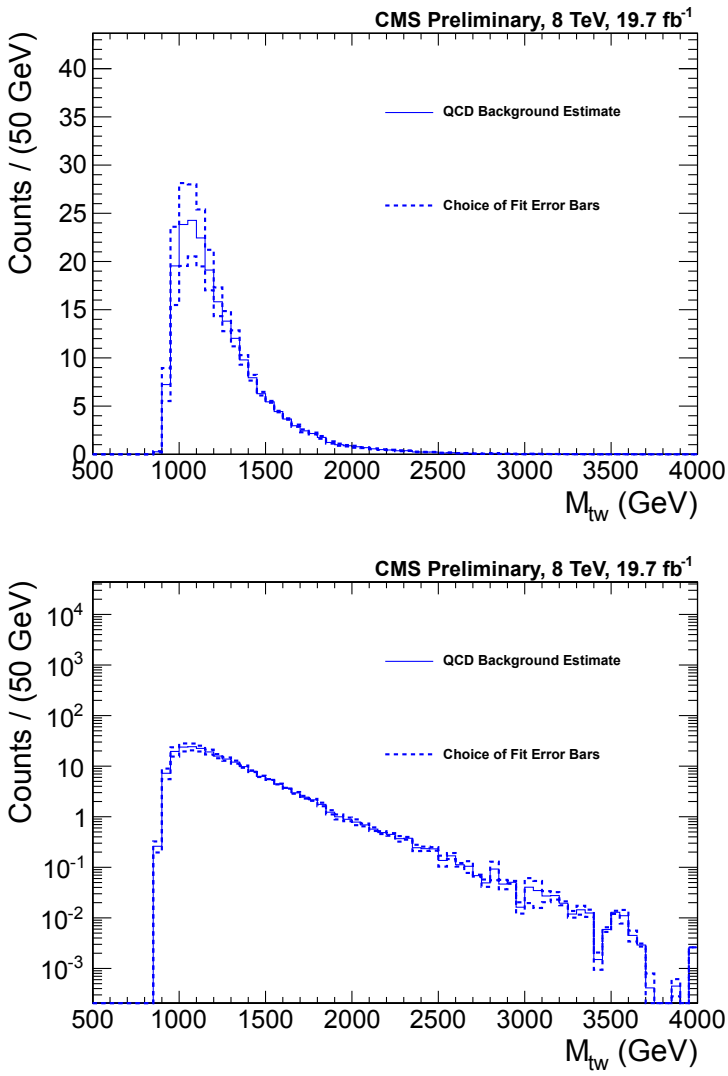

Figure 4.36: Uncertainty on the choice of fit as extracted from the alternative background estimations seen in 4.35. Top and bottom plots are the same but on linear and log y-axis scale.

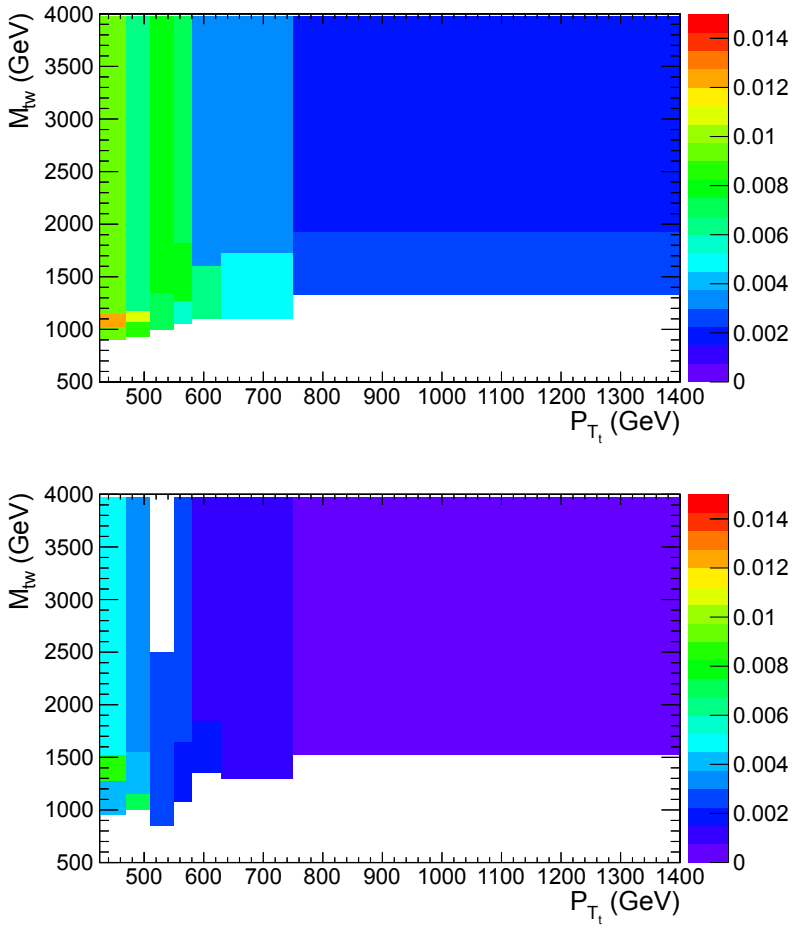

Figure 4.37: Two dimensional parameterization of top-mistagging rate in p_{Tt} and M_{tW}. The x axis binning is identical to the binning in Section 4.3. The y-axis is binned adaptively to approximate equivalent statistics over each y-axis bin per x axis bin. (a) Low η Region (b) High η Region

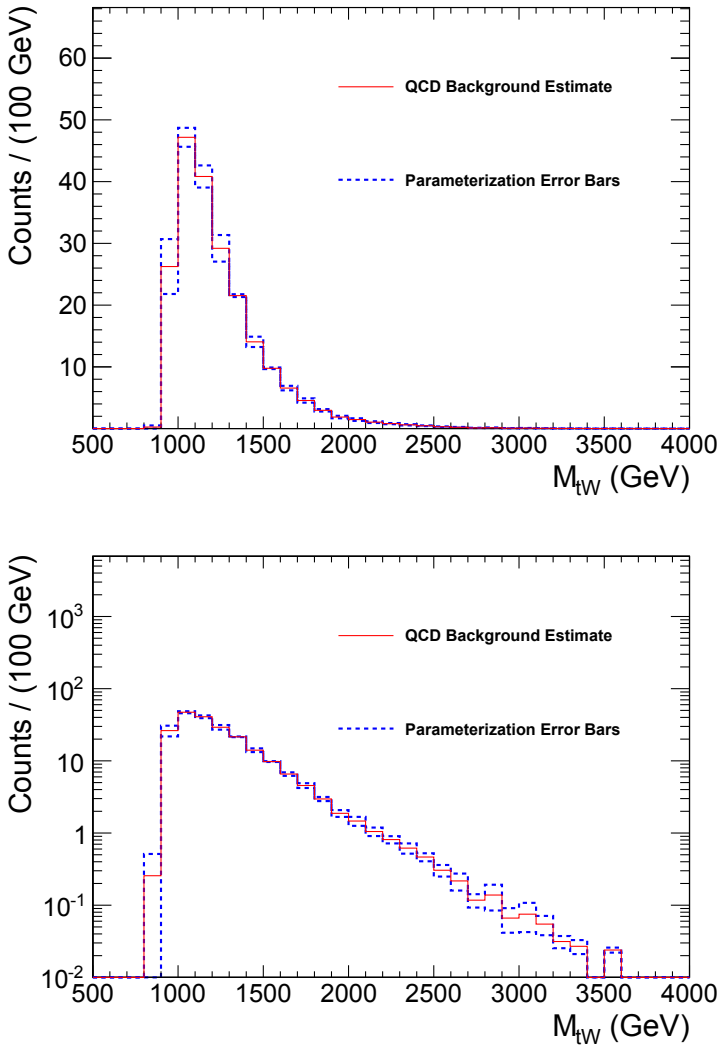

Figure 4.38: Uncertainty on the parameterization choice. Top and bottom plots are the same but on linear and log y-axis scale.

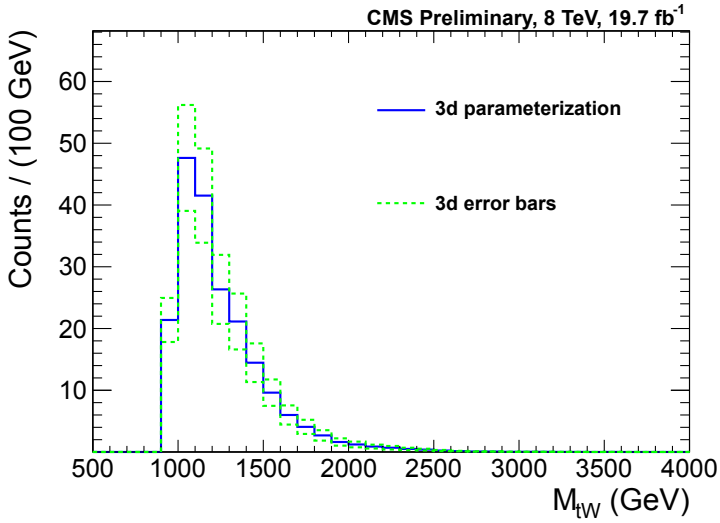

Figure 4.39: Statistical uncertainty on the three dimensional parameterization top-mistagging rate nominal shapes.

4.6 Results

4.6.1 Limits

We set limits on the production cross-section of the b* quark. We compare the number of observed events to the number of events expected given the new physics model. We use the following formula:

$$N_{\text{expected}} = \sigma_{\text{b}^*} \times B_{\text{b}^* \to tW; W \to hadrons} \times \varepsilon \times L \tag{4.6}$$

where σ_{b^*} is the b* cross-section, $B_{\text{b}^* \to tW; W \to hadrons}$ is the branching ratio b* $\to tW$ with both W boson decays constrained to the hadronic branching fraction, ε is the efficiency and L is the integrated luminosity of our dataset.

We perform a shape analysis using the M_{tW} distribution. This analysis uses a binned likelihood fit to compare the distribution from the b* quark signal hypothesis with the SM distribution produced by our background estimation procedure.

We use a Bayesian method to extract 95% CL upper limits on the production of a left- and right-handed b* particle.

The statistical procedure for setting limits is described in Section 3.6.1.

The uncertainty in the jet energy scale, Q^2 scale, trigger, QCD background uncertainties, and jet energy resolution are taken as shape based uncertainties, and the other sources of uncertainty are taken as overall normalizations.

The limits from Theta are shown in Figure 4.49. The expected(observed) exclusion region for the right-handed b* quark hypothesis is between 0.88 TeV and 1.55 TeV (0.82 TeV and 1.43 TeV). The expected(observed) exclusion region for the left-handed b* quark hypothesis is between 0.89 TeV and 1.48 TeV (0.88 TeV and 1.40 TeV). The expected(observed) exclusion region for the vectorlike b* quark hypothesis is between 0.82 TeV and 1.70 TeV (0.8 TeV and 1.53 TeV). Cross-section upper limits for right-handed, left-handed, and vectorlike b* are summarized in Tables 4.10,4.11, and 4.12 respectively.

Table 4.6 gives the values for nuisance parameters after limit setting for each b* mass hypothesis.

The cross section upper limits can be generalized due to the fact that the b* cross-section is dependent on the unknown constants κ and g as can be seen in equations 4.1 and 4.1. The limits can be extrapolated to the g,κ plane as can be seen in figures 4.50 and 4.50 for observed and expected limits respectively.

Rate Effects of Systematic Uncertainties

Sample	JER	JES	Q^2	QCD total	Lumi	top-tagging SF	W-tagging SF	Trigger	$t\bar{t}$ Norm
$M_{b^*} = 1000$	-0.81,+0.51	+17.91,-21.34	—	—	+2.63,-2.57	+12.50,-11.11	+7.60,-7.06	+0.14,-0.14	—
$M_{b^*} = 1100$	-0.51,+0.60	+9.07,-12.13	—	—	+2.63,-2.57	+12.50,-11.11	+7.60,-7.06	+0.07,-0.07	—
$M_{b^*} = 1200$	-0.41,+0.60	+6.12,-9.76	—	—	+2.63,-2.57	+12.50,-11.11	+7.60,-7.06	+0.04,-0.04	—
$M_{b^*} = 1300$	-0.42,+0.41	+4.98,-8.06	—	—	+2.63,-2.57	+12.50,-11.11	+7.60,-7.06	+0.03,-0.03	—
$M_{b^*} = 1400$	-0.53,+0.40	+4.20,-7.65	—	—	+2.63,-2.57	+12.50,-11.11	+7.60,-7.06	+0.02,-0.02	—
$M_{b^*} = 1500$	-0.46,+0.42	+4.50,-7.76	—	—	+2.63,-2.57	+12.50,-11.11	+7.60,-7.06	+0.02,-0.02	—
$M_{b^*} = 1600$	-0.48,+0.37	+3.79,-7.33	—	—	+2.63,-2.57	+12.50,-11.11	+7.60,-7.06	+0.01,-0.01	—
$M_{b^*} = 1700$	-0.34,+0.35	+3.91,-6.43	—	—	+2.63,-2.57	+12.50,-11.11	+7.60,-7.06	+0.01,-0.01	—
$M_{b^*} = 1800$	-0.48,+0.39	+3.71,-7.64	—	—	+2.63,-2.57	+12.50,-11.11	+7.60,-7.06	+0.01,-0.01	—
$M_{b^*} = 1900$	-0.46,+0.44	+3.31,-7.12	—	—	+2.63,-2.57	+12.50,-11.11	+7.60,-7.06	+0.01,-0.01	—
$M_{b^*} = 2000$	-0.46,+0.41	+3.14,-7.29	—	—	+2.63,-2.57	+12.50,-11.11	+7.60,-7.06	+0.01,-0.01	—
$M_{b^*} = 800$	-0.00,+0.56	+29.42,-25.25	—	—	+2.63,-2.57	+12.50,-11.11	+7.60,-7.06	+0.19,-0.19	—
$M_{b^*} = 900$	-0.18,+0.42	+46.46,-35.69	—	—	+2.63,-2.57	+12.50,-11.11	+7.60,-7.06	+0.28,-0.28	—
qcd	—	—	—	+28.14,-27.56	—	—	—	—	—
sts	+nan,+nan	+nan,+nan	—	—	+2.63,-2.57	+12.50,-11.11	+7.60,-7.06	+nan,+nan	—
stt	-0.11,+17.70	+47.87,-16.85	—	—	+2.63,-2.57	+12.50,-11.11	+7.60,-7.06	+0.13,-0.13	—
sttW	+0.01,-0.00	+17.42,-13.16	—	—	+2.63,-2.57	+12.50,-11.11	+7.60,-7.06	+0.09,-0.09	—
ttbar	-0.22,+1.05	+13.20,-14.75	+16.24,-23.58	—	—	—	+7.60,-7.06	+0.10,-0.10	+22.00,-18.03

Table 4.6: Rate effects of the systematic uncertainties as extracted from Theta. The numbers listed under sample specify b* signal MC mass.

b^*_R **Cross-Section Upper Limits**

M_{b^*}	**observed**	**expected**	**expected 1σ**	**expected 2σ**
800	**3.298**	**6.325**	**3.584,11.675**	**1.999,22.481**
900	**0.283**	**0.549**	**0.323,0.953**	**0.202,1.961**
1000	**0.087**	**0.172**	**0.113,0.243**	**0.083,0.355**
1100	**0.122**	**0.112**	**0.077,0.162**	**0.056,0.223**
1200	**0.081**	**0.076**	**0.053,0.110**	**0.039,0.155**
1300	**0.051**	**0.052**	**0.036,0.077**	**0.026,0.107**
1400	**0.059**	**0.041**	**0.029,0.059**	**0.022,0.087**
1500	**0.062**	**0.034**	**0.024,0.049**	**0.017,0.071**
1600	**0.056**	**0.029**	**0.020,0.043**	**0.015,0.060**
1700	**0.035**	**0.025**	**0.018,0.038**	**0.013,0.053**
1800	**0.023**	**0.023**	**0.016,0.033**	**0.011,0.046**
1900	**0.021**	**0.022**	**0.015,0.031**	**0.011,0.044**
2000	**0.023**	**0.021**	**0.015,0.031**	**0.011,0.045**

Table 4.7: b^*_R cross-section upper limits for given b^*_R mass values. Cross-section is in units of pb.

b^*_L **Cross-Section Upper Limits**

M_{b^*}	**observed**	**expected**	**expected 1σ**	**expected 2σ**
800	**7.681**	**8.588**	**5.106,15.127**	**2.798,27.319**
900	**0.355**	**0.674**	**0.395,1.211**	**0.237,2.369**
1000	**0.106**	**0.204**	**0.137,0.297**	**0.099,0.424**
1100	**0.148**	**0.140**	**0.096,0.200**	**0.069,0.273**
1200	**0.107**	**0.100**	**0.069,0.143**	**0.050,0.203**
1300	**0.068**	**0.067**	**0.047,0.102**	**0.035,0.140**
1400	**0.072**	**0.051**	**0.036,0.075**	**0.027,0.108**
1500	**0.081**	**0.045**	**0.031,0.066**	**0.023,0.092**
1600	**0.074**	**0.038**	**0.027,0.057**	**0.020,0.079**
1700	**0.049**	**0.034**	**0.023,0.050**	**0.017,0.070**
1800	**0.031**	**0.030**	**0.021,0.044**	**0.015,0.061**
1900	**0.028**	**0.029**	**0.021,0.041**	**0.015,0.058**
2000	**0.032**	**0.029**	**0.021,0.043**	**0.015,0.060**

Table 4.8: b^*_L cross-section upper limits for given b^*_L mass values. Cross-section is in units of pb.

b^*_{LR} **Cross-Section Upper Limits**

M_{b^*}	**observed**	**expected**	**expected 1σ**	**expected 2σ**
800	**3.917**	**6.568**	**4.072,11.122**	**2.342,18.857**
900	**0.317**	**0.603**	**0.361,1.048**	**0.219,2.099**
1000	**0.095**	**0.187**	**0.124,0.269**	**0.087,0.386**
1100	**0.131**	**0.124**	**0.085,0.182**	**0.063,0.244**
1200	**0.094**	**0.086**	**0.060,0.124**	**0.044,0.177**
1300	**0.059**	**0.059**	**0.041,0.088**	**0.031,0.121**
1400	**0.065**	**0.046**	**0.033,0.066**	**0.024,0.097**
1500	**0.070**	**0.039**	**0.027,0.056**	**0.019,0.082**
1600	**0.065**	**0.033**	**0.023,0.049**	**0.017,0.069**
1700	**0.042**	**0.029**	**0.020,0.043**	**0.014,0.059**
1800	**0.026**	**0.026**	**0.018,0.038**	**0.013,0.053**
1900	**0.025**	**0.025**	**0.017,0.035**	**0.013,0.051**
2000	**0.026**	**0.025**	**0.017,0.036**	**0.013,0.050**

Table 4.9: b^*_{LR} cross-section upper limits for given b^*_{LR} mass values. Cross-section is in units of pb.

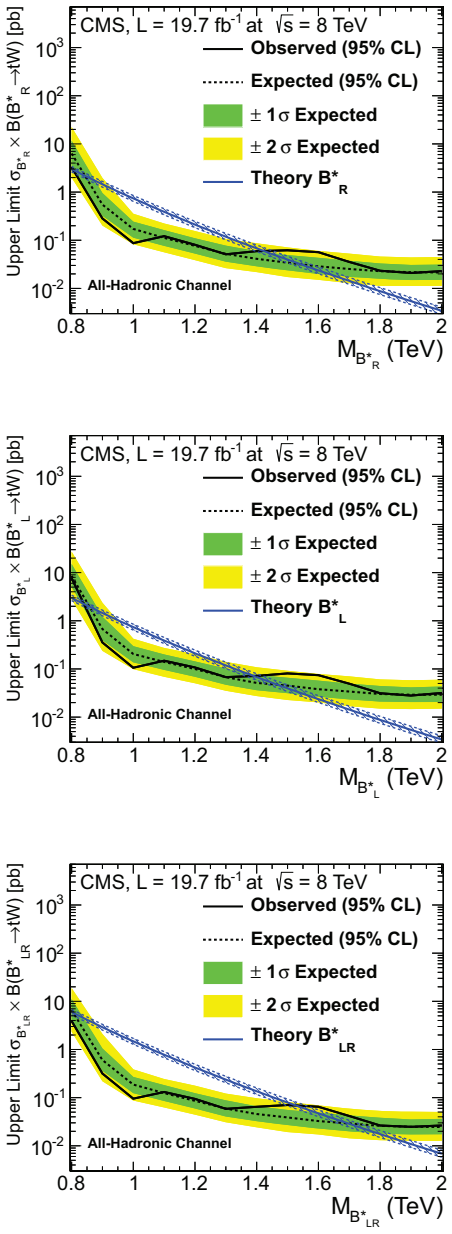

Figure 4.40: The b* quark 95% C.L. production cross-section limits. The expected (dashed black) and observed (solid black) limits as well as b* quark theoretical cross-section (blue) are plotted for comparison. The uncertainty in the expected limit band is shown in green ($\pm 1\sigma$) and yellow ($\pm 2\sigma$). These limits were extracted using the Theta limit setting framework. Here, the signal hypotheses of a right-handed, left-handed, and vectorlike b* quark are shown on the top, middle, and bottom plots respectively.

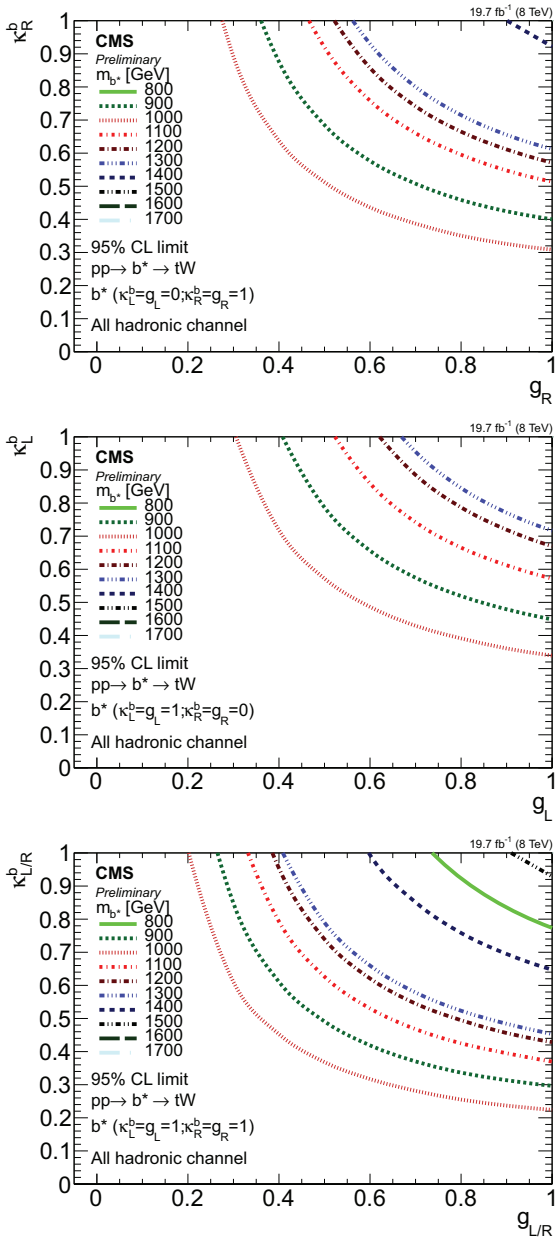

Figure 4.41: observed limit plot in the κ,g plane. The top, middle, and bottom plots show limits for right, left and vectorlike coupling hypotheses respectively.

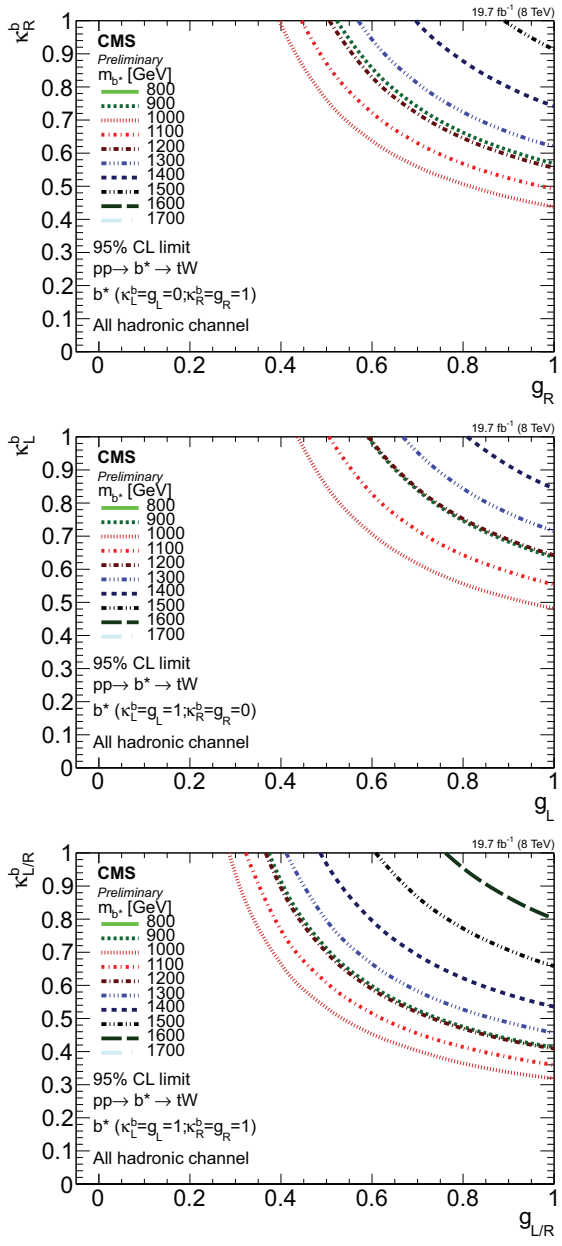

Figure 4.42: expected limit plot in the κ,g plane. The top, middle, and bottom plots show limits for right, left and vectorlike coupling hypotheses respectively.

4.7 Combination

Here we detail the combination of the signal cross section upper limit sensitivity for the semileptonic, all-hadronic, and dileptonic b* decay channels. The specifics for the three searches are detailed in the analysis notes [43–45]. Identical sources of systematic uncertainty are correlated across the channels. The overlap of the signal region events is negligible. There is no overlap between the all-hadronic channel and the other selections. The dileptonic channel and semileptonic have four overlapping events out of 7900 lepton+jets events and 17559 dilepton events. and we set limits using the Bayesian statistical method as implemented by the theta framework to set 95%C.L. upper limits on the b* $\rightarrow$ tW cross-section.

The following systematic uncertainties are correlated across multiple channels (see Section4.5):

- **Jet Energy Scale**
- **Jet Energy Resolution**
- **Luminosity**
- **DiBoson Cross-Section**: The semileptonic and dileptonic channels use the recommended 30% uncertainty on the di-boson cross-section. The all-hadronic channel does not include this background source.
- **Single-top Cross-Section**

- **Z+jets Cross-Section**: The semileptonic and dileptonic channels use the recommended 20% uncertainty on the Z+jets cross-section. The all-hadronic channel does not include this background source.

- $t\bar{t}$ **Cross-Section**: The semileptonic and dileptonic channels use the recommended 5.3% uncertainty on the $t\bar{t}$ cross-section. The all-hadronic channel does not include this uncertainty due to a measurement of the $t\bar{t}$ normalization and uncertainty in the analysis.

Statistical uncertainties are taken into account by using the Barlow-Beeston lite method.

The rate effects of the systematic uncertainties that only affect the semileptonic channel are given in tables 6.1 and 6.2 for the electron and muon channels respectively. The rate effects of the systematic uncertainties that only affect the all-hadronic channel are given in table 6.3. The rate effects of the systematic uncertainties that only affect the dileptonic channel are given in table 6.4. The rate effects of the systematic uncertainties that are correlated over multiple channels are given in table 6.5, 6.6, 6.8, 6.7 for the semileptonic electron, semileptonic muon, all hadronic, and dilepton channels respectively.

The nuisance parameters after the Theta fit can be seen in figure 4.52.

The distributions given to the limit setting macro are shown in figures 4.43, 4.44, and 4.45 for the semileptonic, dileptonic, and all-hadronic channels respectively. The limits for the three channels before combination are shown in figure 4.46, 4.47, and

4.48 for the semileptonic, dileptonic, and all-hadronic channels respectively. The combined limits are shown in Figure 4.49.

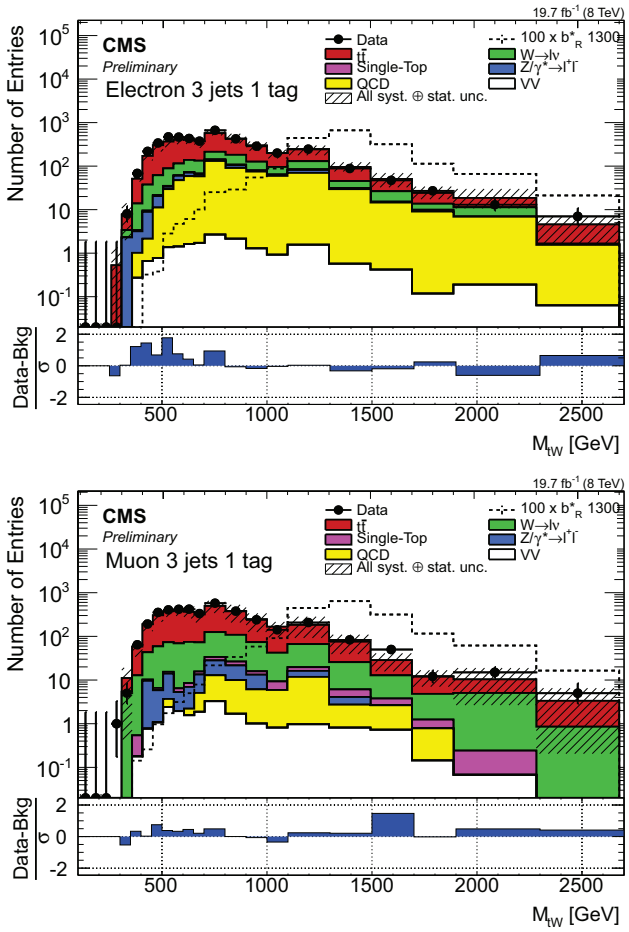

Figure 4.43: The reconstructed b* invariant mass distribution in data, background, and signal. The channel is semileptonic in the electron+jets (top) and muon+jets(bottom).

The cross section upper limits can be generalized due to the fact that the b* cross-section is dependent on the unknown constants κ and g.The limits can be extrapolated to the g,κ plane as can be seen in figures 4.50 and 4.51 for observed and expected limits respectively.

The cross section upper limits for left-handed right-handed and vectorlike b* coupling hypotheses are shown in Tables 4.11 4.10 and 4.12 respectively.

The b* mass exclusion point for each channel is given in table 4.13

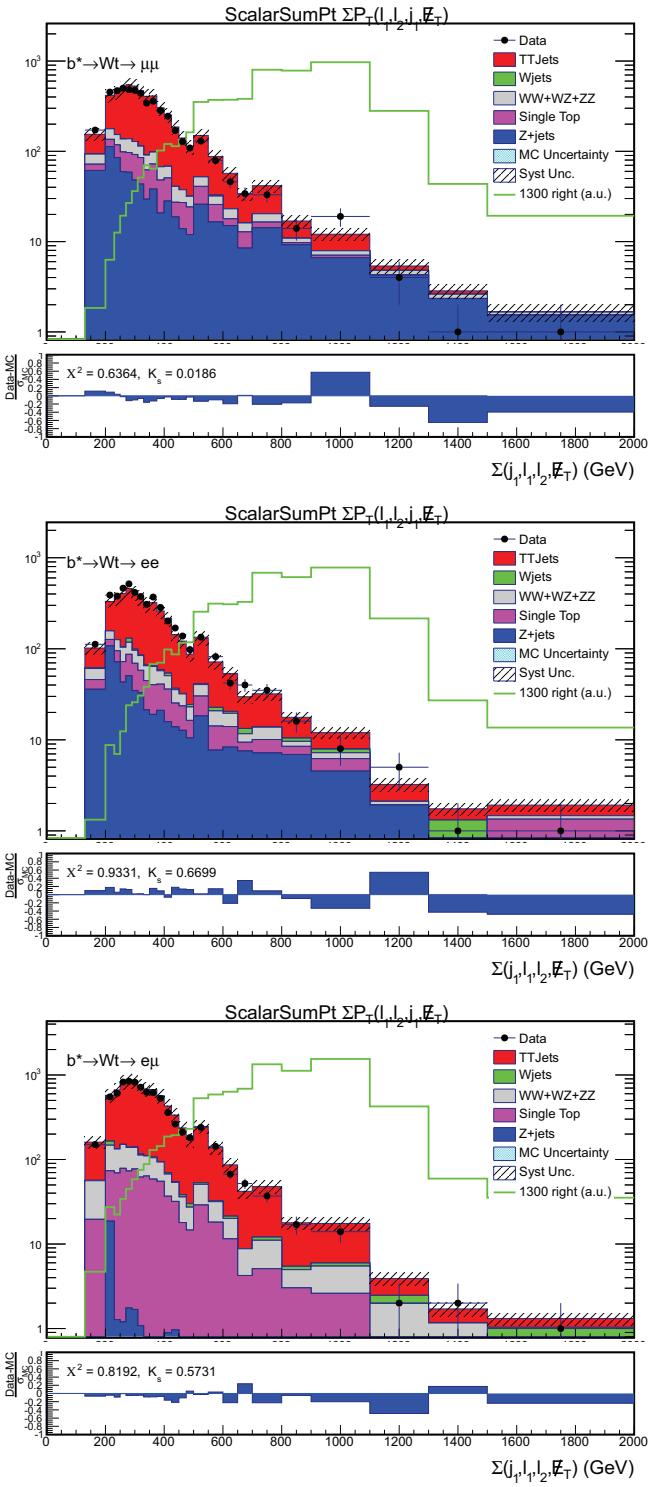

Figure 4.44: The reconstructed scalar p_T sum distribution in data, background, and signal. The channel is dileptonic in the muon+muon (top) electron+electron (middle) and electron+muon (bottom).

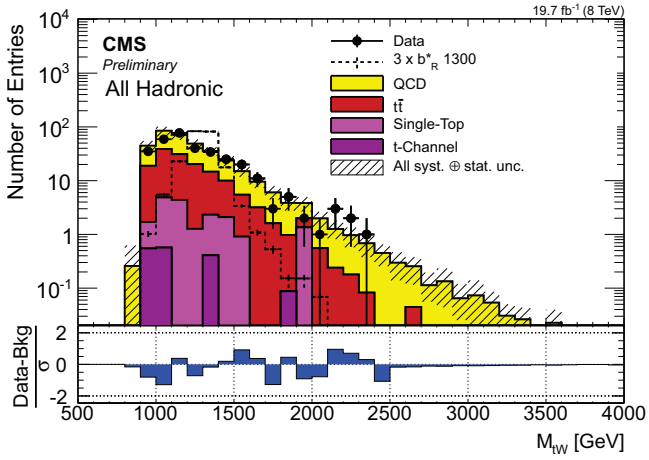

Figure 4.45: The reconstructed b* invariant mass distribution in data, background, and signal. The channel is all-hadronic.

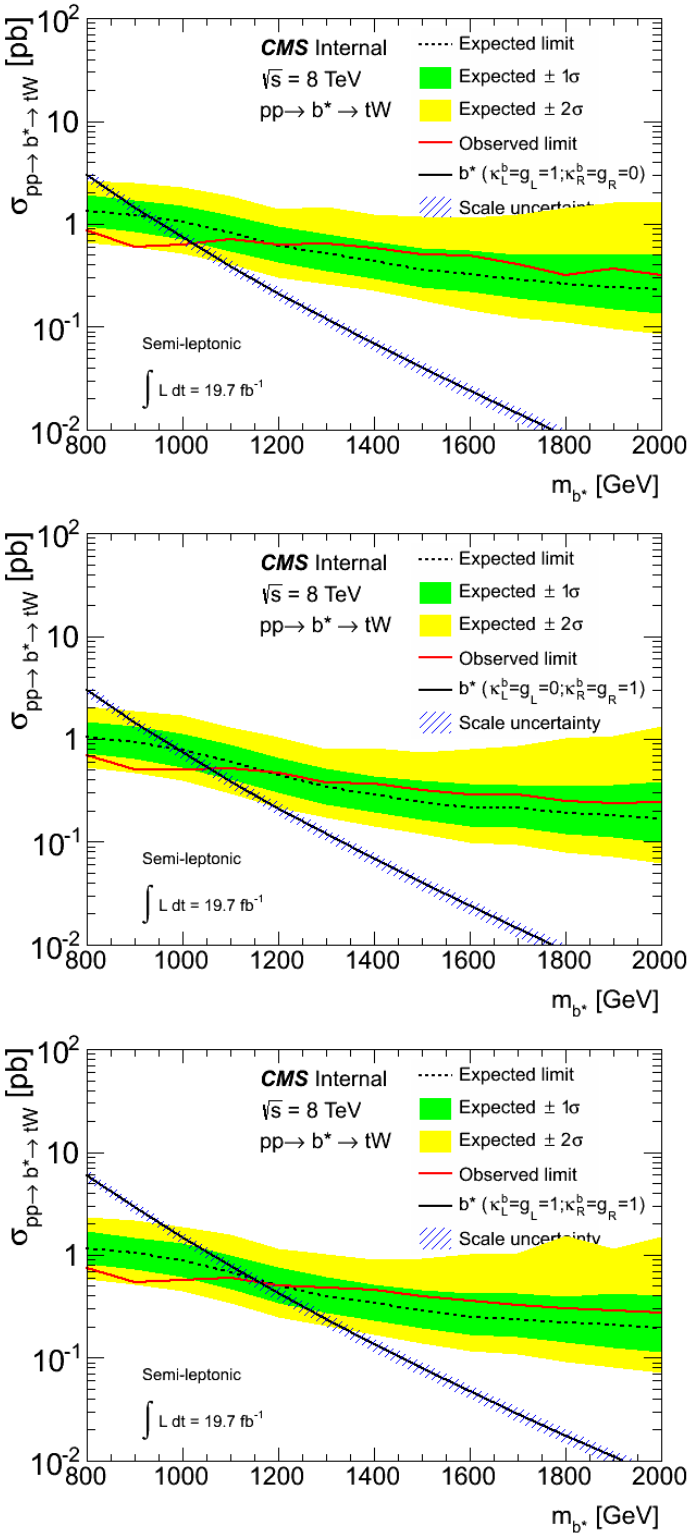

Figure 4.46: limit plot for the left-handed b* (left plot), right handed (middle plot) and vector like (right plot) b^* for lepton+jets channel only. The theory error band including scale uncertainties.

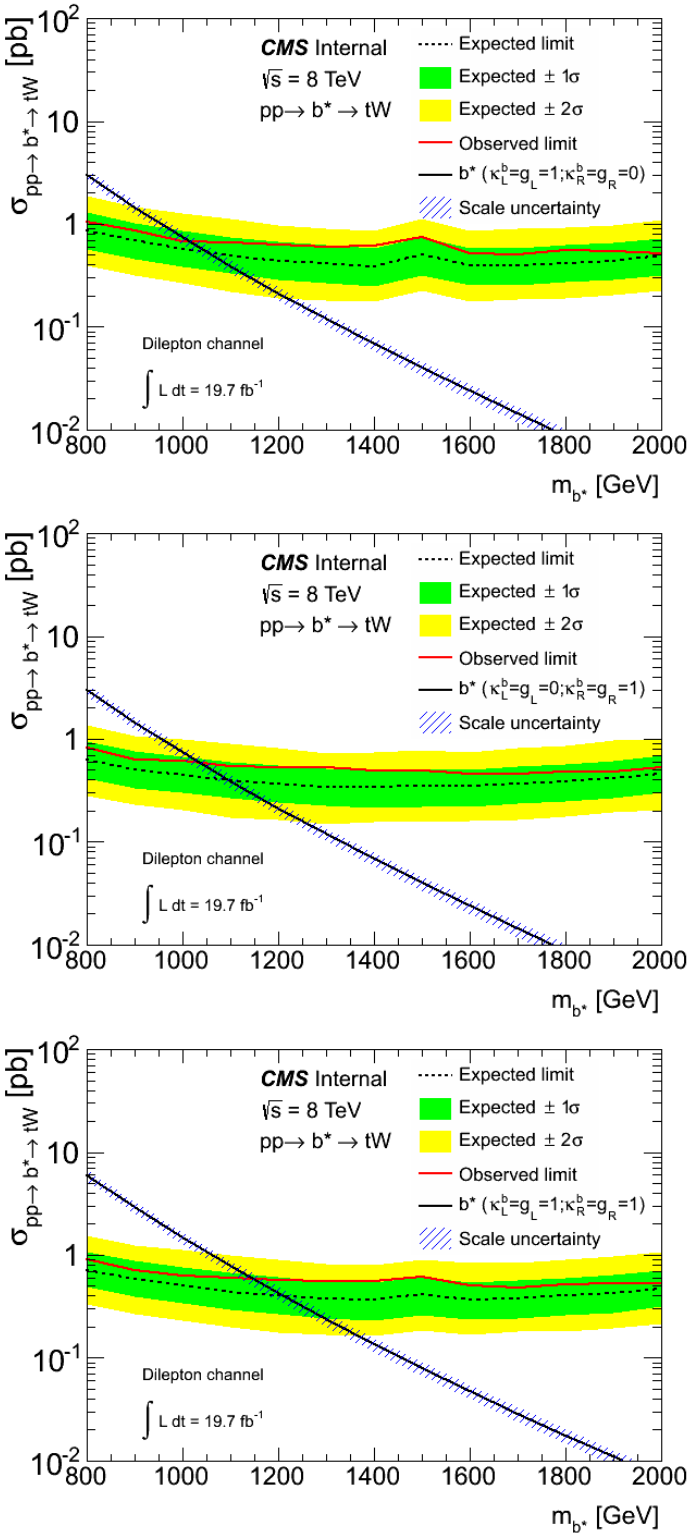

Figure 4.47: limit plot for the left-handed b* (left plot), right handed (middle plot) and vector like (right plot) b^* for dilepton channel only. The theory error band including scale uncertainties.

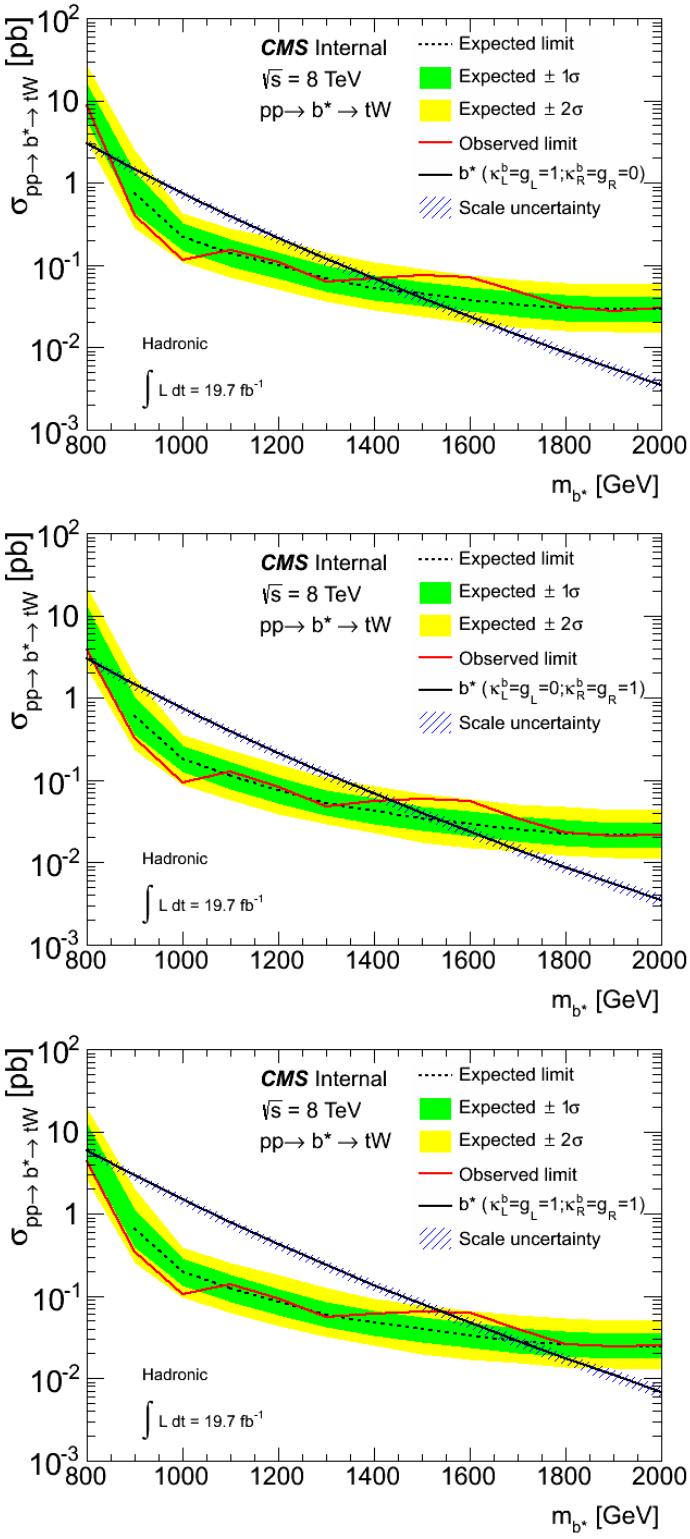

Figure 4.48: limit plot for the left-handed b* (left plot), right handed (middle plot) and vector like (right plot) b^* for full hadronic channel only. The theory error band including scale uncertainties.

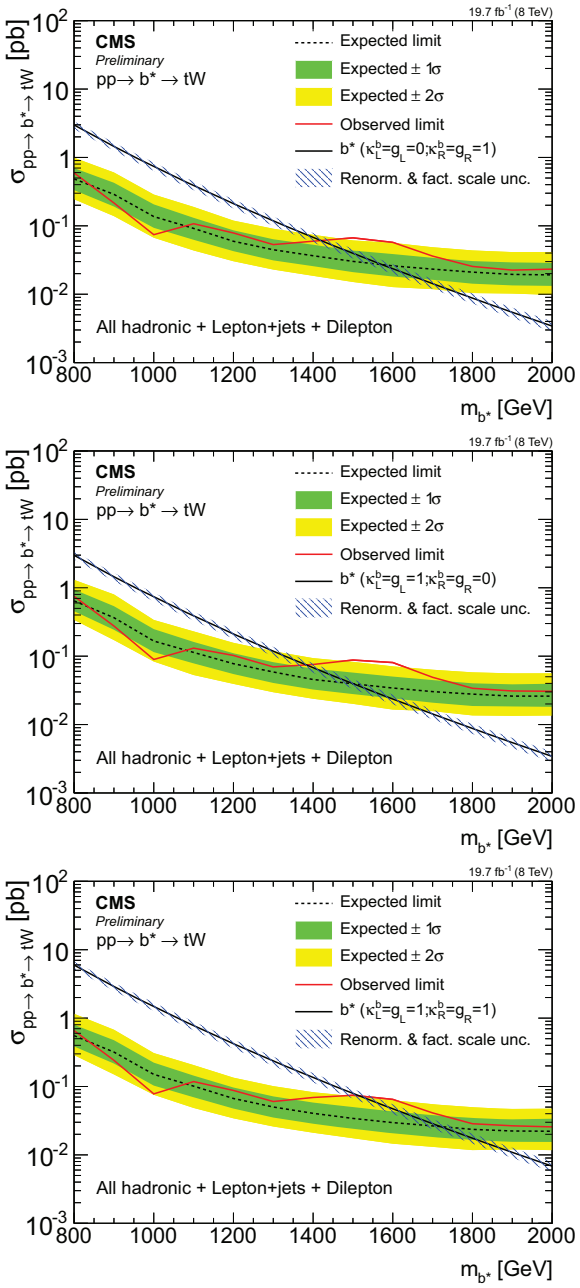

Figure 4.49: The b* quark 95% C.L. production cross-section limits. The expected (black) and observed (red) limits as well as b* quark theoretical cross-section (blue) are plotted for comparison. The uncertainty in the expected limit band is shown in light ($\pm 1\sigma$) and dark grey ($\pm 2\sigma$). These limits were extracted using the Theta limit setting framework. Here, the signal hypotheses of a right-handed, left-handed, and vector-like b* quark are shown on the top, middle, and bottom plots respectively.

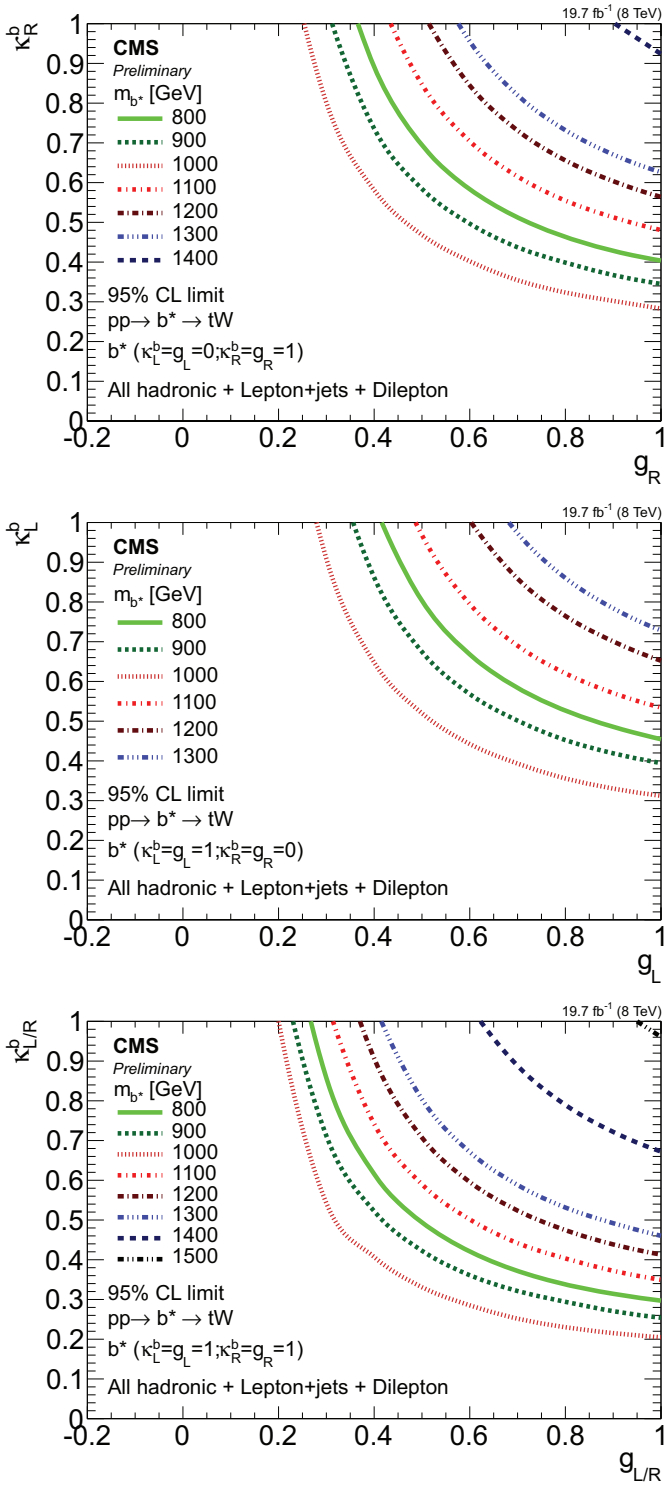

Figure 4.50: observed limit plot in the κ,g plane. The top, middle, and bottom plots show limits for right, left and vector-like coupling hypotheses respectively.

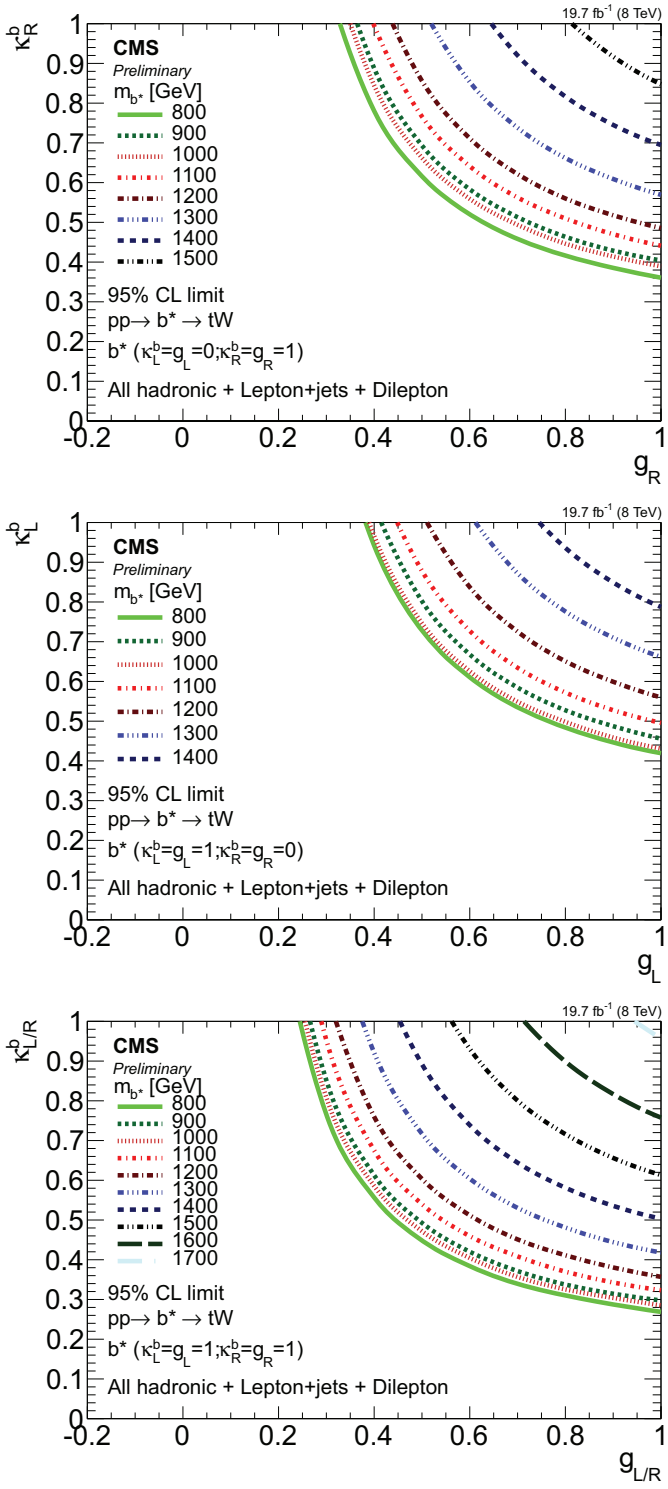

Figure 4.51: expected limit plot in the κ,g plane. The top, middle, and bottom plots show limits for right, left and vector-like coupling hypotheses respectively.

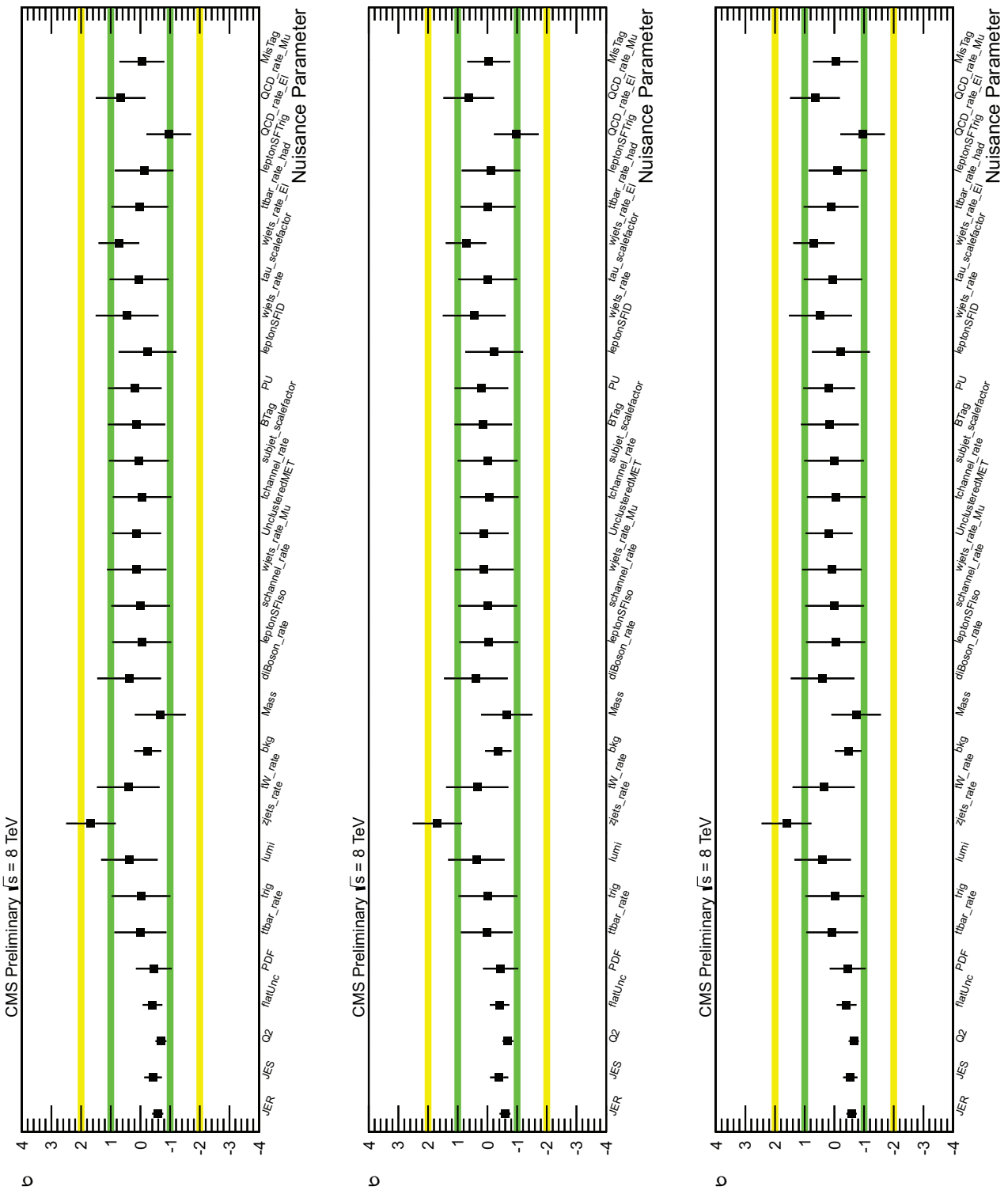

Figure 4.52: Nuisance parameters after the Theta fit. The Signal mass points here are 1200, 1400, and 1600 GeV for the top, middle, and bottom plots respectively.

b^*_R Cross-Section Upper Limits

M_{b^*}	**observed**	**expected**	**expected 1σ**	**expected 2σ**
800	**0.490**	**0.492**	**0.335,0.723**	**0.243,1.039**
900	**0.188**	**0.303**	**0.202,0.446**	**0.140,0.611**
1000	**0.070**	**0.141**	**0.097,0.203**	**0.070,0.279**
1100	**0.103**	**0.096**	**0.068,0.138**	**0.050,0.186**
1200	**0.074**	**0.063**	**0.044,0.092**	**0.032,0.129**
1300	**0.052**	**0.045**	**0.032,0.067**	**0.023,0.098**
1400	**0.063**	**0.038**	**0.027,0.053**	**0.020,0.076**
1500	**0.067**	**0.030**	**0.021,0.043**	**0.015,0.061**
1600	**0.056**	**0.025**	**0.018,0.037**	**0.012,0.052**
1700	**0.037**	**0.023**	**0.016,0.034**	**0.011,0.049**
1800	**0.023**	**0.021**	**0.014,0.030**	**0.010,0.044**
1900	**0.021**	**0.020**	**0.014,0.030**	**0.010,0.042**
2000	**0.021**	**0.020**	**0.013,0.030**	**0.010,0.043**

Table 4.10: b^*_R cross-section upper limits for given b^*_R mass values. Cross-section is in units of pb.

b^*_L **Cross-Section Upper Limits**				
M_{b^*}	**observed**	**expected**	**expected 1σ**	**expected 2σ**
800	**0.617**	**0.666**	**0.454,0.984**	**0.344,1.366**
900	**0.236**	**0.387**	**0.258,0.571**	**0.172,0.782**
1000	**0.086**	**0.173**	**0.119,0.251**	**0.087,0.337**
1100	**0.123**	**0.119**	**0.085,0.174**	**0.063,0.236**
1200	**0.097**	**0.083**	**0.057,0.120**	**0.042,0.173**
1300	**0.068**	**0.059**	**0.042,0.088**	**0.030,0.127**
1400	**0.074**	**0.048**	**0.033,0.067**	**0.025,0.096**
1500	**0.088**	**0.040**	**0.028,0.057**	**0.020,0.082**
1600	**0.077**	**0.034**	**0.023,0.049**	**0.016,0.068**
1700	**0.049**	**0.030**	**0.021,0.044**	**0.014,0.062**
1800	**0.032**	**0.028**	**0.019,0.040**	**0.013,0.059**
1900	**0.031**	**0.027**	**0.018,0.039**	**0.013,0.057**
2000	**0.032**	**0.027**	**0.018,0.040**	**0.014,0.060**

Table 4.11: b^*_L cross-section upper limits for given b^*_L mass values. Cross-section is in units of pb.

b^*_{LR} **Cross-Section Upper Limits**				
M_{b^*}	**observed**	**expected**	**expected 1σ**	**expected 2σ**
800	**0.510**	**0.570**	**0.384,0.840**	**0.285,1.137**
900	**0.208**	**0.337**	**0.226,0.496**	**0.157,0.686**
1000	**0.080**	**0.156**	**0.107,0.220**	**0.079,0.313**
1100	**0.112**	**0.107**	**0.074,0.152**	**0.057,0.210**
1200	**0.084**	**0.072**	**0.050,0.104**	**0.035,0.146**
1300	**0.058**	**0.051**	**0.036,0.076**	**0.026,0.108**
1400	**0.064**	**0.042**	**0.030,0.059**	**0.022,0.085**
1500	**0.074**	**0.034**	**0.024,0.050**	**0.018,0.072**
1600	**0.067**	**0.029**	**0.020,0.042**	**0.014,0.060**
1700	**0.041**	**0.026**	**0.018,0.038**	**0.013,0.054**
1800	**0.027**	**0.024**	**0.016,0.035**	**0.011,0.050**
1900	**0.025**	**0.023**	**0.016,0.033**	**0.011,0.050**
2000	**0.024**	**0.023**	**0.015,0.033**	**0.012,0.050**

Table 4.12: $b^*_L R$ cross-section upper limits for given b^*_{LR} mass values. Cross-section is in units of pb.

	left-handed	right-handed	vector like
Lepton + jets, dilepton and full hadronic channel combined			
expected 95% CL limit [GeV]	1500	1580	1730
observed 95% CL limit [GeV]	1390	1420	1520
Full hadronic channel only			
expected 95% CL limit [GeV]	890 - 1480	880 - 1550	820 - 1700
observed 95% CL limit [GeV]	880 - 1390	820 - 1430	1530
Lepton + jets channel only			
expected 95% CL limit [GeV]	940	990	1130
observed 95% CL limit [GeV]	1030	1070	1170
Dilepton channel only			
expected 95% CL limit [GeV]	1060	1100	1210
observed 95% CL limit [GeV]	1020	1050	1160

Table 4.13: 95% CLs limit for the left-, right-handed and vector like excited bottom quark in the full hadronic, lepton+jets and dilepton channel combined and separately at the benchmark point of unit couplings.

Chapter 5

Summary

5.1 Summary of the W' Search

We have performed a search for new physics in the boosted $\mathrm{t\bar{b}}$ all hadronic final state. The main feature of this topology is a top quark whose decay products merge into a single jet.

We take advantage of additional information provided by the top jet substructure to increase the sensitivity of the analysis. The main background for the search is QCD multijet production, and is predicted by using the average rate of b-tagging derived from the jet substructure sideband region. The other main source of background (SM $\mathrm{t\bar{t}}$ production) is taken from the MC simulation and corrected by a data-driven scale factor.

Using 19.7 fb^{-1} of integrated luminosity collected in 2012 by the LHC, we exclude

a right-handed W′ particle with invariant mass below 2.02 TeV. Additionally, we exclude the left-handed and mixed-coupling W′ particles at 1.94 TeV and 2.14 TeV respectively.

The combined semileptonic and fully-hadronic channels increase the sensitivity of the cross-section limit. Using the combined sensitivity of the two channels, we exclude a right-handed W′ particle with invariant mass below 2.15 TeV

5.2 Summary of the b* Search

We have performed a search for new physics in the boosted tW all hadronic final state. The main feature of a typical event is a boosted top quark and W boson whose decay products merge into single jets resulting in a dijet topology.

We take advantage of additional information provided by the substructure of these merged jets to increase the sensitivity of the analysis. The main background for the search is QCD multijet production, and is predicted by using the average top-mistagging rate derived from the jet substructure sideband region. The other main source of background (SM $t\bar{t}$ production) is taken from the MC simulation and corrected by a data-driven scale factor.

Using 19.7 fb^{-1} of integrated luminosity collected in 2012 by the LHC, the production of a right-handed b* with mass between 0.82 TeV and 1.43 TeV, left-handed b* with mass between 0.88 TeV and 1.39 TeV, and vectorlike b* with mass between

0.8 TeV and 1.53 TeV is excluded at the 95% confidence level.

The combined semileptonic, dileptonic, and fully-hadronic channels increase the sensitivity of the cross-section limit. Using the combined sensitivity of the two channels, we exclude a right-handed b^* particle with invariant mass below 1.42 TeV, a left-handed b^* with invariant mass below 1.39 TeV, and a vectorlike b^* with invariant mass below 1.52 TeV.

Chapter 6

Appendix

6.1 W' Search

6.1.1 CA8 b-tagging

CA8 jet b-tagging comparison to AK5 jets. A 2% uncertainty is applied to signal MC samples in the analysis. Jets are matched between AK5 and CA8 within a Delta(R) size of 0.3. Jets are ensured b flavor from MC truth and are within the pt range of the analysis. The constant fit to the efficiency ratio gives an upper limit to the uncertainty for the change in SF_b for use with CA8 jets. No extra correction is applied to SF_b. The following plots are from Signal MC at $2700/GeV$.

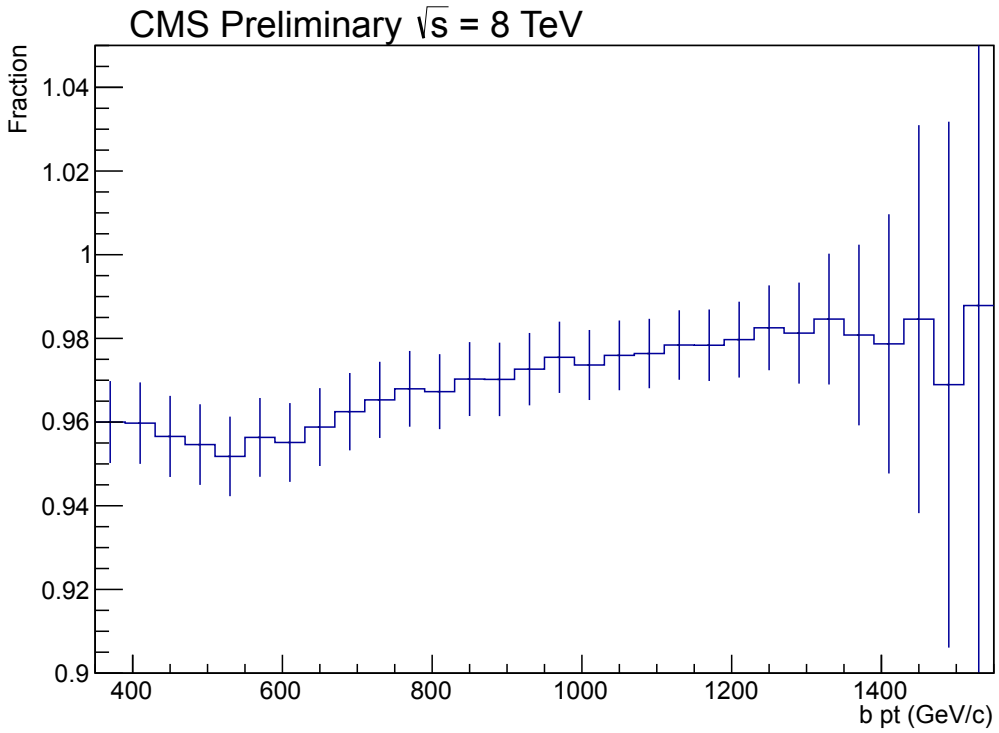

Figure 6.1: Percent of matched jets that register the same value for the CSVM cut.

6.1.2 Signal Region and Sideband Kinematic Comparison

Figure 6.3 shows a comparison in QCD MC of kinematic variables of interest in the CMS top tagger selection and number of subjets sideband used for the determination of the average b-tagging rate. There are some discrepancies seen in the two regions, which is the main reason why we use the average b-tagging rate instead of the sideband itself. Variables constrained to the top candidate jet such as top mass have a drastically different shape, so we need to look at the b candidate jet in the op-

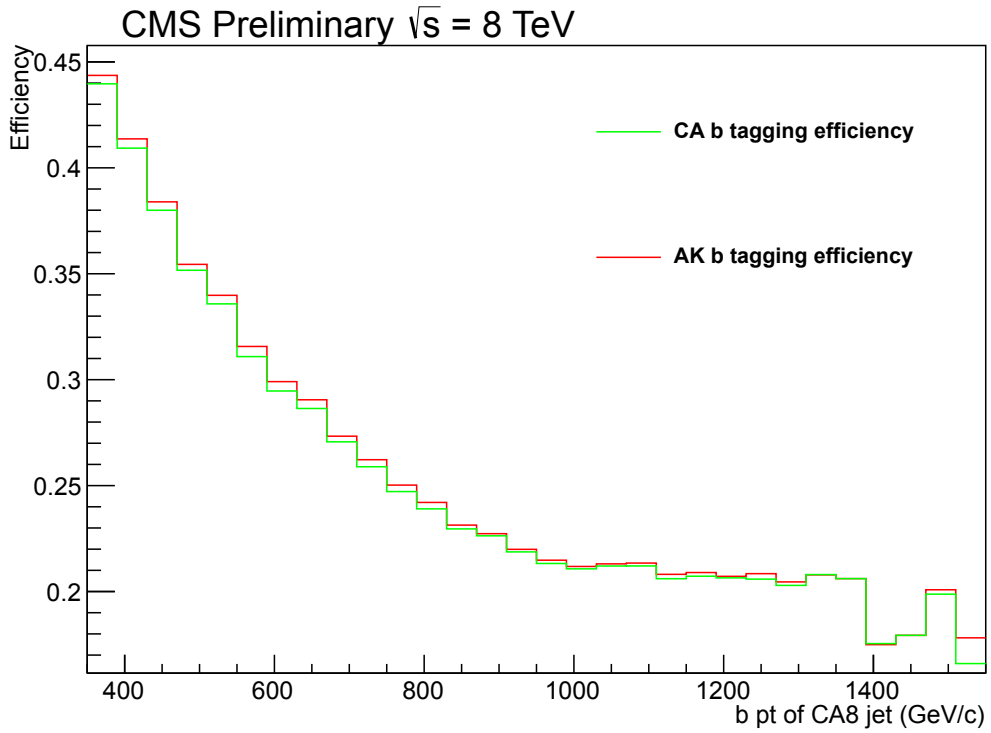

Figure 6.2: Comparison of the efficiency of b-tagging matched CA8 and AK5 jets

posite hemisphere to keep the background estimate unbiased. Additionally, because we parameterize in p_T the influence from the different b candidate p_T shapes does not bias the background estimate. Then the final kinematic variable of interest is b candidate mass which shows good agreement.

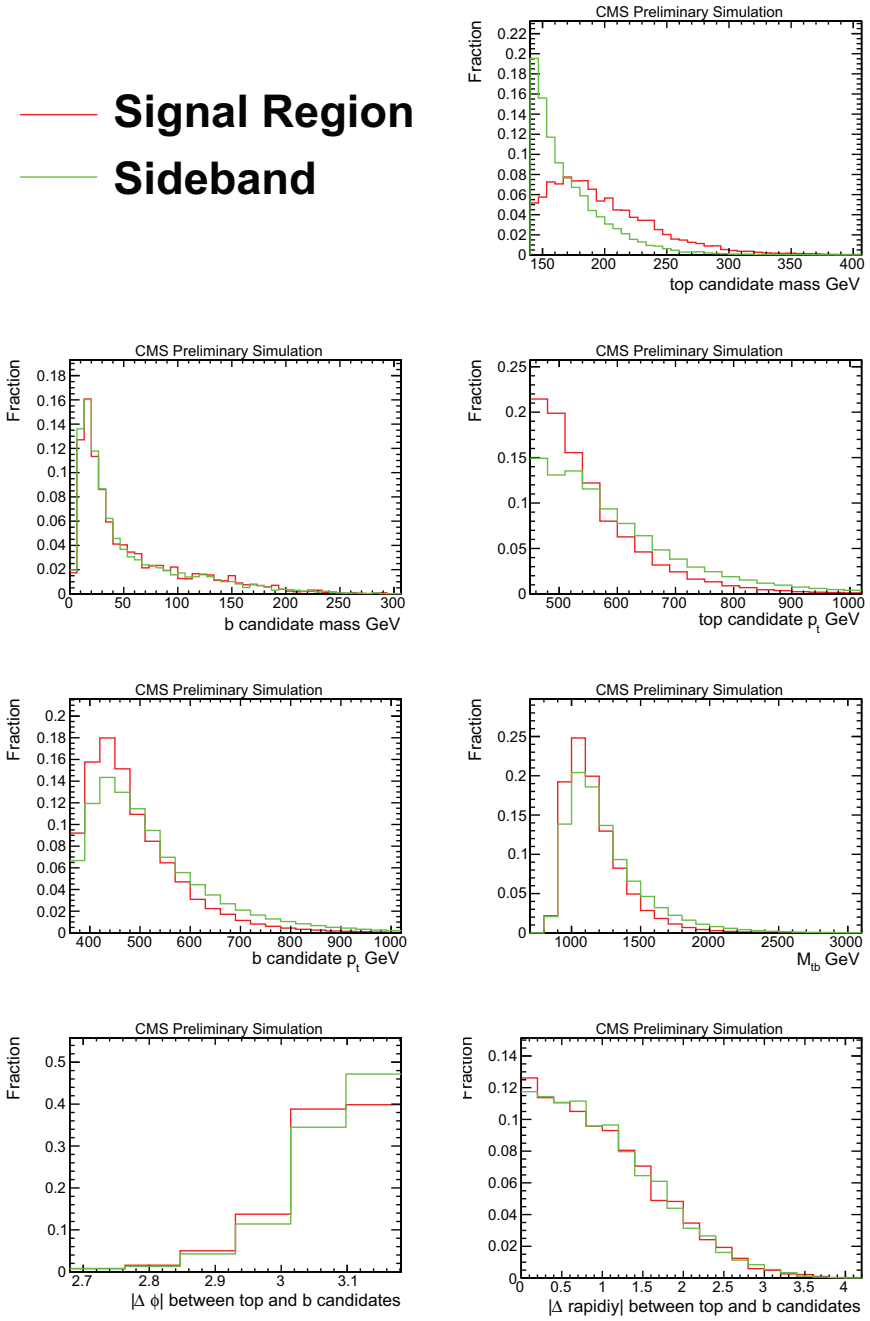

Figure 6.3: Comparison of kinematic variables in QCD MC extracted from the CMS top tagger signal region and number of subjets sideband

6.1.3 QCD Parameterization Uncertainty

The QCD background prediction relies on the probability to tag a b jet. We parameterize this probability using physical variables that have a large effect on the b-tagging rate (p_T and η of the b candidate jet). However, the variable of interest in the analysis is M_{tb}, and the background estimate involves integrating, for every bin in M_{tb}, along the p_T axis. To see this more explicitly, let us consider the signal region only, with pre-b-tag data divided into a two-dimensional matrix along p_T and M_{tb} axes, indexed by indices i and j respectively. Thus n_{ij} is the number of pre-b-tag events within a given p_T bin (index i) and a given M_{tb} bin (index j), $\overline{P}_i$ is the average of true b-tagging probability for a slice in p_T, whereas P_{ij} is the true b-tagging probability for data in n_{ij}.

The true number of b tags in two-dimensional bin (i, j) is then $n_{ij}P_{ij}$. The observed number of events in M_{tb} bin j is $N_j = \sum_i n_{ij}P_{ij}$. However, the background estimate uses the average b-tagging probability, $\overline{P}_i$, averaged over all values of j – that is, over all values of M_{tb}.[1] So a 'perfect' background estimate (using probabilities from the signal region) therefore yields $N_j^{\text{bkg.est.}} = \sum_i n_{ij}\overline{P}_i$.

Our procedure for the estimation of the QCD background *assumes* that P_{ij} is independent of M_{tb} – in other words, that $P_{ij} = \overline{P}_i$. If that is the case, the bias of

[1] In the real measurement we furthermore obtain this number from the sideband, but to elucidate the point it is sufficient to consider the average of true b-tagging probabilities, P_{ij}, from the signal region.

the background estimate

$$\delta N_j = N_j - N_j^{\text{bkg.est.}} = \sum_i n_{ij}(P_{ij} - \overline{P}_i) \tag{6.1}$$

is indeed zero.

If for some reason $P_{ij} \neq \overline{P}_i$, Eq.(6.1), depending on the values of n_{ij}, could result in non-zero bias δN_j – even when the used average tagging probability corresponds to the signal region itself.

Luckily, the assumption that the average b-tagging probability depends only on the jet itself (with $\mathrm{p_T}$ and η of the b jet) is a very good one. However, it is conceivable that second- or third-order effects could create small deviations in $P_{ij} - \overline{P}_i$ and thus result in a small bias. These effects could be caused by other activity in the event, which could be a reason that the same values of $\mathrm{p_T}$ and η could correspond to events with different $\mathrm{p_T}$ of the top jet, and thus M_{tb}. To see that such effects exist (and also that they are small), it is sufficient to consider the top $\mathrm{p_T}$ in Figure 3.24, where there seems to be a small but systematic bias of the background estimate, as evidenced by the pull distribution in the lower pane. We have not studied the causes of these effects, but additional activity in the event (from other jets or pile-up) could contribute additional pixel and strip hits inside the volume of the b jet, and thus impact the average tagging rate at a low level.

To investigate the ability of the b-tagging rate parameterization in $\mathrm{p_T}$ and η to

predict M_{tb}, we incorporate M_{tb} into the b-tagging rate parameterization, The effect is first checked in the second sideband described above. The three-dimensional b-tagging rate shown in Figure 3.42 is compared to the two dimensional tagging rate shown in 3.18 to see if this effect can be the cause of the deviations observed in the low M_{tb} region. Figure 6.4 shows the differences in the three and two dimensional background estimates as well as the differences in the full selection of this control region and the background estimate. From this we conclude that there is an effect and the shape of the deviations is well approximated with this method.

6.1.4 Signal Contamination Studies

The following studies investigate signal contamination within our analysis. These plots use the same color scheme seen in Figure 6.5. The signal contamination within the sideband used for extraction of the average b-tagging rate can be seen in Figure 6.6 (this is signal injected into the post b tagged plots in Figure 3.17). The signal contamination for the signal region can be seen in Figure 6.7.

There is also some signal contamination within the sideband cross checks described in Section 3.3.4. The signal contamination within Figure 3.19 can be seen in Figure 6.8, and the contamination in Figure 3.20 can be seen in Figure 6.9.

6.2 b^* Search

Figure 6.10 shows a comparison of the top-mistagging rate extracted from the W-tagging sideband described in Section 3.3.2 and the top-mistagging rate extracted from the signal region. This plot is taken from QCD MC.

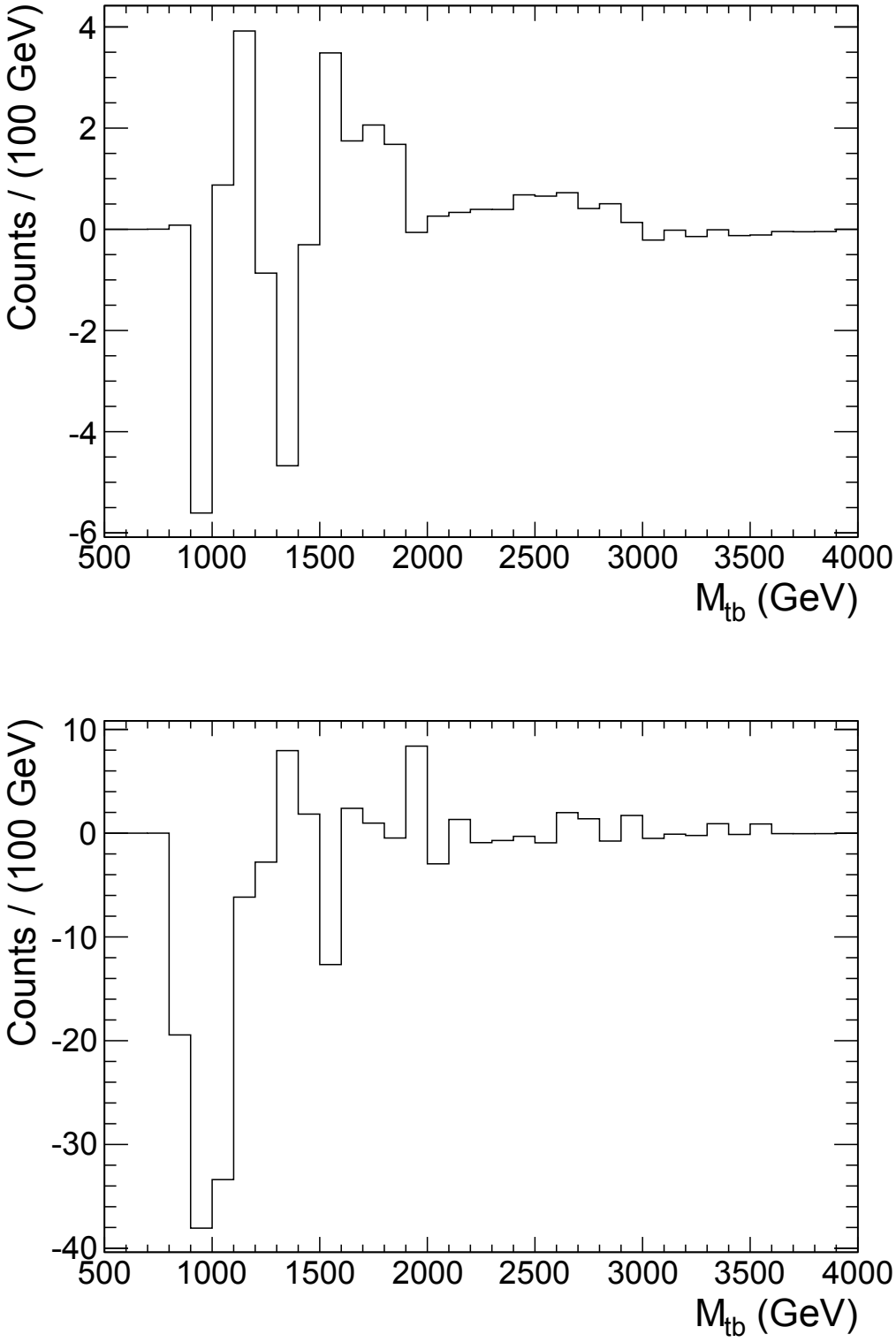

Figure 6.4: (a) Difference of the background estimation from three dimensional and two dimensional tagging rates (b) Difference of the background estimation from second sideband selection and two dimensional tagging rates

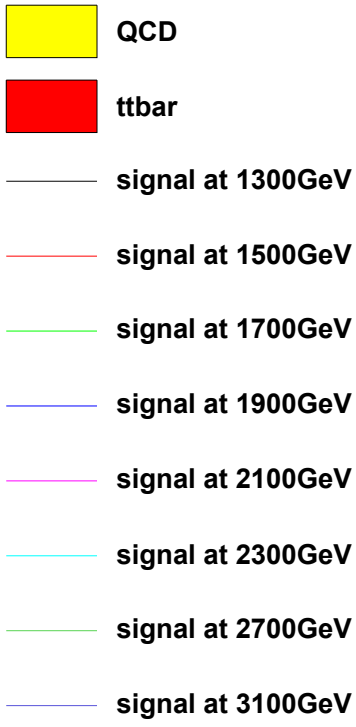

Figure 6.5: Legend for the following studies

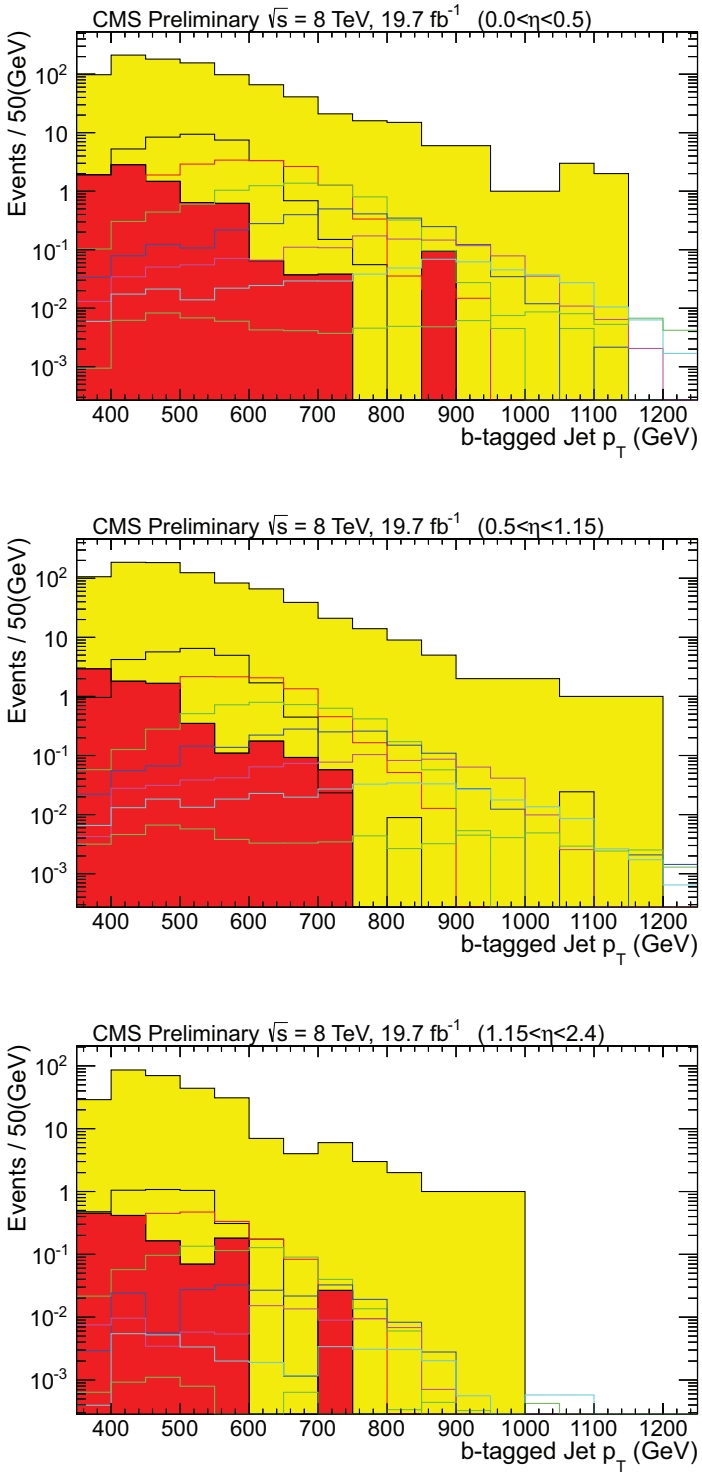

Figure 6.6: Signal contamination in the post b tagged sideband used to extract the average b-tagging rate (a) Low η region (b) Transition η region (c) High η region

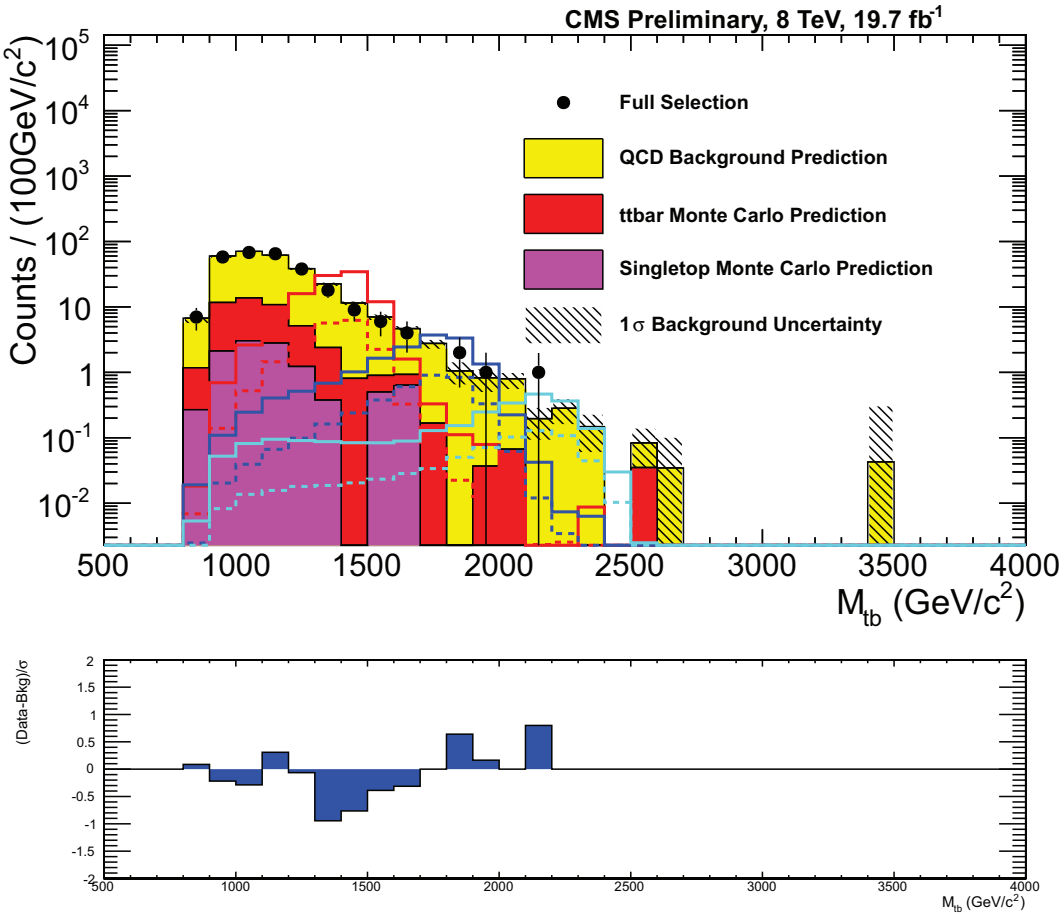

Figure 6.7: Signal contamination for the full selection. The solid lines are the signal that passes the full selection. The dashed lines are the signal that falls through the background estimate.

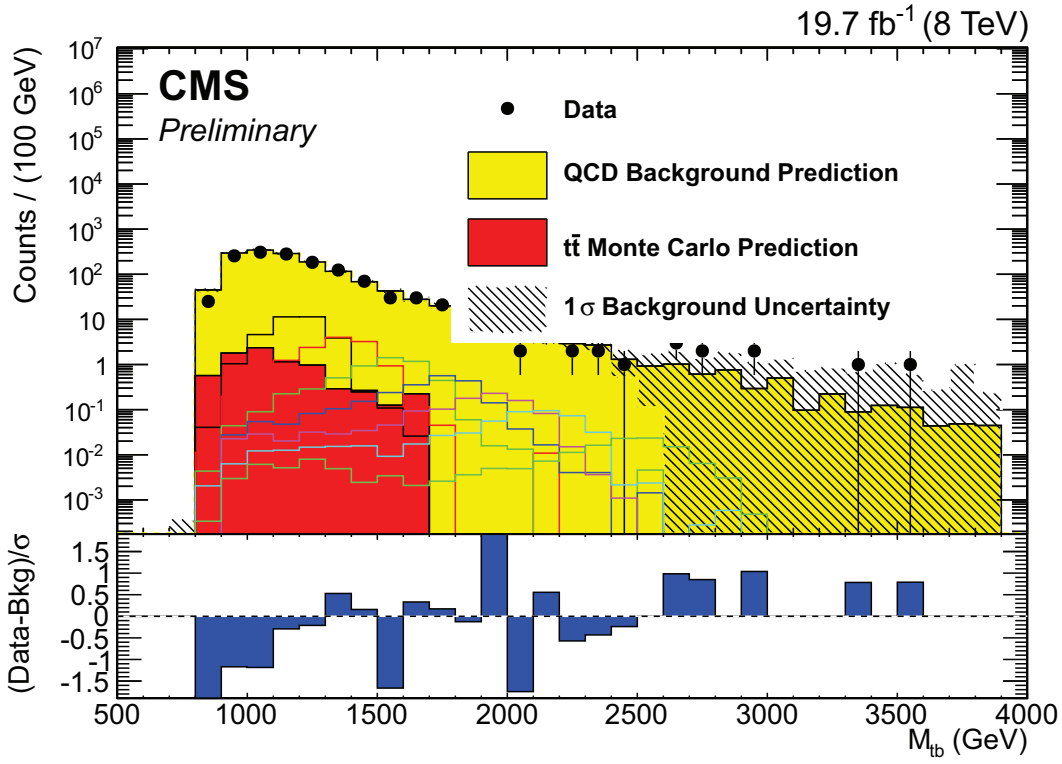

Figure 6.8: Signal contamination in sideband

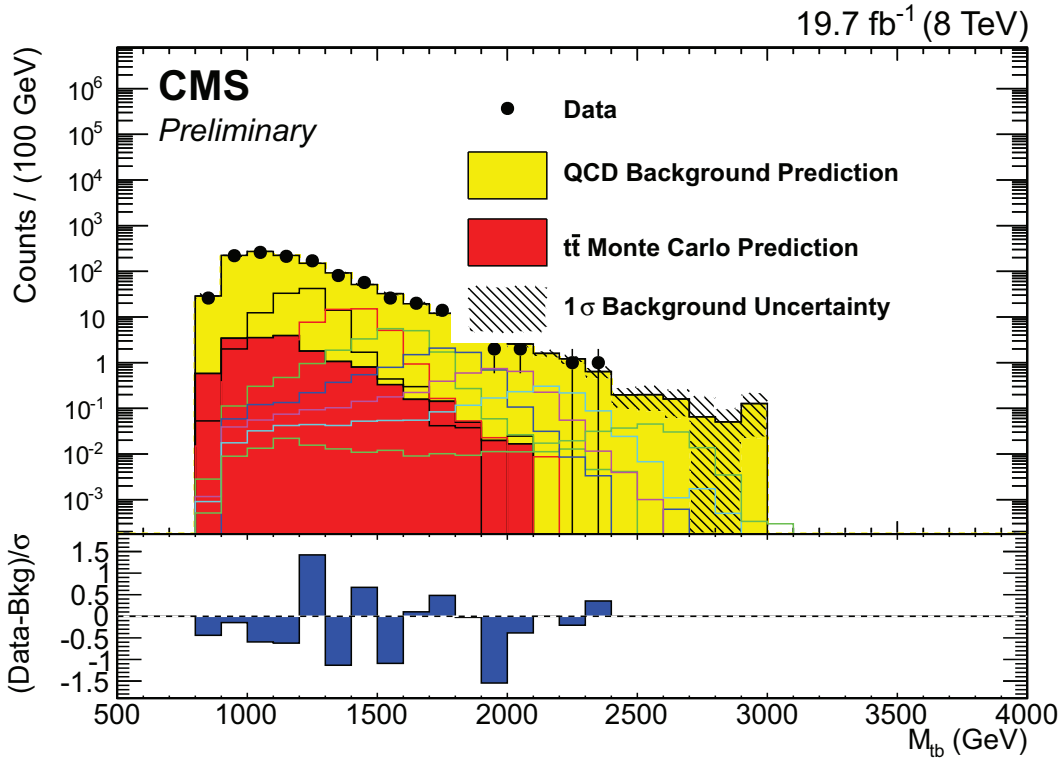

Figure 6.9: Signal contamination in sideband

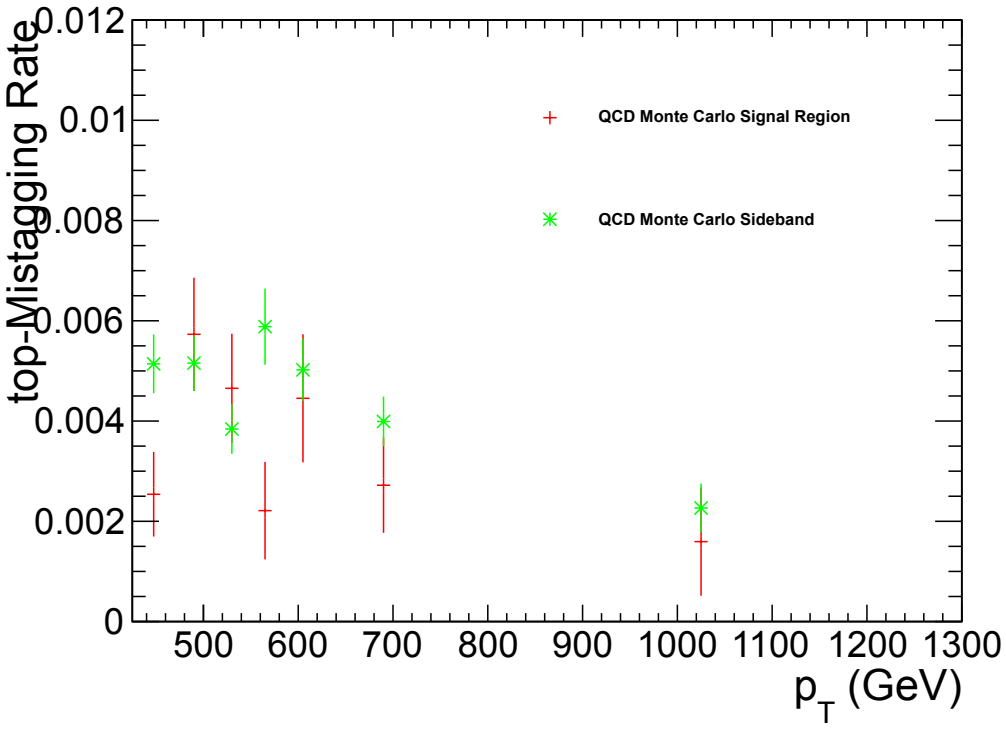

Figure 6.10: A QCD MC comparison of the top-mistagging rate extracted from the W-tagging sideband and the top-mistagging rate extracted from the signal region. The QCD MC quickly runs out of statistics when full top-tagging is applied.

Rate Effects of Systematic Uncertainties

Sample	B-tagging	Mass	Mistag	PDF	Pileup	QCD Rate el	QCD Rate mu	MET	Lepton ID	Isolation	Trigger	W+Jets Rate el	W+Jets Rate mu
WJets	+4.09,-4.14	—	+14.42,+9.44	+41.28,+27.02	-0.36,+0.30	—	—	-0.00,-0.00	+0.26,-0.26	+0.00,+0.00	+0.40,-0.36	+45.00,-31.03	—
ZJets	+3.37,-3.41	—	+8.95,+5.88	+8.53,-7.33	+0.99,+0.20	—	—	+0.00,-0.00	+0.32,-0.29	+0.00,+0.00	+0.54,-0.46	—	—
$M_{Pr=100}$	+2.89,-2.99	—	+0.17,+0.11	+21.15,-17.64	-0.15,+0.14	—	—	+0.00,-0.00	+0.17,-0.17	+0.00,+0.00	+0.26,-0.25	—	—
$M_{Pr=120}$	+2.87,-2.99	—	+0.21,+0.14	+24.18,-19.44	+0.10,-0.12	—	—	-0.00,+0.00	+0.18,-0.18	+0.00,+0.00	+0.27,-0.26	—	—
$M_{Pr=130}$	+2.83,-2.96	—	+0.22,+0.15	+26.63,-21.11	+0.17,-0.19	—	—	-0.00,+0.00	+0.17,-0.17	+0.00,+0.00	+0.26,-0.25	—	—
$M_{Pr=130}$	+2.83,-2.97	—	+0.22,+0.14	+29.94,-22.86	-0.23,+0.30	—	—	-0.00,+0.00	+0.17,-0.17	+0.00,+0.00	+0.26,-0.25	—	—
$M_{Pr=140}$	+2.93,-3.08	—	+0.30,+0.20	+33.63,-24.48	+0.07,-0.08	—	—	+0.00,+0.00	+0.18,-0.18	+0.00,+0.00	+0.27,-0.26	—	—
$M_{Pr=150}$	+2.91,-3.07	—	+0.21,+0.14	+37.67,-26.30	-0.44,+0.33	—	—	-0.00,+0.00	+0.18,-0.18	+0.00,+0.00	+0.27,-0.25	—	—
$M_{Pr=160}$	+2.87,-3.03	—	+0.19,+0.13	+41.53,-27.87	+0.19,-0.02	—	—	-0.00,+0.00	+0.18,-0.18	+0.00,+0.00	+0.27,-0.26	—	—
$M_{Pr=170}$	+2.87,-3.02	—	+0.13,+0.08	+43.74,-29.28	+0.30,-0.23	—	—	+0.00,+0.00	+0.19,-0.18	+0.00,+0.00	+0.28,-0.27	—	—
$M_{Pr=180}$	+2.90,-3.04	—	+0.22,+0.14	+49.25,-31.36	+0.11,-0.16	—	—	-0.00,+0.05	+0.18,-0.18	+0.00,+0.00	+0.28,-0.26	—	—
$M_{Pr=190}$	+2.80,-2.93	—	+0.33,+0.21	+54.09,-32.74	-0.20,+0.17	—	—	+0.00,-0.00	+0.19,-0.18	+0.00,+0.00	+0.28,-0.26	—	—
$M_{Pr=200}$	+2.76,-2.88	—	+0.25,+0.16	+59.05,-34.53	-0.30,+0.14	—	—	+0.00,-0.00	+0.18,-0.18	+0.00,+0.00	+0.27,-0.26	—	—
$M_{Pr=800}$	+2.97,-3.03	—	+0.18,+0.11	+16.35,-14.20	-0.47,+0.38	—	—	-0.00,+0.00	+0.17,-0.17	+0.00,+0.00	+0.27,-0.25	—	—
$M_{Pr=90}$	+2.91,-2.99	—	+0.17,+0.11	+18.45,-15.83	+0.13,-0.05	—	—	-0.00,-0.00	+0.17,-0.17	+0.00,+0.00	+0.27,-0.25	—	—
diBoson	+3.27,-3.36	—	+6.52,+4.28	+4.78,-6.43	-1.05,+1.11	—	—	-0.00,-0.00	+0.24,-0.23	+0.00,+0.00	+0.37,-0.33	—	—
qcd	—	—	—	—	—	+27.00,-21.26	—	—	—	—	—	—	—
sts	+0.80,-1.07	—	-0.10,-0.07	+5.50,-5.51	-0.18,+0.22	—	—	+0.00,+0.00	+0.22,-0.21	+0.00,+0.00	+0.32,-0.29	—	—
stt	+1.32,-1.50	+1.86,-1.87	-0.05,-0.03	+7.39,-5.29	+0.51,-0.53	—	—	-0.00,-0.00	+0.17,-0.17	+0.00,+0.00	+0.26,-0.25	—	—
sttW	+2.56,-2.64	-0.72,-3.66	+0.27,+0.18	+13.56,-10.30	-0.27,+0.30	—	—	+0.00,-0.00	+0.19,-0.18	+0.00,+0.00	+0.29,-0.27	—	—
ttbar	+2.00,-2.12	+0.48,-0.24	+0.18,+0.12	+10.09,-7.81	+0.18,-0.17	—	—	+0.00,+0.00	+0.20,-0.19	+0.00,+0.00	+0.30,-0.28	—	—

Table 6.1: Rate effects of systematic uncertainties used in limit combination. The uncertainty sources listed here affect the semileptonic analysis and are not correlated with uncertainties in the other channels. This table details the semileptonic electron channel. This table considers the right-handed signal hypothesis.

Rate Effects of Systematic Uncertainties

Sample	B-tagging	Mass	Mistag	PDF	Pileup	QCD Rate el	QCD Rate mu	MET	Lepton ID	Isolation	Trigger	W+Jets Rate el	W+Jets Rate mu
WJets	+4.30,-4.34	—	+15.71,+10.24	-4.45,-14.57	-0.34,+0.13	—	—	-0.00,+0.00	+1.88,-1.88	+0.23,-0.28	+1.45,-1.51	—	+30.00,-23.08
ZJets	+3.34,-3.38	—	+5.94,+3.88	+7.50,-7.66	-0.02,+0.35	—	—	+0.00,+0.00	+1.92,-1.91	+0.23,-0.28	+1.51,-1.57	—	—
$M_{Y=100}$	+2.95,-3.05	—	+0.19,+0.12	+21.46,-17.73	-0.15,+0.07	—	—	+0.00,-0.00	+1.62,-1.62	+0.21,-0.25	+1.25,-1.32	—	—
$M_{Y=110}$	+2.86,-2.97	—	+0.25,+0.16	+24.44,-19.66	+0.03,-0.05	—	—	-0.06,-0.06	+1.52,-1.53	+0.20,-0.24	+1.28,-1.36	—	—
$M_{Y=120}$	+2.91,-3.04	—	+0.11,+0.07	+27.64,-21.29	-0.29,+0.29	—	—	-0.03,-0.02	+1.39,-1.40	+0.18,-0.22	+1.24,-1.31	—	—
$M_{Y=130}$	+2.80,-2.95	—	+0.17,+0.11	+30.01,-22.86	-0.03,-0.02	—	—	-0.03,-0.04	+1.35,-1.36	+0.17,-0.21	+1.26,-1.34	—	—
$M_{Y=140}$	+2.85,-3.01	—	+0.16,+0.10	+33.07,-24.31	-0.01,+0.03	—	—	-0.00,-0.00	+1.25,-1.25	+0.16,-0.19	+1.24,-1.31	—	—
$M_{Y=150}$	+2.89,-3.04	—	+0.22,+0.14	+36.65,-25.93	-0.59,+0.55	—	—	-0.00,+0.00	+1.23,-1.24	+0.16,-0.19	+1.24,-1.31	—	—
$M_{Y=160}$	+2.86,-3.02	—	+0.11,+0.07	+42.14,-27.83	+0.10,-0.21	—	—	-0.01,-0.01	+1.14,-1.15	+0.14,-0.17	+1.21,-1.28	—	—
$M_{Y=170}$	+2.82,-2.96	—	+0.07,+0.04	+45.09,-29.45	-0.77,+0.77	—	—	+0.02,+0.02	+1.11,-1.11	+0.14,-0.17	+1.19,-1.26	—	—
$M_{Y=180}$	+2.85,-3.00	—	+0.26,+0.16	+48.71,-31.14	-0.44,+0.47	—	—	-0.00,+0.04	+1.06,-1.06	+0.13,-0.16	+1.16,-1.22	—	—
$M_{Y=190}$	+2.81,-2.94	—	+0.21,+0.13	+52.23,-32.31	-0.20,+0.20	—	—	-0.00,+0.04	+1.10,-1.10	+0.13,-0.16	+1.18,-1.25	—	—
$M_{Y=200}$	+2.72,-2.84	—	+0.30,+0.19	+57.43,-34.13	+0.05,+0.03	—	—	-0.00,+0.00	+0.98,-0.98	+0.12,-0.15	+1.13,-1.20	—	—
$M_{Y=800}$	+2.96,-3.02	—	+0.42,+0.27	+16.63,-14.20	-0.57,+0.45	—	—	-0.00,+0.00	+1.78,-1.79	+0.24,-0.28	+1.23,-1.30	—	—
$M_{Y=900}$	+2.96,-3.03	—	+0.25,+0.16	+19.24,-16.06	-0.16,+0.12	—	—	-0.03,-0.03	+1.67,-1.68	+0.22,-0.26	+1.25,-1.33	—	—
diBoson	+3.80,-3.87	—	+10.37,+6.78	+4.75,-5.89	-0.23,+0.20	—	—	-0.00,+0.00	+1.80,-1.81	+0.23,-0.28	+1.41,-1.48	—	—
qcd	—	—	—	—	—	—	+169.00,-50.00	—	—	—	—	—	—
sts	+0.76,-1.03	—	+0.16,+0.10	+5.98,-5.91	-0.45,+0.55	—	—	+0.00,+0.00	+1.67,-1.68	+0.23,-0.27	+1.21,-1.28	—	—
stt	+1.41,-1.59	+0.54,-2.37	-0.08,-0.05	+6.96,-5.20	-0.28,+0.21	—	—	+0.00,-0.00	+1.62,-1.63	+0.23,-0.27	+1.15,-1.21	—	—
sttW	+2.53,-2.62	-0.64,-3.62	+0.21,+0.14	+13.40,-10.22	-0.27,+0.26	—	—	+0.00,-0.00	+1.71,-1.71	+0.23,-0.27	+1.20,-1.27	—	—
ttbar	+2.01,-2.12	+2.79,-1.07	+0.24,+0.16	+9.87,-7.65	-0.32,+0.31	—	—	-0.01,-0.01	+1.67,-1.67	+0.23,-0.27	+1.18,-1.24	—	—

Table 6.2: Rate effects of systematic uncertainties used in limit combination. The uncertainty sources listed here affect the semileptonic analysis and are not correlated with uncertainties in the other channels. This table details the semileptonic muon channel. This table considers the right-handed signal hypothesis.

Rate Effects of Systematic Uncertainties

Sample	QCD Uncertainty	top-tagging	W-tagging	Trigger	ttbar Rate
$M_{b^*=1000}$	—	**+12.50,-11.11**	**+7.60,-7.06**	**+0.14,-0.14**	—
$M_{b^*=1100}$	—	**+12.50,-11.11**	**+7.60,-7.06**	**+0.07,-0.07**	—
$M_{b^*=1200}$	—	**+12.50,-11.11**	**+7.60,-7.06**	**+0.04,-0.04**	—
$M_{b^*=1300}$	—	**+12.50,-11.11**	**+7.60,-7.06**	**+0.03,-0.03**	—
$M_{b^*=1400}$	—	**+12.50,-11.11**	**+7.60,-7.06**	**+0.02,-0.02**	—
$M_{b^*=1500}$	—	**+12.50,-11.11**	**+7.60,-7.06**	**+0.02,-0.02**	—
$M_{b^*=1600}$	—	**+12.50,-11.11**	**+7.60,-7.06**	**+0.01,-0.01**	—
$M_{b^*=1700}$	—	**+12.50,-11.11**	**+7.60,-7.06**	**+0.01,-0.01**	—
$M_{b^*=1800}$	—	**+12.50,-11.11**	**+7.60,-7.06**	**+0.01,-0.01**	—
$M_{b^*=1900}$	—	**+12.50,-11.11**	**+7.60,-7.06**	**+0.01,-0.01**	—
$M_{b^*=2000}$	—	**+12.50,-11.11**	**+7.60,-7.06**	**+0.01,-0.01**	—
$M_{b^*=800}$	—	**+12.50,-11.11**	**+7.60,-7.06**	**+0.19,-0.19**	—
$M_{b^*=900}$	—	**+12.50,-11.11**	**+7.60,-7.06**	**+0.28,-0.28**	—
qcd	**+28.14,-27.56**	—	—	—	—
sts	—	**+12.50,-11.11**	**+7.60,-7.06**	**+nan,+nan**	—
stt	—	**+12.50,-11.11**	**+7.60,-7.06**	**+0.13,-0.13**	—
sttW	—	**+12.50,-11.11**	**+7.60,-7.06**	**+0.09,-0.09**	—
ttbar	—	—	**+7.60,-7.06**	**+0.10,-0.10**	**+22.00,-18.03**

Table 6.3: Rate effects of systematic uncertainties used in limit combination. The uncertainty sources listed here affect the all-hadronic analysis and are not correlated with uncertainties in the other channels. This table considers the right-handed signal hypothesis.

Rate Effects of Systematic Uncertainties

Sample	Flat Uncertainty	W+jets Rate
WJets	**+16.50,-14.16**	**+30.00,-23.08**
ZJets	**+16.50,-14.16**	—
$M_{b^*=1000}$	**+32.80,-24.70**	—
$M_{b^*=1100}$	**+32.80,-24.70**	—
$M_{b^*=1200}$	**+32.80,-24.70**	—
$M_{b^*=1300}$	**+32.80,-24.70**	—
$M_{b^*=1400}$	**+32.80,-24.70**	—
$M_{b^*=1500}$	**+32.80,-24.70**	—
$M_{b^*=1600}$	**+32.80,-24.70**	—
$M_{b^*=1700}$	**+32.80,-24.70**	—
$M_{b^*=1800}$	**+32.80,-24.70**	—
$M_{b^*=1900}$	**+32.80,-24.70**	—
$M_{b^*=2000}$	**+32.80,-24.70**	—
$M_{b^*=800}$	**+32.80,-24.70**	—
$M_{b^*=900}$	**+32.80,-24.70**	—
diBoson	**+16.50,-14.16**	—
sttW	**+16.50,-14.16**	—
ttbar	**+16.50,-14.16**	—

Table 6.4: Rate effects of systematic uncertainties used in limit combination. The uncertainty sources listed here affect the dilepton analysis and are not correlated with uncertainties in the other channels. This table considers the right-handed signal hypothesis.

Rate Effects of Systematic Uncertainties

Sample	JER	JES	Q^2	DiBoson Rate	Luminosity	s Channel Rate	tW Channel Rate	t Channel Rate	ttbar Rate	Z+Jets Rate
WJets	+0.26,-0.17	+3.01,-3.28	—	—	—	—	—	—	—	—
ZJets	-4.73,+4.80	-2.19,-0.30	—	—	+2.63,-2.57	—	—	—	—	+20.00,-16.67
M_{b^*}=1000	-0.47,+0.27	-0.02,+0.16	—	—	+2.63,-2.57	—	—	—	—	—
M_{b^*}=1100	-0.72,+0.69	+0.41,-0.36	—	—	+2.63,-2.57	—	—	—	—	—
M_{b^*}=1200	+0.05,+0.37	+0.09,-0.05	—	—	+2.63,-2.57	—	—	—	—	—
M_{b^*}=1300	-0.14,+1.11	+0.67,-0.56	—	—	+2.63,-2.57	—	—	—	—	—
M_{b^*}=1400	-0.73,+0.16	-0.10,-0.05	—	—	+2.63,-2.57	—	—	—	—	—
M_{b^*}=1500	+0.07,-0.38	+0.07,-0.51	—	—	+2.63,-2.57	—	—	—	—	—
M_{b^*}=1600	-1.12,+0.14	-0.30,-0.69	—	—	+2.63,-2.57	—	—	—	—	—
M_{b^*}=1700	-0.99,+0.58	-0.17,+0.12	—	—	+2.63,-2.57	—	—	—	—	—
M_{b^*}=1800	-0.50,-0.17	-0.32,-0.08	—	—	+2.63,-2.57	—	—	—	—	—
M_{b^*}=1900	-0.55,+0.61	+0.16,-0.44	—	—	+2.63,-2.57	—	—	—	—	—
M_{b^*}=2000	-0.76,+0.61	-0.31,+0.82	—	—	+2.63,-2.57	—	—	—	—	—
M_{b^*}=800	-0.12,+0.73	+1.04,+0.43	—	—	+2.63,-2.57	—	—	—	—	—
M_{b^*}=900	-0.41,+0.78	+0.45,+0.30	—	—	+2.63,-2.57	—	—	—	—	—
diBoson	+2.20,+1.15	+2.05,-0.97	—	+30.00,-23.08	+2.63,-2.57	—	—	—	—	—
qcd	—	—	—	—	—	—	—	—	—	—
sts	+0.08,+0.34	+1.52,-1.36	—	—	+2.63,-2.57	+30.00,-23.08	—	—	—	—
stt	-0.97,+0.40	+1.73,-2.86	-14.34,-2.92	—	+2.63,-2.57	—	—	+15.00,-13.04	—	—
sttW	-0.21,+0.37	+0.81,-1.04	—	—	+2.63,-2.57	—	+20.00,-16.67	—	—	—
ttbar	-0.48,+0.41	-0.31,-0.23	+9.23,-4.78	—	+2.63,-2.57	—	—	—	+5.30,-5.03	—

Table 6.5: Rate effects of systematic uncertainties used in limit combination. The uncertainty sources listed here are correlated over multiple channels. This table considers the right-handed signal hypothesis And the semileptonic electron analysis.

Rate Effects of Systematic Uncertainties

Sample	JER	JES	Q^2	DiBoson Rate	Luminosity	s Channel Rate	tW Channel Rate	t Channel Rate	ttbar Rate	Z+Jets Rate
WJets	+0.43,-0.74	+2.10,-3.19	—	—	—	—	—	—	—	—
ZJets	+1.41,-2.14	+2.92,+7.70	—	—	+2.63,-2.57	—	—	—	—	+20.00,-16.67
M_{b^*}=1000	-0.22,+0.41	+0.53,+0.13	—	—	+2.63,-2.57	—	—	—	—	—
M_{b^*}=1100	-0.47,+0.13	+0.04,+0.15	—	—	+2.63,-2.57	—	—	—	—	—
M_{b^*}=1200	-0.59,+0.00	-0.05,-0.93	—	—	+2.63,-2.57	—	—	—	—	—
M_{b^*}=1300	-0.59,+0.19	-0.55,-0.05	—	—	+2.63,-2.57	—	—	—	—	—
M_{b^*}=1400	-0.40,+0.53	+0.23,-0.36	—	—	+2.63,-2.57	—	—	—	—	—
M_{b^*}=1500	-0.35,+0.38	+0.42,-0.93	—	—	+2.63,-2.57	—	—	—	—	—
M_{b^*}=1600	-0.88,+0.17	-0.47,-0.10	—	—	+2.63,-2.57	—	—	—	—	—
M_{b^*}=1700	-0.33,-0.04	-0.14,+0.03	—	—	+2.63,-2.57	—	—	—	—	—
M_{b^*}=1800	-0.08,+0.47	-0.39,-0.07	—	—	+2.63,-2.57	—	—	—	—	—
M_{b^*}=1900	-0.10,-0.25	+0.35,-0.15	—	—	+2.63,-2.57	—	—	—	—	—
M_{b^*}=2000	-0.13,-0.11	+0.43,-0.51	—	—	+2.63,-2.57	—	—	—	—	—
M_{b^*}=800	+0.12,+0.23	+0.63,-0.25	—	—	+2.63,-2.57	—	—	—	—	—
M_{b^*}=900	-0.15,+0.51	+0.54,+0.25	—	—	+2.63,-2.57	—	—	—	—	—
diBoson	-1.95,-0.25	+1.88,-5.76	—	+30.00,-23.08	+2.63,-2.57	—	—	—	—	—
qcd	—	—	—	—	—	—	—	—	—	—
sts	-0.38,-0.49	+1.11,-0.99	—	—	+2.63,-2.57	+30.00,-23.08	—	—	—	—
stt	-0.30,-0.68	+2.69,-2.35	-17.72,+7.61	—	+2.63,-2.57	—	—	+15.00,-13.04	—	—
sttW	-0.30,+0.38	+1.33,-1.08	—	—	+2.63,-2.57	—	+20.00,-16.67	—	—	—
ttbar	-0.46,+0.10	-0.69,-0.05	+9.31,+0.11	—	+2.63,-2.57	—	—	—	+5.30,-5.03	—

Table 6.6: Rate effects of systematic uncertainties used in limit combination. The uncertainty sources listed here are correlated over multiple channels. This table considers the right-handed signal hypothesis And the semileptonic muon analysis.

Rate Effects of Systematic Uncertainties

Sample	JER	JES	Q^2	DiBoson Rate	Luminosity	s Channel Rate	tW Channel Rate	t Channel Rate	ttbar Rate	Z+Jets Rate
WJets	+0.00,+0.00	+0.00,+0.00	—	—	+2.63,-2.57	—	—	—	—	—
ZJets	-17.13,-45.69	-17.16,-17.13	—	—	+2.63,-2.57	—	—	—	—	+20.00,-16.67
$M_{b^*=1000}$	+0.00,-0.00	-0.00,+0.00	—	—	+2.63,-2.57	—	—	—	—	—
$M_{b^*=1100}$	+0.00,-0.00	-0.00,+0.00	—	—	+2.63,-2.57	—	—	—	—	—
$M_{b^*=1200}$	-0.00,-0.01	-0.01,+0.00	—	—	+2.63,-2.57	—	—	—	—	—
$M_{b^*=1300}$	-0.00,-0.00	-0.01,-0.00	—	—	+2.63,-2.57	—	—	—	—	—
$M_{b^*=1400}$	-0.00,-0.02	-0.03,+0.01	—	—	+2.63,-2.57	—	—	—	—	—
$M_{b^*=1500}$	-0.01,-0.01	-0.03,+0.01	—	—	+2.63,-2.57	—	—	—	—	—
$M_{b^*=1600}$	-0.01,+0.00	-0.02,+0.01	—	—	+2.63,-2.57	—	—	—	—	—
$M_{b^*=1700}$	+0.01,-0.01	-0.03,+0.02	—	—	+2.63,-2.57	—	—	—	—	—
$M_{b^*=1800}$	-0.00,-0.02	-0.04,+0.01	—	—	+2.63,-2.57	—	—	—	—	—
$M_{b^*=1900}$	+0.00,-0.01	-0.04,+0.03	—	—	+2.63,-2.57	—	—	—	—	—
$M_{b^*=2000}$	+0.02,+0.00	-0.03,+0.05	—	—	+2.63,-2.57	—	—	—	—	—
$M_{b^*=800}$	+0.00,-0.00	+0.00,+0.00	—	—	+2.63,-2.57	—	—	—	—	—
$M_{b^*=900}$	+0.00,-0.00	-0.00,+0.00	—	—	+2.63,-2.57	—	—	—	—	—
diBoson	-0.00,+0.00	-0.00,-0.00	—	+30.00,-23.08	+2.63,-2.57	—	—	—	—	—
sttW	-0.00,-0.00	-0.00,+0.00	—	—	+2.63,-2.57	—	+20.00,-16.67	—	—	—
ttbar	-0.00,+0.00	+0.00,+0.00	—	—	+2.63,-2.57	—	—	—	+5.30,-5.03	—

Table 6.7: Rate effects of systematic uncertainties used in limit combination. The uncertainty sources listed here are correlated over multiple channels. This table considers the right-handed signal hypothesis And the dilepton analysis.

Rate Effects of Systematic Uncertainties

Sample	JER	JES	Q^2	DiBoson Rate	Luminosity	s Channel Rate	tW Channel Rate	t Channel Rate	ttbar Rate	Z+Jets Rate
M_{b^*}=1000	-0.81,+0.51	+17.91,-21.34	—	—	+2.63,-2.57	—	—	—	—	—
M_{b^*}=1100	-0.51,+0.60	+9.07,-12.13	—	—	+2.63,-2.57	—	—	—	—	—
M_{b^*}=1200	-0.41,+0.60	+6.12,-9.76	—	—	+2.63,-2.57	—	—	—	—	—
M_{b^*}=1300	-0.42,+0.41	+4.98,-8.06	—	—	+2.63,-2.57	—	—	—	—	—
M_{b^*}=1400	-0.53,+0.40	+4.20,-7.65	—	—	+2.63,-2.57	—	—	—	—	—
M_{b^*}=1500	-0.46,+0.42	+4.50,-7.76	—	—	+2.63,-2.57	—	—	—	—	—
M_{b^*}=1600	-0.48,+0.37	+3.79,-7.33	—	—	+2.63,-2.57	—	—	—	—	—
M_{b^*}=1700	-0.34,+0.35	+3.91,-6.43	—	—	+2.63,-2.57	—	—	—	—	—
M_{b^*}=1800	-0.48,+0.39	+3.71,-7.64	—	—	+2.63,-2.57	—	—	—	—	—
M_{b^*}=1900	-0.46,+0.44	+3.31,-7.12	—	—	+2.63,-2.57	—	—	—	—	—
M_{b^*}=2000	-0.46,+0.41	+3.14,-7.29	—	—	+2.63,-2.57	—	—	—	—	—
M_{b^*}=800	-0.00,+0.56	+29.42,-25.25	—	—	+2.63,-2.57	—	—	—	—	—
M_{b^*}=900	-0.18,+0.42	+46.46,-35.69	—	—	+2.63,-2.57	—	—	—	—	—
qcd	—	—	—	—	—	—	—	—	—	—
sts	+nan,+nan	+nan,+nan	—	—	+2.63,-2.57	+30.00,-23.08	—	—	—	—
stt	-0.11,+17.70	+47.87,-16.85	—	—	+2.63,-2.57	—	—	+15.00,-13.04	—	—
sttW	+0.01,-0.00	+17.42,-13.16	—	—	+2.63,-2.57	—	+20.00,-16.67	—	—	—
ttbar	-0.22,+1.05	+13.20,-14.75	+16.24,-23.58	—	—	—	—	—	—	—

Table 6.8: Rate effects of systematic uncertainties used in limit combination. The uncertainty sources listed here are correlated over multiple channels. This table considers the right-handed signal hypothesis And the all hadronic analysis.

Bibliography

[1] K. Olive *et al.*, "Review of particle physics," *Chin.Phys.*, vol. C38, p. 090001, 2014.

[2] "Lhc the guide," http://cds.cern.ch/record/1092437/files/CERN-Brochure-2008-001-Eng.pdf.

[3] J. Ocariz, "Probability and Statistics for Particle Physicists," no. arXiv:1405.3402, p. 28 p, May 2014.

[4] D. Griffiths, *Introduction to Elementary Particles*, ser. Physics textbook. Wiley, 2008. [Online]. Available: http://books.google.com/books?id=w9Dz56myXm8C

[5] "Fermilab today," http://www.fnal.gov/pub/today/archive/archive_2009/today09-11-12.html.

[6] C. L. Bennett *et al.*, "The microwave anisotropy probe (map) mission," *Astrophys. J.*, vol. 583, p. 1, 2003.

[7] F. An *et al.*, "Observation of electron-antineutrino disappearance at Daya Bay," *Phys.Rev.Lett.*, vol. 108, p. 171803, 2012.

[8] T. Appelquist, H.-C. Cheng, and B. A. Dobrescu, "Bounds on universal extra dimensions," *Phys. Rev. D*, vol. 64, p. 035002, Jun 2001. [Online]. Available: http://link.aps.org/doi/10.1103/PhysRevD.64.035002

[9] M. Schmaltz and D. Tucker-Smith, "Little higgs theories," *Annual Review of Nuclear and Particle Science*, vol. 55, no. 1, pp. 229–270, 2005.

[10] L. Vecchi, "The Natural Composite Higgs," 2013.

[11] R. Chivukula, E. H. Simmons, and J. Terning, "Limits on noncommuting extended technicolor," *Phys.Rev.*, vol. D53, pp. 5258–5267, 1996.

[12] S. Chatrchyan *et al.*, *CMS Physics: Technical Design Report Volume 1: Detector Performance and Software*, ser. Technical Design Report CMS. Geneva: CERN, 2006, there is an error on cover due to a technical problem for some items.

[13] D0 Collaboration, "Search for w' boson resonances decaying to a top quark and a bottom quark," *Phys. Rev. Lett.*, vol. 100, p. 211803, May 2008. [Online]. Available: http://link.aps.org/doi/10.1103/PhysRevLett.100.211803

[14] V. M. Abazov *et al.*, "Search for $W' \to tb$ resonances with left- and right-handed couplings to fermions," *Phys.Lett.*, vol. B699, pp. 145–150, 2011.

[15] "Search for narrow t + b resonances in the leptonic final state at sqrt(s) = 8 tev," CERN, Geneva, Tech. Rep. CMS-PAS-B2G-12-010, 2013.

[16] "Search for leptonic decays of W' bosons in pp collisions at sqrt(s)=8 TeV," CERN, Geneva, Tech. Rep. CMS-PAS-EXO-12-060, 2013.

[17] "Search for W'/technirho in WZ using leptonic final states," CERN, Geneva, Tech. Rep. CMS-PAS-EXO-12-025, 2013.

[18] ATLAS, "Search for tb resonances in proton-proton collisions at $\sqrt{s}$=7 TeV with the atlas detector," *Phys. Rev. Lett.*, vol. 109, p. 081801, Aug 2012. [Online]. Available: http://link.aps.org/doi/10.1103/PhysRevLett.109.081801

[19] "Search for BSM $t\bar{t}$ Production in the Boosted All-Hadronic Final State," CERN, Geneva, Tech. Rep. CMS-PAS-EXO-11-006, 2011.

[20] T. Muller, J. Ott, and J. Wagner-Kuhr, "theta - a framework for template-based modeling and inference," CMS Internal Note 2010/017, 2010.

[21] C. Oleari, "The POWHEG-BOX," *Nucl.Phys.Proc.Suppl.*, vol. 205-206, pp. 36–41, 2010.

[22] M. Czakon, P. Fiedler, and A. Mitov, "Total Top-Quark Pair-Production Cross Section at Hadron Colliders Through $O(\frac{4}{S})$," *Phys.Rev.Lett.*, vol. 110, no. 25, p. 252004, 2013.

[23] N. Kidonakis, "Differential and total cross sections for top pair and single top production," pp. 831–834, 2012.

[24] E. Boos *et al.*, "CompHEP 4.4: Automatic computations from Lagrangians to events," *Nucl.Instrum.Meth.*, vol. A534, pp. 250–259, 2004.

[25] Z. Sullivan, "Fully differential w' production and decay to next-to-leading order in qcd," *Phys. Rev.*, vol. D66, 2002.

[26] "8 TeV Jet Energy Corrections and Uncertainties based on 19.8 fb^{-1} of data in CMS," Oct 2013.

[27] Y. L. Dokshitzer, G. D. Leder, S. Moretti, and B. R. Webber, "Better Jet Clustering Algorithms," *JHEP*, vol. 08, p. 001, 1997.

[28] M. Wobisch and T. Wengler, "Hadronization corrections to jet cross sections in deep- inelastic scattering," 1998.

[29] M. Cacciari and G. P. Salam, "Dispelling the N**3 myth for the k(t) jet-finder," *Phys. Lett. B*, vol. 641, pp. 57–61, 2006.

[30] M. Cacciari, G. P. Salam, and G. Soyez, "FastJet User Manual," *Eur.Phys.J.*, vol. C72, p. 1896, 2012.

[31] "A Cambridge-Aachen (C-A) based Jet Algorithm for boosted top-jet tagging," CERN, Geneva, Tech. Rep. CMS-PAS-JME-09-001, 2009.

[32] J. Group, "Jet Energy Corrections and Uncertainties. Detector Performance Plots for 2012."

[33] "Jet performance in pp collisions at $\sqrt{s} = 7$ tev," *CMS PAS JME-10-003*, 2010.

[34] "Boosted Top Jet Tagging at CMS," CERN, Geneva, Tech. Rep. CMS-PAS-JME-13-007, 2014.

[35] J. Thaler and K. Van Tilburg, "Maximizing Boosted Top Identification by Minimizing N-subjettiness," *JHEP*, vol. 1202, p. 093, 2012.

[36] "Performance of b tagging at sqrt(s)=8 tev in multijet, ttbar and boosted topology events," CERN, Geneva, Tech. Rep. CMS-PAS-BTV-13-001, 2013.

[37] "Search for Anomalous Top Quark Pair Production in the Boosted All-Hadronic Final State using pp Collisions at sqrt(s) = 8 TeV," CERN, Geneva, Tech. Rep. CMS-PAS-B2G-12-005, 2013.

[38] D. Bourilkov, R. C. Group, and M. R. Whalley, "LHAPDF: PDF use from the Tevatron to the LHC," 2006.

[39] "CMS Luminosity Based on Pixel Cluster Counting - Summer 2013 Update," CERN, Geneva, Tech. Rep. CMS-PAS-LUM-13-001, 2013.

[40] S. Chatrchyan *et al.*, "Search for W' $\rightarrow$ tb decays in the lepton + jets final state in pp collisions at $\sqrt{s} = 8$ TeV," *JHEP*, vol. 1405, p. 108, 2014.

[41] T. M. Tait and C.-P. Yuan, "Single top quark production as a window to physics beyond the standard model," *Phys.Rev.*, vol. D63, p. 014018, 2000.

[42] G. Aad *et al.*, "Search for single b^*-quark production with the ATLAS detector at $\sqrt{s} = 7$ TeV," *Phys.Lett.*, vol. B721, pp. 171–189, 2013.

[43] P. M. Kevin Nash, "Search for single b*-quark production in the all hadronic final state," *CMS Analysis Note*, vol. AN2014/049, 2014. [Online]. Available: cms.cern.ch/iCMS/jsp/openfile.jsp?tp=draft&files=AN2014_049_v3.pdf

[44] G. C. X. M. S. S. H. Zhang and S. Zhu, "Search for singly produced b* decaying to Wt in the lepton+jets channel with the CMS detector at s = 8 TeV," *CMS Analysis Note*, vol. AN2014/103, 2014. [Online]. Available: cms.cern.ch/iCMS/jsp/openfile.jsp?tp=draft&files=AN2014_103_v3.pdf

[45] H. Z. Rachel Bartek, Freya Blekman, "Search for single b*-quark production in the dilepton final state," *CMS Analysis Note*, vol. AN2013/415, 2013. [Online]. Available: cms.cern.ch/iCMS/jsp/openfile.jsp?tp=draft&files=AN2013_415_v3.pdf

Vita

Education

- Ph.D. Physics, Johns Hopkins University, Expected 2015.
- M.A. Physics, Johns Hopkins University, 2012.
- B.S. Physics, James Madison University, 2009.

Experience

- Research
  - **CMS Collaboration**, 2010–Present
  - **Jefferson Lab**, 2009–2010
  - **MINERvA Experiment**, 2008-2009
- Teaching

  - Johns Hopkins University, 2010–2012

- Outreach

  - USA Science and Engineering Festival, 2013,2014

  - High School Basic Research Presentations, 2013

  - JHU Physics Fair, 2011,2012,2013,2014

Publications and Physics Analysis Summaries (in order of contribution)

- *Search for* $W' \to t\bar{b}$ *in the all-hadronic final state*, The CMS Collaboration, **CMS Physics Analysis Summary**, CMS PAS B2G-12-009 2014 (manuscript in preparation)

- *Search for singly produced* b^* *decaying to tW in the lepton+jets, dilepton and full hadronic channel with the CMS detector at* $\sqrt{s} = 8$ *TeV*, The CMS Collaboration, **CMS Physics Analysis Summary**, CMS PAS B2G-14-005 2014 (not yet public)

- *Boosted Top Jet Tagging at CMS*, The CMS Collaboration, **CMS Physics Analysis Summary**, CMS PAS JME-13-007 2013

- *Search for new physics using the $t\bar{t}$ invariant mass distribution in pp collisions at $\sqrt{s} = 8\ TeV$*, The CMS Collaboration, **Phys. Rev. Lett.** PhysRevLett.111.211804 2013

Presentations at Conferences

- *Boosted top quarks in physics analyses*, **Boost 2014**, London, UK., August 2014